# Confinement effect of Nickel in mesoporous silica-based catalysts for syngas production by reforming of methane with CO2

Marie-Nour Kaydouh

# Université Pierre et Marie Curie (UPMC)

Ecole doctorale de Physique et Chimie des Matériaux – ED 397

*Laboratoire de Réactivité de Surface (LRS)*

# University of Balamand (UOB)

*Department of Chemical Engineering*


# Confinement effect of Nickel in mesoporous silica-based catalysts for syngas production by reforming of methane with $CO_2$


By Marie-Nour KAYDOUH


Doctoral Thesis in Chemistry

Co-directed by Mrs. Pascale MASSIANI and Mrs. Nissrine EL HASSAN

Defense expected on November 3, 2016

Jury members:

| | | |
|---|---|---|
| Mr. Antoine GEDEON | Professor (UPMC) | President |
| Mrs. Anne-Cécile ROGER | Professor (University of Strasbourg) | Reviewer |
| Mrs. Maya BOUTROS | Professor (Lebanese University) | Reviewer |
| Mr. Axel LOFBERG | CNRS Researcher (University Lille 1) | Examiner |
| Mr. Paolo YAMMINE | Associate Professor (UOB) | Examiner |
| Mrs. Pascale MASSIANI | Professor (UPMC) | Co-supervisor |
| Mrs. Nissrine EL HASSAN | Associate Professor (UOB) | Co-supervisor |

# Université Pierre et Marie Curie (UPMC)

Ecole doctorale de Physique et Chimie des Matériaux – ED 397

*Laboratoire de Réactivité de Surface (LRS)*

# University of Balamand (UOB)

*Department of Chemical Engineering*


# Effet de confinement du nickel dans des catalyseurs à base de silice mésoporeuse pour la production de gas de synthèse par reformage du méthane avec le $CO_2$


Par Marie-Nour KAYDOUH


Thèse de doctorat de Chimie

Co-dirigée par Mme Pascale MASSIANI et Mme Nissrine EL HASSAN

Soutenance prévue le 3 Novembre 2016

Devant un jury composé de :

| | | |
|---|---|---|
| M. Antoine GEDEON | Professeur (UPMC) | Président |
| Mme Anne-Cécile ROGER | Professeur (Université de Strasbourg) | Rapporteur |
| Mme Maya BOUTROS | Professeur (Université Libanaise) | Rapporteur |
| M. Axel LOFBERG | Chercheur CNRS (Université Lille 1) | Examinateur |
| M. Paolo YAMMINE | Associate Professor (UOB) | Examinateur |
| Mme Pascale MASSIANI | Professeur (UPMC) | Co-directrice de thèse |
| Mme Nissrine EL HASSAN | Associate Professor (UOB) | Co-directrice de thèse |

*To my parents*

*To my sister*

# Acknowledgements

When I came to write my acknowledgments, I realized how fruitful these past three years were. I did not only promote my scientific maturity but I also acquired experience in different domains and I gained true friends for life.

This work was performed in collaboration between the Laboratoire de Réactivité de Surface at the University Pierre et Marie Curie and the Department of Chemical Engineering at the University of Balamand, between 2013 and 2016. It was carried out thanks to the Balamand Internal Research Grant BIRG 14/2012 and the Innovation Voucher from the Center for Innovation & Technology (CIT). The French-Lebanese CEDRE Hubert Curien Partnership (PHC) financially supported the mobility between the two countries (project number 30962ZH, 2014-2015).

My biggest gratitude goes first to my supervisors who have greatly invested in this thesis. Their guidance, valuable advices and continuous motivation were essential for the completion of this work. Specifically, I begin by expressing my gratitude to my PhD co-supervisor, Dr. Nissrine El Hassan. I thank her for the trust she placed in me by giving me the privilege of being her first PhD student. I thoroughly enjoyed working with her not only because of her deep scientific skills but also for her adorable personal qualities. Indeed, she motivated me throughout this project to bring out the best in me. I will be forever indebted to her for promoting and nourishing my intellectual maturity. She will remain my role model who embody hard work, resolution and success.

I also owe my deepest gratitude to my PhD co-supervisor, Dr. Pascale Massiani. She constituted a backbone of this work. Her supervision motivated and enriched my development as a researcher. The ideas and skills we shared were very fruitful for shaping up my research. I appreciate the time she spent teaching me how to interpret and present my work, carefully taking care of all the details. Without her, I would not have been as independent and responsible as I am today. The exceptional smile she wears on her face will always reflect optimism and positive energy.

Further recognition should be offered to my moderator, Dr. Anne Davidson. I greatly recognize her availability at all times and I specially thank her for sharing her knowledge and experience with me.

It is a pleasure to thank Dr. Maya Boutros and Dr. Anne-Cécile Roger for accepting to read my manuscript and give their objective opinion about this work. I am honored by their presence with Dr. Paolo Yammine, Dr. Axel Lofberg and Dr. Antoine Gédeon as jury members to evaluate my work.

I would like to thank Mrs. Sandra Casale for the TEM/SEM observations, Mr. Christophe Calers for the XPS measurements, Mrs. Hala Fallah for the XRD experiments, Dr. Jean-Marc Krafft for teaching me how to conduct the Raman experiments and Dr. Simon Yunes from Micromeritics, USA for his help in technical problems. A special thanks also goes to Dr. Henri El Zakhem, the chairperson of the chemical engineering department, for his continuous support.

On a more personal level, I would like to address my gratitude to Mr. Gabriel and Mrs. Marie-Jeanne Peltre for their kind hospitality in France. Also, I would like to thank Mr. Ghassan Akkary because he believed in me and continuously encouraged me.

To live alone in a foreign city would not have been easy without the presence of Mariame, Achraf and Olfa with whom I have shared lots of beautiful moments and unforgettable memories. Thank you dear friends for being my home away from home. I cannot forget the kindness of Jane, Nabil, Alice, Xiaojing and all the staff of the LRS.

Back to my Lebanon, I deeply appreciate the presence of Hala, Michella, Katia, Makram and Joy by my side throughout this time. Your support and encouragement were worth more than I can express. A special thanks goes to Adib who shared this journey with me, especially during its most difficult times. He was readily available to listen to my nagging then comfort me with his meaningful words.

At the end, words fail to convey my appreciation to my parents, Georges and Dola, and to all my family for their unconditional love and support. I owe them my achievements and success. They were always there to encourage and comfort me when necessary. The courage of my parents and their determination to achieve their goals has been and will always be an example for me to follow. And to the world's best little sister, my Eliane, "I'm everything I am, because you loved me!"

To all of them, thank you.

# Table of Content

# GENERAL INTRODUCTION

Fossil fuels have enormously contributed in the development of the industrial sector and the global economy. Nevertheless, petroleum resources are limited and, in addition, their use has significantly affected the environment through the emission of pollutants contributing, among other problems, in global warming. Alternatively, hydrogen ($H_2$) and carbon monoxide (CO) play a significant role in the production of food, fuel and chemicals. Indeed, important applications of hydrogen include ammonia synthesis, hydrotreating, hydrocracking and fuel cells, and both hydrogen and carbon monoxide are essential reactants for methanol and Fisher-Tropsch syntheses of alkanes. These processes require large amounts of $H_2$ and CO in order to achieve large capacity production. Consequently, multiple pathways have been considered for the generation of hydrogen and carbon monoxide; among them, one can list the catalytic steam reforming, dry reforming, partial oxidation and auto-thermal reforming. These processes mainly rely on the reforming of methane that is widely available in natural gas and in emissions from gasification of biomass.

In Lebanon, in particular, studies have recently shown that the Lebanese offshore is rich in natural gas. In addition, the garbage crisis in Lebanon is an alarming situation that requires great attention and urgent solution. In the absence of waste management strategies and national awareness campaigns about the importance of recycling, measures should be taken as soon as possible to conserve the natural image of our country. In this context, the waste utilization and conversion into higher-value products, like liquid fuels and electricity, is extremely important. On one hand, it can reduce the environmental impact of the trash crisis and can limit, on the other hand, the elevated energy cost paid by the industrial sector.

The present study is applied for the reaction of dry reforming of methane. So far, this process still encounters difficulties related to the existing catalysts. Indeed, the most active and stable catalysts, based on noble metals, are expensive while cheaper catalysts, based on transition metals, particularly nickel, suffer from carbon deposition and active phase sintering under the reaction conditions. It is thus important to develop performing and stable catalysts while ensuring reasonable cost.

The recent publications available are interested in mesoporous supports that seem to exert a confinement effect on the supported metal particles, preventing their sintering and hence contributing in their superior stability. However, the preparation methods do not provide a

complete internal deposition of the metals inside the pores. Therefore, in this work, we will check if the confinement effect, particularly on silica-based mesoporous materials, is a key parameter for enhanced catalytic stability. We will also investigate the potential beneficial effect of forming very small metal nanoparticles highly dispersed inside the support towards better coke resistance.

The research was conducted in a joint PhD - or "cotutelle" thesis - between the Laboratoire de Réactivité de Surface at the Université Pierre et Marie Curie (France) and the Department of Chemical Engineering at the University of Balamand (Lebanon), on the basis of alternating six months periods.

The manuscript is divided into six main chapters. Chapter I is an introductory chapter that will provide a general overview on reforming processes and on the dry reforming of methane, in specific. It also details the successive efforts carried out in literature to improve the characteristics of the catalysts in the domain.

Chapter II describes the experimental work and characterization methods used in this thesis. It will thus describe (i) the preparation of the samples and (ii) the characterization techniques used at different stages of synthesis and activation. The chapter also contains the setup and conditions of catalytic dry reforming test in addition to an evaluation of the thermodynamic equilibrium of the reaction under varying experimental conditions.

Chapter III is intended to study if the confinement of nickel nanoparticles inside a SBA-15 silica support is important for a good catalytic stability. The support is synthesized in small batch and impregnated with different nickel loadings using the two solvents method. The samples are characterized in order to evaluate the porosity of the supports and impregnated samples as well as the nature, size, dispersion and reducibility of nickel nanoparticles. The reduced catalysts are next evaluated in dry reforming of methane at 500°C. The chapter also considers the effect of Ce addition on these catalysts.

Chapter IV focuses on the extension of the study towards a larger scale synthesis and the comparison of the resulting catalysts to commercial silica-based mesoporous supports with different textural properties. Finally, the successful amelioration of the SBA-15 synthesis by application of hydrothermal treatment is considered. In this chapter, the catalysts are tested in methane dry reforming at 650°C, which is closer to the industrial conditions.

In Chapter V, we will show that the variation of the nickel deposition method, the nature of the nickel precursor salt and the conditions for thermal activation are all strategies that affect the final dispersion of nickel particles and the consequent catalytic activity and stability. The use of a promoter/dopant with nickel will also be analyzed. The chapter ends with a preliminary evaluation of the use of mesoporous $CeO_2$ as support instead of SBA-15.

Chapter VI details the careful evaluation of carbon deposition on the spent catalysts. It also considers the effects of more severe reaction conditions like higher gas hourly space velocity and higher pressure.

The manuscript ends with a summary of the main results of this work in addition to proposed perspectives for future research.

Finally, supplementary data are provided in three appendixes. Appendix 1 reports a non-exhaustive bibliography on catalysts used in dry reforming of methane, Appendix 2 gives insights about the attributions of the NiO reduction peaks and Appendix 3 introduces preliminary attempts for shaping Ni/SBA-15 catalysts into solid bodies.

# CHAPTER I

# Literature Review

Hydrogen ($H_2$) and carbon monoxide (CO) are important reagents for the production of food, fuel and chemicals. The large quantities required can be produced via different reactions of reforming of methane. In this chapter, we will present the common methane resources and detail the various pathways for the production of $H_2$ and CO from methane. Next, we will explain our particular interest in dry reforming of methane that uses $CO_2$ as co-reactant. The subsequent state of the art presents a summary of the progress achieved in the preparation of highly performing catalysts for dry reforming of methane. Based on this brief review, the general comments deduced will lead to the formulation of the objectives of the present thesis.

## I.1 Methane dry reforming: general context

### I.1.1 Methane resources

The abundance, availability and consequently low price of methane are all elements that increase its potential in the production of $H_2$ and CO, which can later replace oil resources and contribute in the energy supply. Methane is found in natural resources such as natural gas and shale gas (natural gas trapped within shale formations) as well as in renewable ones like biogas from biomass.

- Natural gas

Facing the excessive increase in energy demand, natural gas currently plays an important energetic role due to its large world proven reserves. In opposition to the depleting oil reserves, the annually published BP statistical Review of Word Energy reported an increase of the proved natural gas reserves from 118.4 trillion cubic meters in 1993 to about 185.7 trillion cubic meters in 2013 (Fig. I-1). According to the estimations, this quantity is sufficient to meet 55 years of global production.[1] The increasing proved reserves are predominantly located in the Middle East and Europe & Eurasia regions (Fig. I-1). In Lebanon, in particular, recent reports have shown that the Lebanese offshore is petroliferous and highly prospective. While the Ministry of Energy and Water has suggested the potential existence of 2.7 trillion cubic meters of gas reserves,[2,3]

other investigations postulated the existence of only 0.7 trillion cubic meters of gas reserves.[3,4] Regardless of the exact numbers, the quantity of natural gas in Lebanon remains very significant compared to a total area of only 10452 Km², equivalent to <0.002% of the world total area.

In details, methane is the essential component of natural gas (70-98%). Depending on its origin, the latter can also contain traces of hydrocarbons (ranging from ethane to heptane) and other impurities such as sulfur compounds ($H_2S$), nitrogen compounds, carbon dioxide ($CO_2$) or heavy metals (Hg, Pb, As), that should be removed before use.[5]

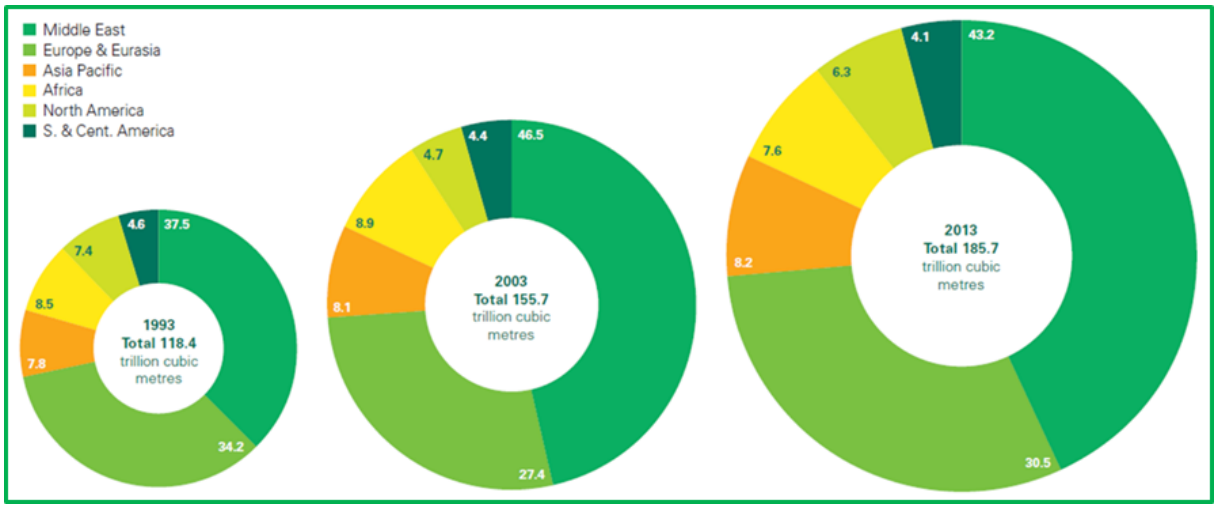


Figure I-1: Distribution of proved reserves (in percentage, %) in 1993, 2003 and 2013 [Source: BP statistical Review of Word Energy, 2014[1]]

- Biomass

Biomass includes wood, agricultural crops, municipal organic wastes or any other organic matter derived from plants or animals available on a renewable basis. The methods available for the conversion of complex organic compounds in biomass can be divided into two main categories: thermo-chemical and biological conversion routes.[6] The thermo-chemical routes include gasification or combustion in the presence of oxygen (or air) and pyrolysis or torrefaction in an oxygen-free environment. The biological conversion is a four-phase enzymatic process that comprises hydrolysis, fermentation, acetogenesis, and methanogenesis.[7,8] Biomass is thus a potential renewable energy source, for both the rich and the developing countries. In Lebanon, in particular, 1.6 million tons of wastes are generated per year with an annual increase of 1.5%. If

the processes of conversion of methane (which will be detailed below) are well-optimized, biomass can become an important feedstock for reforming processes.

### I.1.2 Pathways for methane-to-syngas conversion

Since large amounts of natural gas are mainly found in remote areas,[9] its full exploitation is thus hindered due to cost ineffective gas transportation. Because of its low density, it is not easy to store natural gas or transport it by vehicles. Indeed, gas pipelines are impractical across oceans, since the gas needs to be cooled down and compressed, as the friction in the pipeline causes the gas to heat up. This challenge increases the need for onsite gas-to-liquids conversion. Consequently, the conversion of methane into heavier – more easily transportable – compounds, such as liquid fuels, represents an attractive and challenging target, offering economical and energetic benefits.

Methane can be converted into useful products via two distinct routes: the direct and indirect conversions. The direct conversion is a one-step reaction of methane with oxygen. However, this process is very difficult and requires very severe conditions because of the strong C-H bond that is very stable and hard to break.[10,11] This use of direct methane conversion in industry is consequently restricted. Alternatively, the most prominent use of methane in the chemical industry is through the indirect process that consists on first converting methane to synthesis gas, often referred to as **syngas**, which can be later converted into the desired products. Syngas is, in fact, a mixture of hydrogen and carbon monoxide in varying amounts, depending on its way of production. This amount (commonly identified as $H_2$:CO molar ratio) should be adapted with respect to the subsequent intended application, as will be detailed below.

Different methods can be used in order to convert methane into syngas, the main ones being: steam reforming, partial oxidation, auto-thermal reforming and dry reforming (Table I-1).[12] Despite their advantages that will be presented below, these techniques are not yet fully controlled. Only steam and auto-thermal reforming are currently industrialized.

Table I-1: Methane reforming reactions[13,14]

| Reaction | Equation | $\Delta H^0_{298\,K}$ (KJ.mol$^{-1}$) | $H_2$:CO | Main application |
|---|---|---|---|---|
| Steam reforming of methane (SRM) | $CH_{4(g)} + H_2O_{(g)} \rightarrow 3H_{2(g)} + CO_{(g)}$ | 206 | 3 | Hydrogen production |
| Partial oxidation of methane (POM) | $CH_{4(g)} + \frac{1}{2}O_{2(g)} \rightarrow 2H_{2(g)} + CO_{(g)}$ | -36 | 2 | Methanol synthesis |
| Auto-thermal reforming (ATR) | $CH_{4(g)} + \frac{x}{2}O_{2(g)} + (1\text{-}x)H_2O_{(g)} \rightarrow (3\text{-}x)H_{2(g)} + CO_{(g)}$ | 206.2-241.8$x$* | variable | Dependent on the ratio |
| Dry reforming of methane (DRM) | $CH_{4(g)} + CO_{2(g)} \rightarrow 2H_{2(g)} + 2CO_{(g)}$ | 247 | 1 | Fischer-Tropsch Synthesis |

*$x$ is a variable between 0 and 1

- The catalytic **steam reforming** of methane (SRM) generates syngas with a high $H_2$/CO ratio (value of 3), which makes this process the most widespread for hydrogen production.[15] This reaction is highly endothermic and requires temperatures as high as 800°C. Industrially, it is performed at elevated pressures greater than 10 bar.[16,17]
- **Partial oxidation** of methane (POM) produces a lower $H_2$:CO ratio (around 2), adequate for methanol synthesis ($2H_2 + CO \rightarrow CH_3OH$).[18,19] However, this process is highly exothermic and results in the formation of hot spots on the reactor, leading to difficulties in process control.[20,21] Furthermore, the need for "on-site" oxygen production further complicates the process. Thus, it is not yet industrially applied for converting methane to syngas.[10]
- These two previous processes can be combined in order to obtain the **auto-thermal reforming** (ATR)[14,22] in which methane first undergoes combustion in the presence of oxygen in order to obtain $CO_2$, CO and $H_2O$, then the resultant gases are passed over the catalyst in the bottom section of the reactor to produce syngas. The non-catalytic partial oxidation step is operated at temperatures around 1900°C whereas the temperature in the catalytic steam reforming zone is between 900 and 1200°C and the pressure is in the range of 20-35 bars.

- In **dry reforming** of methane (DRM), also known as $CO_2$ reforming of methane, steam is replaced by carbon dioxide (compared to SRM). This process is also endothermic and requires high temperatures (>640°C) in order to achieve high conversions.[23,24] However, it results in an equimolar product feed ($H_2$:CO ratio of 1) that can be directly used for the production of liquid hydrocarbons via Fischer-Tropsch Synthesis (FTS),[25] as will be detailed below.

Other recently emerging methods for methane-to-syngas conversion include:

- **Bi-reforming** that is a combination of steam and dry reforming: it produces an $H_2$:CO molar ratio of 2, called "metgas", that can be used for the preparation of methanol and subsequently derived hydrocarbon products.[18] Compared to dry reforming, the presence of steam in bi-reforming can facilitate the oxidation of carbon species.[26] Nevertheless, this process requires lots of energy because it is highly endothermic.
- **Tri-reforming** that is a combination of steam reforming, dry reforming and partial oxidation. This process is advantageous because: (1) it offers the possibility of controlling the $H_2$:CO molar ratio in the product by varying the relative amounts of gas reagents, (2) it is less endothermic due to the occurrence of partial oxidation and (3) it can reduce coke formation due to the presence of oxidants ($H_2O$ and $O_2$).[27] However, the need for oxygen and steam production further complicates the process.

### I.1.3 Advantages of dry reforming of methane

Among the most important applications of syngas, the Fischer-Tropsch synthesis (FTS) is of particular interest. This process converts syngas into a mixture of valuable products,[28] particularly alkanes ($C_nH_{2n+2}$, with $n \geq 2$), that can be further refined to synthetic fuels, lubricants and petrochemicals.

The production of alkanes by FTS is represented by the general reaction:

$$nCO + (2n+l)H_2 \rightarrow C_nH_{2n+2} + nH_2O \qquad \text{(Eq. 1)}$$

However, it is always accompanied by the water gas shift reaction:

$$nH_2O + nCO \leftrightarrow nCO_2 + nH_2 \qquad \text{(Eq. 2)}$$

Thus, the final overall reaction becomes:

$$2nCO + (n+l)H_2 \rightarrow C_nH_{2n+2} + nCO_2 \qquad \text{(Eq. 3)}$$

To obtain alkanes by FTS, the required initial $H_2$:CO reactant ratio is therefore (n + 1):2n. Although the value of n can vary, this means that the $H_2$:CO ratio in the used syngas should be lower than one.[25] In the case of steam reforming, such desired ratio below 1 cannot be achieved directly, but only after application of additional treatments like the use of selective membranes, which is expensive and time consuming. Then, a more convenient and more direct solution is to use methane dry reforming that gives the lowest $H_2$:CO ratio (Table I-1), readily utilizable for the production of energy resources (hydrocarbons) by FTS.

Dry reforming of methane followed by FTS is thus an interesting gas-to-liquid pathway. In addition to the **energetic and economic benefits** offered by this conversion, already discussed at the beginning of section I.2, dry reforming of methane provides an important supplementary advantage related to the protection of the environment. Indeed, facing the climate change and the resulting gradual increase of the earth's temperature, humanity is strongly concerned by the reduction of greenhouse gas emissions. In specific, an increasing concern is focused over the rise of carbon dioxide into the atmosphere.[24] Indeed, $CO_2$ emissions have increased by 90 ppm in about 200 years since 1800.[29] More recently (from 1975 to 2002), they have increased by about 1.5 ppm per year. According to the EPA report,[30] the greenhouse gases globally emitted in 2012 included 82% of $CO_2$ and 9% of $CH_4$. These emissions are mainly related to electricity generation, transportation and industry. Accordingly, dry reforming of methane offers a highly recommended advantage, related to the **simultaneous conversion of both methane and carbon dioxide** into higher-value products.

### I.1.4 Main and side reactions during dry reforming of methane

The reaction of methane dry reforming, which will be in the core of this research, is recalled in Table I-2 that also emphasizes on the side reactions that can occur simultaneously and thus influence the equilibrium of DRM. The reverse water gas shift (RWGS) reaction consumes hydrogen and produces more carbon monoxide, thus resulting in a lower $H_2$:CO molar ratio. Methane decomposition and Boudouard or CO disproportionation reaction result in solid carbon formation.

Table I-2: Methane dry reforming and associated side reactions[13]

| Reaction | | Equation | $\Delta H^0_{298\,K}$ (KJ.mol$^{-1}$) | Effect on DRM |
|---|---|---|---|---|
| Main reaction | Dry reforming of methane (DRM)* | $CH_{4(g)}+CO_{2(g)}\rightarrow 2H_{2(g)}+2CO_{(g)}$ | 247 | - |
| Side reactions | Reverse water gas shift reaction (RWGS) | $CO_{2(g)}+H_{2(g)}\rightarrow CO_{(g)}+H_2O_{(g)}$ | 41 | Lower $H_2$:CO ratio |
| | Methane decomposition | $CH_{4(g)}\rightarrow C_{(s)}+2H_{2(g)}$ | 75 | Carbon formation |
| | Boudouard or CO disproportionation reaction | $2CO_{(g)}\rightarrow C_{(s)}+CO_{2(g)}$ | -171 | Carbon formation |

* Theoretical $H_2$/CO product ratio of 1

The thermodynamics of the DRM reaction will be discussed in details at the end of Chapter II (section II.4). However, preliminary equilibrium plots calculated at 1 atm using an equimolar inlet feed ratio (Fig. I-2) show that water generation (by RWGS) and carbon deposition (by methane decomposition and/or Boudouard reaction) remain significant at temperatures up to about 800°C.[13] Accordingly, a temperature as high as 900°C is needed in order to favor the DRM reaction over all the side reactions and to obtain the desired $H_2$:CO molar ratio with full reactants conversions. Moreover, because of the high stability of the two reactants molecules, this reaction hardly takes place without a catalyst.

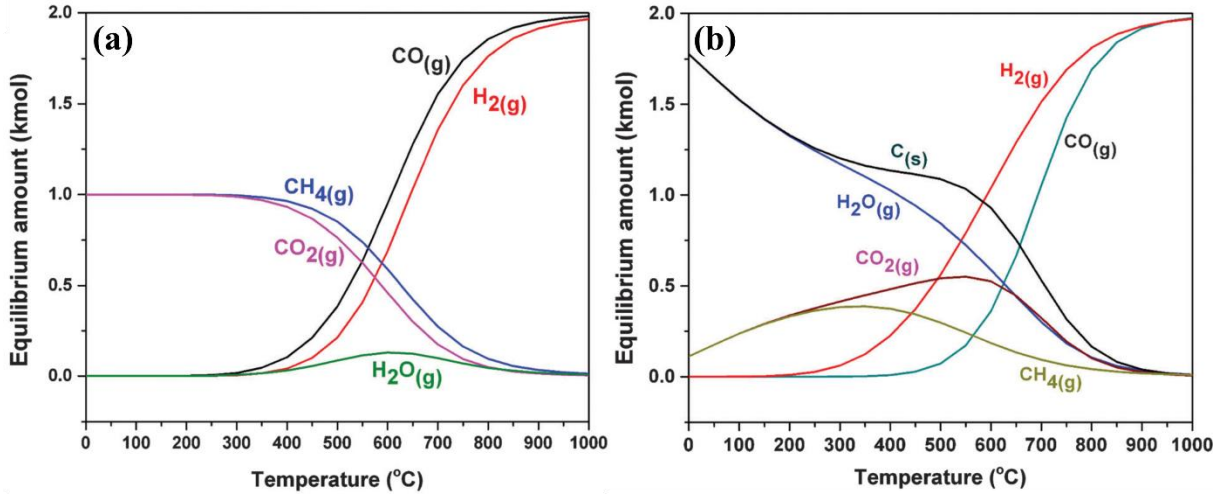


Figure I-2: Thermodynamic equilibrium plots for DRM at 1 atm and inlet feed ratio of $CO_2/CH_4$ = 1. (a) Assuming no carbon formation occurs (b) assuming that carbon formation occurs[31]

## I.2 Methane dry reforming catalysts: general overview

Based on literature, catalytic activation of DRM is always carried out on reduced metal(s) dispersed on a support. According to proposed mechanisms, methane is first adsorbed on the catalyst surface and decomposes into hydrogen and partially hydrogenated $CH_x$ species or adsorbed carbon.[23] Shah & Gardner[32] described that carbon dioxide can either participate in the reforming reaction directly from the gas phase (Eley-Rideal mechanism) like on some alumina-supported catalysts[33,34] or simultaneously adsorb on the catalyst surface and dissociate into CO and adsorbed oxygen (Langmuir-Hinshelwood mechanism). In the latter case, it was proposed that $CO_2$ reacts with the adsorbed hydrogen to form CO and adsorbed hydroxyl groups. These groups react with $CH_x$ at the metal-support interface in order to form $CH_xO$ which then dissociates into CO and $H_2$.[35] Consequently, each constituent of the catalyst plays a role in the mechanism of reaction.[13] Depending on the nature of the support and the consequent metal-support interactions, different activities can be obtained during the reforming reaction,[34] as will be detailed below.

A non-exhaustive bibliography on catalysts used in dry reforming of methane is summarized in brief tables in the appendix of this thesis, mainly including the reaction conditions employed along with the initial and final reactants conversions and $H_2$:CO molar ratios obtained. Table A-1 focuses on non-nickel-based catalysts, such as cobalt and noble metals and Table A-2 concerns supported

Ni-based catalysts. The promotion of Ni-based catalysts with noble metals is evoked in Table A-3, while other promoters are listed in Table A-4. In general, most of the reported catalysts consist of a metal such as Ni, Ru, Rh, Pd, Ir, Pt or Co, on an oxide support like $SiO_2$, $Al_2O_3$, MgO, $TiO_2$, CaO, $CeO_2$, $ZrO_2$, or $La_2O_3$.[13]

### I.2.1 High performance of noble metals

Among the DRM catalysts, researchers agree that noble metals (Rh, Ru, Pt, Ir and Pd) are the most active and resistant to carbon deposition.[31,33,36,37,38,39,40] Table A-1 of the Appendix reports few bibliographic data on catalysts based on noble metals. The catalytic activity and stability of different noble metals decreased in the following order: Rh~Ru>Ir> Pd >Pt.[37,41] Although Rh and Pt are among the most studied elements,[41,42,43,44,45,46,47,48] the most efficient catalysts were those containing Rhodium (Rh) and Ruthenium (Ru). However, despite their excellent activity, stability and selectivity, the high cost of noble metals and their restricted availability hinder their industrial application. In fact, the price of noble metals does not only depend on the nature of the metal, but also on the type of precursor. In comparison to nickel, the price of noble metals can be 1500-15000 times higher.

Consequently, noble metals are most often used in bimetallic systems, as shown in Table A-3 of the Appendix. Doping of catalysts with noble metals in small quantities remains more economic than the use of these precious metals as active phases. The addition of Pt[43], Pd[49], Ru[50] or Rh[51,52] to Ni-based catalysts improved carbon resistance during the dry reforming reaction. The Ni-Rh clusters formed on mesoporous $Al_2O_3$,[53] $SiO_2$[54] and boron nitride[55] supports enriched the surface of the catalysts with Ni and enhanced the reforming activity. The main advantage of these noble metals is associated with their $H_2$ spillover effect, when $H_2$ molecules dissociate on the surface of the noble metal to hydrogen species, which are highly mobile and can diffuse easily on adjacent ones via the support surface.[48,56,57] This improves the reducibility of metal oxides and ameliorates the catalytic stability by limiting heavy coke formation.

### I.2.2 Use of transition metals and importance of nickel

Non-noble metals like Ni and Co became attractive alternatives due to their lower cost and higher availability.[58,59] Indeed, studies on methane dry reforming over Ni and Co catalysts started as early

as the 1920s by Fischer and Tropsch.[11] However, these catalysts were subjected to severe deactivation due to carbon deposition. Thus, people quickly dropped the research on such application. Later, few studies in the 1980s reported that these active phases were relatively active on $SiO_2$ supports, in opposition to CuO and $Fe_3O_4$ catalysts that deactivated rapidly.[60] Succeeding studies used silica[61,62] and alumina[25,62,63] as supports. Nevertheless, the conversions obtained did not meet the equilibrium values and side reactions continued to affect the final conversions.

At the beginning of the 21st century, the increased concerns about global warming and the depletion of petroleum oil reserves promoted renewed interests in dry reforming of methane. Since then, the importance of this topic of research continuously increased with time. We statistically considered the articles obtained by looking for either the words "$CO_2$ dry reforming" using the Web of Science search engine, or "Methane dry reforming" using Google Scholar (Fig. I-3). Some variations are observed between the two search engines, however, the trend is the same. The resulting bar-charts reveal a significant increase in the number of publications after 2010, up to mid-2016.

Furthermore, statistics were done on some of the most studied elements in dry reforming of methane obtained by looking for "Methane dry reforming" and the corresponding metal using Google Scholar (Fig. I-3). The plot shows that Ru, Rh and Pt are no longer greatly studied, due to their high cost, as discussed earlier. In opposition, extensive studies are concerned with the use of Co and more importantly Ni.

In this literature, Co-based catalysts usually show lower coke deposition in comparison to Ni-based systems;[64,65,66,67] however they remain less performing in DRM.[46] Therefore, Ni-based catalysts are considered as the most promising alternatives among the non-noble metals. Indeed, close resemblance in the catalytic activity was obtained on Rh and Ni-based catalysts;[41] however, Ni-based catalysts are subjected to heavy coke deposition and consequent catalytic deactivation. Therefore, several approaches are being studied in literature in order to increase the stability of these catalysts and enhance their coke-resistance. The studies mainly focus on the nature of supports, catalyst preparation methods and addition of promoters. These topics will also be important concerns of this thesis.

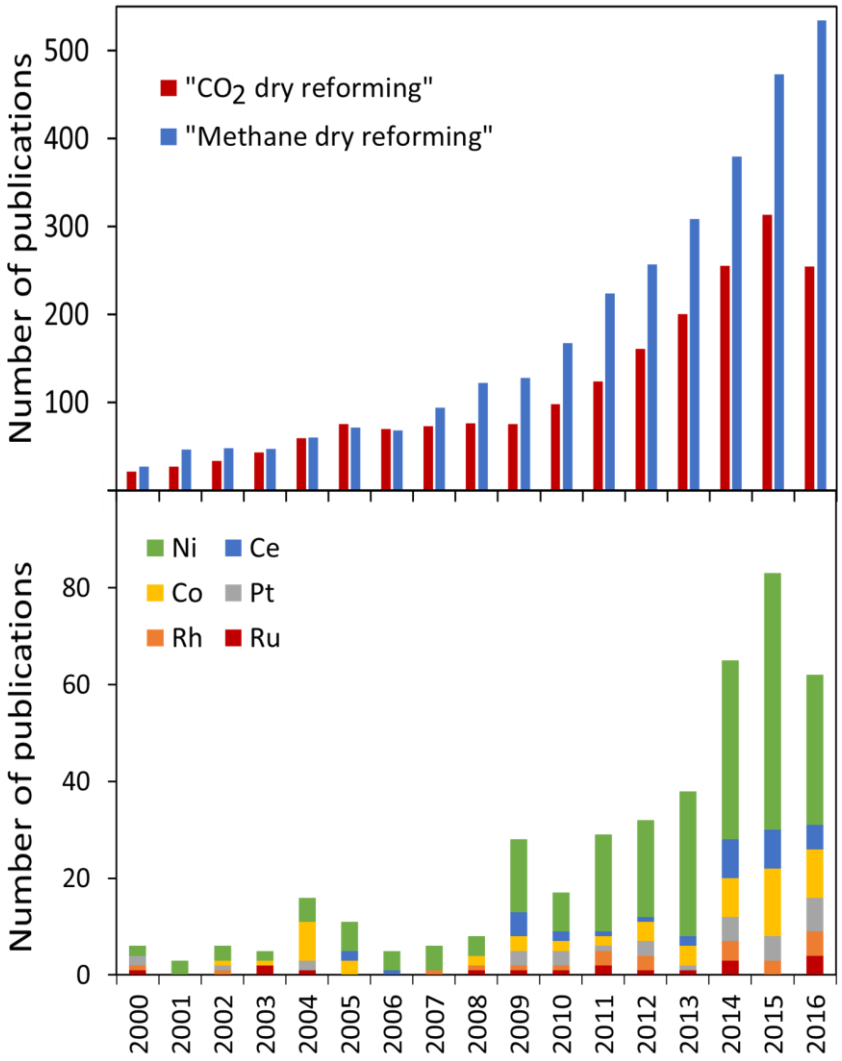


Figure I-3: Number of publications on DRM from 2000 to mid-2016 based on the topic or on the nature of the metal active phase

### I.2.3 Existing industrial processes

Because of its low cost and important activity, nickel is already involved into two existing industrial processes, in which a part can be viewed as dry reforming of methane, as described by Shah et al.[32]

- A graded Ni-based catalyst bed is used in the CALCOR process (Caloric Gmbh). Various levels of activity and catalyst geometries are employed to minimize carbon deposition. However, in this case, the dry reforming of natural gas (or of liquefied petroleum) takes

place in presence of excess $CO_2$. In addition, syngas is produced with a high concentration of carbon monoxide (CO).

- Ni-based catalysts are also implemented in the SPARG (sulfur passivity reforming) process, created by Haldor-Topsoe. This process operates at 915-945°C and coke deposition on the catalyst is minimized in this case by pre-treatment of the catalyst with sulfur. However, this process uses mixtures of $CO_2$ and $H_2O$ and hence it is rather considered as a combined dry and steam reforming process.[68] Moreover, it produces different syngas compositions with $H_2$/CO ratios not lower than 1.8.

Consequently, there is still no industrial application consisting on dry reforming of methane that uses $CH_4$ and $CO_2$ to produce an equimolar $H_2$:CO syngas mixture, best adapted for FTS. Because of its endothermic aspect, the high energy cost required can be compensated by the use of solar energy, which is an abundant renewable source, to generate the heat required for the reaction.[69,70] However, the main reason that still hinders the commercialization of the dry reforming process is related to the unavailability of cheap and effective catalysts that can resist active phase sintering and carbon deposition, especially under the high temperatures required for the reaction.

## I.3 Ni-based catalysts for methane dry reforming

Active phase sintering causes an increase in the metal particle size and a significant reduction of its surface area, leading to lower catalytic activity. The reduction of nickel particles size promotes carbon resistance. In literature, different critical particle sizes have been selected for the inhibition/reduction of carbon formation, like 7 nm on Ni/alumina aerogel,[71] 10 nm on Ni-Mo/SBA-15[72] and Ni/$Al_2O_3$-$La_2O_3$,[73] and 15 nm on Ni/meso-$Al_2O_3$[74] and Pt/Ni-MCM-41.[46] Baudouin et al. studied the impact of nickel particle size in the range of 1.6 to 7.3 nm on dry reforming of methane at 500°C.[75] However, this range remained below the threshold determined by other authors and this explains why they found an independent relationship between catalytic activity and particle size in their study. Thus, it is generally agreed that the dispersion of active metal (Ni) is of particular importance for an efficient nickel reforming catalyst. When nano-sized nickel particles were obtained with narrow distribution in Ni/SBA-15 catalysts, the catalytic activity was even higher than that on Ru-catalysts for ammonia decomposition.[76] Nonetheless,

the formation of well-dispersed active metals in supported catalysts is greatly affected by metal precursors, loading techniques and supporting materials.

In general, nickel nitrate is the most commonly used precursor due to its commercial availability, low cost, high solubility in water and easy decomposition at moderate temperatures.[77,78] Nevertheless, other precursors like nickel chloride, acetate, citrate or formate are tested as well.[27,79,80,81,82,83,84,85] The use of chloride precursors generates large particles, as observed on $Ni/Al_2O_3$,[84] $Ni/TiO_2$,[83] $Ni/CeO_2$,[27] and Fe/SBA-15[79] whereas nitrate and acetate precursors appear to be efficient for small particles formation, good metal dispersion and subsequent high catalytic activities.[83,81,82]

The catalyst preparation procedure can also play an important role in the dispersion of the active phase. For instance, different preparation techniques such as impregnation (co-impregnation or sequential, in the case of bimetallic catalysts), precipitation, direct synthesis (also known by single-step or one-pot synthesis), ion exchange, plasma treatment and many more are reviewed.[86,87,31] While plasma treatment is quite expensive, other procedures are preferred due to their simplicity and their possible implementation in laboratory as well as in industry. The incipient wetness impregnation, in particular, is the most widely used method but it does not always lead to good metal dispersion.[88]

Furthermore, the selection of catalytic supports plays a critical role in enhancing the catalytic activity and suppressing carbon formation.[87] In dry reforming of methane, non-porous supports mainly consisting of $Al_2O_3$, MgO, $CeO_2$ and/or $ZrO_2$, microporous supports like zeolites and mesoporous supports including $Al_2O_3$, $CeO_2$ and/or $ZrO_2$, MCM-41, SBA-15 and MgO were tested. The differences of reactivity of Ni-species on these supports are detailed below.

### I.3.1 Structural approaches to limit nickel sintering and coke resistance

The initial $CH_4$ and $CO_2$ conversions of some bibliographic data on Ni-based catalysts are plotted as a function of reaction temperature (Fig. I-4), regardless of the test conditions (particularly nickel content, space velocity and reagents feed dilution). The majority of the studies evaluated the dry reforming reaction at temperatures between 600 and 800°C, while a limited number of tests were performed in the range of 400-500°C. In general, the plots show that low conversions are obtained on Ni-based catalysts involving non-porous supports (yellow

points). While the use of mesoporous supports (blue points), in particular, is in favor of high reactants conversions. For instance, several authors found lower catalytic stability when using non-porous supports like bulk $LaNiO_3$,[89] Ni-CaO-$ZrO_2$[90] and Ni/MgO-$Al_2O_3$ catalysts.[91] The deactivation was mainly attributed to metal particles sintering on non-porous supports. In addition, the study of the effects of the support phase ($Al_2O_3$, $SiO_2$ and MgO) on DRM[92] indicated that the pore structure of the support and metal-support interaction significantly affected the catalytic activity and coking resistance. The catalyst with well-developed porosity exhibited higher catalytic activity.

In the same direction, Zhang et al. succeeded in stabilizing nickel particles inside phyllosilicate (PS) nanotubes and obtained catalysts with excellent performances and coke resistance in ethanol steam reforming.[93] The introduction of nickel particles in PS nanotubes maintained the Ni size between 6 and 7 nm and increased the resistance of metal particles towards carbon deposition. Similarly, Ma et al. found that nickel nanoparticles located inside carbon nanotubes are more reducible and resistant to sintering as well as catalytically more active and stable than those loaded outside the nanotubes.[94] A better metal dispersion is thus achieved on porous materials due to their higher surface area, inducing improved accessibility of reactants to the metal active phase.

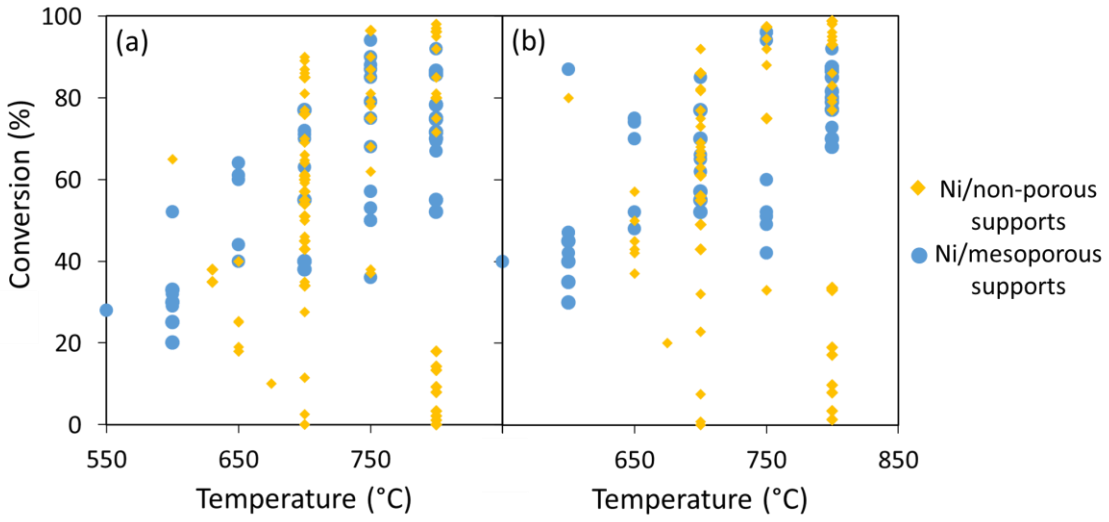


Figure I-4: Some bibliographic data reporting the initial (a) $CH_4$ and (b) $CO_2$ conversions over Ni-based catalysts using non-porous or mesoporous supports

- Macroporous and microporous supports

During dry reforming of methane at 400°C,[95] an analogous deactivation was observed on both non-structured and macro-structured Ni/$La_2O_3$-$ZrO_2$ catalysts. The deactivation was mainly caused by the presence of graphitic carbon on both catalysts in addition to reoxidation of Ni into NiO on the macro-structured sample. The latter was also the reason behind the deactivation of nickel supported on naturally available macropous diatomites.[96] Microporous supports received some attention in dry reforming of methane because of their well-defined structure, high surface area and high affinity for $CO_2$. The stability of 3 to 7 wt% Ni on zeolites A, X, Y and ZSM-5 at 700°C slightly varied between the various supports.[97] Frontera et al.[98] investigated the effect of silylation treatment before Ni impregnation on the support by substituting the OH groups with larger organosilane ones. This procedure allowed the formation of smaller and more reducible nickel species which improved the $CH_4$ conversion and reduced coke deposition. However, the microporous zeolites are characterized with high acidity, that limits their exploitation in the reforming processes.

- Mesoporous supports

In the last ten years, mesoporous supports gained the greatest attention among porous materials. High catalytic activity and long-term stability were obtained on ordered mesoporous NiO-$Al_2O_3$ composite oxides,[99] attributed to the higher number of active sites for the reactants on the mesoporous wall surfaces and the stabilization of the active sites by the alumina matrix due to the confinement effect induced by the mesopores. Newnham et al. prepared Ni-incorporated mesoporous alumina materials with different Ni loadings (7, 10 and 15 wt%),[74] which displayed high stability compared to conventional materials with the same compositions. The high stability of the catalysts was attributed to the sintering resistance of Ni nanoparticles under the used conditions, due to a strong Ni-support interaction and/or active metal particles being confined to the mesoporous channels of the support. Similarly, a recent study on mesoporous $ZrO_2$[100] demonstrated that a well-defined mesoporous structure can maintain Ni particle size at around 7 nm throughout the test, thus keeping high catalytic performance for more than 80 hours. Whereas a poorly defined mesoporous structure can result in activity loss due to the formation of large Ni particles, of about 15 nm, during reaction. The superior thermal stability of the catalyst was attributed to the "anchoring effect" of the mesoporous structure and the formation of multiple

points of contact between the metal and the support. Thus the well-formed mesoporous structure can impose a spatial restriction on Ni particles, preventing their sintering and resulting in better stability during reaction.[101] Consequently, it appears that the textural properties of the mesoporous supports can have an influence on the stability of the catalyst, as will be discussed in succeeding chapters.

- SBA-15 mesoporous supports

The synthesis of silica-based mesoporous materials was pioneered by the discovery of MCM-41 in 1992,[102] followed by the invention of SBA-15 in 1998.[103] More recently (in 2009), Liu et al.[104] showed that the catalysts supported on SBA-15 were more stable in dry reforming of methane than those supported on MCM-41 due to high structural stability of SBA-15, much uniform mesopore distribution and unique pore structure. In the same way, Wang et al.[89] obtained higher initial $CH_4$ and $CO_2$ conversions on $LaNiO_3$/MCM-41 than on $LaNiO_3$/SBA-15 catalysts. However, the superior performance of $LaNiO_3$/SBA-15 in the long-term stability was credited to the maintained hexagonal mesoporous arrangement of SBA-15 in comparison to a structure collapse of MCM-41. The authors further reported that SBA-15 supports can minimize heat diffusion problems of the highly endothermic dry reforming reaction and thus prevent the formation of cold points in the catalytic bed.

At the beginning of this PhD research, very few studies were concerned with the use of SBA-15 as supports in dry reforming of methane.[72,105,106] It is only after 2013 that this type of materials started to be reported for this application, owing to their high specific surface areas (600-1000 $m^2.g^{-1}$), uniform two-dimensional hexagonal pore arrangements, interconnected porosity, large tunable pore sizes (5-30 nm) and thick pore walls (3-7 nm). All these properties can give way to improved dispersion of metal particles and better accessibility of reactants to the active sites.

*When clay is molded to form a bowl, it is the empty space that makes the bowl useful*. In analogy with this image, the essence in working with porous materials can be visualized. We can shape them, generate pores in varying sizes and structures and finally exploit the surface and the empty space for various applications. In this direction, we were interested to study the stabilization of Ni inside SBA-15 systems in dry reforming of methane. First, the studies were conducted at 500°C. This temperature limits carbon formation, as previously seen on the thermodynamic

curves, and favors lower energy consumption. Furthermore, to the best of our knowledge, few works dealing with the stability behavior of Ni-based catalysts at low temperatures have been published.[62,75,95,107,108,109]

### I.3.2 Chemical approaches to enhance carbon resistance

In addition to the above mentioned criteria, the stabilization of nickel particles inside porous channels can be accomplished through the addition of a second metal. This metal can either enhance the dispersion by reducing the metal particle size or improve coke resistance through the modification of the surface basicity of the support or its redox properties.

- Addition of promoters: effect of basicity

Concerning the non-noble metal promotion, the major metals usually studied in literature are cerium, lanthanum and magnesium (Table A-4 of the Appendix). Various promoters (La, Mg, Co, and Zn) were studied on $Ni/SiO_2$ catalysts in dry reforming of methane.[110] All the promoters presented a significant improvement of the catalytic activity. Indeed, the addition of promoters influences the dispersion of Ni particles and their interaction with the support, providing thus more active sites for the reforming process to take place. In particular, the addition of Mg and La reduces the contribution of the reverse water-gas shift reaction (RWGS), increasing thus the hydrogen yield.[110] Furthermore, these two promoters improve the electronic properties of the catalyst and increase the basicity of the support. Basic supports favor the activation of $CO_2$ on the surface of the support rather than the metallic site. Consequently, $CO_2$ strongly adsorbs on the La or Mg species while $CH_4$ decomposes on the Ni particles.[48,111] Therefore, no filamentous or encapsulating carbon was observed on the spent Ni/8MgO-SBA-15 catalyst. Whereas on Ni/SBA-15 catalyst, the Ni particles were separated from the surface by the carbon filaments and remained accessible on the tips. However, as more filaments were formed, the catalyst particles were destroyed and the reactor plugged during the long-term test.

- Addition of promoters: effect of redox properties

In general, like other promoters, the addition of ceria causes an enhancement of Ni nanoparticles dispersion and a consequent improvement of stability.[112,113,114,115,116,117,118] More particularly, $CeO_2$ is characterized by excellent low-temperature redox properties ($Ce^{4+} \leftrightarrow Ce^{3+}$) that promote

the formation of oxygen vacancies. The high oxygen storage capacity and increased surface oxygen mobility facilitate carbon gasification on metallic particles.[113,114,119,120] In addition, reduced $Ce_2O_3$ can spontaneously reduce NiO to Ni, maintaining high Ni activity.

These positive effects of $CeO_2$ addition were observed in Rh/MgO systems for partial oxidation of methane[121] and in $Pt/ZrO_2$ systems for both partial oxidation and combined reforming of methane.[122] In ethanol steam reforming, the CeNi/SBA-15 catalysts possessed homogeneous Ni-Ce distribution and increased Ni-$CeO_2$ interface.[123] This strong interaction between nickel particles and ceria, together with the confinement inside the SBA-15 support, retained the small nickel particle size (5.2 nm), revealing excellent sintering-resistance. In the same direction, the performances of ceria-doped mesoporous Ni/SBA-16 in DRM were increased through metal-support interactions.[120] The presence of Ce inhibited the migration of Ni particles to the external surface of the support and prevented structural collapse of SBA-16.

Nevertheless, despite the improved nickel dispersion and catalytic stability, comparable coke deposition was observed with and without Ce. Similarly, carbon nanotubes formation was observed on Ce-enriched Ni/SBA-15 catalyst.[113] It was reported that the Ce/Si atomic ratio had to be kept below 0.04 to avoid pore blocking. Moreover, the formation of clustered layers of ceria-zirconia mixed oxides and NiO phases on SBA-15 supports[114] also led to partial or complete blockage of the pores. Therefore, low metal dispersion and very slight enhancement of the catalytic stability were obtained, in spite of the presence of ceria. In steam reforming of methane, high $CH_4$ conversion and CO selectivity were obtained on both Ni/SBA-15 and $Ni/Ce_xZr_{1-x}O_2$/SBA-15 catalysts.[124] The excellent stability of the unpromoted catalysts at 800°C was rather owed to the porous structure of SBA-15 that prevented nickel particles aggregation.

## I.4 Aim of this work

The above literature review reveals the importance of dry reforming of methane as an advantageous process that deserves attention for industrial implementation. Nowadays, the economical Ni-based catalysts have a great potential in such applications. From most recent data, the occlusion of small nickel nanoparticles inside high surface area mesoporous supports, which is not yet well achieved, could hinder their sintering and improve their carbon resistance. When more metal active sites are available for the reactants, higher catalytic activity and selectivity

towards $H_2$ and CO products can be obtained. Otherwise, promoters can alternatively contribute in the mechanism of reaction by either improving the basicity of the support for better reactants adsorption or enhancing the redox properties of the catalyst for better carbon oxidation. Consequently, the type of support, the preparation method, and the use of promoters or dopants are all factors that seem to greatly affect the final results.

The focal target of the present doctoral study relies on the evaluation of the effect of confinement of nickel particles inside a well-defined mesoporous structure towards high performance in dry reforming of methane. We will examine first if the occlusion of nickel particles inside accessible pores is a key parameter for enhanced catalytic stability. Then, we will consider the potential effect of forming very small metal nanoparticles highly dispersed inside mesoporous supports (mainly silica-based ones) in order to achieve better resistance to nickel sintering and to carbon deposition.

The confinement effect of nickel particles inside silica-based materials (mainly SBA-15) was evaluated through the variation of the synthesis parameters such as the grain morphology of the support, the nickel precursor salt, the nickel deposition method on the support… The synthesis of mesoporous $CeO_2$ support using SBA-15 as the hard template was also considered in order to combine the properties of mesoporous SBA-15 silica support with the benefits of $CeO_2$ oxides. The best catalysts were also tested under more severe conditions: longer test durations, higher temperatures and under pressure. Throughout the study, the evaluation was not only limited to the effects on the catalytic performances in dry reforming of methane but also included the effects on the physico-chemical properties of the resulting catalysts, at different stages of preparation and activation. In addition to these main objectives, other important aspects were also covered during this work like the setup of the catalytic test at the University of Balamand and the validation of the SBA-15 extrapolation synthesis into larger batches.

## I.5 References

[1] BP Statistical Review of World Energy, June 2014.

[2] *Lebanon Economic Report, Containing the cost of delay in an economy with huge potential*, Bank Audi, 2013.

[3] *Oil and Gas in Lebanon, Market and Economic Research Division*, Bank MED, 2014.

[4] *Oil & Gas Sector: A New Economic Pillar for Lebanon*, Credit Libanais Economic Research Unit, January 2015.

[5] K. Aasberg-Petersen, I. Dybkjær, C.V. Ovesen, N.C. Schjodt, J. Sehested, S.G. Thomsen, *Natural gas to synthesis gas-Catalysts and catalytic processes*, Journal of Natural Gas Science and Engineering 3 (2011) 423-459.

[6] M. Balat, M. Balat, E. Kırtay, H. Balat, *Main routes for the thermo-conversion of biomass into fuels and chemicals. Part 1: Pyrolysis systems*, Energy Conversion and Management 50 (2009) 3147-3157.

[7] C.M. Drapcho, N.P. Nuhan, T.H. Walker, *Methane. Biofuels engineering process technology* (2008) pp. 329-345 New York: McGraw-Hill.

[8] B.Y. Tao, *Biomass* (2008) New York: McGraw-Hill.

[9] V. Havran, M.P. Dudukovic, C.S. Lo, *Conversion of Methane and Carbon Dioxide to Higher Value Products*, Industrial Engineering & Chemistry Resources 50 (2011) 7089-7100.

[10] R. Horn, R. Schlogl, *Methane activation by heterogeneous catalysis*, Catalysis Letters 145 (2015) 23-39.

[11] J.R.H. Ross, A.N.J. van Keulen, M.E.S. Hegarty, K. Seshan, *The catalytic conversion of natural gas to useful products*, Catalysis Today 30 (1996) 193-199.

[12] V. Dal Santo, A. Gallo, A. Naldoni, M. Guidotti, R. Psaro, *Bimetallic heterogeneous catalysts for hydrogen production*, Catalysis Today 197 (2012) 190- 205.

[13] M.S. Fan, A. Zuhairi Abdullah, S. Bhatia, *Catalytic technology for carbon dioxide reforming of methane to synthesis gas*, ChemCatChem 1 (2009) 192-208.

[14] S. Ayabe, H. Omoto, T. Utaka, R. Kikuchi, K. Sasaki, Y. Teraoka, K. Eguchi, *Catalytic autothermal reforming of methane and propane over supported metal catalysts*, Applied Catalysis A: General 241 (2003) 261-269.

[15] F. Basile, G. Fornasari, F. Trifiro, A. Vaccari, *Partial oxidation of methane: Effect of reaction parameters and catalyst composition on the thermal profile and heat distribution*, Catalysis Today 64 (2001) 21-30.

[16] L. Chen, Q. Hong, J. Lin, F.M. Dautzenberg, *Hydrogen production by coupled catalytic partial oxidation and steam methane reforming at elevated pressure and temperature*, Journal of Power Sources 164 (2007) 803-808.

[17] A. Iulianelli, G. Manzolini, M. De Falco, S. Campanari, T. Longo, S. Liguori, A. Basile, *$H_2$ production by low pressure methane steam reforming in a Pd-Ag membrane reactor over a Ni-based catalyst: Experimental and modeling*, International Journal of Hydrogen Energy 35 (2010) 11514-11524.

[18] G.A. Olah, A. Goeppert, M. Czaun, G.K. Surya Prakash, *Bi-reforming of methane from any source with steam and carbon dioxide exclusively to metgas (CO-2$H_2$) for methanol and hydrocarbon synthesis*, Journal of American Chemical Society 135 (2013) 648-650.

[19] G. A. Olah, A. Goeppert, G.K.S. Prakash, *Beyond oil and gas: The methanol economy*, Wiley-VCH, Weinheim, Germany, 2006.

[20] T.V. Choudhary, V.R. Choudhary, *Energy-Efficient Syngas Production through Catalytic Oxy-Methane Reforming Reactions*, Angewandte Chemie 47(2008) 1828-1847.

[21] K. Tomishige, *Oxidative steam reforming of methane over Ni catalysts modified with noble metals*, Journal of the Japan Petroleum Institute 50 (2007) 287–298.

[22] M.A. Pena, J.P. Gomez, J.L.G. Fierro, *New catalytic routes for syngas and hydrogen production*, Applied Catalysis A: General 144 (1996) 7-57.

[23] M. C. J. Bradford, M. A. Vannice, *$CO_2$ reforming of $CH_4$*, Catalysis Reviews: Science and Engineering 41:1 (1999) 1-42.

[24] S. Kawi, Y. Kathiraser, J. Ni, U. Oemar, Z. Li, E. Toon Saw, *Progress in synthesis of highly active and stable nickel-based catalysts for carbon dioxide reforming of methane*, ChemSusChem 8 (2015) 3556-3575.

[25] A. Gadalla, B. Bower, *The role of catalyst support on the activity of nickel for reforming methane with $CO_2$*, Chemical Engineering Science 43 (1988) 3049-3062.

[26] M.A. Soria, C. Mateos-Pedrero, A. Guerrero-Ruiz, I. Rodrıguez-Ramos, *Thermodynamic and experimental study of combined dry and steam reforming of methane on Ru/ $ZrO_2$-$La_2O_3$ catalyst at low temperature*, International Journal of Hydrogen Energy 36 (2011) 15212-15220.

[27] J. Manuel García-Vargas, J. Luís Valverde, A. de Lucas-Consuegra, B. Gómez-Monedero, P. Sánchez, F. Dorado, *Precursor influence and catalytic behaviour of Ni/$CeO_2$ and Ni/SiC catalysts for the tri-reforming process*, Applied Catalysis A: General 431-432 (2012) 49-56.

[28] A.P. Steynberg, M.E. Dry, eds., *Fischer-Tropsch Technology*, *Studies in Surface Science and Catalysis* 152 (2004) 1-700.

[29] I. Omae, *Aspects of carbon dioxide utilization*, Catalysis Today 115 (2006) 33-52.

[30] EPA 430-R-12-001, *Inventory of U. S. Green House Gas Emissions and Sinks: 1990-2012*, U. S. Environmental Protection Agency: Washington, DC, 2012.

[31] D. Pakhare, J. Spivey, *A review of dry ($CO_2$) reforming of methane over noble metal catalysts*, Chemical Society Reviews 43 (2014) 7813-7837.

[32] Y.T. Shah, T.H. Gardner, *Dry reforming of hydrocarbon feedstocks*, Catalysis Reviews: Science and Engineering, 56:4 (2014) 476-536.

[33] J. F. Múnera, S. Irusta, L. M. Cornaglia, E. A. Lombardo, D. Vargas Cesar, M. Schmal, *Kinetics and reaction pathway of the $CO_2$ reforming of methane on Rh supported on lanthanum-based solid*, Journal of Catalysis 245 (2007) 25-34.

[34] A.M. O'Connor, Y. Schuurman, J.R.H. Ross, C. Mirodatos, *Transient studies of carbon dioxide reforming of methane over Pt/$ZrO_2$ and Pt/$Al_2O_3$*, Catalysis Today 115 (2006) 191-198.

[35] M.C.J. Bradford, M.A. Vannice, *Catalytic reforming of methane with carbon dioxide over nickel catalysts: II. Reaction kinetics*, Applied Catalysis A: General 142 (1996) 97-122.

[36] M. Rezaei, S.M. Alavi, S. Sahebdelfar, Z. Yan, *Syngas production by methane reforming with carbon dioxide on noble metal catalysts*, Journal of Natural Gas Chemistry 15 (2006) 327-334.

[37] A. I. Tsyganok, M. Inaba, T. Tsunoda, S. Hamakawa, K. Suzuki, T. Hayakawa, *Dry reforming of methane over supported noble metals: a novel approach to preparing catalysts*, Catalysis Communications 4 (2003) 493-498.

[38] C. Carrara, J. Munera, E. A. Lombardo, L. M. Cornaglia, *Kinetic and stability studies of $Ru/La_2O_3$ used in the dry reforming of methane*, Topics in Catalysis 51 (2008) 98-106.

[39] P. Djinovic, I. Gasan Osojnik Crnivec, J. Batista, J. Levec, A. Pintar, *Catalytic syngas production from greenhouse gasses: Performance comparison of $Ru\text{-}Al_2O_3$ and $Rh\text{-}CeO_2$ catalysts*, Chemical Engineering and Processing 50 (2011) 1054-1062.

[40] P. Ferreira-Aparicio, C. Marquez-Alvarez, I. Rodriguez-Ramos, Y. Schuurman, A. Guerrero-Ruiz, C. Mirodatosy, *A transient kinetic study of the carbon dioxide reforming of methane over supported Ru catalysts*, Journal of Catalysis 184 (1999) 202-212.

[41] Z. Hou, P. Chen, H. Fang, X. Zheng, T. Yashima, *Production of synthesis gas via methane reforming with $CO_2$ on noble metals and small amount of noble-(Rh-) promoted Ni catalysts*, International Journal of Hydrogen Energy 31 (2006) 555-561.

[42] S. Ozkara-Aydinoglu, A. Erhan Aksoylu, *$CO_2$ reforming of methane over $Pt\text{-}Ni/Al_2O_3$ catalysts: Effects of catalyst composition, and water and oxygen addition to the feed*, International Journal of Hydrogen Energy 36 (2011) 2950-2959.

[43] S.R. de Miguel, I.M.J. Vilella, S.P. Maina, D. San José-Alonso, M.C. Román-Martínez, M.J. Illán-Gómez, *Influence of Pt addition to Ni catalysts on the catalytic performance for long termdry reforming of methane*, Applied Catalysis A: General 435-436 (2012) 10-18.

[44] M. Garcia-Dieguez, I.S. Pieta, M.C. Herrera, M.A. Larrubia, L.J. Alemany, *Improved Pt-Ni nanocatalysts for dry reforming of methane*, Applied Catalysis A: General 377 (2010) 191-199.

[45] F. Meshkani, M. Rezaei, *Nanocrystalline MgO supported nickel-based bimetallic catalysts for carbon dioxide reforming of methane*, International Journal of Hydrogen Energy 35 (2010) 10295-10301.

[46] D. Liu, W. Ni Evelyn Cheo, Y. Wen Yvonne Lim, A. Borgna, R. Lau, Y. Yang, *A comparative study on catalyst deactivation of nickel and cobalt incorporated MCM-41 catalysts modified by platinumin methane reforming with carbon dioxide*, Catalysis Today 154 (2010) 229-236.

[47] P. Djinovic, J. Batista, A.Pintar, *Efficient catalytic abatement of greenhouse gases: Methane reforming with $CO_2$ using a novel and thermally stable $Rh\text{-}CeO_2$ catalyst*, International Journal of Hydrogen Energy 37 (2012) 2699-2707.

[48] L. Qian, W. Cai, L. Zhang, L. Ye, J. Li, M. Tang, B. Yue, H. He, *The promotion effect of hydrogen spillover on $CH_4$ reforming with $CO_2$ over Rh/MCF catalysts*, Applied Catalysis B: Environmental 164 (2015) 168-175.

[49] B. Steinhauer, M. Reddy Kasireddy, J. Radnik, A. Martin, *Development of Ni-Pd bimetallic catalysts for the utilization of carbon dioxide and methane by dry reforming*, Applied Catalysis A: General 366 (2009) 333-341.

[50] S. Yasyerli, S. Filizgok, H. Arbag, N. Yasyerli, G. Dogu, *Ru incorporated Ni-MCM-41 mesoporous catalysts for dry reforming of methane: Effects of Mg addition, feed composition and temperature*, International Journal of Hydrogen Energy 36 (2011) 4863-4874.

[51] H. Arbag, S. Yasyerli, N. Yasyerli, G. Dogu, *Activity and stability enhancement of Ni-MCM-41 catalysts by Rh incorporation for hydrogen from dry reforming of methane*, International Journal of Hydrogen Energy 35 (2010) 2296-2304.

[52] W. Cai, L. Ye, L. Zhang, Y. Ren, B. Yue, X. Chen, H. He, *Highly Dispersed Nickel-Containing Mesoporous Silica with Superior Stability in Carbon Dioxide Reforming of Methane: The Effect of Anchoring*, Materials 7 (2014) 2340-2355.

[53] Z. Hou, O. Yokota, T. Tanaka, T. Yashima, *Investigation of $CH_4$ reforming with $CO_2$ on meso-porous $Al_2O_3$-supported Ni catalyst*, Catalysis Letters 89 (2003) 121-127.

[54] W.K. Jozwiak, M. Nowosielska, J. Rynkowski, *Reforming of methane with carbon dioxide over supported bimetallic catalysts containing Ni and noble metal: I. Characterization and activity of $SiO_2$ supported Ni-Rh catalysts*, Applied Catalysis A: General 280 (2005) 233-244.

[55] J.C.S. Wu, H.C. Chou, *Bimetallic Rh-Ni/BN catalyst for methane reforming with $CO_2$*, Chemical Engineering Journal 148 (2009) 539-545.

[56] W.C. Conner, J. L. Falconer, *Spillover in Heterogeneous Catalysis*, Chemical Reviews 95 (1995) 759-708.

[57] L.P.R. Profeti, E.A. Ticianelli, E.M. Assaf, *Production of hydrogen via steam reforming of biofuels on Ni/$CeO_2$-$Al_2O_3$ catalysts promoted by noble metals*, International Journal of Hydrogen energy 34 (2009) 5049-5060.

[58] J.R. Rostrup-Nielsen, J-H. Bak Hansen, *$CO_2$ reforming of methane over transition metals*, Journal of Catalysis 144 (1993) 38-49.

[59] J.H. Edwards, A.M. Maitra, *The chemistry of methane reforming with carbon dioxide and its current and potential applications*, Fuel Processing Technology 42 (1995) 269-289.

[60] T. Sodesawa, A. Dobashi, F. Nozaki, *Catalytic reaction of methane with carbon dioxide*, Reaction Kinetics & Catalysis Letters 12 (1979) 107-111.

[61] V.C.H. Kroll, H.M. Swaan, C. Mirodatos, *Methane reforming reaction with carbon dioxide over Ni-$SiO_2$ catalyst-deactivation studies*, Journal of Catalysis 161 (1996) 409-422.

[62] P. Ferreira-Aparicio, A. Guerrero-Ruiz, I. Rodriguez-Ramos, *Comparative study at low and medium reaction temperatures of syngas production by methane reforming with carbon dioxide over silica and alumina supported catalysts*, Applied Catalysis A: General 170 (1998) 177-187.

[63] A. M. Gadalla, M. E. Sommer, *Carbon dioxide reforming of methane on nickel catalysts*, Chemical Engineering Science 44 (1989) 2825-2829.

[64] A. Wahyu Budiman, S.H. Song, T.S. Chang, C.H. Shin, M.J. Choi, *Dry reforming of methane over cobalt catalysts-A literature review of catalyst development*, Catalysis Surveys from Asia 16 (2012) 183-197.

[65] J.L. Ewbank, L. Kovarik, C.C. Kenvin, C. Sievers, *Effect of preparation methods on the performance of Co/$Al_2O_3$ catalysts for dry reforming of methane*, Green Chemistry 16 (2014) 885-896.

[66] A. Elhag Abasaeed, A. Sadeq Al-Fatesh, M. Awais Naeem, A. Aidid Ibrahim, A. Hamza Fakeeha, *Catalytic performance of $CeO_2$ and $ZrO_2$ supported Co catalysts for hydrogen production via dry reforming of methane*, International Journal of Hydrogen Energy 40 (2015) 6818-6826.

[67] N. El Hassan, M.N. Kaydouh, H. Geagea, H. El Zein, K. Jabbour, S. Casale, H. El Zakhem, P. Massiani, *Low temperature dry reforming of methane on rhodium and cobalt based catalysts Active phase stabilization by confinement in mesoporous SBA-15,* Applied Catalysis A: General 520 (2016) 114-121.

[68] A. P. E. York, T. Xiao, M.L.H. Green, J.B. Claridge, *Methane Oxyforming for Synthesis Gas Production*, Catalysis Reviews 49:4 (2007) 511-560.

[69] S. Wang, G. Q. (Max) Lu, *Carbon Dioxide reforming of methane to produce synthesis gas over metal-supported catalysts: State of the art*, Energy & Fuels 10 (1996) 896-904.

[70] T. Kodama, A. Kiyama, K.-I. Shimizu, *Catalytically activated metal foam absorber for light-to-chemical energy conversion via solar reforming of methane*, Energy & Fuels 17 (2003) 13-17.

[71] J. Kim, D. Jin Suh, T. Park, K. Kim, *Effect of metal particle size on coking during $CO_2$ reforming of $CH_4$ over Ni-alumina aerogel catalysts*, Applied Catalysis A: General 197 (2000) 191-200.

[72] T. Huang, W. Huang, J. Huang, P. Ji, *Methane reforming reaction with carbon dioxide over SBA-15 supported Ni-Mo bimetallic catalysts,* Fuel Processing Technology 92 (2011) 1868-1875.

[73] R. Martinez, E. Romero, C. Guimon, R. Bilbao, *$CO_2$ reforming of methane over coprecipitated Ni-Al catalysts modified with lanthanum*, Applied Catalysis A: General 274 (2004) 139-149.

[74] J. Newnham, K. Mantri, M. Hassan Amin, J. Tardio, S.K. Bhargava, *Highly stable and active Ni-mesoporous alumina catalysts for dry reforming of methane*, International Journal of Hydrogen Energy 37 (2012) 1454-1464.

[75] D. Baudouin, U. Rodemerck, F. Krumeich, A. de Mallmann, K.C. Szeto, H. Ménard, L. Veyre, J.P. Candy, P.B. Webb, C. Thieuleux, C. Copéret, *Particle size effect in the low temperature reforming of methane by carbon dioxide on silica-supported Ni nanoparticles*, Journal of Catalysis 297 (2013) 27-34.

[76] H. Liu, H. Wang, J. Shen, Y. Sun, Z. Liu, *Preparation, characterization and activities of the nano-sized Ni/SBA-15 catalyst for producing $CO_x$-free hydrogen from ammonia*, Applied Catalysis A: General 337 (2008) 138-147.

[77] S. He, L. Zhang, S. He, L. Mo, X. Zheng, H. Wang, Y. Luo, *Ni/$SiO_2$ catalyst prepared with nickel nitrate precursor for combination of $CO_2$ reforming and partial oxidation of methane: characterization and deactivation mechanism investigation*, Journal of Nanomaterials (2015) 1-8.

[78] E. Marceau, M. Che, J. Cejka, A. Zukal, *Nickel(II) Nitrate vs. Acetate: Influence of the precursor on the structure and reducibility of Ni/MCM-41 and Ni/Al-MCM-41 catalysts*, ChemCatChem 2 (2010) 413-422.

[79] C. Cornu, J.L. Bonardet, S. Casale, A. Davidson, S. Abramson, G. Andre, F. Porcher, I.Grcic, V. Tomasic, D. Vujevic, N. Koprivanac, *Identification and location of iron species in Fe/SBA-15 Catalysts: Interest for catalytic Fenton reactions*, Journal of Physical Chemistry C 116 (2012) 3437-3448.

[80] C. Hoang-Van, Y. Kachaya, S.J. Teichner, *Characterization of nickel catalysts by chemisorption techniques, X-ray diffraction and magnetic measurements: Effects of support, precursor and hydrogen pretreatment*, Applied Catalysis 46 (1989) 281-296.

[81] F. Li, X. Yi, W. Fang, *Effect of organic nickel precursor on the reduction performance and hydrogenation activity of $Ni/Al_2O_3$ catalysts*, Catalysis Letters 130 (2009) 335-340.

[82] R. Shi-Biao, S. Zhou, Z. Ping, W. Zhi-Cai, L. Zhi-Ping, P. Chun-Xiu, K. Shi-Gang, S. Heng-Fu, *Highly dispersed Ni/SBA-15 catalysts prepared with different nickel salts as nickel precursors: Effects of activation atmospheres*, Journal of Fuel Chemistry and Technology 42(5) (2014) 591-596.

[83] K. Urasaki, Y. Tanpo, Y. Nagashima, R. Kikuchi, S. Satokawa, *Effects of preparation conditions of $Ni/TiO_2$ catalysts for selective CO methanation in the reformate gas*, Applied Catalysis A: General 452 (2013) 174-178.

[84] S. Wang, G.Q. Lu, *Reforming of methane with carbon dioxide over $Ni/Al_2O_3$ catalysts: Effect of nickel precursor*, Applied Catalysis A: General 169 (1998) 271-280.

[85] G. Wu, C. Zhang, S. Li, Z. Han, T. Wang, X. Ma, J. Gong, *Hydrogen production via glycerol steam reforming over $Ni/Al_2O_3$: Influence of nickel precursors*, ACS Sustainable Chemistry & Engineering1 (2013) 1052-1062.

[86] P. Kumar, Y. Sun, R.O. Idem, *Nickel-based ceria, zirconia, and ceria-zirconia catalytic systems for low-temperature carbon dioxide reforming of methane*, Energy & Fuels 21 (2007) 3113-3123.

[87] M. Usman, W.M.A.Wan Daud, H. F. Abbas, *Dry reforming of methane Influence of process parameters-A review*, Renewable and Sustainable Energy Reviews 45 (2015) 710-744.

[88] J. Taghavimoghaddam, G.P. Knowles, A.L. Chaffee, *Preparation and characterization of mesoporous silica supported cobalt oxide as a catalyst for the oxidation of cyclohexanol*, Journal of Molecular Catalysis A: Chemical 358 (2012) 79-88.

[89] N. Wang, X. Yu, Y. Wang, W. Chu, M. Liu, *A comparison study on methane dry reforming with carbon dioxide over $LaNiO_3$ perovskite catalysts supported on mesoporous SBA-15, MCM-41 and silica carrier*, Catalysis Today 212 (2013) 98-107.

[90] N. Sun, X. Wen, F. Wang, W. Wei, Y. Sun, *Effect of pore structure on Ni catalyst for $CO_2$ reforming of $CH_4$*, Energy Environmental Science 3 (2010) 366-369

[91] L. Xu, H. Song, L. Chou, *Ordered mesoporous $MgO$-$Al_2O_3$ composite oxides supported Ni based catalysts for $CO_2$ reforming of $CH_4$: Effects of basic modifier and mesopore structure*, International Journal of Hydrogen Energy 38 (2013) 7307-7325.

[92] S. Wang, G.Q.M. Lu, *$CO_2$ reforming of methane on Ni catalysts: Effects of the support phase and preparation technique*, Applied Catalysis B: Environmental 16 (1998) 269-277.

[93] C. Zhang, W. Zhu, S. Li, G. Wu, X. Ma, X. Wang, J. Gong, *Sintering-resistant Ni-based reforming catalysts obtained via the nanoconfinement effect*, Chemical Communications 49 (2013) 9383-9385.

[94] Q. Ma, D. Wang, M. Wu, T. Zhao, Y. Yoneyama, N. Tsubaki, *Effect of catalytic site position: Nickel nanocatalyst selectively loaded inside or outside carbon nanotubes for methane dry reforming*, Fuel 108 (2013) 430-438.

[95] S. Sokolov, E.V. Kondratenko, M. Pohl, A. Barkschat, U. Rodemerck, *Stable low-temperature dry reforming of methane over mesoporous $La_2O_3$-$ZrO_2$ supported Ni catalyst*, Applied Catalysis B: Environmental 113-114 (2012) 19-30.

[96] K. Jabbour, N. El Hassan, A. Davidson, P. Massiani, S. Casale, *Characterizations and performances of Ni/diatomite catalysts for dry reforming of methane*, Chemical Engineering Journal 264 (2015) 351-358.

[97] A. Luengnaruemitchai, A. Kaengsilalai, *Activity of different zeolite-supported Ni catalysts for methane reforming with carbon dioxide*, Chemical Engineering Journal 144 (2008) 96-102.

[98] P. Frontera, A. Macario, A. Aloise, F. Crea, P.L. Antonucci, J.B. Nagy, F. Frusteri, G. Giordano, *Catalytic dry-reforming on Ni-zeolite supported catalyst*, Catalysis Today 179 (2012) 52-60.

[99] L. Xu, H. Song, L. Chou, *Carbon dioxide reforming of methane over ordered mesoporous NiO-$Al_2O_3$ composite oxides*, Catalysis Science & Technology 1 (2011) 1032-1042.

[100] X. Zhang, Q. Zhang, N. Tsubaki, Y. Tan, Y. Han, *Carbon dioxide reforming of methane over Ni nanoparticles incorporated into mesoporous amorphous $ZrO_2$ matrix*, Fuel 147 (2015) 243-252.

[101] S. Li, J. Gong, *Strategies for improving the performance and stability of Ni-based catalysts for reforming reactions*, Chemical Society Reviews 43(2014) 7245-7256.

[102] J. S. Beck, J. C. Vart Uli, W. J. Roth, M. E. Leonowicz, C. T. Kresge, K. D. Schmitt, C. T-W. Chu, D. H. Olson, E. W. Sheppard, S. B. McCullen, J. B. Higgins, J. L. Schlenkert, *A new family of mesoporous molecular sieves prepared with liquid crystal templates*, Journal of American Chemical Society 114 (1992) 10834-10843.

[103] D. Zhao, J. Feng, Q. Huo, N. Melosh, G.H. Fredrickson, B.F. Chmelka, G.D. Stucky, *Triblock copolymer syntheses of mesoporous silica with periodic 50 to 300 Angstrom pores*, Science 279 (1998) 548-552.

[104] D. Liu, X. Quek, H. Hui Adeline Wah, G. Zeng, Y. Li, Y. Yang, *Carbon dioxide reforming of methane over nickel-grafted SBA-15 and MCM-41 catalysts*, Catalysis Today 148 (2009) 243-250.

[105] Z. Meili, J. Shengfu, H. Linhua, Y. Fengxiang, L. Chengyue, L. Hui, S*tructural characterization of highly stable Ni/SBA-15 catalyst and its catalytic performance for methane reforming with $CO_2$*, Chinese Journal of Catalysis 27(2006) 777-782.

[106] H. Liu, Y. Li, H. Wu, H. Takayama, T. Miyake, D. He, *Effects of β-cyclodextrin modification on properties of Ni/SBA-15 and its catalytic performance in carbon dioxide reforming of methane*, Catalysis Communications 28 (2012) 168-173.

[107] S. Sokolov, E.V. Kondratenko, M. Pohl, U. Rodemerck, *Effect of calcination conditions on time on-stream performance of Ni/$La_2O_3$-$ZrO_2$ in low-temperature dry reforming of methane*, International Journal of Hydrogen Energy 38 (2013) 16121-16132.

[108] S. Irusta, L. M. Cornaglia, E. A. Lombardo, *Hydrogen production using Ni-Rh on $ZrO_2$ as potential low-temperature catalysts for membrane reactors*, Journal of Catalysis 210 (2002) 263-272.

[109] X. Xie, T. Otremba, P. Littlewood, R. Schomacker, A. Thomas, *One-Pot synthesis of supported, nanocrystalline nickel manganese oxide for dry reforming of methane*, ACS Catalysis 3 (2013) 224-229.

[110] J. Zhu, X. Peng, L. Yao, J. Shen, Do. Tong, C. Hu, *The promoting effect of La, Mg, Co and Zn on the activity and stability of Ni/$SiO_2$ catalyst for $CO_2$ reforming of methane*, International Journal of Hydrogen Energy 36 (2011) 7094-7104.

[111] N. Wang, X. Yu, K. Shen, W. Chu, W. Qian, Synthesis, *Characterization and catalytic performance of MgO-coated Ni/SBA-15 catalysts for methane dry reforming to syngas and hydrogen*, International Journal of Hydrogen Energy 38 (2013) 9718-9731.

[112] A. Khan, T. Sukonket, B. Saha, R. Idem, *Catalytic activity of various 5 wt % Ni/$Ce_{0.5}Zr_{0.33}M_{0.17}O_{2-\delta}$ catalysts for the $CO_2$ reforming of $CH_4$ in the presence and absence of steam*, Energy Fuels 26 (2012) 365-379.

[113] N. Wang, W. Chu, T. Zhang, X.S. Zhao, *Synthesis, characterization and catalytic performances of Ce-SBA-15 supported nickel catalysts for methane dry reforming to hydrogen and syngas*, International Journal of Hydrogen Energy 37 (2012) 19-30.

[114] A. Albarazi, P. Beaunier, P. Da Costa, *Hydrogen and syngas production by methane dry reforming on SBA-15 supported nickel catalysts: On the effect of promotion by $Ce_{0.75}Zr_{0.25}O_2$ mixed oxide*, International Journal of Hydrogen Energy 38 (2013) 127-139.

[115] A. Nandini, K.K. Pant, S.C. Dhingra, *K-, $CeO_2$-, and Mn-promoted Ni/$Al_2O_3$ catalysts for stable $CO_2$ reforming of methane*, Applied Catalysis A: General 290 (2005) 166-174.

[116] N. Laosiripojana, W. Sutthisripok, S. Assabumrungrat, *Synthesis gas production from dry reforming of methane over $CeO_2$ doped Ni/$Al_2O_3$: Influence of the doping ceria on the resistance toward carbon formation*, Chemical Engineering Journal 112 (2005) 13-22.

[117] K. Wang, B. Dou, B. Jiang, Y. Song, C. Zhang, Q. Zhang, H. Chen, Y. Xu, *Renewable hydrogen production from chemical looping steam reforming of ethanol using xCeNi/SBA-15 oxygen carriers in a fixed-bed reactor*, International Journal of Hydrogen Energy 41 (2016) 12899-12909.

[118] Y. Fu, Y. Wu, W. Cai, B. Yue, H. He, *Promotional effect of cerium on nickel-containing mesoporous silica for carbon dioxide reforming of methane*, Science China Chemistry 58 (2015) 148-155.

[119] J. Zhu, X. Peng, L. Yao, X. Deng, H. Dong, D. Tong, C. Hu, *Synthesis gas production from $CO_2$ reforming of methane over Ni-Ce/$SiO_2$ catalyst: The effect of calcination ambience*, International Journal of Hydrogen Energy 38 (2013) 117-126.

[120] S. Zhang, S. Muratsugu, N. Ishiguro, M. Tada, *Ceria-Doped Ni/SBA-16 catalysts for dry reforming of methane*, ACS Catalysis 3 (2013) 1855-1864.

[121] H. Tanaka, R. Kaino, K. Okumura, T. Kizuka, K. Tomishige, *Catalytic performance and characterization of Rh-$CeO_2$/MgO catalysts for the catalytic partial oxidation of methane at short contact time*, Journal of Catalysis 268 (2009) 1-8.

[122] W. Wang, S.M. Stagg-Williams, F.B. Noronha, L.V. Mattos, F.B. Passos, *Partial oxidation and combined reforming of methane on Ce-promoted catalysts*, Catalysis Today 98 (2004) 553-563.

[123] D. Li, L. Zeng, X. Li, X. Wang, H. Ma, S. Assabumrungrat, J. Gong, *Ceria-promoted Ni/SBA-15 catalysts for ethanol steam reforming with enhanced activity and resistance to deactivation*, Applied Catalysis B: Environmental 176-177 (2015) 532-541.

[124] H. Wan, X. Li, S. Ji, B. Huang, K. Wang, C. Li, *Effect of Ni loading and $Ce_xZr_{1-x}O_2$ promoter on Ni-Based SBA-15 catalysts for steam reforming of methane*, Journal of Natural Gas Chemistry 16 (2007)139-147.

# CHAPTER II

# Experimental Part

Chapter II describes the experimental part of this PhD thesis research. It is presented in four main parts. The first one describes the methods applied for materials preparation, the second one details the various characterization techniques used to identify the physico-chemical properties of the samples (before and after catalytic test), and the third one is devoted to the conditions of catalytic dry reforming test. The fourth one ends the chapter with an assessment of the thermodynamic equilibrium of the reaction under varying experimental conditions, evaluated in order to correctly position and discuss the catalytic performances with respect to expected equilibrium values.

## II.1 Materials Preparation

Most of the synthesized or selected supports were silica-based materials. The metal precursor salts (in the form of aqueous solutions) were first added to the supports, then calcination in air was applied to form supported metal oxides. Next, reduction was carried out under hydrogen to convert the supported metal oxides into metal nanoparticles, which are the active phases of the reaction of methane dry reforming. Accordingly, the first part of this section describes the preparation of the various supports, next the methods employed for the deposition of the active phase on the supports are detailed.

### II.1.1 Supports

The different supports used for Ni deposition, either synthesized or commercial, are listed below. Their specific synthesis conditions or their commercial origins are detailed in the subsequent sections a, b and c. The detailed quantities of reagents used, the nomenclature of the supports and their major characteristics are also summarized at the end of this section, in Table II-1.

- Two batches of mesoporous SBA-15 (SBA-$A_1$ and SBA-$A_2$) were synthesized on small scale (4 g), without hydrothermal treatment (see below), to carry out preliminary catalytic studies,

- One batch of mesoporous SBA-15 was synthesized at larger scale, which allowed preparing10 g of support without hydrothermal treatment (SBA-$A_3$) and around 60 g of support with hydrothermal treatment (SBA-$B_1$),
- One batch of mesoporous SBA-15 support (SBA-$B_2$) was prepared on small scale while changing the concentration of the initial HCl solution, in order to change the grain morphology, as reported by Choi et al.,[1]
- Two synthesized mesoporous $CeO_2$ supports ($CeO_2$-A and $CeO_2$-C) were prepared via hard-template method in order to evaluate the interesting properties of ceria-based materials (as will be detailed later),
- Several commercial silica supports (either non-porous or mesoporous with various grain morphologies) were selected as reference materials for comparison, based on their structural and morphological properties.

*a) SBA-15 silica supports syntheses*

All synthesized SBA-15 silica supports were prepared according to the well-known method developed by Zhao et al.[2] in 1998 based on the cooperative sol-gel self-assembly mechanism well reported in literature (Fig. II-1).[3,4,5]

The surfactant used was the triblock copolymer poly (ethylene glycol)-poly (propylene glycol)-poly(ethylene glycol), known as P123 with typical molecular weight of 5800 $g.mol^{-1}$ (Sigma Aldrich, 435465, 9003-11-6). Briefly, under acidic medium (0.3 or 1.9M HCl), the P123 containing hydrophobic tails and hydrophilic heads self-assemble into spherical micelles (step 1-Fig. II-1) that are later elongated and transformed into micellar rods upon addition of tetraethylorthosilicate (TEOS from Sigma Aldrich, 86578, 78-10-4) as silica source (step 2-Fig. II-1). For all syntheses, the TEOS to P123 molar ratio was maintained around 60. Next, these cylinders begin to aggregate into a two-dimensional hexagonal structure (step 3-Fig. II-1). The condensation of the silica results in cross-linking and covalent bonding between the coronas and thus SBA-15 grains are formed.

Based on this procedure, the resulting material can be either directly filtered and calcined or submitted to a hydrothermal treatment (often carried out at 95°C) before filtration and calcination. As usually done,[3] the SBA-15 silica supports will be called SBA-A when prepared without hydrothermal treatment or SBA-B when subjected to hydrothermal treatment at 95°C. The

calcination step is performed to remove the organic template and obtain the final mesoporous SBA-15 support. In this work, this calcination was done in air at 500°C (heating rate of 2°C.min$^{-1}$) for 9 hours in a muffle furnace (Nabertherm, LE6/11).

The first preliminary preparations were carried out on small scale (Fig. II-2A) to obtain around 4 g of calcined material, as frequently reported in literature.[1,2,3,4,5,6] These supports were named SBA-$A_1$ and SBA-$A_2$ (Table II-1). In order to have a greater SBA-15 quantity, sufficient for allowing comparative experiments starting from the same support material, a larger scale preparation was carried out using a 4L double-jacketed reactor (Fig. II-2B), leading to 10 g of SBA-$A_3$ and 60 g of SBA-$B_2$ (Table II-1).

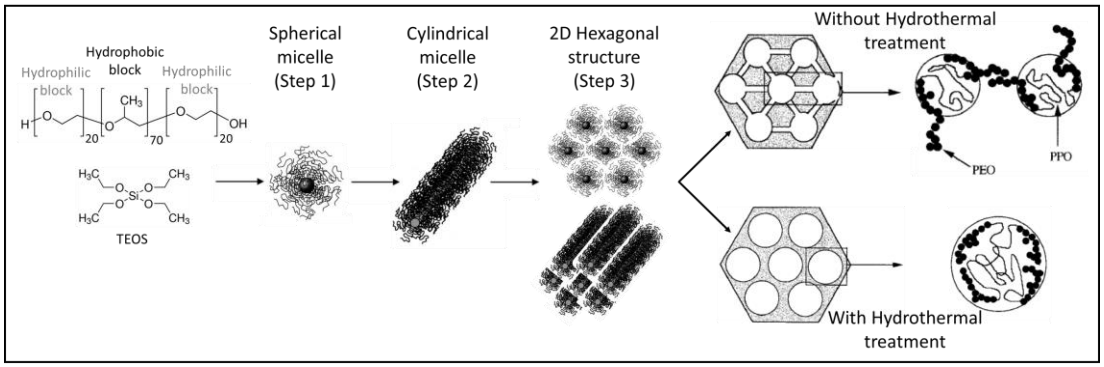


Figure II-1: Schematic illustration of the synthesis mechanism of mesoporous silica support[7,8]

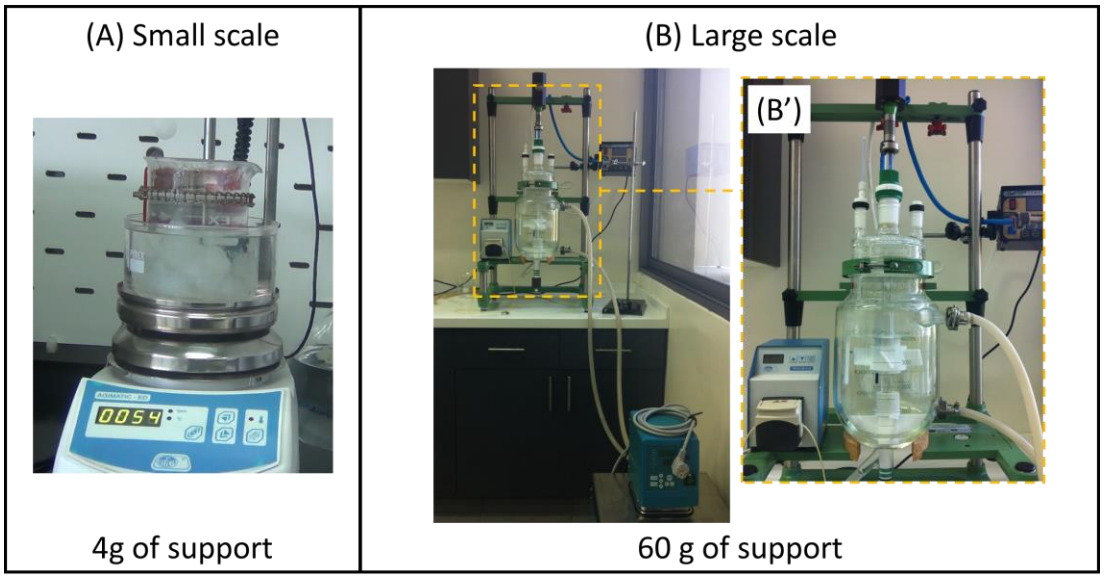


Figure II-2: Small scale (A) and large scale (B) reactor setups for support preparation

*b) Mesoporous $CeO_2$ support synthesis*

The mesoporous $CeO_2$ support was prepared using the hard template method (Fig. II-3), also known as nanocasting, which consists in using a hard porous structure to shape the materials.[9,10] Thus, the precursor is first introduced inside the channels of the hard template, where it is shaped according to the morphology and structure of the template, and later the template is removed.

In our case, two SBA-15 silica supports were used as the hard templates: an SBA-A prepared under analogous conditions as SBA-$A_1$ and SBA-$A_2$ (without hydrothermal treatment) and SBA-C subjected to hydrothermal treatment at 130°C. The addition of cerium nitrate to the SBA-15 was done using two solvents impregnation. In details, 1g of SBA-15 was first stirred in 20 ml hexane for 15 min and then 1.5 ml of cerium solution (prepared by dissolving 9g of cerium nitrate in 10 ml of distilled water) was added drop by drop to the suspension (step 1-Fig. II-3). The resulting supports were left to dry in air for 24hours and were next calcined at 450°C (heating rate 0.5°C.min$^{-1}$) for 5 hours, leading to the formation of Ce/SBA-15. The same procedure was repeated again for a second impregnation of Ce and the 2Ce/SBA-15 sample was obtained (step 2-Fig. II-3). After calcination, the SBA-15 template needs to be removed in order to keep only the shaped $CeO_2$nanoparticles (step 3-Fig. II-3).

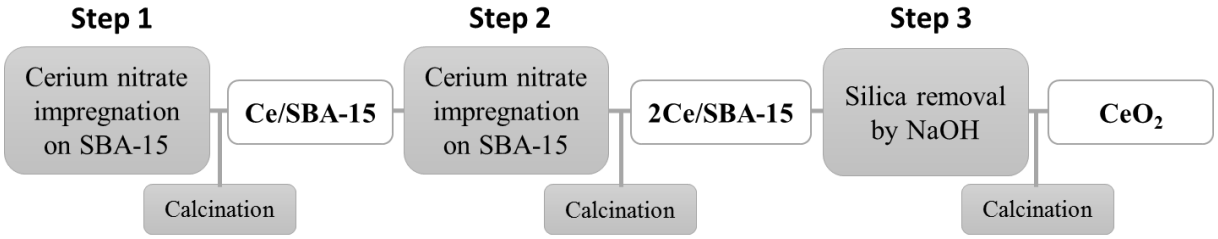


Figure II-3: Process of preparation of mesoporous $CeO_2$ support

According to literature, silica removal is usually done using a 2M NaOH aqueous solution[11,12,13] and we chose to also apply this procedure. Thus, 50 ml of NaOH (2M) solution were added to 1 g of calcined 2Ce/SBA-15 and stirred for 2 hours before centrifugation at ambient temperature. Next, different procedures are reported[11,12,13] and therefore many trials were done before selecting the optimum conditions for this step:

- Washing after centrifugation resulted in loss of material and only trace amounts of cerium were collected after filtration.
- The duration of centrifugation was minimized from 20 min to 5 min at 3000 rpm.
- It was noticed that the temperature of centrifugation played an important role in the separation of the two phases, thus it was decreased from 35 to around 20°C.

Consequently, after many attempts, the optimum conditions adopted were based on the centrifugation at 3000 rpm for 5 min at 20°C, followed by drying for 24 hours and then calcination at 450°C (heating rate 0.5°C.min$^{-1}$) for 5hours. The resulting support was named $CeO_2$-A or $CeO_2$-C, depending on the type of initial SBA-15 used.

*c) Commercial supports*

Reference silica materials were selected based on their textural properties and used for comparison with the synthesized supports (Table II-1). These commercial silica-based supports are the following:

- $SiO_2$ is a nonporous fumed silica (Sigma Aldrich, 381276, 112945-52-5), used to study the effect of porosity,
- meso-$SiO_2$ is a mesoporous silica (Sigma Aldrich,748161, 7631-86-9) composed of spherical grains with a pore size of 4 nm, used to study the effect of grain morphology,
- com-SBA-15 is a mesoporous SBA-15 (Sigma Aldrich, 777242, 7631-86-9), used to compare the synthesized mesoporous SBA-15 support to the commercial one.

Table II-1: Nomenclature and synthesis conditions of supports

**II-1(a) Synthesized mesoporous SBA-15 supports***

| Support Name | P123 (g) | HCl (M) | HCl (ml) | TEOS (ml) | TEOS Addition | Hydrothermal treatment | Available amount after calcination(g) |
|---|---|---|---|---|---|---|---|
| SBA-$A_1$<br>SBA-$A_2$ | 8.0 | 1.9 | 252 | 18.4 | Burette<br>Drop by drop | None | 4 |
| SBA-$A_3$ | 115 | 1.9 | 3620 | 364.5 | Peristaltic Pump<br>15 ml.min$^{-1}$ | None | 10 and 60 |
| SBA-$B_1$ | | | | | | 95°C/48h | |
| SBA-$B_2$ | 10.6 | 0.3 | 200 | 24.6 | Rapid | 95°C/24h | 5 |

* All syntheses done at 35°C

**II-1(b) Synthesized mesoporous $CeO_2$ support**

| Support Name | Characteristic | Preparation method | Available amount after calcination (g) |
|---|---|---|---|
| $CeO_2$-A | Mesoporous | Hard template using SBA-A | 1 |
| $CeO_2$-C | Mesoporous | Hard template using SBA-C | 1 |

**II-1(c) Commercial silica-based supports**

| Support Name | Reference number (Sigma Aldrich) | CAS Number | Characteristic |
|---|---|---|---|
| $SiO_2$ | 381276 | 112945-52-5 | Non-porous silica |
| meso-$SiO_2$ | 748161 | 7631-86-9 | Spherical silica grains |
| com-SBA-15 | 777242 | 7631-86-9 | Mesoporous SBA-15 |

### II.1.2 Addition of metal salts

The previously mentioned supports were used for the deposition of the precursor metal salts. The precursor salts employed in this work are mentioned in Table II-2 with their formulas and product numbers. The nature of the used nickel precursor salt, in particular, will be specified

between parentheses in the nomenclature of the samples at the end of this section (Table II-3). Specifically, "N" will refer to nickel nitrate, "Cl" to nickel chloride and "A" to nickel acetate. The deposition of precursors on the supports, in the form of aqueous solutions, was done mainly using the two solvents impregnation (2S). Two additional techniques were employed for comparison: incipient wetness impregnation (IWI) or direct synthesis (DS). The nickel content was varied between 2.5 and 7.5 wt% on the SBA-$A_1$ and SBA-$A_2$ supports, between 6.2 and 16 wt% on the $CeO_2$ supports, and was maintained at 5.0wt% in the remaining samples, as specified in the name of each sample (Table II-3). A "Ni-free" $Ni_0$/SBA-$A_2$ sample was also prepared by submitting the SBA-$A_2$ support to the two solvents procedure but without metal addition (to be used for comparative purposes). In addition to the main active phase (Ni), additional phases (like Rh, Ce, La and Mg) were also carried out for enhancement of the properties, as will be detailed in the corresponding chapters. The co-impregnation was applied for adding 6 wt% Ce, Mg and La with 5.0 wt% Ni, whereas0.1 or 0.5 wt% Rh were added to the calcined $Ni_{5.0}$/SBA-$B_1$(N).

Table II-2: Precursor salts used for impregnation

| **Precursor salt** | **Linear formula** | **Product number (Sigma Aldrich)** | **CAS Number** |
|---|---|---|---|
| Nickel (II) nitrate hexahydrate | $Ni(NO_3)_2.6H_2O$ | 72253 | 13478-00-7 |
| Nickel (II) acetate tetrahydrate | $Ni(OCOCH_3)_2.4H_2O$ | 72225 | 6018-89-9 |
| Nickel (II) chloride hexahydrate | $NiCl_2.6H_2O$ | 31462 | 7791-20-0 |
| Rhodium (III) nitrate hydrate | $Rh(NO_3)_3.xH_2O$ | 83750 | 10139-58-9 |
| Cerium (III) nitrate hexahydrate | $Ce(NO_3)_3.6H_2O$ | 238538 | 10294-41-4 |
| Lanthanum (III) nitrate hexahydrate | $La(NO_3)_3.6H_2O$ | 331937 | 10277-43-7 |
| Magnesium (II) nitrate hexahydrate | $Mg(NO_3)_2.6H_2O$ | 237175 | 13446-18-9 |

*a) Two solvents impregnation (2S)*

The two solvents or double solvents impregnation method is an attractive technique that is reported to favor the homogeneous deposition of the metal oxide precursors inside the porosity of the support.[11,14,15,16] Indeed, n-hexane is an organic solvent poorly miscible with water. When the silica grains are suspended in the solvent, only one/two layers of water remain attached to

silica walls inside the pores. Later, when the aqueous solution is added drop-by-drop, it easily penetrates inside the pores leading to a high dispersion of the initial salt.

Practically speaking, the required amount of metal precursor salt is dissolved in a volume of water equal to the porous volume of the support. From $N_2$ sorption (detailed in section II.2), an average porous volume of 1.2 ml/g of support is considered for the impregnation of the hydrothermally treated supports, 0.7 ml/g of non-treated SBA-15 supports, 1 ml/g of com-SBA-15 and 4 ml/g of $SiO_2$. The support is stirred for 15 minutes in n-hexane and then the aqueous solution containing the desired metal is added dropwise to the support with manual stirring. Finally, after drying overnight the hexane is evaporated and the dried powder is calcined at 450°C (thin bed conditions, heating rate 0.5°C.min$^{-1}$) for 5 hours in order to remove the nitrates or chlorides and keep the metal oxides.

*b) Incipient wetness impregnation (IWI)*

Another impregnation technique, commonly reported in literature[17] owing to its simplicity, is the incipient wetness impregnation (also known as dry impregnation) in which the volume of metal precursor aqueous solution is equal to the pore volume of support. In order to work under similar conditions, an average porous volume of 1.2 ml/g of support is here also chosen for impregnation. The same calcination conditions mentioned before are used in this case.

*c) Direct synthesis (DS)*

While the two previous impregnation techniques are post-synthesis procedures, direct synthesis or single-step procedure appears as an interesting way to save time and energy. To test this method, the procedure by Park et al. is adapted[6] while maintaining the same TEOS to P123 molar ratio of 60. This synthesis consists on dispersing 10g of P123 in 322 ml of distilled water under agitation at 300 rpm at 40°C, maintained using silicone oil bath. After complete dissolution, 52 g of 2M HCl solution are added and the agitation and heating are kept overnight. Afterwards, the addition of 20.5 g of TEOS is followed by the addition of 21 g of nickel nitrate and the resulting solution is kept at 40°C without agitation for 24 hours. Next, the solution is transferred for hydrothermal treatment in Nalgene bottles at 95°C for another 24hours. Finally, the solution is filtered and the powder left to dry in air overnight before calcination. The resulting calcined sample is referred to as $Ni_{5.0}$/SBA-15(DS).

Table II-3: List of Ni-based samples prepared by two-solvents method

| Support | Sample Name | Nickel precursor salt | Metal Content (wt%) | | Order of impregnation |
|---|---|---|---|---|---|
| | | | Ni | Co-metal | |
| $SBA\text{-}A_1$ | $Ni_{2.5}/SBA\text{-}A_1(N)$ | Nitrate | 2.5 | - | Only Ni |
| | $Ni_{5.0}/SBA\text{-}A_1(N)$ | | 5.0 | - | |
| | $Ni_{7.5}/SBA\text{-}A_1(N)$ | | 7.5 | - | |
| $SBA\text{-}A_2$ | $Ni_0/SBA\text{-}A_2(N)$ | - | 0 | - | - |
| | $Ni_{2.5}Ce_6/SBA\text{-}A_2(N)$ | Nitrate | 2.5 | 6 | Ce then Ni |
| | $Ni_{5.0}Ce_6/SBA\text{-}A_2(N)$ | | 5.0 | 6 | |
| | $Ni_{7.5}Ce_6/SBA\text{-}A_2(N)$ | | 7.5 | 6 | |
| $SBA\text{-}A_3$ | $Ni_{5.0}/SBA\text{-}A_3(N)$ | Nitrate | 5.0 | - | Only Ni |
| $SBA\text{-}B_1$ | $Ni_{5.0}/SBA\text{-}B_1(N)$ | | | - | |
| | $Ni_{5.0}/SBA\text{-}B_1(R)$[a] | | | - | |
| | $Ni_{5.0}/SBA\text{-}B_1(Cl)$ | Chloride | | - | |
| | $Ni_{5.0}/SBA\text{-}B_1(A)$ | Acetate | | - | |
| | $Ni_{5.0}Ce_6/SBA\text{-}B_1(N)$ | Nitrate | | 6 | Co-impregnation |
| | $Ni_{5.0}Mg_6/SBA\text{-}B_1(N)$ | | | | |
| | $Ni_{5.0}La_6/SBA\text{-}B_1(N)$ | | | | |
| | $Ni_{5.0}Rh_{0.1}/SBA\text{-}B_1(N)$ | | | 0.1 | Ni then Rh |
| | $Ni_{5.0}Rh_{0.5}/SBA\text{-}B_1(N)$ | | | 0.5 | |
| | $Ni_{5.0}/SBA\text{-}B_1(N_{IWI})$[b] | | | - | Only Ni |
| | $Rh_{0.5}/SBA\text{-}B_1$ | - | - | 0.5 | Only Rh |
| $SBA\text{-}B_2$ | $Ni_{5.0}/SBA\text{-}B_2(N)$ | Nitrate | 5.0 | - | Only Ni |
| $CeO_2\text{-}A$ | $Ni_{6.2}/CeO_2\text{-}A(N)$ | | 6.2 | - | |
| $CeO_2\text{-}C$ | $Ni_{6.2}/CeO_2\text{-}C(N)$ | | | - | |
| $CeO_2\text{-}C$ | $Ni_{16}/CeO_2\text{-}C(N)$ | | 16 | - | |
| com-SBA-15 | $Ni_{5.0}$/com-SBA-15(N) | | 5.0 | - | |
| meso-$SiO_2$ | $Ni_{5.0}$/meso-$SiO_2$(N) | | | - | |
| $SiO_2$ | $Ni_{5.0}/SiO_2(N)$ | | | - | |
| SBA-15 | $Ni_{5.0}/SBA\text{-}15(N_{DS})$[c] | | | - | - |

[a]Sample directly reduced without calcination
[b]Sample prepared by incipient wetness impregnation
[c]Sample prepared by direct synthesis

## II.2 Characterization techniques

The properties of the samples at different stages of synthesis and activation (calcined, reduced and spent after reaction) were evaluated using different characterization techniques. In this section, the principle of each technique, the operating conditions, then the resulting type of information that can be obtained will be described. The specificity and complementarity of the various methods will be underlined along the descriptions.

### II.2.1 $N_2$ adsorption-desorption isotherms

*Principle:* Some of the textural properties of the samples can be evaluated by nitrogen sorption. Fig. II-4 illustrates the ASAP 2020 (Micromeritics) apparatus used in this work, with both degas and analysis schematics of the equipment. Degas, or vacuum outgassing, is first performed in order to remove all physisorbed species from the surface of the sample. Then, the $N_2$ isotherms are collected using point-by-point procedure. Nitrogen gas is introduced in successive amounts, the system is allowed sufficient time to reach equilibrium pressure, and then each point on the isotherm is determined by measuring the **volume of nitrogen gas ($V_{exp}$)**adsorbed (or desorbed). This procedure is done at a constant temperature (liquid $N_2$, ~77K or -196.15°C) over a range of **relative pressures($P/P_0$)** between 0 and 1.

Different types of isotherms can be obtained, depending on the textural properties of the samples. Detailed description of each type can be found in the recently updated technical IUPAC report published in 2015.[18]

In our work, the isotherms mainly encountered are (i) type II isotherm given by physisorption of gases on nonporous or macroporous adsorbents and (ii) type IV(a) isotherm given by mesoporous adsorbents (Fig. II-5a). The inflection point (marked as point B on the isotherms) corresponds to monolayer coverage of the surface. Further increase in relative pressure results in multi-layer coverage. A typical feature of type IV(a) isotherms is the final saturation plateau up to $P/P_0 = 1$.

Furthermore, when adsorption and desorption plots do not coincide, a hysteresis loop is observed and is attributed to mesoporous structure (type IV(a) isotherms). The hysteresis loops are also classified according to their shapes into 6 characteristic types (Fig. II-5b). These will be further described in the following chapters, depending on the results obtained.

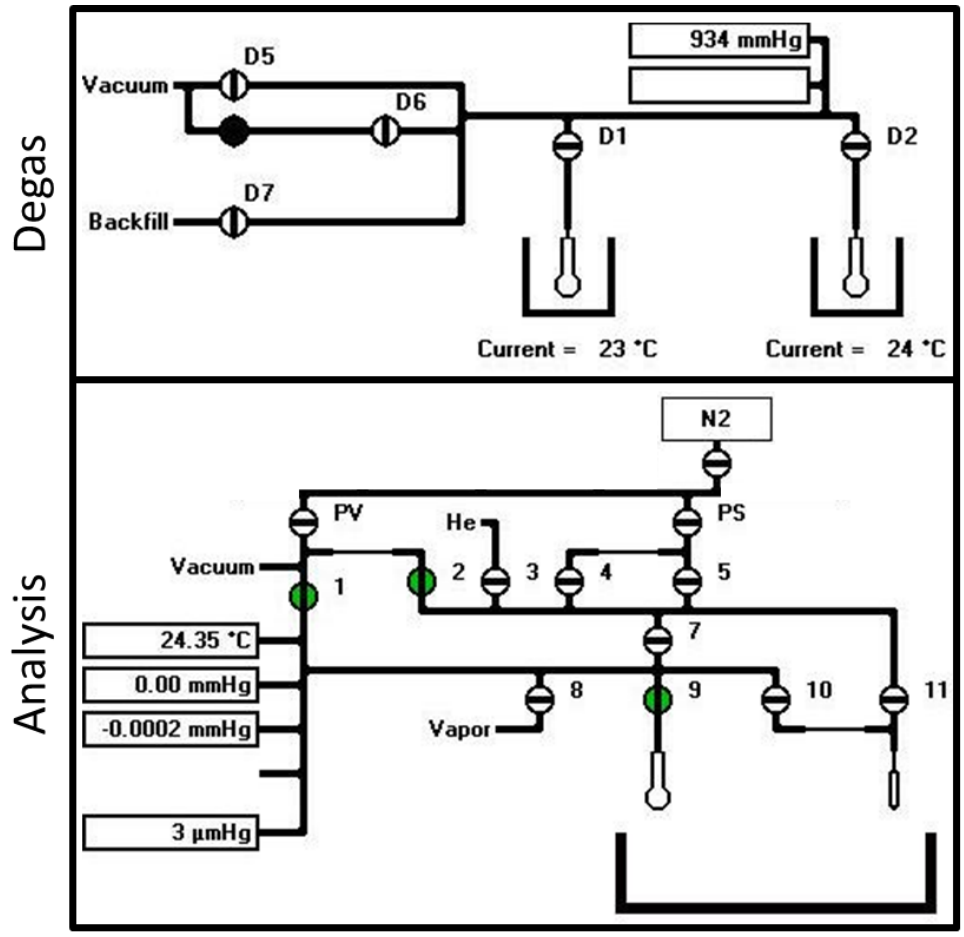


Figure II-4: Schematic of degas and analysis on the ASAP 2020

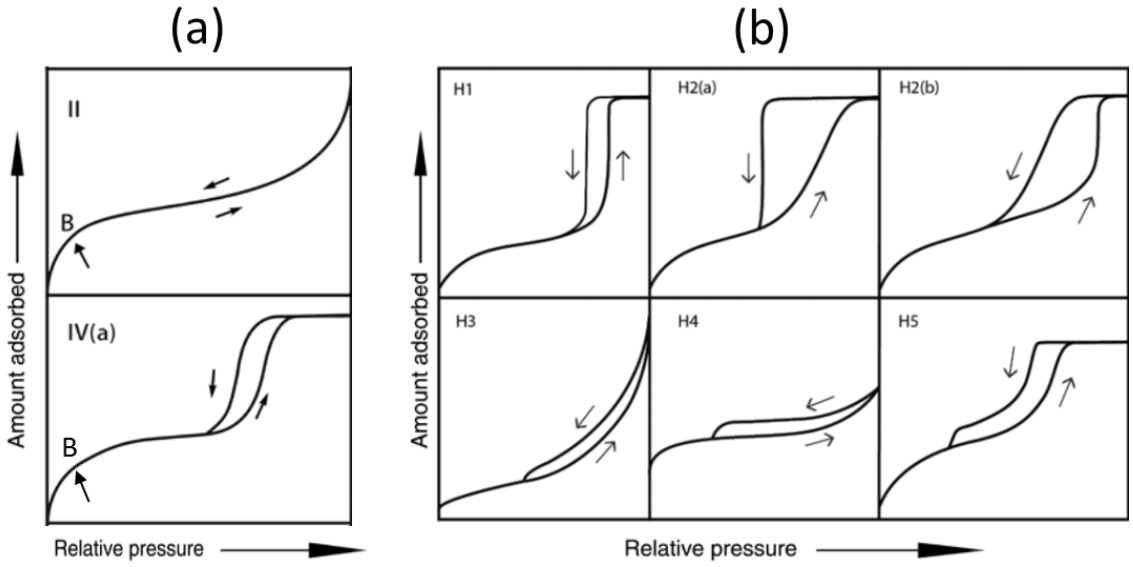


Figure II-5: Updated classification of (A) physisorption isotherms and (B) hysteresis loops[18]

*Procedure:* In our case, around 40-60 mg of powder is used for measurement. Prior to experiment, the sample is first degassed in vacuum (1.3 Pa) for 2hours at 250°C. For the expression of results, we have chosen to fix the y-axis of all isotherms at a maximum of 800 $cm^3/g$ at standard temperature and pressure of $N_2$ adsorbed, in order to facilitate the comparison between samples.

*Type of information:* The evaluation of surface area is done using the commonly known Brunauer–Emmett–Teller (BET) method for relative pressures between 0.05 and 0.30:

$$\frac{C}{V_{exp}(P_0 - P)} = \frac{1}{V_m} + \frac{(C-1)}{V_m}\frac{P}{P_0}$$

Where:

- $V_m$ is the volume of monolayer of gas adsorbed

- C is the BET constant, characteristic of the interaction between the nitrogen molecule and the surface, related to the heat of adsorption of nitrogen on the surface. A sharp point B is indicative of a high value of C and thereby of a high adsorbent-adsorbate interaction.

The BET plot of $C/V_{exp}$ ($P_0$-P) as a function of $P/P_0$ generates a line whose y-intercept corresponds to $1/V_m$ and its slope can be used to determine C.

Next, the **total BET surface area ($S_{BET}$)** is obtained from $V_m$ by applying:

$$S_{BET} = \frac{V_m N_A A}{V}$$

Where:

- $N_A$ is Avogadro's number ($6.023 \times 10^{23}$ molecules.$mol^{-1}$)

- A is the area of a single adsorbed nitrogen molecule (16.2 $Å^2$)

- V is the molar volume of $N_2$ (22414 $cm^3.mol^{-1}$).

The **total pore volume ($V_p$)** is derived from the amount of $N_2$ adsorbed at a relative pressure close to unity, when all pores are assumed to be filled with nitrogen in the bulk liquid state. The

pore size distribution is estimated using the Barett, Joyner, Halenda (BJH) method, based on the Kelvin equation.

To determine the **micropore volume ($V_{micro}$)** and **external surface area (SA)**, the t-plot method is used. The volume adsorbed is plotted against the **thickness of the adsorbed layer (t)**that is determined by:

$$t = t_m \frac{V_{exp}}{V_m}$$

where $t_m$ is the thickness of a monolayer, for nitrogen $t_m$ = 3.54 Å. The intercept of the low linear region with the y-axis corresponds to the micropore volume, while the slope of the higher linear region corresponds to the external surface area.

### II.2.2 Scanning Electron Microscopy (SEM)

*Principle*: Micrographs are produced by scanning the specimen with a focused beam of electrons. The electrons interact with atoms in the sample; secondary ones are generated and emitted from the surface of the specimen by inelastic scattering interactions with beam electrons, generating images that can be used for information about the surface topography and composition. In addition to this secondary electron detection mode, SEM can also operate in backscattered mode, for a better visualization of external particles. By collecting retro-diffused or back-scattered electrons (emitted by elastic scattering interactions), contrast between areas with different chemical compositions can be observed since heavy elements backscatter electrons more strongly than light elements, and thus appear brighter in the image.

*Procedure*: The SEM images are observed on a Hitachi SU-70 Scanning Electron Microscope with a Field Emission Gun (SEM-FEG). A low voltage of 1 keV is employed at a maximum distance up to 2.4 mm between the electron source and the sample, without the need to cover the sample with a carbon or gold conducting film previous to observations. The images are recorded in a mixed mode to obtain simultaneous information on the surface morphology of the grains (70% of secondary electrons signal) and on the external Ni-based species, if present (30% of retro-diffused signal).

*Type of information*: The shape of the grains (width, height and thickness) and the external particles are observed by SEM. Any modification of grain morphology upon thermal treatments can be identified, using this technique. On the spent samples, after reaction, carbon deposition (in the form of single or multi-walled carbon nanotubes) can be also viewed by SEM.

### II.2.3 Transmission Electron Microscopy (TEM)

*Principle*: A beam of electrons goes through an ultra-thin specimen. Depending on the thickness, density and chemical composition of the sample, electrons are absorbed. An image can thus be formed from the interaction of the electrons transmitted with the sample. When high-resolution images are obtained, the reticular distance can be measured and used to identify the nature of the particle, based on the reticular distance found on the ICDD (International Center for Diffraction Data) sheets. TEMs can also be equipped with energy dispersive spectroscopy (EDS) that can reveal the chemical composition of the specimen. If the incident beam has enough energy, it may eject a core-level electron energy (Ea) from an atom. The electron vacancy at the core level is filled by a higher-level electron energy (Eb). As a result of this electron transition, an X-ray of energy (Eb-Ea), characteristic of the element, is emitted. The resulting spectra may contain different peaks at various energies, indicative of the presence of different elements.

*Procedure*: TEM images are collected using a 2010 JEOL JEM-200 electron microscope operating at 200 keV (LaB6 gun) equipped with an energy dispersive spectroscopy (EDS). Few milligrams of powder are diluted in ethanol and deposited on a copper grid coated with a 10 nm carbon membrane.

*Type of information*: The morphology of the support (pore widths and distribution) and the dispersion of the supported particles are studied by TEM. Light and dark areas on the images are influenced by the thickness of the observed specimen. When the electron beam is parallel to the main axis of the silica grains, the 2D hexagonal structure of the SBA-15 can be observed (Fig. II-6). When the beam is perpendicular to the main axis of the grains, the mesoporous channels of the SBA-15 are seen as an alternating pattern of light and dark grey. The supported particles appear in dark on the grey silica walls owing to their higher electronic density. Their distribution along the channels of the support or on the external surface can thus be easily distinguished. A

statistical counting of at least 500 particles is done to estimate the average particles diameter size by using a software named *Comptage de particules, LRS*.

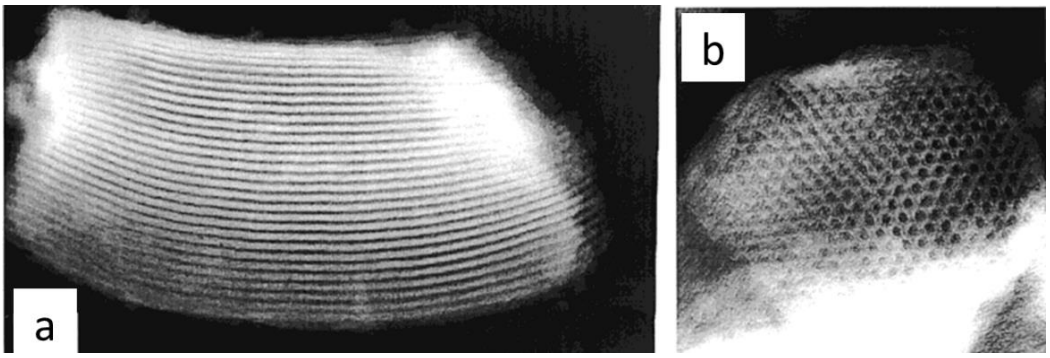


Figure II-6: TEM images of SBA-15 when the electron beam is (a) perpendicular or (b) parallel to the main axis of the pores[2]

### II.2.4 X-ray diffraction (XRD)

*Principle*: The X-ray beam is directed towards the sample and the intensity of the diffracted rays is collected. To explain the phenomena, a simple 2D scheme is in general proposed (Figure II-7). In this scheme, if a single line of equidistant atoms is considered, the Bragg relation can be introduced and the angle between the incident rays and the sample is identical to the angle between the reflected rays and the sample. If a second line of atoms is considered, it will also diffract the incident beam and constructive interactions will result in an increased diffracted intensity. A diffratogram is thus collected by plotting the diffracted intensities as a function of angles. On this plot, each family of reticular planes, identified by Miller hkl indices, will give a characteristic diffraction peak.

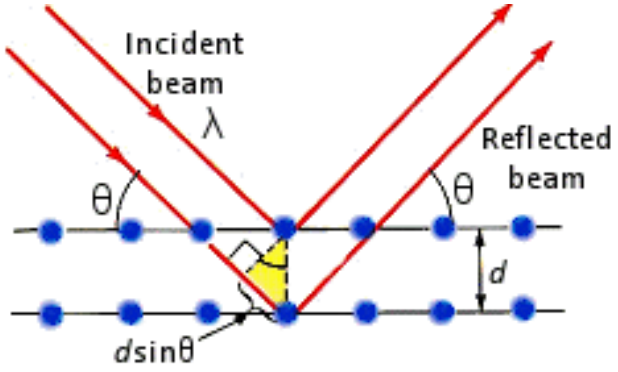


Figure II-7: Principle of X-ray diffraction

The Bragg relation is applied to convert the **observed angles(θ)** into **reticular distance (d)** between the planes:

$$2\ d\ sin\theta = n\ \lambda$$

Where:

- θ is half the diffraction angle,

- n is the order of diffraction (equal to 1 in this case),

- λ is the wavelength of the radiation.

Several databases exist in order to attribute the peaks to a specific crystalline phase based on the positions of peaks and their relative intensities. Thus the composition and crystal structure of the solid can be determined by comparing the diffraction pattern with known patterns, the ICDD (International Center for Diffraction Data). The crystalline phases identified in the present work are listed in Table II-4.

Table II-4: Main phases identification and characteristics

| **Phase identified** | **ICDD reference number** | **Main diffraction peaks** | **Structure** |
|---|---|---|---|
| NiO | 73-1523<br>89-5881<br>04-0835 | 37, 43, 62, 76, 81° | Face-centered cubic lattice (Fm-3m) |
| $Ni^0$ | 65-0380<br>65-2865 | 44, 52, 76° | Face-centered cubic lattice(Fm-3m) |
| $CeO_2$ | 81-0792<br>75-5980 | 28, 33, 47, 56, 69° | Face-centered cubic lattice (Fm-3m) |
| Rh | 75-3848 | 44° | cubic lattice (Fm-3m) |

*Procedure*: For small angles, the diffractogarms are collected between 0.5 and 5° either on the SWING beamline of synchrotron SOLEIL[19] or on a Brüker D8 diffractometer (at LRS, Paris,

Bragg-Brentano, CuKα = 1.5418Å) using a step size of 0.01° at 1s per step and operating at 30 kV and 10 mA. For wide angles, the diffractograms are registered between 5 and 90°, either on the same Brüker D8 diffractometer as above but using a step size of 0.03° at 1s per step, or on a Panalytical XPert$^3$ diffractometer (at UOB, Lebanon) with still the same Cu Kα radiation, 30 kV and 10 mA conditions, and using a step size of 0.04° at 500s per step. The profiles shown on Fig. II-8 correspond to results obtained for the same sample using the last two mentioned diffractometers. When the signal registered on the Brüker equipment is multiplied by 3, the background noise is more important; the measurement made with the Panalytical is less noisy but has implied much longer measurements (500 s and not 1s by step). However, the intensity of the peaks and their full width at half maximum are comparable with the two equipments. This implies that the calculated average particle sizes will be the same regardless of the equipment used.

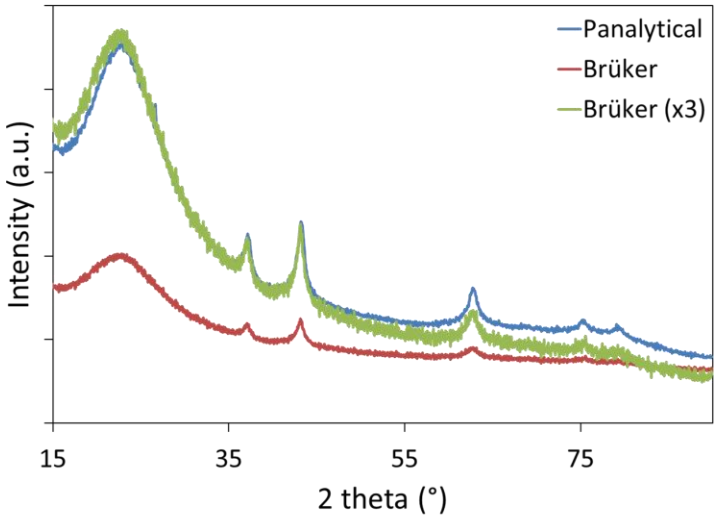


Figure II-8: XRD profiles obtained on different diffractometersfor the same sample

*Type of information*: The XRD were done to evaluate the crystallinity and phase identification of the samples. Typical X-ray diffractograms obtained at low and wide angles are shown in Fig. II-9. The small angle X-ray diffraction allows the assessment of structure and crystallinity of supports. For example, mesoporous SBA-15 materials with periodically ordered pores give a profile analogous to the one in Fig. II-9(a). The three diffraction peaks can be associated to (100)

(110) and (200) planes formed by regular mesopores. The **unit cell parameter (a)** is calculated from the most intense (100) peak position based on the following geometric relationship:

$$a = \frac{2}{\sqrt{3}} d_{(100)}$$

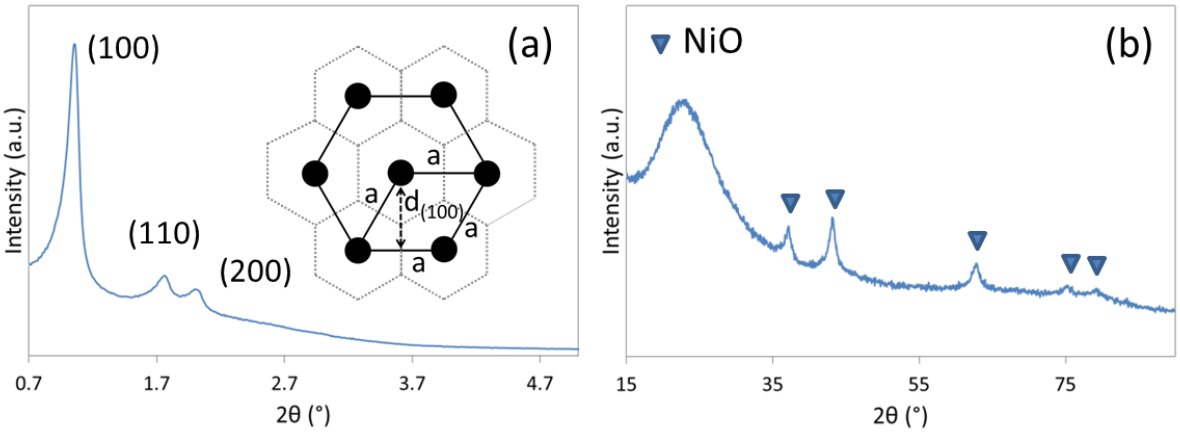


Figure II-9: Typical X-ray diffractograms of (a) SBA-15 silica support at small angle and (b) nickel oxide on SBA-15 at wide angle

The narrow peaks observed on the wide angle XRD (Fig. II-9(b)) are attributed to NiO particles. The wide angle XRD can be used to calculate the **average diameter (D)** of crystalline particles estimated based on the full width at half maximum (FWHM), using Scherrer equation:

$$D = \frac{0.9\,\lambda}{\beta\,cos\theta}$$

Where:

- 0.9 is a dimensionless factor used for spherical particles,

- λ is the wavelength (1.54 Å),

- Θ is the Bragg angle

- ß is the line broadening at half the maximum intensity, calculated from the Warren equation:

$$\beta = \sqrt{\beta^2_{measured} - \beta^2_{reference}}$$

with $\beta_{reference}$=0.18 ° or 0.003 rad.

### II.2.5 Temperature-programmed reduction (TPR)

*Principle*: A constant gas flow is passed through the sample placed inside a quartz reactor (blue circuit on Fig. II-10). The sample is heated based on a predetermined temperature ramp. This technique is based on the measurement of the quantity of hydrogen consumed as a function of temperature through the variation of the Thermal Conductivity Detector (TCD) signal. During the reaction, water is generated:

$$NiO_{(s)} + H_{2\,(g)} \rightarrow Ni^{0}_{(s)} + H_2O_{(g)}$$

Therefore, a bath of ice and NaCl salt is usually used to trap this water and ensure the detection of the sole reduction process.

*Procedure*: The measurements are performed on an AutoChem 2920 (Micromeritics). 100 mg of powder is supported on quartz wool inside a U-tube quartz reactor and the temperature is increased from room temperature up to 900°C (heating rate of 10°C.min$^{-1}$) under a flow of 5 vol % $H_2$/Ar (20 mL.min$^{-1}$) at atmospheric pressure.

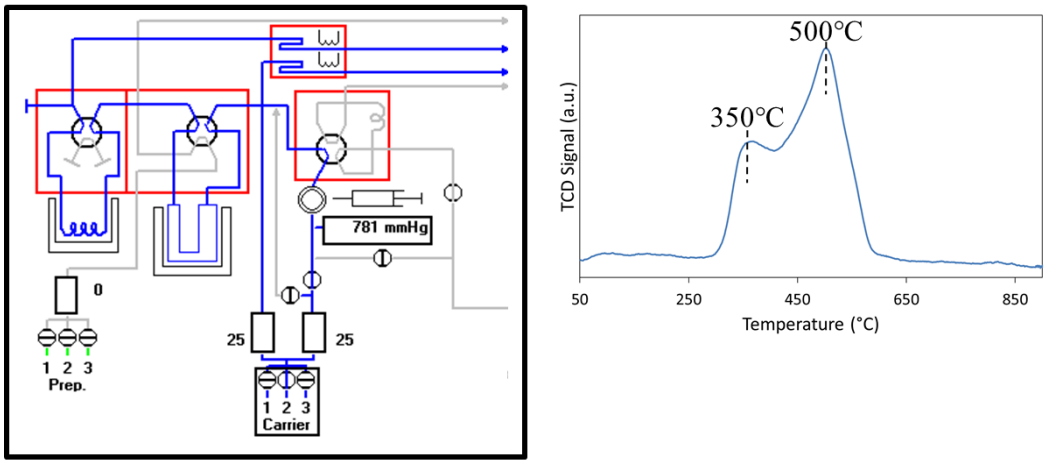


Figure II-10: Schematic representation (left) and typical profile of TPR (right)

*Type of information*: The reducibility of oxide particles is evaluated by temperature-programmed reduction. In general, a typical TCD signal (Fig. II-10, right figure) shows different reduction peaks whose temperatures give an idea on the reducibility of supported nickel, that depend on the nature of the species and on the degree of interaction of the particles with the support. Greater interaction requires higher reduction temperatures. The total amount of hydrogen consumed is measured by integrating the area of the signal, while the integration of the compositing peaks reveals the relative percentages of the present species.

### II.2.6 Thermogravimetric analysis coupled to mass spectrometry (TGA-MS)

*Principle*: Thermogravimetric differential thermal analysis (TGA) measures both heat flow & weight changes in a material either as a function of increasing temperature, or isothermally as a function of time, under a controlled atmosphere. As the temperature increases, various components of the sample are decomposed and the corresponding weight loss is calculated. Changes in weight can be more clearly distinguished in the first derivative TGA curve. The effluent gases from the TGA equipment are transferred to the MS where the components can be identified. The results from thermogravimetric analysis may be presented by mass versus temperature (or time) curve, referred to as the thermogravimetric curve, or rate of mass loss versus temperature curve, referred to as the differential thermogravimetric curve.

*Procedure*: Measurements are performed on a SDT Q600 (TA Instruments) having a horizontal dual beam balance design, coupled to a Thermostar GDS 301T3 mass spectrometer (Pfeiffer). The samples are heated from room temperature to 900°C at a rate of 10°C.min$^{-1}$ under air (50 ml.min$^{-1}$).

*Type of information*: This technique is mainly used in this work for the study and quantification of carbon deposition. Higher weight loss indicates higher carbon deposition. In all cases, as seen in Fig. II-11, the major weight loss takes place at high temperatures (~600°C) due to the oxidation of carbon:

$$C_{(s)} + O_{2\,(g)} \rightarrow CO_{2\,(g)}$$

The exothermic aspect of the reaction is reflected by the positive increase in heat flow curve. The oxidation is verified by the formation of $CO_2$ through the increase of the MS signal corresponding to the mass 44 (Fig. II-11).

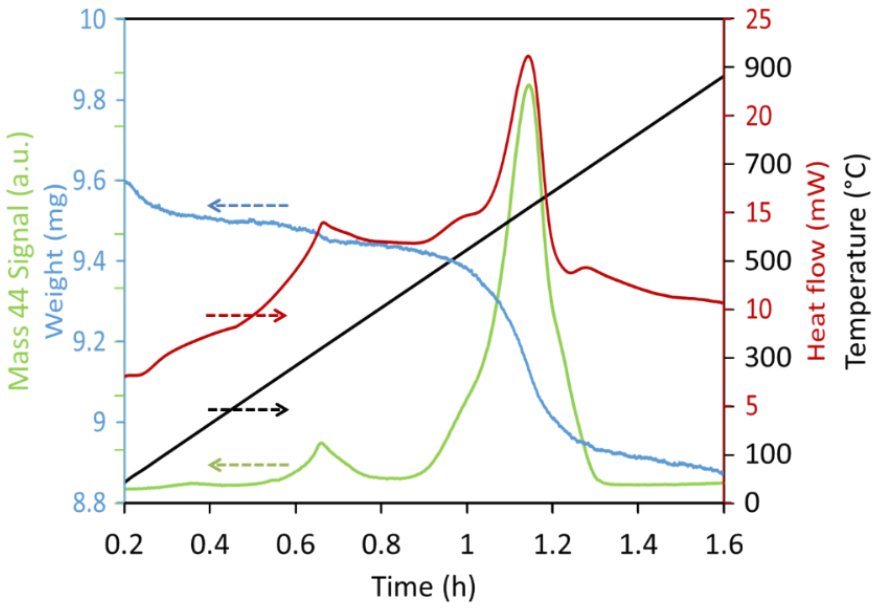


Figure II-11: Typical TGA-MS curves of spent Ni/SBA-15 catalyst

### II.2.7 Raman spectroscopy

*Principle*: In Raman spectroscopy, the sample is illuminated with a monochromatic laser beam which interacts with the molecules and originates a scattered light. The majority of the scattered light is of the same frequency as the excitation source; this is known as Rayleigh or elastic scattering. A very small amount of the scattered light (ca. 10-5% of the incident light intensity) is shifted in energy from the laser frequency due to interactions between the incident electromagnetic waves and the vibrational energy levels of the molecules in the sample. Plotting the intensity of this "shifted" light versus frequency results in a Raman spectrum of the sample. Every band in the Raman spectrum corresponds directly to a specific vibrational frequency of a bond within the molecule. This technique consists on localized analysis on the surface of the sample, with very limited depth.

*Procedure*: An optical microscope (Kaiser Optical System, objective: 50×) is used to focus the laser beam and the spectra are recorded in the 50-3500 $cm^{-1}$ range in our study. Each analysis is the result of 30 acquisitions of 10s. The laser power is set at 7 mW, to avoid fluorescence effect.

*Type of information*: The crystallinity of the deposited carbon is evaluated using the Raman experiments. Atypical spectrum of our spent catalysts is shown in Fig. II-12, indicative of carbon-containing materials. Indeed, graphene is the fundamental building block of carbon materials. Graphite, in particular, consists of stacks of $sp^2$ bonded planar graphene sheets with the main band, known as the G band, located at 1582 $cm^{-1}$ in the Raman spectrum.[20,21] Carbon nanotubes are rolled up graphene sheets in the form of hollow tubes; they can form single-wall or multi-wall nanotubes, depending on the number of wrapped graphene layers. For such materials, an additional prominent band, known as the D band, is observed at around 1350 $cm^{-1}$ in the Raman spectrum. It indicates the presence of some disorder to the graphene structure. This band is often referred to as the disorder band or the defect band and its intensity relative to that of the G band is often used as a measure of the quality of nanotubes. A higher $I_D/I_G$ ratio points out high disorder in the structure while a lower one reveals high degree of crystallinity.

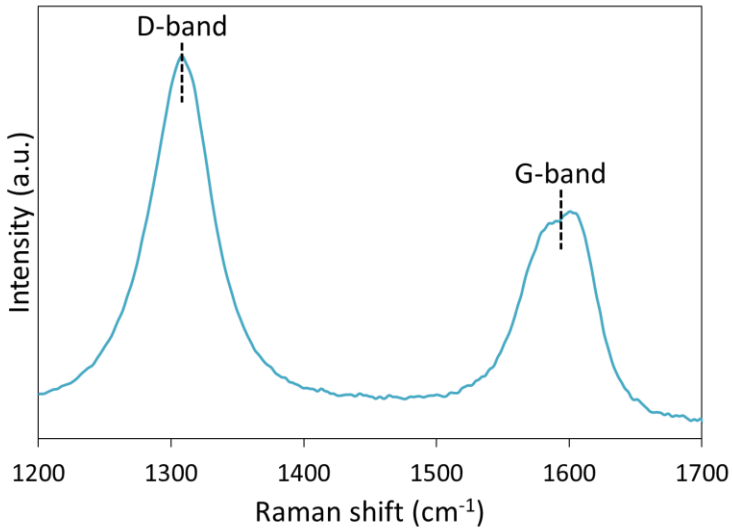


Figure II-12: Typical Raman spectrum of spent Ni/SBA-15 catalyst

## II.2.8 Temperature programmed hydrogenation (TPH)

*Principle*: During Temperature Programmed Hydrogenation coupled to mass spectrometry (TPH/MS), carbon deposits are hydrogenated according to the following equation:

$$C_{(s)} + 2H_{2\,(g)} \rightarrow CH_{4\,(g)}$$

*Procedure*: These experiments are done using the same AutoChem 2920 coupled to a MKS mass spectrometer as that described in section II.2.5. Typically, 30-40 mg of spent catalysts are deposited on quartz wool in a quartz reactor and the temperature is increased up to 900°C (heating rate of 10°C.min$^{-1}$) under a flow of 5 vol % $H_2$/Ar (30 mL.min$^{-1}$) at atmospheric pressure.

*Type of information*: TPH-MS is an interesting way for quantification of coke and identification of its type. The quantity of carbon deposited can be calculated from the quantity of hydrogen consumed during reaction while the nature of the deposited carbon can be assessed from the temperature of formation of $CH_4$.

### II.2.9 X-ray photoelectron spectroscopy (XPS)

*Principle*: The sample is introduced into a first chamber (called the inlet chamber) where it is evacuated through secondary pumping. Once vacuum is reached (<$10^{-7}$ mbar), the sample is transferred to the analysis chamber and XPS study can begin. A monochromatic X-ray (usually Al or Mg Kα radiation) is used to irradiate the sample and excite the electrons. Electrons from core energy levels of different atoms in the sample are ejected after X-ray bombardment and are called photoelectrons. They are collected by an electron analyzer that measures their kinetic energy ($E_k$), which can be then converted into binding energy ($E_B$), given the incident energy of the X-ray beam (hυ):

$$h\upsilon = E_K + E_B$$

Thus the XPS spectra can be plotted as the emitted photoelectron intensity versus binding energy. Each energy peak on the spectrum corresponds to a specific element.

*Procedure*: XPS spectra are collected on an Omicron (ESCA+) X-ray photoelectron spectrometer using an Al Kα (hν = 1486.6 eV) X-ray source. After collection, the binding energies are calibrated with respect to the C components of the C1s peak (binding energy = 284.7 eV). All spectra processing is carried out using the Casa XPS software package.

*Type of information*: The elemental composition of a surface of material can be provided by XPS up to a depth of 10 nm.

## II.3 Catalytic test

An important aspect in this work was the setup of the catalytic test that was not yet established at the University of Balamand. After positioning the equipment with the adequate gas delivery system, the operating reaction conditions are optimized, the effluent gas analysis method by chromatography is created and the results obtained are validated.

Two instruments are employed for this end: a Microactivity-Reference Catalytic Reactor (MAR, Fig. II-13) and a Microactivity-Efficient Catalytic Reactor (EFFI, Fig. II-14) from PID Eng & Tech company, Spain. The EFFI reactor resembles the MAR equipment since both are equipped with the same type of reactors, furnaces, mass flow controllers…but the main advantage of the EFFI reactor is that it has two reactors. These reactors can be mounted in parallel, where two completely independent catalytic reactions can take place. This can be interesting if the second reactor is to be operated under regeneration mode, for example. When both reactors are used in series, the outlet of the 1$^{st}$ reactor can be used as a feed for the second one. The principle of both instruments is the same.

### II.3.1 General description of the equipment

The dry reforming reaction takes place in gas phase, inside a tubular vertical fixed bed reactor. Three main parts can be distinguished:

- The first zone corresponds to the gas delivery system. The required gases (5 vol%$H_2$/Ar, 10 vol% $CH_4$/Ar, 10 vol% $CO_2$/Ar, Ar, and He) are positioned and connected to the specific mass flow controllers. Pure argon and helium inert gases are needed in order to purge the system while the remaining feeds of $H_2$, $CH_4$ and $CO_2$ are required as reactants.
- Zone 2 is referred to as the hot box that houses the reactor. The hot box allows the system to be kept at temperatures up to 180°C owing to an electric forced convection heater, in order to avoid possible condensation in the lines. Once the gases are preheated, the streams merge and flow to a 6-port valve that can be switched into two possible flow paths: either towards the reactor or towards the system's gas outlet (by-passing the reactor). The second option is used to obtain the initial equilibrium gas concentrations before reaction.

- Zone 2’ designates the fixed bed tubular reactor. The flow inside the reactor is up-down, whereby the reactant mixture is fed through the upper part of the reactor and the effluent stream is collected from the lower part. When the flow of reactants is directed towards the reactor, it passes through filters, positioned at both the inlet and outlet of the reactor that can protect the arrangement of valves from possible finely-separated catalyst particles. The thermocouple is inserted through the upper end and is in contact with the catalyst bed. The inside of the reactor is fitted with a porous plate on which the catalyst is usually deposited between two layers of quartz wool, so that it is always on the same position and subjected to the same temperature. This ascertains the reproducibility of the reaction conditions over different catalytic experiments.
- At the reactor outlet, the remaining reactants (if any) and reaction products pass out of the hot box to the liquid-gas separator which acts as a condenser by means of a Peltier cell. This cell allows the condensation of liquids at low temperature. The upper part of the separator features the outlet for gases, which are reintroduced into the hot box, directed to the pressure control system, then towards subsequent analysis by chromatography for accurate monitoring of the reaction (zone 3).

Finally, it is important to note that the experiments are programmed in various sessions. The first and last sessions always correspond to secure shutdown of the system. Subsequent sessions correspond to the operating conditions under which the experiment is to be performed, and their duration should be sufficient in order to allow the system to reach stable operating settings.

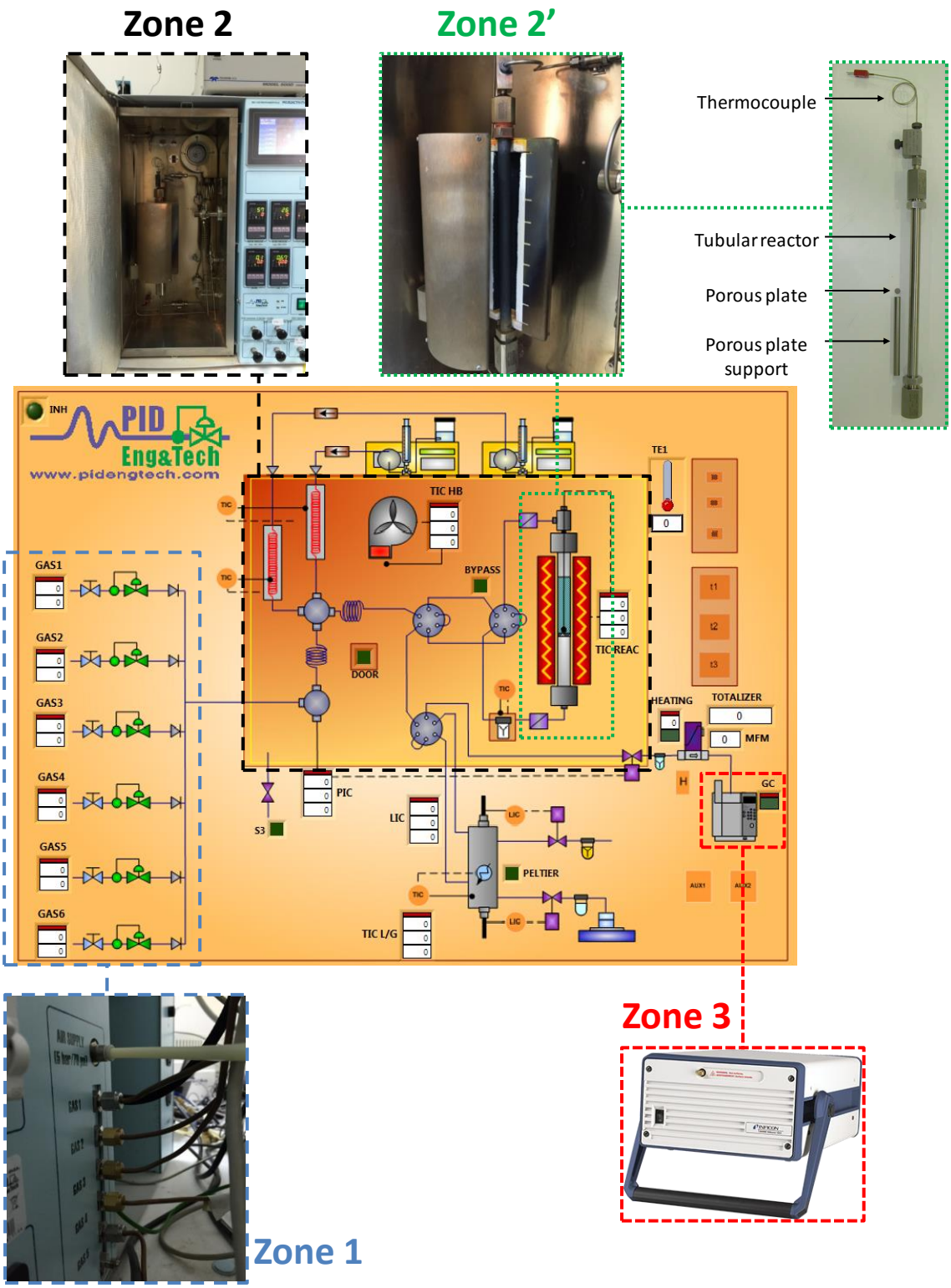


Figure II-13: General scheme of the MAR system

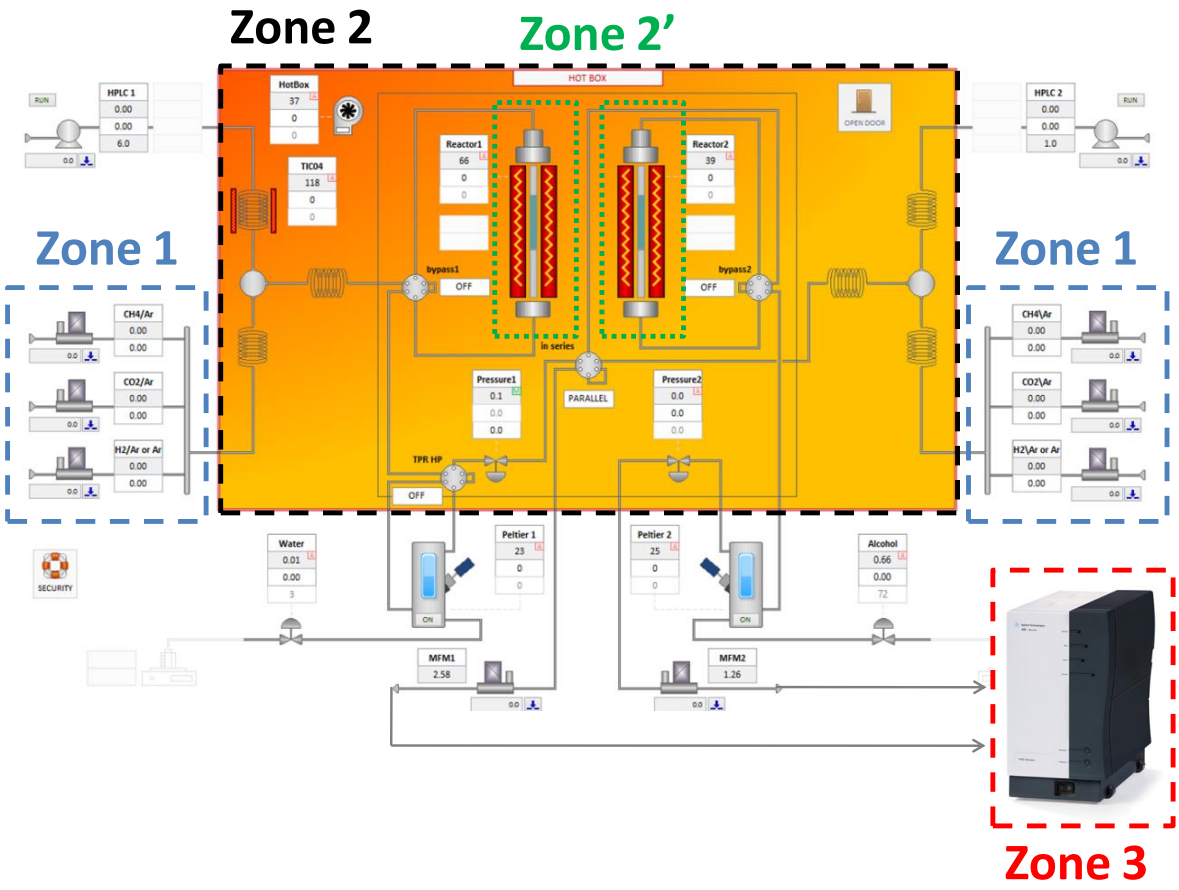


Figure II-14: General scheme of the EFFI system

### II.3.2 Operating procedure

The catalytic test takes place in different consecutive steps illustrated in Fig. II-15, starting from the calcined sample.

- *Leak test*

This test is executed by introducing an inert gas flow in the system until reaching a certain pressure (working pressure or higher). Once the required pressure is attained, the gas inlet and remaining valves are closed. The pressure in the system is supposed to remain constant over a period of time; otherwise, a soapy solution is used to locate possible leaks.

- *Catalyst pretreatment*

The initial step of the reaction consists of the catalyst pretreatment by hydrogen, to convert nickel oxides into metallic nickel, which is the active phase of the reaction. During *in-situ* reduction, a 30 ml.min$^{-1}$ flow of 5 vol% $H_2$/Ar is passed through the reactor while the temperature is increased from room temperature up to 650°C (heating rate of 10°C.min$^{-1}$) and then maintained at this temperature for 2 hours to ensure a complete reduction of nickel species.

- *Catalyst activity and stability*

After this step, the reactor is allowed to cool to about 200°C without any flow. During this bypass, reactants gas streams, composed of 10% $CH_4$/Ar at 28 ml.min$^{-1}$ and 10% $CO_2$/Ar at 32 ml.min$^{-1}$, are directed towards the system's gas outlet. This is important in order to stabilize the detector, reach stable operating conditions of 200°C and 1 bar and obtain the initial reactants concentrations in the feed. After these two hours, the feed is switched to the reactor and the activity of the catalyst is evaluated in dry reforming of methane while increasing the temperature from 200 to 800°C at a rate of 5°C.min$^{-1}$. Finally, the temperature is lowered to a defined value (500 or 650°C) under the reactants stream and maintained under these conditions for stability assessment.

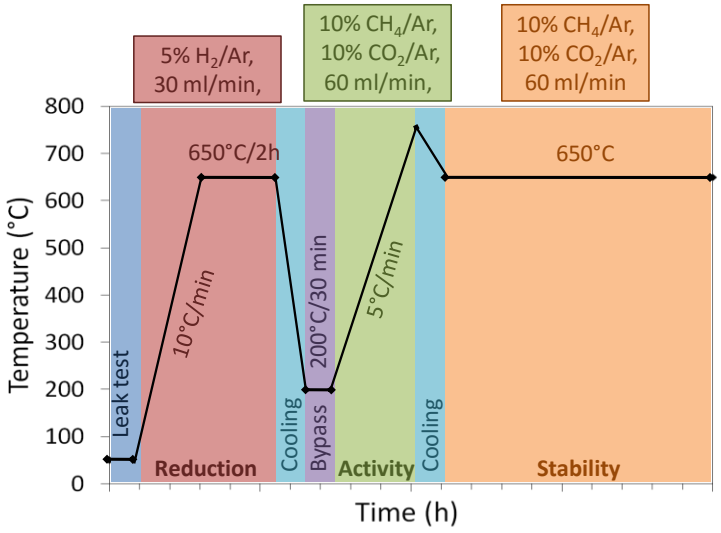


Figure II-15: Variation of temperature with time during reduction, activity and stability measurements

### II.3.3 Effluent gas analysis

The effluent stream from the MAR reactor is analyzed in a micro-GC Inficon3000 apparatus equipped with a thermal conductivity detector (TCD) and two columns in parallel while the effluent streams from the EFFI reactor are analyzed in an Agilent 490 Micro GC equipped with four independent channels, two for each reactor. The detection of $H_2$ (retention time: 0.86 min), $CH_4$ (retention time: 2.1 min), and CO (retention time: 3.25 min) takes place on the Molecular Sieve column with argon carrier and the detection of $CO_2$ (retention time: 0.65 min) on the plot-U column with helium carrier (Fig. II-16). For optimum analysis, the columns, injector and sample inlet temperatures are set at 60°C and 25 psi.

For the calibration of the Micro-GCs, a certified gas standard mixture including the target compounds is used. The mixture is composed of 13% methane, 13% carbon dioxide, 26% carbon monoxide, 26% hydrogen and balanced with argon. To generate a multipoint calibration, different gas concentrations are needed. For that reason, a range of dilutions with argon is used to collect the points. Once the calibration curve is generated, the peak area is plotted versus concentration for each compound, using linear regression. The correlation factor ($r^2$) for the line created must be greater than 0.95 for the calibration to be acceptable. It should be noted that the expected concentrations of the reactants and products are within the concentration range of the multipoint calibration. As shown in Fig. II-16, the peaks are well defined and based on the calibration done, the concentrations of the main reactants and products are directly obtained. Column regeneration is performed from time to time to remove any adsorbed molecules and impurities.

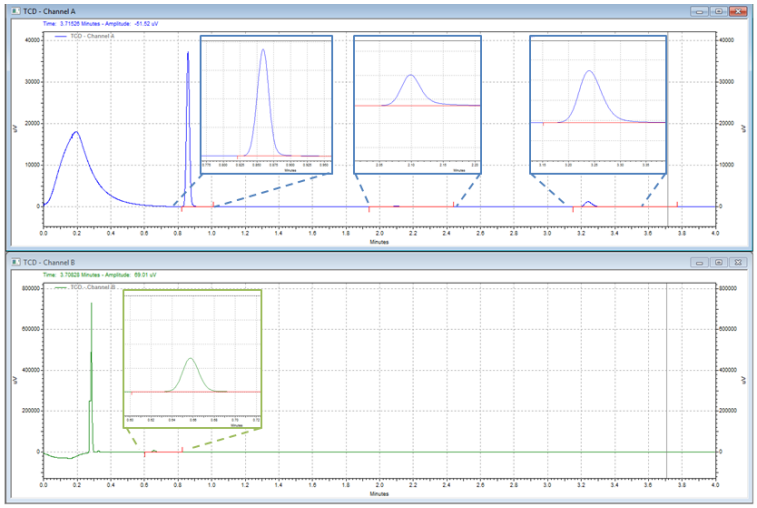

*External Standard Report* Page 1 of 1

**Method Name:** C:\E ZIQ\Projects\Default\Method\Method 23 2 2015.met
**Data:** C:\E ZIQ\Projects\Default\Data\Marie-Nour 2015\PMN62_50mg_rep\activity\024.dat
**User:** System
**Acquired:** 5/10/2016 3:41:55 PM
**Printed:** 5/11/2016 11:03:49 AM

TCD - Channel A Results

| Pk # | Name | Retention Time | Area | Concentration |
|---|---|---|---|---|
| 1 | H2 | 0.859 | 4800503 | 8.749 |
| 2 | CH4 | 2.098 | 63712 | 0.493 |
| 3 | CO | 3.240 | 426385 | 7.826 |

TCD - Channel B Results

| Pk # | Name | Retention Time | Area | Concentration |
|---|---|---|---|---|
| 1 | CO2 | 0.658 | 804269 | 0.577 |

Figure II-16: Micro-GC response and analysis report of an injection during the activity measurement of Ni/SBA-15 sample

## II.3.4 Expression of results

The conversions during the activity and stability measurements are calculated as follows:

$$CH_4 conversion\ (\%) = 100\ x\ \frac{CH_{4in} - CH_{4out}}{CH_{4in}} \quad (1)$$

$$CO_2 conversion\ (\%) = 100\ x \frac{CO_{2in} - CO_{2out}}{CO_{2in}} \quad (2)$$

$$H_2{:}\,CO\ molar\ ratio = \frac{H_2}{CO} \quad (3)$$

The initial conversions are obtained during the bypass stage.

The **activity** is evaluated as the variation of $CH_4$ and $CO_2$ conversions and $H_2$:CO molar ratio as a function of temperature while the **stability** tests are performed at a fixed temperature and the conversions and $H_2$:CO molar ratio are evaluated as a function of time.

### II.3.5 Validation and reproducibility of the test

Once the test is setup correctly and the experiments run fluently, several verifications were required to check the reproducibility of results.

- The dry reforming test was repeated on different dates using the same catalyst under same experimental conditions. The results on Fig.II-17 show similar catalytic behavior during the increase of temperature and during stability test at 650°C for 20 hours.

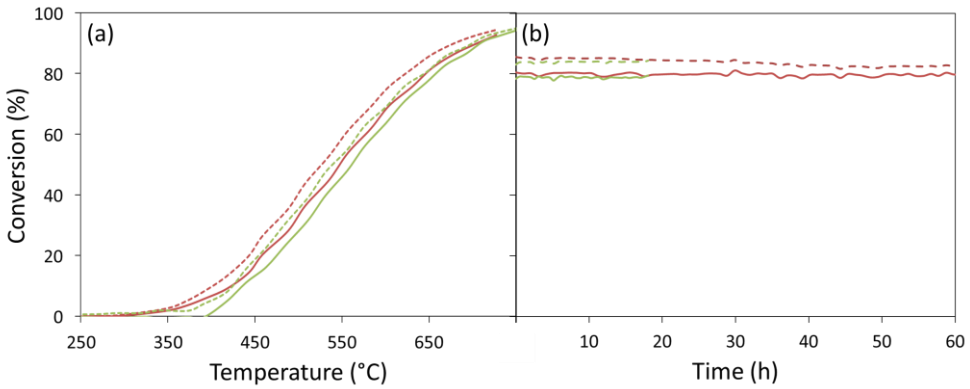


Figure II-17: Activity (a) and stability (b) measurements of the same catalyst repeated after few months

- Two types of reactors were employed in this work: the quartz reactor mainly used for atmospheric pressure applications and the metallic Hastelloy-X reactor that can support higher temperatures and pressures. The use of quartz reactor and metallic Hastelloy-X reactor resulted in analogous results for both activity and stability measurements (Fig. II-18).

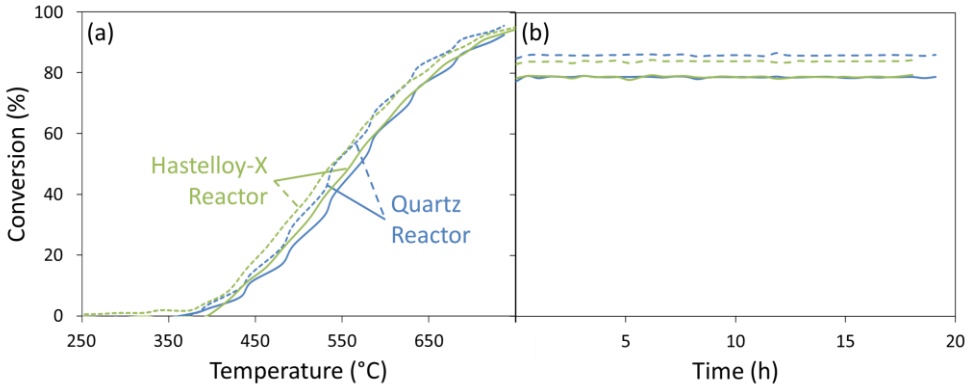


Figure II-18: Activity (a) and stability (b) measurements of the same catalyst repeated using different type of reactors

- Few tests are performed on the EFFI reactor during this work but a validation of the results that can be obtained from this equipment is required. Therefore, two different catalysts are compared during activity and stability at 650°C for a certain time. The conversions and $H_2$:CO molar ratios obtained using the EFFI reactor are very close to those obtained on the MAR reactor, as shown in Fig. II-19, which confirms the efficiency of both equipment.

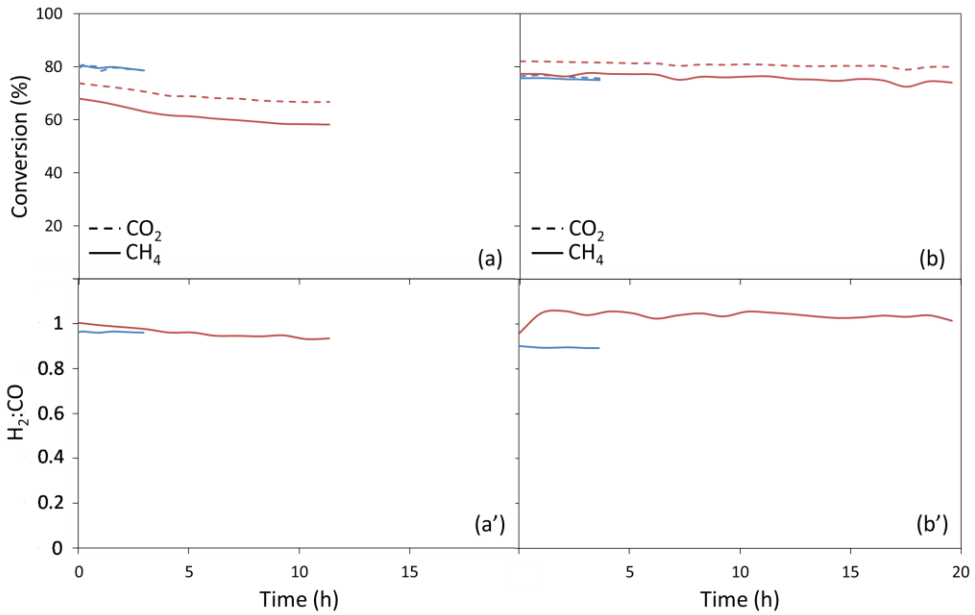


Figure II-19: Comparison of conversions and $H_2$:CO molar ratios of (a,a') $Ni/SiO_2$ and (b,b') Ni/SBA-15 using the MAR (red) and EFFI (blue) microreactors

## II.4 Thermodynamics of the reaction

Before performing the dry reforming tests, it is important to evaluate the thermodynamic equilibrium of this reaction in order to get an idea about the expected values under the used conditions.

The thermodynamic data are thus calculated using the HSC chemistry software (version 7.0). In fact, HSC chemistry is a thermodynamic calculation software where H stands for enthalpy, S for entropy and C for heat capacity. It can be used to study the effects of different variables on the chemical system at equilibrium. For example, if the raw materials, amounts and other conditions of a chemical process are provided, the software will give the amounts of products as a result. Therefore, different cases are studied in order to evaluate the effect of gas dilution, carbon deposition and pressure on the reaction of dry reforming of methane between 200 and 1000°C.

### II.4.1 Effect of dilution

As mentioned previously, diluted test conditions are adopted in this study, mainly due to security concerns when handling compressed gases. The results of the evaluation of $CH_4$, $CO_2$, $H_2$, CO and $H_2O$ components under pure and diluted feed conditions are shown in Fig. II-20. They are expressed in terms of number of moles of reactants and products and in terms of reactants conversions and $H_2$:CO molar ratio as a function of temperature.

As expected under both conditions, with the increase of temperature, the number of moles of $CH_4$ and $CO_2$ reactants decreased while that of the products increased. Under pure reactant feed conditions (Fig. II-20a,a'), the reaction starts to take place after 400°C and the production of water from the reverse water gas shift reaction occurs between 400 and 800°C. After 900°C, almost full conversion is obtained with an $H_2$:CO molar ratio equal to one.

When argon is added to the feed in a molar ratio $CH_4$:$CO_2$:Ar = 5:5:90 (Fig. II-20b,b'), the reactants conversions start to increase from around 300°C and full conversions are achieved at 800°C. Further dilution, using $CH_4$:$CO_2$:Ar = 1:1:98, induces an additional decrease in the corresponding temperatures and an $H_2$:CO molar ratio equals to unity is obtained at around 600°C instead of 900°C observed in the absence of any dilution. Therefore, it is clear that the dilution of the feed with an inert gas shifts the equilibrium towards lower temperatures and thus

higher conversions can be achieved at lower energy. This agrees with the findings of Parkhamenko et al.[22] who obtained higher conversions under more diluted feed conditions.

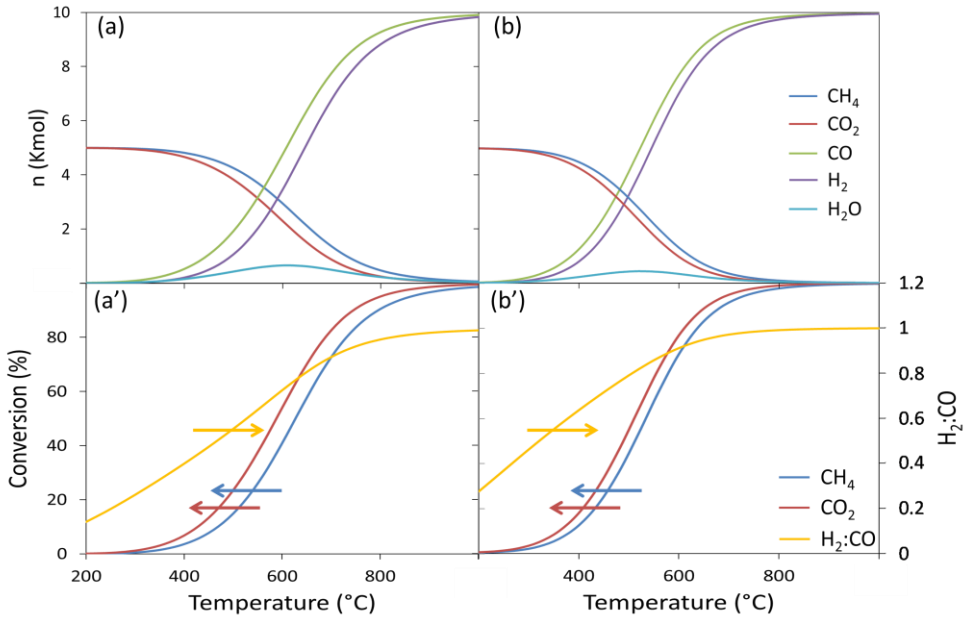


Figure II-20: Variation of (a,b) number of moles of reactants and products and (a',b') reactants conversions and $H_2$:CO molar ratio as a function of temperature using (a,a') $CH_4$:$CO_2$ = 50:50 and (b,b') $CH_4$:$CO_2$:Ar = 5:5:90

## II.4.2 Effect of carbon deposition

It is commonly known that the occurrence of the dry reforming of methane is usually accompanied with different side reactions like water gas shift reaction, Boudouard reaction and methane decomposition. Therefore, it is important to get equilibrium data while taking into consideration carbon deposition during reaction (Boudouard reaction and methane decomposition). This case is not frequently reported in literature and deserves special attention.

Based on this assessment, the results are obtained with and without dilution (Fig. II-21). When a pure equimolar feed of reactants is introduced, the variation of number of moles of all the components ($CH_4$, $CO_2$, $H_2$, CO, $H_2O$ and C(s)) as well as the reactants conversions and $H_2$:CO molar ratio are plotted as a function of temperature. The addition of C(s) to the calculations changes the shape of the curves classically obtained. Apparently, the production of $CO_2$, from

the Boudouard reaction, takes place between 500 and 700°C and thus the number of moles of $CO_2$ increases in this range of temperature and its conversion is reduced. The consumption of $CH_4$ in the dry reforming reaction and the methane decomposition results in the rapid decrease of the number of moles of methane and almost full conversion is obtained at around 700°C in this case. Both water and carbon are produced from 200°C and their quantity is reduced as the temperature increases. This means that at elevated temperatures the occurrence of the side reactions is limited and the main dry reforming reaction is favored, with an $H_2$:CO molar ratio of about 1.1 reached at 1000°C.

The effect of dilution in this case (Fig. II-21b) is only observed at temperatures lower than 700°C where higher conversions are obtained when argon is added to the feed for the same temperature.

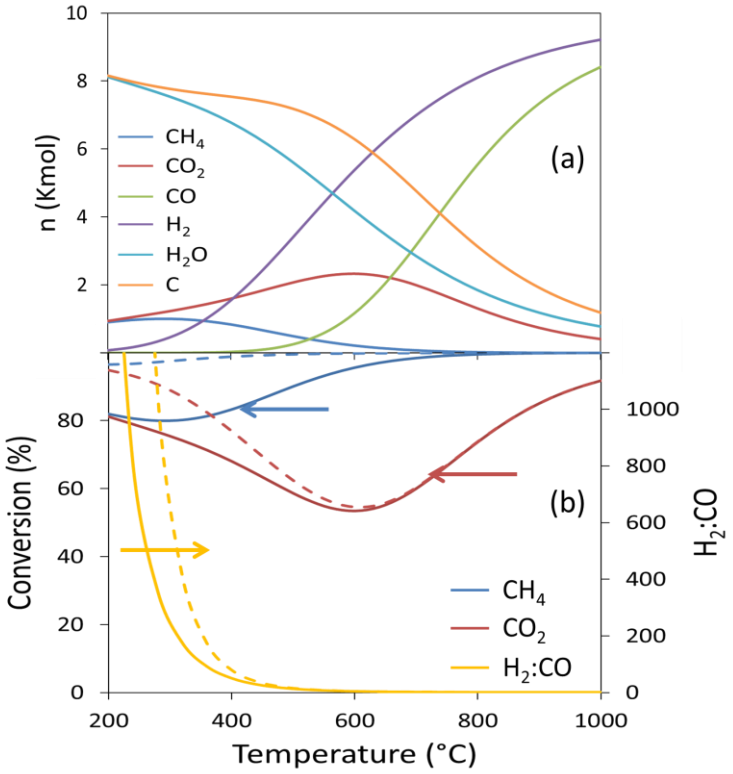


Figure II-21: Variation of (a) number of moles of reactants and products and (b) reactants conversions and $H_2$:CO molar ratio as a function of temperature (full lines: $CH_4$:$CO_2$ = 50:50 and dashed lines: $CH_4$:$CO_2$:Ar = 5:5:90)

### II.4.3 Effect of pressure

On an industrial level, it is always preferred to work using pressurized systems. The effect of pressure on the evolution of the dry reforming reaction is evaluated using equimolar pure reactants feed at 1 and 9 bars and the results are plotted on Fig. II-22 in terms of conversions and $H_2$:CO ratio as a function of temperature. While 50% $CH_4$ and $CO_2$ conversions are obtained at 640 and 600°C, respectively at 1 bar, the values are shifted towards 760 and 680°C, respectively at 9 bars. At 1000°C, full reactants conversions are not achieved at 9 bars nor an $H_2$:CO molar ratio of one. This indicates that working at high pressures shift the equilibrium towards higher temperatures.

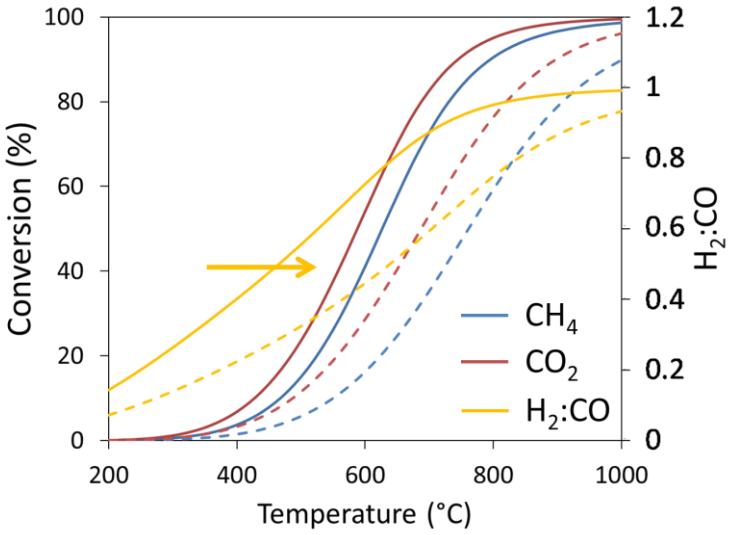


Figure II-22: Variation of reactants conversions and $H_2$:CO molar ratio as a function of temperature (full line: P=1 bar; dashed lines: P=9 bars)

Indeed, according to Le Chatelier's Principle, *if a dynamic equilibrium is disturbed by a change in the conditions, the position of equilibrium moves to counteract this change*. Therefore, any increase of pressure should be counteracted by producing fewer molecules of gases. Recalling that the dry reforming reaction ($CH_4 + CO_2 \leftrightarrow 2H_2 + 2CO$) reacts two molecules of reactants in order to form 4 molecules of products, this means that a change in pressure will eventually shift the equilibrium towards the reactants, to the left. Consequently, working at low pressures allows higher

conversions to be obtained at lower temperatures and at 1bar, the water formation appears to be limited to 700°C.

The prepared samples will be activated and tested in dry reforming of methane, based on the mentioned conditions. The results obtained will be compared to the thermodynamic values expected under the used experimental conditions. The different catalytic behaviors between the samples will be interpreted based on their characterizations after calcination, activation and catalytic test, as will be detailed in the following chapters.

## II.5 References

[1] M. Choi, W. Heo, F. Kleitz, R. Ryoo, *Facile synthesis of high quality mesoporous SBA-15 with enhanced control of the porous network connectivity and wall thickness*, Chemical Communications (2003) 1340-1341.

[2] D. Zhao, J. Feng, Q. Huo, N. Melosh, G.H. Fredrickson, B.F. Chmelka, G.D. Stucky, *Triblock copolymer syntheses of mesoporous silica with periodic 50 to 300 Angstrom pores*, Science 279 (1998) 548-552.

[3] M. Imperor-Clerc, P. Davidson, A. Davidson, *Existence of a microporous corona around the mesopores of silica-based SBA-15 materials templated by triblock copolymers*, Journal of American Chemical Society 122 (2000) 11925-11933.

[4] M. Imperor-Clerc, I. Grillo, A.Y. Khodakov, D. Durand, V.L. Zholobenko, *New insights into the initial steps of the formation of SBA-15 materials: an in situ small angle neutron scattering investigation*, Chemical Communications (2007) 834-836.

[5] V.L. Zholobenko, A.Y. Khodakov, M. Impéror-Clerc, D. Durand, I. Grillo, *Initial stages of SBA-15 synthesis: An overview*, Advances in Colloid and Interface Science 142 (2008) 67-74.

[6] Y. Park, T. Kang, J. Lee, P. Kim, H. Kim, J. Yi, *Single-step preparation of Ni catalysts supported on mesoporous silicas (SBA-15 and SBA-16) and the effect of pore structure on the selective hydrodechlorination of 1,1,2-trichloroethane to VCM*, Catalysis Today 97 (2004) 195-203.

[7] A. Galarneau, H. Cambon, F. Di Renzo, F. Fajula, *True Microporosity and Surface Area of Mesoporous SBA-15 Silicas as a Function of Synthesis Temperature*, Langmuir 2001, 17, 8328-8335.

[8] S. Förster, M. Antonietti, *Amphiphilic block copolymers in structure-controlled nanomaterial hybrids*, Advanced Materials 10 (1998) 195-217.

[9] A. Lu, F. Schuth, *Nanocasting pathways to create ordered mesoporous solids*, Comptes Rendus Chimie 8 (2005) 609-620.

[10] A. Lu, D. Zhao, Ying Wan, *Principles of Nanocasting*, The Royal Society of Chemistry, 2010.

[11] M. Imperor-Clerc, D. Bazin, M.D. Appay, P. Beaunier, A. Davidson, *Crystallization of β-$MnO_2$ nanowires in the pores of SBA-15 silicas: In-situ investigation using synchrotron radiation*, Chemistry of Materials 16 (2004) 1813-1821.

[12] S. Naito, T. Shingaki, T. Hakeda, A. Yoshida, *Unique active site structure for $C_2$ oxygenated compound formation in CO-$H_2$ reaction over ordered mesoporous $CeO_2$ supported Rh catalysts*, Catalysis Today 251 (2015) 14-18.

[13] F. Ying, S. Wang, C. T. Au, S.Y. Lai, *Highly active and stable mesoporous Au/$CeO_2$ catalysts prepared from MCM-48 hard-template*, Microporous and Mesoporous Materials 142(1) (2011) 308-315.

[14] J. van der Meer, I. Bardez-Giboire, C. Mercier, B. Revel, A. Davidson, R. Denoyel, *Mechanism of metal oxide nanoparticle loading in SBA-15 by the double solvent technique*, Journal of Physical Chemistry C 114 (2010) 3507-3515.

[15] X. Huang, W. Dong, G. Wang, M. Yang, L. Tan, Y. Feng, X. Zhang, *Synthesis of confined Ag nanowires within mesoporous silica via double solvent technique and their catalytic properties*, Journal of Colloid and Interface Science 359 (2011) 40-46.

[16] I. Lopes, N. El Hassan, H. Guerba, G. Wallez, A. Davidson, *Size-induced structural modifications affecting $Co_3O_4$nanoparticles patterned in SBA-15 silicas*, Chemistry of Materials 18 (2006) 5826-5828.

[17] C. Perego, P. Villa, *Catalyst preparation methods*, Catalysis Today 34 (1997) 281-305.

[18] M. Thommes, K. Kaneko, A.V. Neimark, J.P. Olivier, F. Rodriguez-Reinoso, J. Rouquerol, K.S.W. Sing, *Physisorption of gases, with special reference to the evaluation of surface area and pore size distribution (IUPAC Technical Report)*, Pure Applied Chemistry 87(9-10) (2015) 1051-1069.

[19] E. Paineau, I. Dozov, A. Philippe, I. Bihannic, F. Meneau, C. Baravian, L.J. Michot, P. Davidson, *In-situ SAXS study of aqueous clay suspensions submitted to alternating current electric fields*, Journal of Physical Chemistry B 116 (2012) 13516-13524.

[20] A. Serrano-Lotina, L. Daza, *Long-term stability test of Ni-based catalyst in carbon dioxide reforming of methane*, Applied Catalysis A: General 474 (2014) 107-113.

[21] M. Khavarian, S.P. Chai, A.R. Mohamed, *Direct use of as-synthesized multi-walled carbon nanotubes for carbon dioxide reforming of methane for producing synthesis gas*, Chemical Engineering Journal 257 (2014) 200-208.

[22] K. Parkhomenko, A. Tyunyaev, L. Marcela Martinez Tejada, D. Komissarenko, A. Dedov, A. Loktev, I. Moiseev, A.C. Roger, *Mesoporous amorphous silicate catalysts for biogas reforming*, Catalysis Today 189 (2012) 129-135.

# CHAPTER III

# Active and Stable Ni/SBA-15 Catalysts at 500°C

As mentioned in Chapter I, the substitution of expensive yet performing noble metals by cheaper transition metals, especially nickel, is nowadays attractive due to economic and accessibility constraints. However, as also described, Ni-based catalysts suffer from heavy carbon deposition and particles' sintering during reaction, which limit their commercialization.

In this context, the aim of this chapter is to study the stability of nickel particles inside SBA-15 mesoporous supports. We recall that the organized SBA-15 mesoporous silica is advantageous because of its ordered channel system with high internal surface area and pore volume that give high capability to disperse and stabilize oxide and metal nanoparticles. This choice is also based on recent results reporting promising behaviors of Ni-based SBA-15 catalysts in DRM.[1,2,3] In these works, however, the catalysts were prepared by classical incipient wetness impregnation[1,2] and nickel depositions both inside and outside the pores were observed. Thus, our purpose here is to use the two solvents impregnation method to prepare improved Ni/SBA-15 catalysts with active Ni nanoparticles highly dispersed all over the support and predominantly (if not fully) located at the interior of the mesoporous channels.

Furthermore, various authors reported a promoting effect of ceria in such catalysts due to (i) enhancement of Ni nanoparticles dispersion, reactivity and stability,[1,2,4,5,6,7] (ii) high redox potentials of Ce(IV)/Ce(III) species and (iii) high availability and mobility of oxygen atoms that inhibit coke formation. Therefore, we promoted some samples with ceria in order to check the enhancement it can add, especially when nickel is well dispersed on the support.

## III.1 Material preparation

As already presented in section II.1 (Tables II-1 and II-3) and recalled in Table III-1, the SBA-$A_1$ and SBA-$A_2$ silica supports were prepared at laboratory scale and impregnated with nickel and/or cerium nitrate using the two solvents method. The two supports were prepared without applying a hydrothermal treatment step (SBA-15 being then commonly referred to as SBA-A). In order to

consider the effect of cerium addition, 6 wt% Ce were impregnated on the SBA-$A_2$ support before the addition of nickel. On both series, the effect of nickel loading was evaluated by varying the nickel content between 2.5, 5.0 and 7.5 wt%. Each metal impregnation was followed by calcination of the dried sample in air at 450°C for 5hours. The resulting calcined samples were named $Ni_x$/SBA-$A_1$(N) and $Ni_xCe_6$/SBA-$A_2$(N), where x represents the weight percent of nickel used. Finally, as a reference, SBA-$A_2$ was submitted to the two solvents procedure but without metal addition in order to obtain the Ni-free $Ni_0$/SBA-$A_2$(N) sample.

Table III-1: Nomenclature and synthesis conditions of the samples

| Support | Sample Name | Metal content (wt%) | | Order of impregnation | Calcination |
|---|---|---|---|---|---|
| | | Ni | Ce | | |
| SBA-$A_1$ | $Ni_{2.5}$/SBA-$A_1$(N) | 2.5 | - | Only Ni | 450°C / 5h |
| | $Ni_{5.0}$/SBA-$A_1$(N) | 5.0 | - | | |
| | $Ni_{7.5}$/SBA-$A_1$(N) | 7.5 | - | | |
| SBA-$A_2$ | $Ni_0$/SBA-$A_2$(N)* | - | - | - | |
| | $Ni_{2.5}Ce_6$/SBA-$A_2$(N) | 2.5 | 6 | Ce then Ni | |
| | $Ni_{5.0}Ce_6$/SBA-$A_2$(N) | 5.0 | 6 | | |
| | $Ni_{7.5}Ce_6$/SBA-$A_2$(N) | 7.5 | 6 | | |

*Ni-free sample prepared by two solvents procedure without metal addition

## III.2 Physico-chemical properties of supports and calcined samples

In this part, we will be primarily interested in the properties of the two used supports before moving to the evaluation of the impregnated samples.

### III.2.1. Textural properties of the SBA-$A_1$ and SBA-$A_2$ supports

The textural properties of the supports were evaluated by nitrogen physisorption (Fig. III-1). For easier comparison, the isotherms of the impregnated samples are also shown on the same figure and the porosity and surface area values estimated from these curves are reported in Table III-2, in which the grey lines correspond to the properties of the supports. We have also chosen to

represent the curves at a scale that will be kept constant in the all the manuscript to facilitate comparisons from one chapter to another.

The isotherms for both SBA-$A_1$ and SBA-$A_2$ supports (Fig. III-1a and a') are of type IV(a), with a H1 hysteresis loop typical of well-ordered porous materials with parallel mesopores. The surface areas and pore volumes are estimated to 455 $m^2.g^{-1}$ and 0.51 $cm^3.g^{-1}$ for SBA-$A_1$ and 632 $m^2.g^{-1}$ and 0.62 $cm^3.g^{-1}$ for SBA-$A_2$, respectively (Table III-2). In SBA-$A_1$, a lower adsorbed volume is observed in comparison to SBA-$A_2$, especially at $P/P_0$ below 0.035 (Fig. III-1a and a' respectively). This indicates a smaller content of micropores in the former silica sample.

Hence, although these batches were prepared under similar conditions, slightly different textural properties were observed on both supports. This can be explained by the absence of hydrothermal condensation step during the synthesis of these parent samples (due to practical laboratory reasons), which makes them more sensitive to structural shrinking during calcination.[8] Indeed, it was reported that a hydrothermal treatment increases pore sizes, decrease wall thicknesses and improves the thermal stability of the material.[9,10,11] Thus the variances observed between both supports can be related to the absence of this aging step. More precisely, this can be due to variations in the rate of TEOS addition, which is difficult to control when a simple drop-by-drop manual addition using the burette is applied.

A complementary explanation can also be considered in view of the low-angle X-ray diffractograms (Fig. III-2). Indeed, the (100), (110) and (200) diffraction peaks characteristic of highly ordered hexagonal mesoporous supports structure (p6mm)[12] are shown for both silica supports. Indeed, these diffraction peaks are less intense for SBA-$A_1$and moreover split in two contributions (red arrows on the figure). Considering the most intense (100) diffraction peak, these contributions correspond to unit-cell parameters of 110.6 and 106.6 Å suggesting that SBA-$A_1$ is a physical mixture of partially uncalcined (less porous) and calcined (porous) silica grains. This could be due to incomplete organic removal during SBA-$A_1$ calcination, leading to lower porosity compared to SBA-$A_2$.

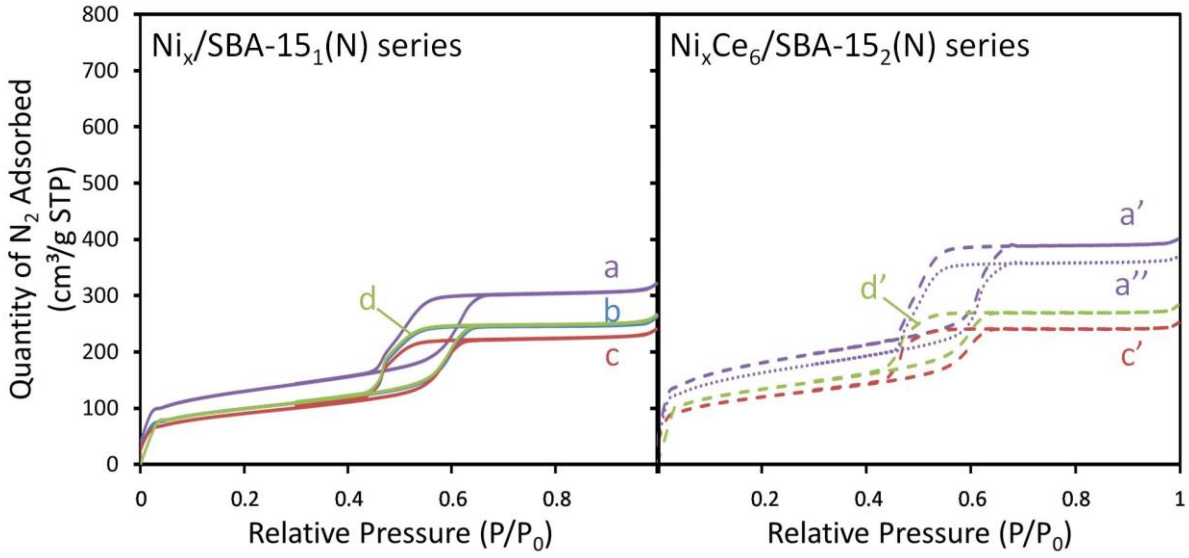


Figure III-1: $N_2$ adsorption-desorption isotherms for (a) SBA-$A_1$, (b) $Ni_{2.5}$/SBA-$A_1$(N), (c) $Ni_{5.0}$/SBA-$A_1$(N), (d) $Ni_{7.5}$/SBA-$A_1$(N) and (a') SBA-$A_2$, (a'') $Ni_0$/SBA-$A_2$(N), (c') $Ni_{5.0}Ce_6$/SBA-$A_2$(N), (d') $Ni_{7.5}Ce_6$/SBA-$A_2$(N) calcined samples

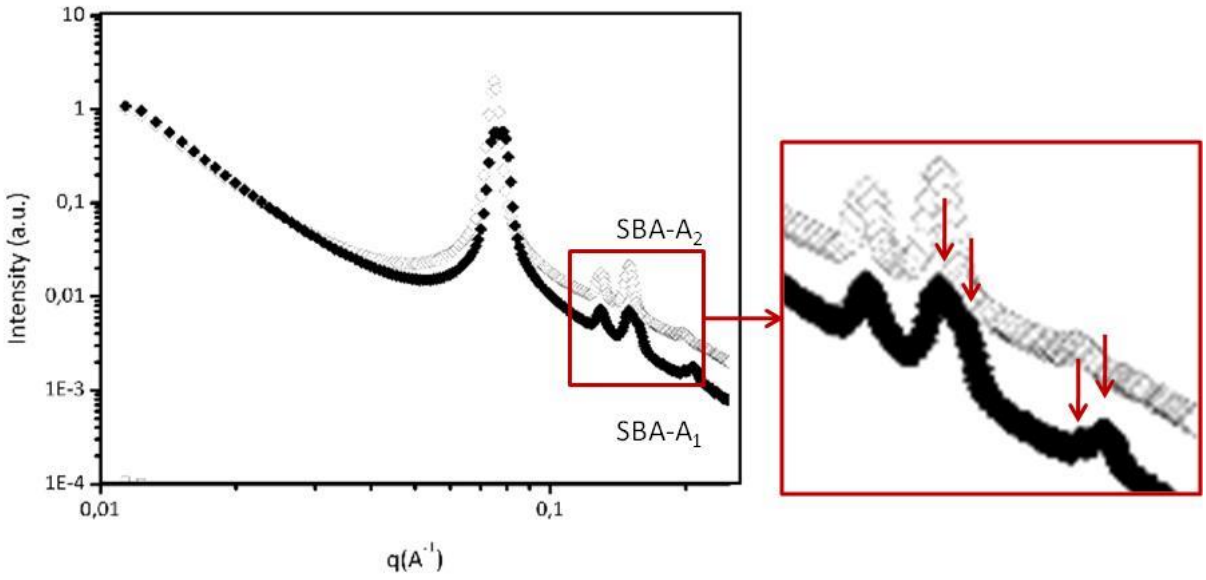


Figure III-2: Low-angle XRD profiles of the calcined SBA-$A_1$ and SBA-$A_2$ silica supports. Red arrows highlight the split of the peaks for the SBA-$A_1$ sample.

### III.2.2. Porosity of calcined impregnated samples

Concerning the $Ni_x$/SBA-$A_1$(N) and $Ni_xCe_6$/SBA-$A_2$(N) impregnated samples (Fig. III-1b,c,d,c' and d'), the $N_2$ sorption results still present a type IV(a) isotherm, characteristic of well-ordered mesoporous materials with parallel and cylindrical mesopores. However, the shape of the hysteresis loop is modified, since a systematic deformation of the desorption branch is observed when Ni (and eventually Ce) is deposited. This is typical of partial plugging and limited access to the mesopores, which is in strong agreement with the hypothesis of metal species deposition inside the pores.[13] The surface areas of $Ni_x$/SBA-$A_1$(N) series are between 320 and 350 $m^2.g^{-1}$ while those of the $Ni_xCe_6$/SBA-$A_2$(N) series range between 420 and 470 $m^2.g^{-1}$ (Table III-2). Moreover, both series reveal comparable pore volumes in the range of 0.4-0.5 $cm^3.g^{-1}$. Thus, in spite of successive impregnation and calcination steps, relatively high pore volumes and surface areas are still detected after Ni and Ce deposition.

Table III-2: Textural properties of the calcined $Ni_x$/SBA-$A_1$(N) and $Ni_xCe_6$/SBA-$A_2$(N) series

| **Sample Name** | **Total Surface area ($m^2.g^{-1}$)** | **Pore volume ($cm^3.g^{-1}$)** | **Mean Pore size (Å)** |
|---|---|---|---|
| SBA-$A_1$ | 455 | 0.51 | 42 |
| $Ni_{2.5}$/SBA-$A_1$(N) | 348 | 0.43 | 40 |
| $Ni_{5.0}$/SBA-$A_1$(N) | 320 | 0.38 | 40 |
| $Ni_{7.5}$/SBA-$A_1$(N) | 348 | 0.47 | 41 |
| SBA-$A_2$ | 632 | 0.62 | 41 |
| $Ni_0$/SBA-$A_2$(N) | 571 | 0.58 | 41 |
| $Ni_{2.5}Ce_6$/SBA-$A_2$(N) | n.d. | n.d. | n.d. |
| $Ni_{5.0}Ce_6$/SBA-$A_2$(N) | 419 | 0.38 | 38 |
| $Ni_{7.5}Ce_6$/SBA-$A_2$(N) | 468 | 0.42 | 38 |

n.d. not determined

Furthermore, when SBA-$A_2$ (Fig. III-1a') was submitted to the two solvents procedure (without metal addition) to give Ni-free $Ni_0$/SBA-$A_2$(N), the pore volumes and pore diameters slightly

decreased (Fig. III-1a'' and Table III-2). This reveals some textural instability of the mesoporous silica during metal impregnation and calcination. However, the effect is very limited since 90% of the pore volumes and surface areas are preserved. Besides, the mean pore diameter remains unchanged. In contrast, the mean pore diameter decreases from 42 Å to 40 Å (about 5%) and from 41 Å to 38 Å (around 8%) in the $Ni_x$/SBA-$A_1$(N) and $Ni_xCe_6$/SBA-$A_2$(N) series (Table III-2), respectively. The more important decrease on the samples containing both Ni and Ce species further supports the presence of oxide nanoparticles inside the pores.

Moreover, regardless of the Ni content, the porosity loss is almost of the same order of magnitude. It is slightly accentuated in the $Ni_xCe_6$/SBA-$A_2$(N) series, due to the combination of (i) the repetition of impregnation treatments that may have provoked some additional silica collapse and (ii) the co-presence of Ce and Ni species in these samples.

### III.2.3. Identification and size of supported nanoparticles

Wide-angle X-ray diffractograms were registered in order to identify the nature and structure of the deposited nickel species and estimate their size in the calcined samples (Fig. III-3).

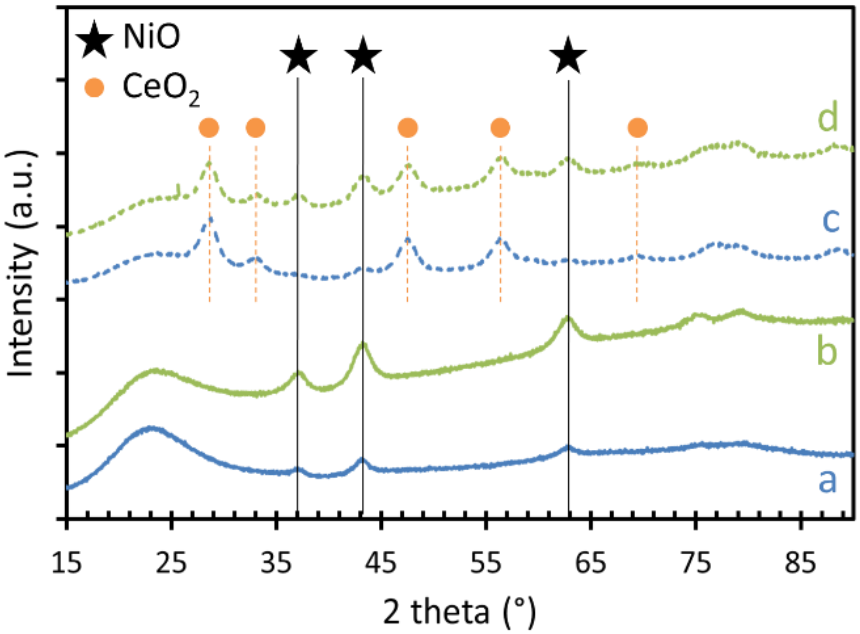


Figure III-3: X-ray diffractograms of calcined (a) $Ni_{2.5}$/SBA-$A_1$(N), (b) $Ni_{7.5}$/SBA-$A_1$(N), (c) $Ni_{2.5}Ce_6$/SBA-$A_2$(N) and (d) $Ni_{7.5}Ce_6$/SBA-$A_2$(N)

First, the broad signal observed on all diffractograms at around 22° is due to diffusion by amorphous silica walls. Second, the narrower diffraction peaks visible in the $Ni_x$/SBA-$A_1$(N) series (Fig. III-3a and b) at 37, 43 and 63°, correspond to nickel oxide nanoparticles (ICDD 04-0835). Their relative positions correspond to (111), (012) and (110) indexations and agree with a face-centered cubic lattice (Fm-3m) having a unit cell parameter equal to 4.17 Å. Third, the intensity of these diffraction peaks increases with increasing nickel content, in line with a higher amount of nanoparticles in the metal richer samples. Forth, the width of the peaks does not significantly vary from one sample to another, indicating that the mean particle size remains comparable regardless of the Ni content. From standard FWHM analysis of the peak situated at 43°, the average size of NiO crystallographic domains is in the range of 5-7 nm (Table III-3) which is interestingly significantly smaller than the sizes reported in literature (always above 10 nm) for Ni-based nanoparticles supported on $SiO_2$[14,15] or even on mesoporous SBA-15[2,16,17,18,19,20] with or without promoter.

Table III-3: Estimated average particles size (nm) for the calcined and spent catalysts

| Support | Sample Name | Calcined Catalysts | | | | Spent Catalysts | | |
|---|---|---|---|---|---|---|---|---|
| | | Ø $CeO_2$ | Ø NiO | | Ni/Si atomic ratio[b] | Ø $Ni^0$ | | Ni/Si atomic ratio[b] |
| | | XRD TEM | XRD[a] | TEM[b] | | XRD[a] | TEM[b] | |
| SBA-$A_1$ | $Ni_{2.5}$/SBA-$A_1$(N) | - | 7 | 6 | 0.04-0.07 | n.d. | 8 | 0.04-0.09 |
| | $Ni_{5.0}$/SBA-$A_1$(N) | - | 5 | 5 | 0.07-0.08 | 8 | n.d. | n.d. |
| | $Ni_{7.5}$/SBA-$A_1$(N) | - | 5 | 6 | 0.09-0.17 | 4 | 5 | 0.16-0.19 |
| SBA-$A_2$ | $Ni_{2.5}Ce_6$/SBA-$A_2$(N) | 5 | 6 | 7 | 0.04-0.14 | n.d. | n.d. | 0.03-0.05 |
| | $Ni_{5.0}Ce_6$/SBA-$A_2$(N) | 5 | 5 | 7 | 0.05-0.20 | n.d. | n.d. | n.d. |
| | $Ni_{7.5}Ce_6$/SBA-$A_2$(N) | 5 | 5 | 5 | 0.12-0.32 | 5 | n.d. | 0.08-0.35 |

[(a)]Calculated using Sherrer equation
[(b)]From TEM images of calcined and spent catalysts
n.d. not determined

In the $Ni_xCe_6$/SBA-$A_2$(N) series of samples (Fig. III-3c and d), a NiO pattern as above is present in addition to new peaks at 2θ = 28, 33, 47, 56 and 69° characteristics of face-centered cubic $CeO_2$ crystalline nanoparticles with a cell parameter of 5.41 Å (ICDD 75-5980). Using FWHM, the average size of the coherent domains for $CeO_2$ nanoparticles is found near5 nm, in the same range as for NiO nanoparticles. Therefore, well dispersed NiO and $CeO_2$ crystalline nanoparticles co-exist in the silica grains and the introduction of ceria before nickel in SBA-$A_2$ porous channels did not modify the characteristics of NiO nanoparticles formation.

### III.2.4. Location of the supported nanoparticles

The location and dispersion of the supported NiO and $CeO_2$ species is further viewed by electron microscopy both in scanning (Fig. III-4) and transmission (Fig. III-5) modes. The scanning mode mainly reveals the grain morphologies and the external particles deposition, whereas by transmission, both internal and external particles are distinguished. Therefore, it is interesting to couple the results of these two complementary techniques for a better assessment of the nanoparticles location.

- Internal location of NiO and $CeO_2$ nanoparticles

First, on the SEM images of the non-impregnated supports, most of the silica grains are mainly elongated (Fig. III-4a) while others are apparently shorter (Fig. III-4b). This irregular shape of the grains is due to the irregular rate of TEOS addition, using the burette. On the images recorded in a partial retro-diffused mode for the impregnated samples (Fig. III-4c), the heavier elements (here Ni) appear more brilliant. The detection of these bright spots on the surface of the grains indicates that they are located outside the silica grains.

Second, on the TEM micrographs taken parallel (Fig. III-5a and b) or perpendicular (Fig. III-5c) to the main axis of the silica grains, the linear channel system is still well identified, even after Ni impregnation and calcination. Indeed, the grain seen perpendicularly (Fig. III-5c), with its main elongation axis parallel to the electron beam, clearly reveals the regular 2D hexagonal order between mesopores. Thus, in agreement with porosity data, the linear porous system and the nanosized hexagonal pore apertures characteristic of the SBA-15 structure are well preserved in the prepared catalysts. Few amorphous silica deposits originating from the support syntheses or the two solvents deposition step are also noticed at the surface of the silica grains, but in low amounts (Fig. III-5a).

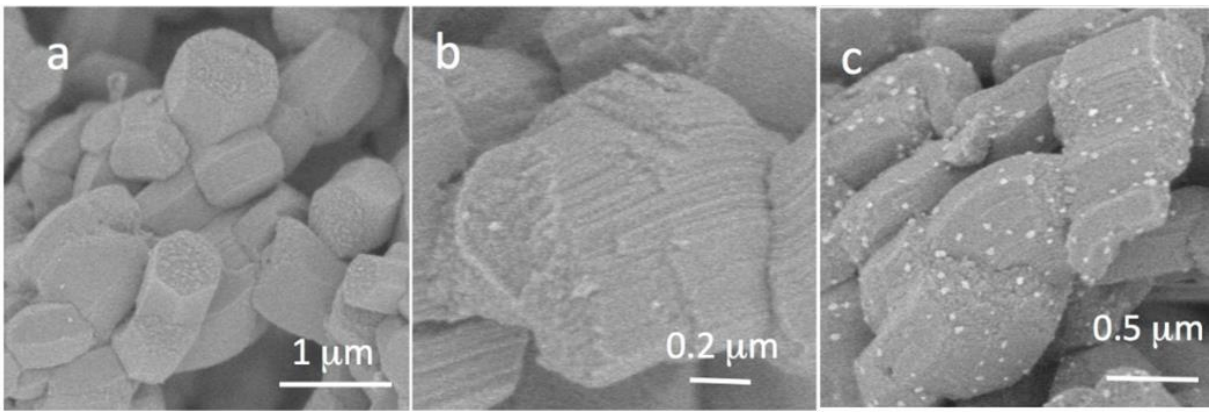


Figure III-4: SEM images of calcined samples (a,b) SBA-$A_1$ and (c) $Ni_{7.5}$/SBA-$A_1$(N)

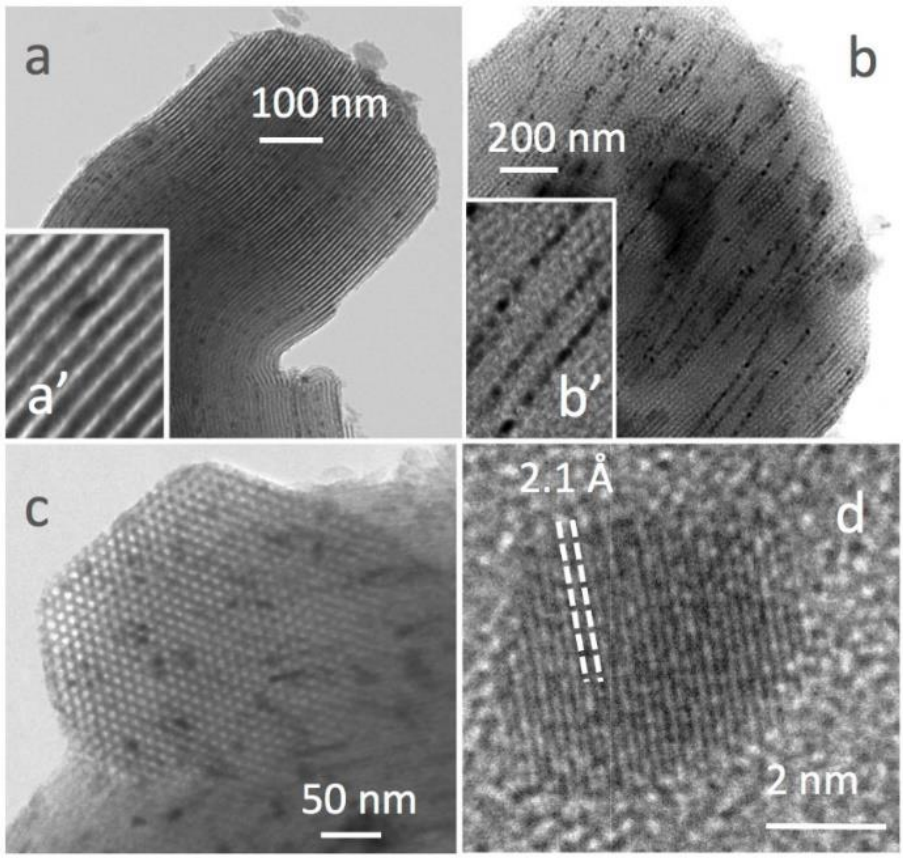


Figure III-5: TEM micrographs of calcined $Ni_{7.5}$/SBA-$A_1$(N) samples showing highly dispersed NiO nanoparticles in the SBA-15 pores: observations of isolated particles (a,a') along or (b) perpendicular to the channels, (c) particles aligned along the channels and (d) high resolution image of a NiO nanoparticle

Third, on these micrographs (Fig. III-5), the dispersed Ni-based nanoparticles appear in dark on the grey silica walls owing to their higher electronic density. They are present inside the pores (Fig. III-5a, b and c) and are most often aligned along the channels, forming worm-like curved lines (Fig. III-5b). In agreement with XRD, they show a reticular $d_{012}$ distance of 2.1 Å typical of NiO (zoom in Fig. III-5d). Moreover, their mean size is about 5-6 nm (Table III-3), slightly higher than the pore diameters (Table III-2). Thus, the channel walls effectively contribute to high nickel dispersion by restricting the growth of the supported particles. As a result, the channels are partially filled, in line with the decrease in pore volumes discussed above. This illustrates the efficiency of the two solvents impregnation procedure towards predominant deposition of the metal species inside the channels. Nevertheless, few bigger particles are identified on the surface of the silica grains on $Ni_{7.5}$/SBA-$A_1$(N) with high Ni content (Fig. III-6a), as also viewed by SEM (Fig. III-4c).

Fourth, on the $Ni_xCe_6$/SBA-$A_2$(N) series, the nickel oxide nanoparticles are predominantly located inside the pores, with almost no particles visible outside (Fig. III-6b and c). This was coupled with the presence of small $CeO_2$ nanoparticles shaped into small dots (Fig. III-6b and c), along the channels.

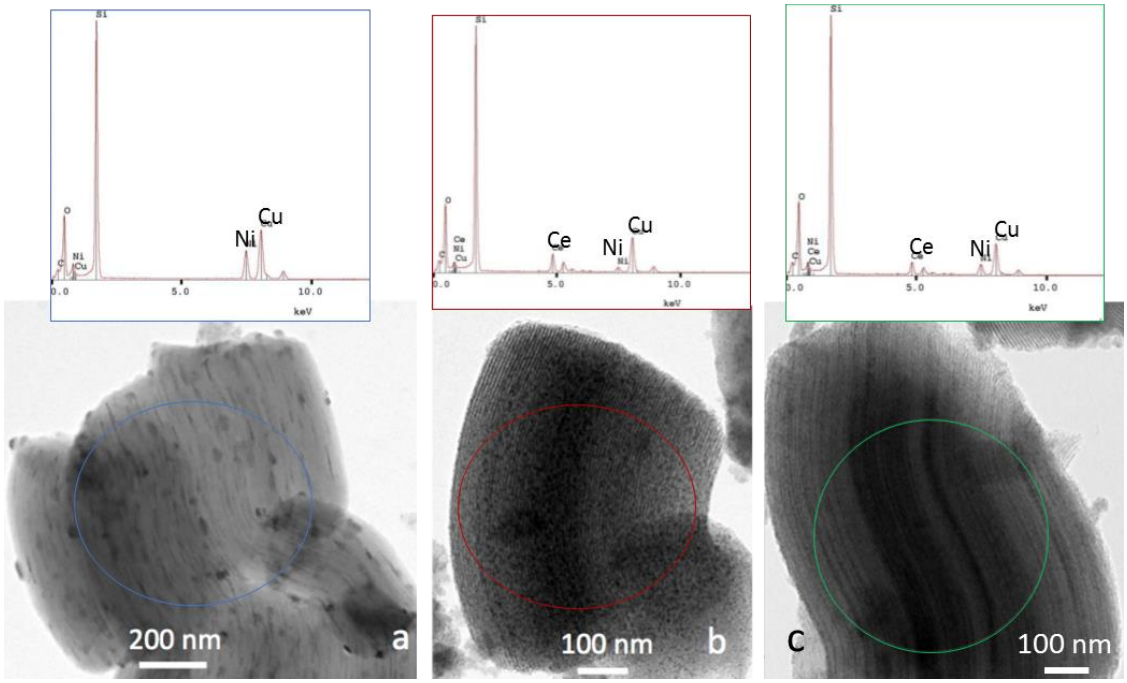


Figure III-6: TEM micrographs and corresponding EDS showing (a) external and internal NiO nanoparticles in $Ni_{7.5}$/SBA-$A_1$(N), (b) a Ce-rich grain in $Ni_{2.5}Ce_6$/SBA-$A_2$(N) and (c) co-presence of Ni and Ce on a grain of $Ni_{2.5}Ce_6$/SBA-$A_2$(N)

- Heterogeneous dispersion of NiO and $CeO_2$ nanoparticles

In view of the TEM images of the various samples, the pores of some silica grains appeared empty while others were highly loaded with nanoparticles. Chemical analysis by EDS was used on some TEM micrographs to get qualitative information on the nanoparticles dispersion (Fig. III-6). On the $Ni_x$/SBA-$A_1$(N) series, the local atomic Ni/Si ratios were as follows:

- between 0.04 and 0.07 on $Ni_{2.5}$/SBA-$A_1$(N),
- around 0.08 on $Ni_{5.0}$/SBA-$A_1$(N),
- between 0.09 and 0.17 on $Ni_{7.5}$/SBA-$A_1$(N).

Based on the amount of Ni impregnated on each sample, the atomic Ni/Si ratios are expected to be at 0.034, 0.068 and 0.1 for x = 2.5, 5.0 and 7.5, respectively. Thus, taking into account that some silica grains remain empty, the experimental and theoretical values are in good agreement. Nevertheless, these atomic ratios were not constant on all the loaded grains of the same sample. Indeed, this ratio did not vary from one grain to another, but also changed in a same grain depending on the zone. Consequently, the NiO nanoparticles are not homogeneously distributed among the silica grains in the $Ni_x$/SBA-$A_1$(N) series.

This observation was also valid on the $Ni_xCe_6$/SBA-$A_2$(N) series. In this case, some grains were enriched with only Ce or Ni-species (Fig. III-6b) whereas others contained both elements (Fig. III-6c). Moreover, Ce was even more heterogeneously dispersed because the atomic Ce/Si ratio was as high as 0.16 in some grains. This value is much higher than the value of 0.025 expected for 6 wt% Ce loading.

### III.2.5. Reducibility of calcined samples

Because the reduced metal nanoparticles constitute the active phase during the dry reforming reaction, it is important to evaluate the reducibility of NiO and consider the influence of Ce addition on Ni. For this purpose, the $H_2$-TPR experiments were carried out using 5 vol% $H_2$/Ar and the resulting profiles are shown in Fig. III-7. It is known that NiO is directly reduced to $Ni^0$ without passing by intermediate oxides.[21]However, the TPR profiles (Fig. III-7) indicate that, in all catalysts, the reduction took place at two ranges of temperature: 200-450 and 450-650°C. Similar to previous findings,[20,22,23,24] the low temperature peak is assigned to the reduction of large NiO

nanoparticles in weak interaction with the support while that at high temperature rather corresponds to small NiO nanoparticles in stronger interactions with the silica walls. No significant difference in the nickel reduction process between the samples with only Ni (Fig. III-7a and b) and with Ni and Ce (Fig. III-7cand d) was noted. On all samples, the NiO nanoparticles are fully transformed into metallic $Ni^0$ at 650°C.

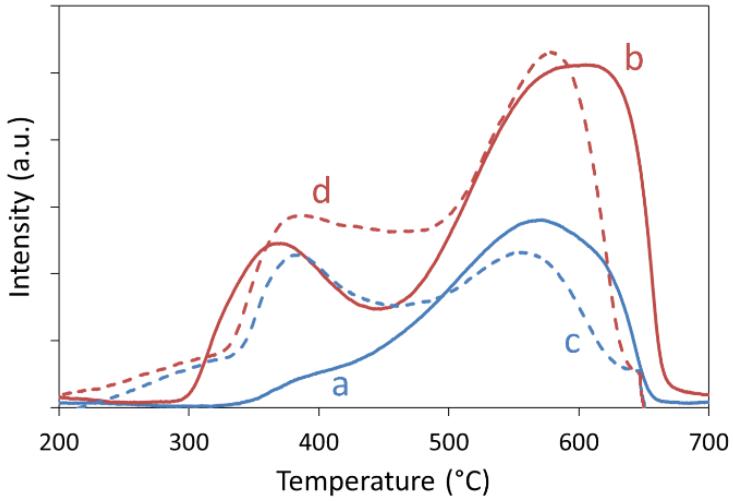


Figure III-7: $H_2$-TPR profiles for (a) $Ni_{2.5}$/SBA-$A_1$(N), (b) $Ni_{5.0}$/SBA-$A_1$(N), (c) $Ni_{2.5}Ce_6$/SBA-$A_2$(N) and (d) $Ni_{5.0}Ce_6$/SBA-$A_2$(N) samples

Summary of section III.2: Physico-chemical properties of supports and impregnated samples

- The SBA-$A_1$ and SBA-$A_2$ supports prepared under identical conditions, without hydrothermal treatment, show close textural properties.
- Reasonable surface areas (320-470 $m^2.g^{-1}$) and pore volumes (0.4-0.5 $cm^3.g^{-1}$) are maintained after metal addition, on both $Ni_x$/SBA-$A_1$(N) and $Ni_xCe_6$/SBA-$A_2$(N) series of calcined samples.
- Good dispersion of NiO nanoparticles (5-7 nm) is always observed, in addition to $CeO_2$ nanoparticles (5 nm) in the $Ni_xCe_6$/SBA-$A_2$(N) calcined samples.
- The distribution of NiO and $CeO_2$nanoparticles between the mesoporous silica grains is heterogeneous.
- Complete reduction of NiO to $Ni^0$ is reached at 650°C, with no significant difference in the reduction process upon addition of Ce.

## III.3 Catalytic performance in dry reforming of methane

For the assessment of the catalytic performance in dry reforming of methane, the samples are first reduced *in-situ* (in the catalytic reactor) under 5% $H_2$/Ar at 650°C for 2 hours, in order to completely convert metal oxides into active metals (Fig. III-8 zone 1). Afterwards, the temperature is cooled down to 200°C, and then the flow is switched to that of the reactants. The catalytic performance is primary evaluated while increasing the temperature from 200 to 800°C (light-off curves, Fig. III-8 zone 2). Next, stability measurements are conducted at constant temperature of 500°C for 12 hours (Fig. III-8 zone 3). The choice of this stability temperature value is explained later in section III.3.2.

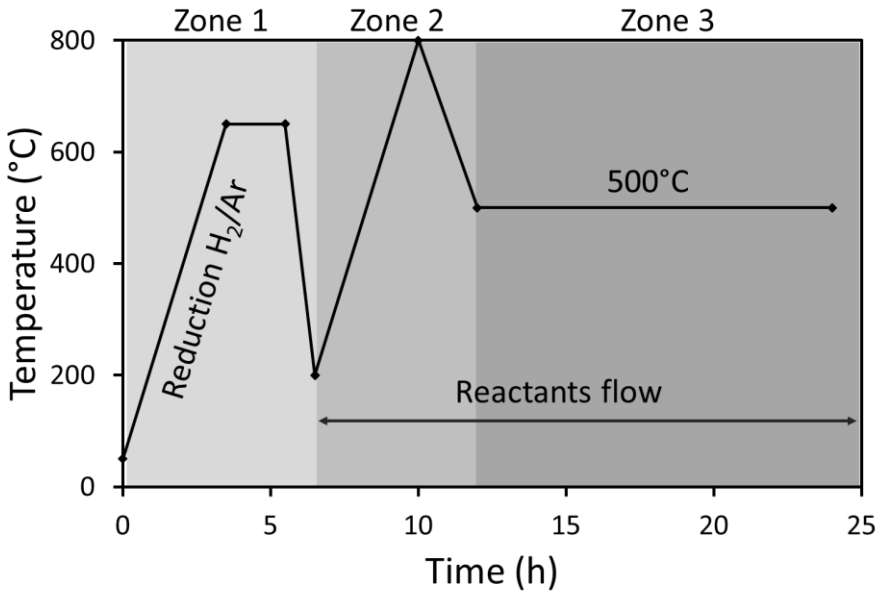


Figure III-8: Temperature profile during reduction and subsequent catalytic activity and stability tests

### III.3.1 Catalytic activity

During catalytic activity evaluation, the evolutions of the conversions of $CH_4$ (Fig. III-9A) and $CO_2$ (Fig. III-9B) as well as of the $H_2$/CO molar ratio (Fig. III-9C) were recorded as a function of temperature. For simplicity, we report on the graphs the values for the catalysts containing the lowest ($Ni_{2.5}$/SBA-$A_1$(N)) and the highest nickel loading ($Ni_{7.5}$/SBA-$A_1$(N) and $Ni_{7.5}Ce_6$/SBA-$A_2$(N)), in addition to the thermodynamic data (red curves) expected under the used diluted

conditions. Table III-4 details the values obtained during light-off experiments at 500 and 650°C for all samples.

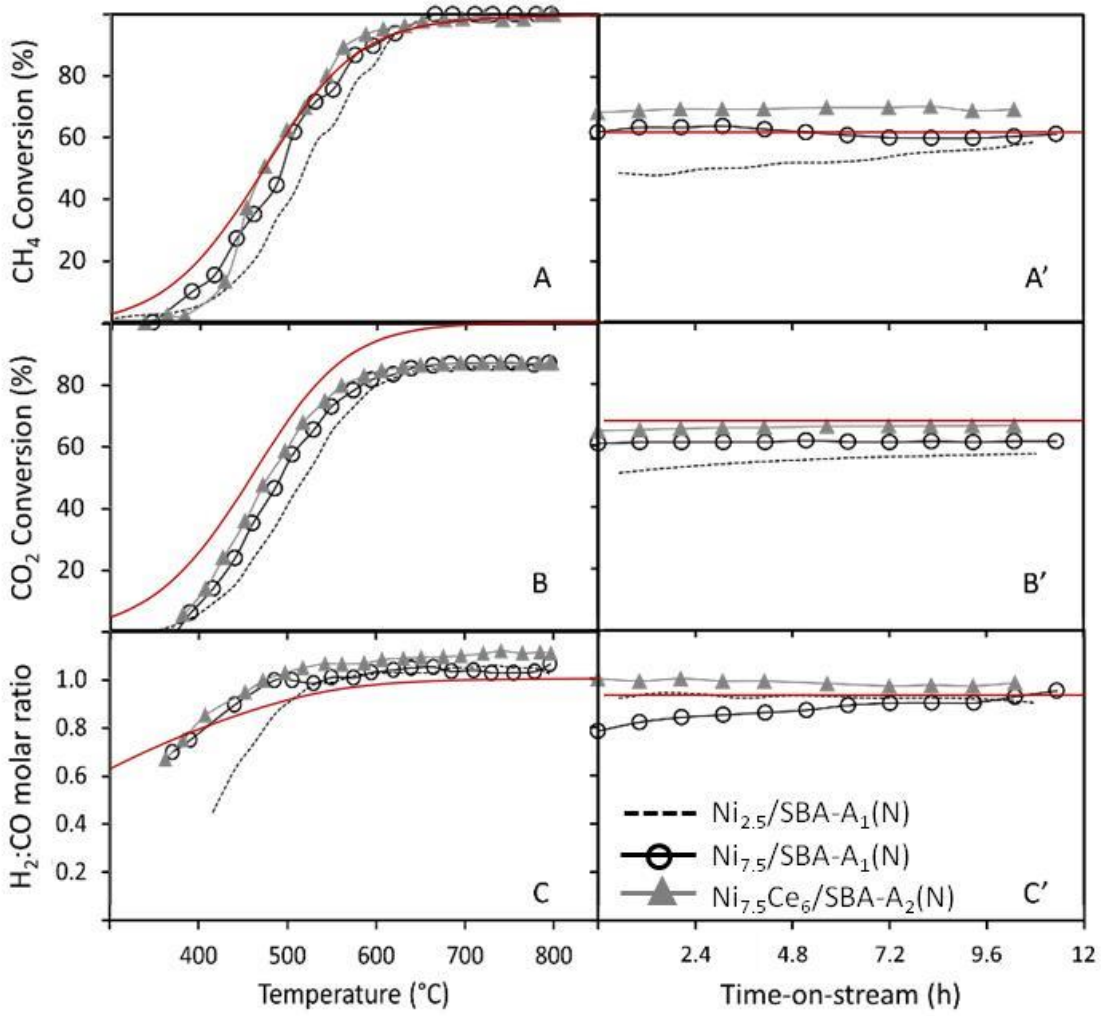


Figure III-9: Variation of (A,A') $CH_4$ conversions, (B,B') $CO_2$ conversions and (C,C') $H_2$:CO molar ratios as a function of (A,B,C) temperature and (A',B',C') time-on-stream at 500°C on 100 mg of $Ni_{2.5}$/SBA-$A_1$(N), $Ni_{7.5}$/SBA-$A_1$(N) and $Ni_{7.5}Ce_6$/SBA-$A_2$(N) ($CH_4$:$CO_2$ = 1:1, GHSV = 52.8 $L.g^{-1}.h^{-1}$). Red curves correspond to equilibrium data calculated under the used conditions

First, the regular increase of both $CH_4$ and $CO_2$ conversions with temperature (Fig. III-9A, B) validates the endothermic character of the reaction. Their increase is in agreement with the increase in equilibrium curves, calculated with the HSC chemistry software when considering the experimental $CH_4$ and $CO_2$ dilution conditions applied at 1 bar. However, the $CH_4$ conversions appear closer to the equilibrium values than the $CO_2$ conversions. For all catalysts, they are slightly

higher than those of $CO_2$ (Fig. III-9 and Table III-4). This may indicate the occurrence of some methane decomposition ($CH_4 \rightarrow 2H_2 + C$) as secondary reaction,[25,26,27,28] which produces $H_2$. This side reaction causes an increase of the $H_2$:CO molar ratio, as demonstrated on Fig. III-9C.

Second, for all Ni-containing SBA-$A_1$ catalysts, the $CH_4$ conversions are between 40% and 65% at 500°C and close to 100% at 650°C (Table III-4 and Fig. III-9A). For comparison, a reference $Ni_{5.0}/SiO_2$(N) catalyst was prepared by incipient wetness impregnation of 5 wt% Ni on non-porous fumed silica support, as previously detailed in Chapter II (Table II-3). At 650°C, the $CH_4$ and $CO_2$ conversions only reached a maximum of 85 and 73%, respectively on this sample. These values were even obtained at lower space velocity the one used for the SBA-15 supported catalysts (Table III-4). Consequently, higher conversions were achieved on all $Ni_x$/SBA-$A_1$(N) samples than on $Ni_{5.0}/SiO_2$(N). This can be related to the mesoporous structure of the SBA-15 silica support, as will be further detailed later.

Third, a slight increase in reactants conversions is observed with the increase of nickel loading from 2.5 to 5.0 wt% (Table III-4). The conversions measured with 7.5 wt% nickel loading are almost identical to those at 5 wt% loading. The slight amelioration of the catalytic activity with the increase of nickel content from 2.5 to 7.5 wt% is very low compared to the active phase content that is three times higher. Furthermore, upon addition of Ce, similar trends in the light-off curves are observed with and without Ce (Fig. III-9 and Table III-4). Hence, the activity levels obtained on all $Ni_x$/SBA-$A_1$(N) and $Ni_xCe_6$/SBA-$A_2$(N) samples are quite comparable, due to the fact that, under the conditions employed, and in view of the good catalytic performances of the samples, the thermodynamic equilibrium is reached. Consequently, no major differences are observed between samples since (i) even with the lower Ni content, sufficient active sites are present for the reactants when using 100 mg of powder and (ii) the presence of Ce in the $Ni_xCe_6$/SBA-$A_2$(N) series cannot enhance the "apparent" catalytic activity compared to the Ce-free samples since it is already maximum. This could have been also the case in recent reports[2,29] claiming the absence of the promoting effect of ceria frequently reported on Ni-based catalysts in DRM at high reaction temperatures (above 700°C).[1,2,4,5,6]

In order to allow better comparison between samples, more severe conditions were applied and 20 mg of catalyst were tested (Table III-4). The gas hourly space velocity (GHSV) was thus increased from 52.8 to 264 $L.g^{-1}.h^{-1}$. Again, the results show comparable $CH_4$ and $CO_2$

conversions obtained when using 20 or 100 mg of catalyst (Table III-4) showing that even more drastic conditions should be needed to allow proper comparison. Nevertheless, comparison with the nickel free samples show that $Ni^0$ plays an essential role in the reaction since neither the SBA-15 support alone, nor a $Ce_6$/SBA-$A_2$ sample tested for comparison, are active.

Being close to the thermodynamic equilibrium limits the possibilities of comparison and analysis of the effect of Ce addition and Ni loading. However, the results obtained show good catalytic behaviors of $Ni_x$/SBA-$A_1$(N) and $Ni_xCe_6$/SBA-$A_2$(N) series of samples in DRM. Indeed, the $CH_4$ and $CO_2$ conversions obtained are even much better than those recently reported[1,2,18,25,40,41,42] on Ni-based SBA-15 materials prepared with classical methods of impregnations and higher Ni loading (Fig. III-10) and tested at even lower space velocities. In details, more than 80% $CH_4$ conversion is achieved at 600°C in our work whereas at the same temperature it reached only 45% on 12% Ni/SBA-15[1] and varied between 5 and 65% for other 10% Ni/SBA-15 catalysts.[2,18,40,41] With the Ceria or Ceria-zirconia (CZ) promotion, the $CH_4$ conversion exceeded 96% in our work while only 44 and 60% conversions were achieved for 12% NiCe/SBA-15[1] and 10% Ni/CZ/SBA-15[2,25] catalysts, respectively. Furthermore, an almost equimolar $H_2$ and CO composition is attained on our catalysts, as for a 10%Ni-CZ/SBA-15 material[2], while the $H_2$:CO ratio was between 0.7 and 0.8 (i.e. notably lower than 1) on Ni-Ce/SBA-15[1] and ceria-doped Ni/SBA-16 catalysts.[42] It is worth adding that in most of these papers an equimolar feed ratio ($CH_4$:$CO_2$=1) was employed, but the authors did not specify if a pure or diluted feed was used. This could affect the activity comparisons since, as mentioned in section II.4.1, the dilution favors higher conversions for a given temperature. Unfortunately, eventual differences in experimental conditions could not be considered here in details, due to the absence of precisions in bibliography. In spite of this, the comparison shows high potential of Ni/SBA-15 catalysts in DRM.

Table III-4: Conversion (%) and selectivity of the catalysts (as deduced from light-off curves)

| **Support** | **GHSV ($L.g^{-1}.h^{-1}$)** | 52.8 | | | | | | 264 | | | | | |
|---|---|---|---|---|---|---|---|---|---|---|---|---|---|
| | **Temperature (°C)** | 500 | | | 650 | | | 500 | | | 650 | | |
| | **Sample name** | $CH_4$ | $CO_2$ | $H_2$:CO | $CH_4$ | $CO_2$ | $H_2$:CO | $CH_4$ | $CO_2$ | $H_2$:CO | $CH_4$ | $CO_2$ | $H_2$:CO |
| | | | | | | | | | | | | | |
| **SBA-$A_1$** | $Ni_{2.5}$/SBA-$A_1$(N) | 40 | 42 | 0.85 | 97 | 85 | 1.01 | 42 | 38 | 0.85 | 86 | 80 | 1 |
| | $Ni_{5.0}$/SBA-$A_1$(N) | 54 | 56 | 0.96 | 98 | 88 | 1.03 | 48 | 44 | 0.85 | 97 | 84 | 0.97 |
| | $Ni_{7.5}$/SBA-$A_1$(N) | 64 | 57 | 0.9 | 97 | 87 | 1.03 | 46 | 40 | 0.85 | 88 | 80 | 1 |
| | | | | | | | | | | | | | |
| **SBA-$A_2$** | $Ni_{2.5}Ce_6$/SBA-$A_2$(N) | 46 | 32 | n.d. | 95 | 78 | n.d. | 32 | 26 | 0.83 | 86 | 82 | 1.02 |
| | $Ni_{5.0}Ce_6$/SBA-$A_2$(N) | 61 | 56 | 0.96 | 98 | 88 | 1.01 | 46 | 49 | 0.85 | 92 | 86 | 1.02 |
| | $Ni_{7.5}Ce_6$/SBA-$A_2$(N) | 64 | 60 | 1 | 98 | 86 | 1.09 | 46 | 42 | 0.87 | 94 | 85 | 1.03 |
| | | | | | | | | | | | | | |
| **$SiO_2$** | $Ni_{5.0}$/$SiO_2$(N)* | 53 | 47 | n.d. | 85 | 73 | 1.05 | | | | | | |

n.d. not determined

* GHSV of 21.1 $L.g^{-1}.h^{-1}$

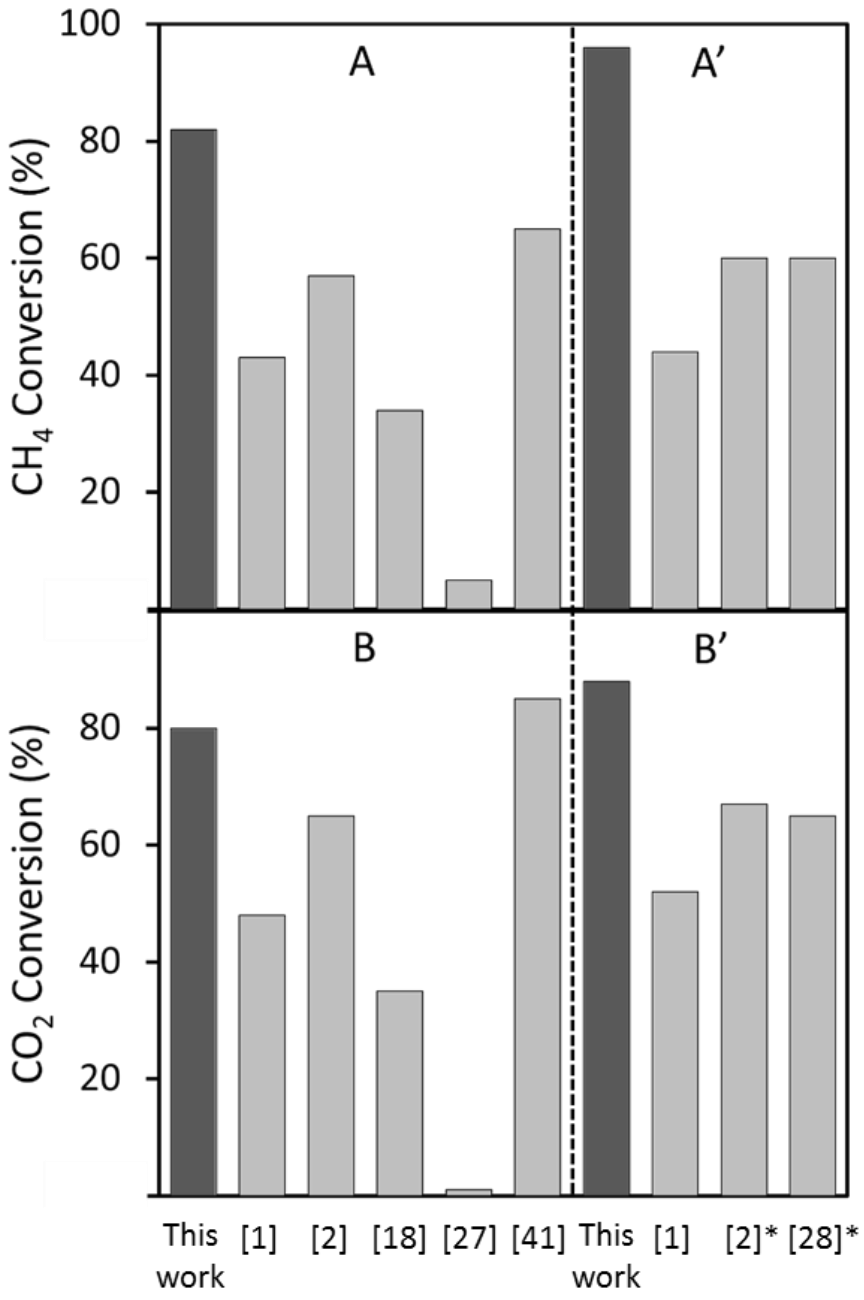


Figure III-10: Comparison of the conversions of $CH_4$ (A,A') and $CO_2$ (B,B') at 600°C on Ni/SBA-15 catalysts without (A,B) and with Ce (A',B'): this study (black columns, samples with 5 wt% Ni) and bibliographic data (grey columns, catalysts with Ni contents between 10 and 12 wt%). * Samples containing zirconia

### III.3.2 Catalytic stability and selectivity

After assessment of the catalytic activity, the temperature is reduced and maintained at 500°C in order to follow the catalytic stability for 12 hours (Fig. III-8 zone 3). Few works dealing with the stability behavior of Ni-based catalysts at low temperatures have been published.[30,31,32,33,34,35] This medium temperature was chosen in this section because it gives intermediate conversions (40-60%, not too high) that are appropriate to study the evolution of activity with time. Even if moderate conversions are achieved at such temperatures, the efficiency of the system can be increased by using membrane reactors that selectively remove hydrogen and shift the equilibrium towards the products.[36,37,38] Thus, operating at 500°C would allow using such catalysts in membrane reactors where the hydrogen permeation flux declines if the membrane is submitted to temperature above 550°C.[39]

For all samples, around 65% $CH_4$ conversions (Fig. III-9A') and 60% $CO_2$ conversions (Fig. III-9B') were maintained during the test, with $H_2$:CO ratios (Fig. III-9C') close to unity. Thus high activity is achieved on all the catalysts at the applied temperature. Moreover, slightly better conversions are obtained at 500°C compared to those during light-off curve, regardless of the nickel content. This can be due to differences in heat and mass transfer between the transition and steady state regimes. Furthermore, this can indicate some beneficial transformation of the nickel species (for instance better reduction) and/or enhanced accessibility of reactants after intermediate heating of the samples at high temperature.

After 12 hours, the conversions are almost unchanged, indicating the high stability of the catalysts. Besides, not only the stability but also the selectivity towards DRM is excellent at 500°C, regardless of the sample and the catalytic step, as seen from the $H_2$:CO ratios close to one. On $Ni_{7.5}Ce_6$/SBA-$A_2$(N), the $CH_4$ conversion (Fig. III-9A') remained slightly higher than the desired value, in accordance with the occurrence of methane decomposition, that increases the $H_2$:CO molar ratio (Fig. III-9C').

Summary of section III-3: Ni(Ce)/SBA-A catalytic performance in dry reforming of methane

- For all $Ni_x$/SBA-$A_1$(N) catalysts, the $CH_4$ conversions are between 40% and 65% at 500°C and close to 100% at 650°C.
- A slight increase in reactants conversions is observed with the increase of nickel loading from 2.5 to 7.5 wt% and the addition of Ce does not apparently enhance the catalytic activity. This is because the thermodynamic equilibrium is reached under the test conditions used.
- Comparable $CH_4$ and $CO_2$ conversions are obtained when using 20 or 100 mg of catalyst, suggesting limited accessibility hindrance to the active sites and/or diffusional limitations.
- The catalytic results obtained show better catalytic behaviors than those reported on Ni/SBA-15 prepared with classical methods of impregnations and higher Ni loading and tested at lower GHSV.

## III.4 Physico-chemical properties of spent catalysts

After catalytic measurements, the spent catalysts were characterized by XRD and TEM in order to check the preservation of the dispersion of the Ni-based and Ce-based nanoparticles during the catalytic run.

First, in the spent catalysts (after 12hours at 500°C), diffraction peaks at 44, 52 and 76° are observed for all samples (Fig. III-11), assignable to metallic $Ni^0$ with a face-centered cubic lattice (Fm-3m) and a unit cell parameter of 3.51 Å (ICDD 71-4655). The presence of $Ni_{0.98}C_{0.02}$ (ICDD 74-5561) with typical diffraction peaks at the same position cannot be excluded. These signals confirm the preservation of the reduction state of the nickel active phase in the DRM reaction.

More importantly, the mean crystallite sizes of the Ni particles calculated using the Scherrer equation on these samples are between 5 and 8 nm (Table III-3), which is very close, only slightly higher, than the sizes identified before test for the NiO particles in the calcined samples (Table III-3). Therefore, if present, the sintering of the supported nanoparticles during reduction and reaction remains very limited. Moreover, with respect to Ce, the $CeO_2$ peaks are no longer detected after test. Either no peaks or very small ones assignable to partially reduced $CeO_{1.675}$ (ICDD 89-8430) are found, depending on the sample. This suggests cerium spreading upon reductive thermal treatments possibly in the form of $Ce^{3+}$ or $Ce^{4+}$ ions and/or formation of non-crystalline phases.

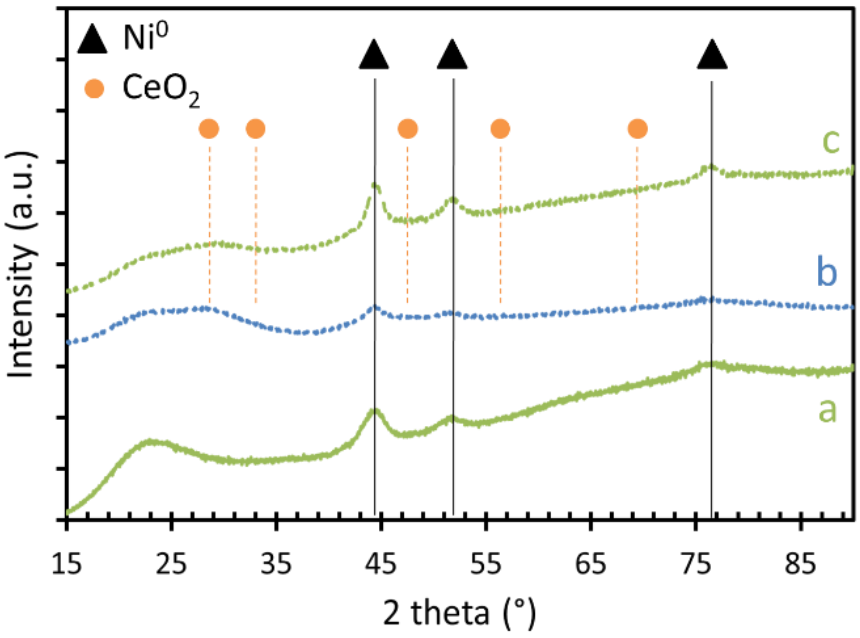


Figure III-11: X-ray diffractograms of spent (a) $Ni_{7.5}$/SBA-$A_1$(N), (b) $Ni_{2.5}Ce_6$/SBA-$A_2$(N) and (c) $Ni_{7.5}Ce_6$/SBA-$A_2$(N)

Second, the TEM images confirm the preservation of the mesoporous channel system and the ordered hexagonal structure after test (Fig. III-12a,b), as well illustrated by representative images of $Ni_{5.0}$/SBA-$A_1$(N) (Fig. III-12a,b) and $Ni_{7.5}Ce_6$/SBA-$A_2$(N) (Fig. III-12c). No major difference in particles dispersions between $Ni_x$/SBA-$A_1$(N) and $Ni_xCe_6$/SBA-$A_2$(N) catalysts is observed. Similar to the calcined samples, no external Ni particles are observed on the spent catalysts. The nickel nanoparticles are well maintained inside the pores of the SBA-15 silica support.

In addition, very limited carbon deposition was observed on the spent catalysts, after catalytic run at the medium temperature of 500°C. Few carbon nanotubes were formed at the interface between the $Ni^0$active species and the support.[40] In such case, the nickel metal particles are progressively pushed away from the surface, which can occur with particles deposited outside the pores, as was indeed observed - although rarely - on the spent Ni-richest $Ni_{7.5}$/SBA-$A_1$(N) catalyst (Fig. III-12e). As reported elsewhere, some kinds of carbon nanotubes do not affect the stability of the catalysts.[27] This agrees with the previous assumption of methane decomposition, which takes place at a very small extent. In contrast, such carbon nanotubes formation is totally hindered inside the SBA-15 pores due to steric constraints and to the stabilization of the small $Ni^0$ nanoparticles that remain strongly

attached and blocked inside the pores. An additional confirmation of the preservation of the nickel dispersion after catalytic run is further given by the atomic Ni/Si ratio values (EDS analyses) that stayed globally comparable to those after calcination in both Ni/SBA-$A_1$(N) and $NiCe_6$/SBA-$A_2$(N) series (Table III-3).

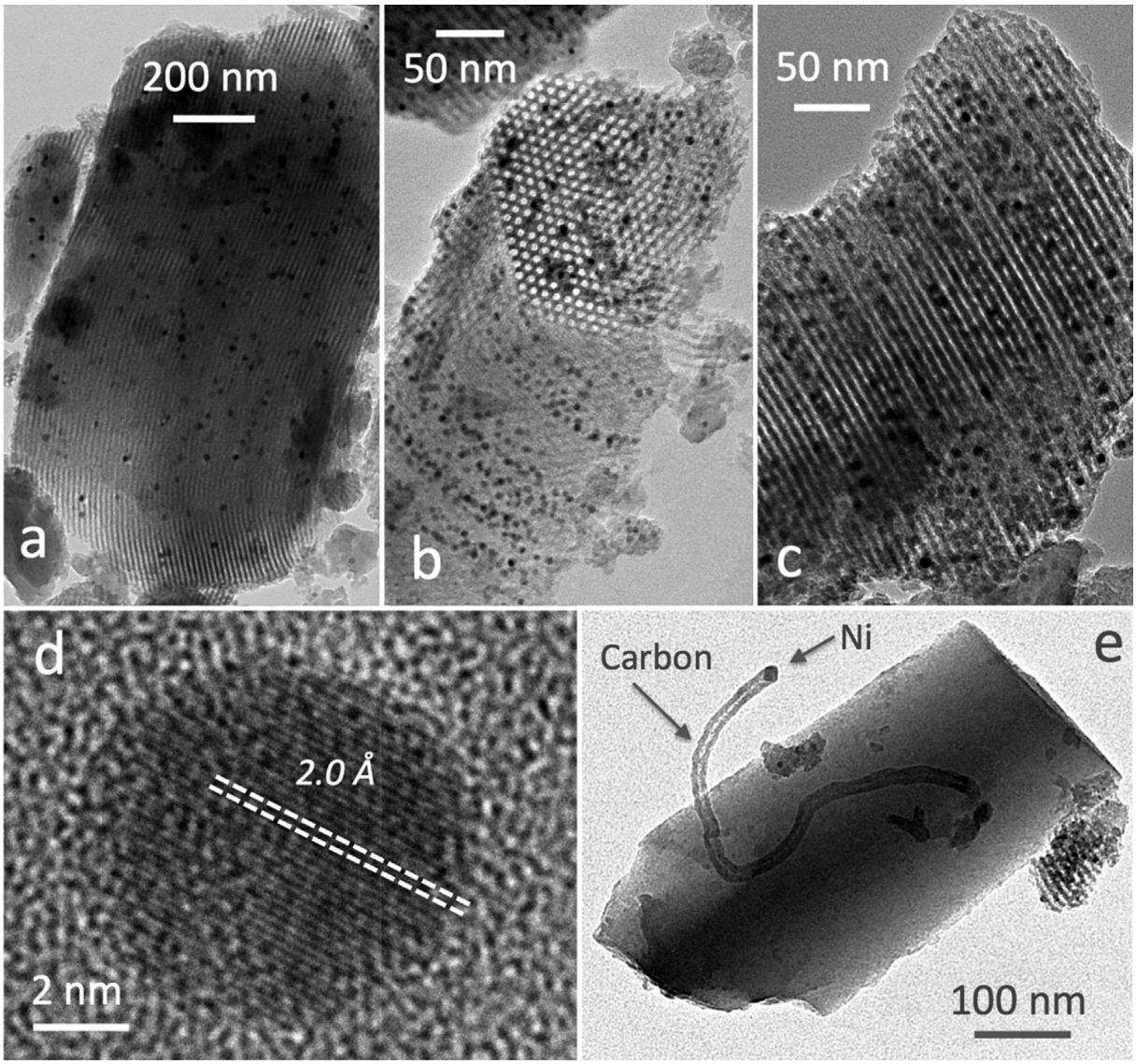


Figure III-12: TEM micrographs of the spent catalysts after heating at 800°C and 12h at 500°C under reactants: $Ni^0$ dispersed in SBA-15 grains in (a,b) $Ni_{5.0}$/SBA-$A_1$(N), and (c) $Ni_{7.5}Ce_6$/SBA-$A_2$(N) (d) high resolution image of a $Ni^0$ nanoparticle and (e) carbon nanotube grown between the support and a nickel nanoparticle

Consequently, the high activity of both $Ni_x$/SBA-$A_1$(N) and $Ni_xCe_6$/SBA-$A_2$(N) series of catalysts can be explained by the excellent Ni dispersion seen after calcination and maintained after reduction and catalytic testing, as demonstrated by TEM and XRD. Thus it appears that the SBA-15 support exerts a very positive confinement effect for high catalytic stability. The confinement limits the growth of Ni particles to few nanometers during pre-treatment and reaction and results in a better Ni dispersion. Consequently, the number of accessible $Ni^0$ nanoparticles inside the pores and therefore of available active sites increases (even if some nickel is not easily accessible). Compared to previous bibliographic reports on Ni/SBA-15 catalysts,[20,40,41,43,44,45,46,47] the effect is here strongly accentuated owing to the two solvents metal deposition method used for the catalysts preparation that permitted a significant increase of the dispersion of nickel deep inside the pores.[43,48,49,50]

Summary of section III-5: dispersion of Ni and $CeO_2$ nanoparticles after test

- The excellent $Ni^0$ dispersion was maintained on all catalysts after test.
- Limited $Ni^0$ sintering (5-8 nm) and carbon deposition were observed on the spent catalysts.
- The use of SBA-15 mesoporous silica support limits the growth of Ni particles to few nanometers.

## III.5 Conclusion

To sum up, high dispersion of nickel and cerium inside the channels of mesoporous SBA-15 is obtained using the two solvents deposition method. The catalysts reduced and tested in DRM show good activity up to 800°C and high stability at 500°C. After reaction, Ni metallic particles, stable in air, are still well dispersed inside the pores while no ceria is detected. Under the experimental conditions tested here, the thermodynamic equilibrium is reached. Therefore, the variation of Ni loading and the addition of Ce to Ni/SBA-15 did not affect the "apparent" catalytic performance in dry reforming of methane. In addition, limited interaction between Ce and Ni was obtained on our samples, since Ni and Ce species were present on separate grains of the support. This can be due to the sequential impregnation method employed.

Promising results were obtained when using mesoporous SBA-15 silica supports to stabilize the Ni nanoparticles. However, different small batches had to be prepared in this part of the work to

obtain sufficient quantities of SBA-15. The absence of hydrothermal treatment and the variations in TEOS addition rates (due to manual addition) caused some variations in the textural properties of the supports. Consequently, the SBA-15 support preparation scale should be enlarged in order to have one large batch with sufficient quantity of support for further experiment. The materials also should be tested under more severe conditions, to be more realistic (closer to industrial scale). This will be the concern of the following chapter.

**Outcome of this part of the doctoral work:**

- **M.N. Kaydouh**, N. El Hassan, A. Davidson, S. Casale, H. El Zakhem,P. Massiani, Microporous and Mesoporous Materials 220 (2016) 99-109. Doi: 10.1016/j.micromeso.2015.08.034
- **Marie-Nour Kaydouh**, Nissrine El Hassan, Anne Davidson, Sandra Casale, Henri El Zakhem, Pascale Massiani, Comptes Rendus Chimie, 18 (2015) 293-301. Doi: 10.1016/j.crci.2015.01.004
- **Poster** at the **AWAP conference**, "Stable promoted Ni/SBA-15 catalysts for dry reforming of methane", Poland 2014.
- **Oral presentation** at the **GECat conference**, "Des catalyseurs stables pour le reformage sec du méthane à température modérée: Ni, Ni-Ce/SBA-15 par imprégnation 2 solvants", France 2014.
- **Poster** and **short oral communication** at the **EUROPACAT conference**, "Dry reforming of methane at medium-temperature on highly dispersed Ni/SBA-15 and Ni-Ce/SBA-15 catalysts prepared by a "two solvents" method", France 2014.

## III.6 References

[1] N. Wang, W. Chu, T. Zhang, X.S. Zhao, *Synthesis, characterization and catalytic performances of Ce-SBA-15 supported nickel catalysts for methane dry reforming to hydrogen and syngas*, International Journal of Hydrogen Energy 37 (2012) 19-30.

[2] A. Albarazi, P. Beaunier, P. Da Costa, *Hydrogen and syngas production by methane dry reforming on SBA-15 supported nickel catalysts: On the effect of promotion by* $Ce_{0.75}Zr_{0.25}O_2$ *mixed oxide*, International Journal of Hydrogen Energy 38 (2013) 127-139.

[3] H. Wan, X. Li, S. Ji, B. Huang, K. Wang, C. Li, *Effect of Ni loading and $Ce_xZr_{1-x}O_2$ promoter on Ni-based SBA-15 catalysts for steam reforming of methane*, Journal of Natural Gas Chemistry 16 (2007)139-147.

[4] A. Khan, T.Sukonket, B.Saha, R. Idem, *Catalytic activity of various 5 wt % $Ni/Ce_{0.5}Zr_{0.33}M_{0.17}O_{2-\delta}$ catalysts for the $CO_2$ reforming of $CH_4$ in the presence and absence of steam*, Energy & Fuels 26 (2012) 365-379.

[5] A. Nandini, K.K. Pant, S.C. Dhingra, *K-, $CeO_2$-, and Mn-promoted $Ni/Al_2O_3$ catalysts for stable $CO_2$ reforming of methane*, Applied Catalysis A: General 290 (2005) 166-174.

[6] N. Laosiripojana, W. Sutthisripok, S. Assabumrungrat, *Synthesis gas production from dry reforming of methane over $CeO_2$ doped $Ni/Al_2O_3$: Influence of the doping ceria on the resistance toward carbon formation*, Chemical Engineering Journal 112 (2005) 13-22.

[7] K. Wang, B. Dou, B. Jiang, Y. Song, C. Zhang, Q. Zhang, H. Chen, Y. Xu, *Renewable hydrogen production from chemical looping steam reforming of ethanol using xCeNi/SBA-15 oxygen carriers in a fixed-bed reactor*, International Journal of Hydrogen Energy 41 (2016) 12899-12909.

[8] F. Boubekr, A. Davidson, S. Casale, P. Massiani, *Ex-nitrate Co/SBA-15 catalysts prepared with calibrated silica grains: Information given by TPR, TEM, SAXS and WAXS*, Microporous and Mesoporous Materials 141 (2011) 157-166.

[9] M. Imperor-Clerc, P. Davidson, A. Davidson, *Existence of a microporous corona around the mesopores of silica-based SBA-15 materials templated by triblock copolymers*, Journal American Chemical Society 122 (2000) 11925-11933.

[10] A. Galarneau, H. Cambon, F. Di Renzo, F. Fajula, *True microporosity and surface area of mesoporous SBA-15 silicas as a function of synthesis temperature*, Langmuir 17 (2001) 8328-8335.

[11] P. Feng, X. Bu, D. J. Pine, *Control of pore sizes in mesoporous silica templated by liquid crystals in block copolymer-cosurfactant-water systems*, Langmuir 16 (2000) 5304-5310.

[12] C. Zhang, W. Zhu, S. Li, G. Wu, X. Ma, X. Wang, J. Gong, *Sintering-resistant Ni-based reforming catalysts obtained via the nanoconfinement effect*, Chemical Communications 49 (2013) 9383-9385.

[13] M. Ogura, R. Guillet-Nicolas, D. Brouri, S. Casale, J. Blanchard, K. A. Cychosz, M. Thommes, C. Thomas, *Insights into the accessibility of Zr in Zr/SBA-15 mesoporous silica supports with increasing Zr loadings*, Microporous and Mesoporous Materials 225 (2016) 440-449.

[14] J. Zhu, X. Peng, L. Yao, X. Deng, H. Dong, D. Tong, C. Hu, *Synthesis gas production from $CO_2$ reforming of methane over Ni-Ce/$SiO_2$ catalyst: The effect of calcination ambience*, International Journal of Hydrogen Energy 38 (2013) 117-126.

[15] X. Lv, J. Chen, Y. Tan, Y. Zhang, *A highly dispersed nickel supported catalyst for dry reforming of methane*, Catalysis Communications 20 (2012) 6-11.

[16] H. Zhang, M. Li, P. Xiao, D. Liu, C.J. Zou, *Structure and catalytic performance of Mg-SBA-15-supported nickel catalysts for $CO_2$reforming of methane to syngas*, Chemical Engineering and Technology 36(10) (2013) 1701-1707.

[17] Z. Zuo, C. Shen, P. Tan, W. Huang, *Ni based on dual-support Mg-Al mixed oxides and SBA-15 catalysts for dry reforming of methane*, Catalysis Communications 41 (2013) 132-135.

[18] N. Wang, X. Yu, K. Shen, W. Chu, W. Qian, *Synthesis, characterization and catalytic performance of MgO-coated Ni/SBA-15 catalysts for methane dry reforming to syngas and hydrogen*, International Journal of Hydrogen Energy 7307(2013) 9718-9731.

[19] J.R.A. Sietsma, J.D. Meeldijk, M.Versluijs-Helder, A. Broersma, A. Jos van Dillen, P.E. de Jongh, K.P. de Jong, *Ordered Mesoporous Silica to Study the Preparation of Ni/$SiO_2$ ex Nitrate Catalysts: Impregnation, Drying, and Thermal Treatments*, Chemistry Materials 20 (2008) 2921-2931.

[20] F. Habimana, X. Li, S. Ji, B. Lang, D. Sun, C. Li, *Effect of Cu promoter on Ni-based SBA-15 catalysts for partial oxidation of methane to syngas*, Journal of Natural Gas Chemistry 18 (2009) 392-398.

[21] H. Wan, X. Li, S. Ji, B. Huang, K. Wang, C. Li, *Effect of Ni Loading and $Ce_xZr_{1-x}O_2$ Promoter on Ni-Based SBA-15 Catalysts for Steam Reforming of Methane*, Journal of Natural Gas Chemistry 16 (2007) 139-147.

[22] K. Wang, X. Li, S. Ji, X. Shi, J. Tang, *Effect of $Ce_xZr_{1-x}O_2$ Promoter on Ni-Based SBA-15 Catalyst for Steam Reforming of Methane*, Energy & Fuels 23 (2009) 25-31.

[23] B.S. Liu, C.T. Au, *Carbon deposition and catalyst stability over $La_2NiO_4/\gamma$-$Al_2O_3$ during $CO_2$ reforming of methane to syngas*, Applied Catalysis A: General 244 (2003) 181-195.

[24] H. Liu, H. Wang, J. Shen, Y. Sun, Z. Liu, *Preparation, characterization and activities of the nano-sized Ni/SBA-15 catalyst for producing $CO_x$-free hydrogen from ammonia*, Applied Catalysis A: General 337 (2008) 138-147.

[25] A. Serrano-Lotina, L. Daza, *Influence of the operating parameters over dry reforming of methane to syngas*, International Journal of Hydrogen Energy 39 (2014) 4089-4094.

[26] H. Wu, G. Pantaleo, V. La Parola, A. M. Venezia, X. Collard, C. Aprile, L.F. Liotta, *Bi- and trimetallic Ni catalysts over $Al_2O_3$ and $Al_2O_3$-$MO_x$ (M=Ce or Mg) oxides for methane dry reforming: Au and Pt additive effects*, Applied Catalysis B: Environmental 156-157 (2014) 350-361.

[27] J. Z. Luo, Z. L. Yu, C. F. Ng, C. T. Au, *$CO_2/CH_4$ Reforming over Ni-$La_2O_3$/5A: An Investigation on Carbon Deposition and Reaction Steps*, Journal of Catalysis 194 (2000) 198-210.

[28] C. Enrique Daza, J. Gallego, F. Mondragón, S. Moreno, R. Molina, *High stability of Ce-promoted Ni/Mg-Al catalysts derived from hydrotalcites in dry reforming of methane*, Fuel 89 (2010) 592-603.

[29] A. Albarazi, M.E. Gálvez, P. Da Costa, *Synthesis strategies of ceria-zirconia doped Ni/SBA-15 catalysts for methane dry reforming*, Catalysis Communications 59 (2015) 108-112.

[30] S. Sokolov, E. V. Kondratenko, M.M. Pohl, A. Barkschat, U. Rodemerck, *Stable low-temperature dry reforming of methane over mesoporous $La_2O_3$-$ZrO_2$ supported Ni catalyst*, Applied Catalysis B: Environmental 113-114 (2012) 19-30.

[31] S. Sokolov, E.V. Kondratenko, M.M. Pohl, U. Rodemerck, *Effect of calcination conditions on time on-stream performance of Ni/$La_2O_3$-$ZrO_2$ in low-temperature dry reforming of methane*, International Journal of Hydrogen Energy 38 (2013) 16121-16132.

[32] P. Ferreira-Aparicio, A. Guerrero-Ruiz, I. Rodriguez-Ramos, *Comparative study at low and medium reaction temperatures of syngas production by methane reforming with carbon dioxide over silica and alumina supported catalysts*, Applied Catalysis A: General 170 (1998) 177-187.

[33] S. Irusta, L. M. Cornaglia, E. A. Lombardo, *Hydrogen production using Ni-Rh on $ZrO_2$ as potential low-temperature catalysts for membrane reactors*, Journal of Catalysis 210 (2002) 263-272.

[34] D. Baudouin, U. Rodemerck, F. Krumeich, A. de Mallmann, K. C. Szeto, H.Ménard, L. Veyre, J.P. Candy, P.B. Webb, C.Thieuleux, C. Copéret, *Particle size effect in the low temperature reforming of methane by carbon dioxide on silica-supported Ni nanoparticles*, Journal of Catalysis 297 (2013) 27-34.

[35] X. Xie, T.Otremba, P. Littlewood, R.Schomacker, A. Thomas,*One-pot synthesis of supported nanocrystalline nickel manganese oxide for dry reforming of methane*, ACS Catalysis 3 (2013) 224−229.

[36] A.K. Prabhu, R. Radhakrishnan, S. Ted Oyama, *Supported nickel catalysts for carbon dioxide reforming of methane in plug flow and membrane reactors*, Applied Catalysis A: General 183 (1999) 241-252.

[37] P. Ferreira-Aparicio, I. Rodriguez-Ramos, A. Guerrero-Ruiz, *On the applicability of membrane technology to the catalyzed dry reforming of methane*, Applied Catalysis A: General 237 (2002) 239-252.

[38] J. Múnera, S. Irusta, L. Cornaglia, E. Lombardo, *$CO_2$ reforming of methane as a source of hydrogen using a membrane reactor*, Applied Catalysis A: General 245 (2003) 383-395.

[39] P. Ferreira-Aparicio, M.J. Benito, *High performance membrane reactor system for hydrogen production from methane*, Industrial Engineering Chemistry Resources 44 (2005) 742-748.

[40] M.E. Galvez, A. Albarazi, P. Da Costa, *Enhanced catalytic stability through non-conventional synthesis of Ni/SBA-15 for methane dry reforming at low temperatures*, Applied Catalysis A: General 504 (2015) 143-150.

[41] B. Li, S. Zhang, *Methane reforming with $CO_2$ using nickel catalysts supported on yttria-doped SBA-15 mesoporous materials via sol-gel process*, International Journal of Hydrogen Energy 38 (2013) 14250-14260.

[42] S. Zhang, S. Muratsugu, N. Ishiguro, M. Tada, *Ceria-doped Ni/SBA-16 catalysts for dry reforming of methane*, ACS Catalysis 3 (2013) 1855-1864.

[43] I. Lopes, N. El Hassan, H. Guerba, G. Wallez, A. Davidson, *Size-induced structural modifications affecting $Co_3O_4$nanoparticles patterned in SBA-15 silicas*, Chemistry Materials 18 (2006) 5826-5828.

[44] T. Huang, W. Huang, J. Huang, P. Ji, *Methane reforming reaction with carbon dioxide over SBA-15 supported Ni-Mo bimetallic catalysts*, Fuel Processing Technology 92 (2011) 1868-1875.

[45]A.J. Brungs, A.P.E. York, J.B. Claridge, C. Marquez-Alvarez, M.L.H. Green, *Dry reforming of methane to synthesis gas over supported molybdenum carbide catalysts*, Catalysis Letters 70 (2000) 117-122.

[46] A. Djaidja, S. Libs, A. Kiennemann, A. Barama, *Characterization and activity in dry reforming of methane on NiMg/Al and Ni/MgO catalysts*, Catalysis Today 113 (2006) 194-200.

[47] L. Xu, H. Song, L. Chou, *Ordered mesoporous MgO-$Al_2O_3$ composite oxides supported Ni based catalysts for $CO_2$ reforming of $CH_4$: Effects of basic modifier and mesopore structure*, International Journal of Hydrogen Energy 38 (2013) 7307-7325.

[48] M. Imperor-Clerc, D. Bazin, M.D. Appay, P. Beaunier, A. Davidson, *Crystallization of β-$MnO_2$nanowires in the pores of SBA-15 silicas: In-situ investigation using synchrotron radiation*, Chemistry Materials 16 (2004) 1813-1821.

[49] J. van der Meer, I. Bardez-Giboire, C. Mercier, B. Revel, A. Davidson, R. Denoyel, *Mechanism of metal oxide nanoparticle loading in SBA-15 by the double solvent technique*, Journal Physical Chemistry C 114 (2010) 3507-3515.

[50] J. Woo Han, C. Kim, J. Seong Park, H. Lee, *Highly coke-resistant Ni nanoparticle catalysts with minimal sintering in dry reforming of methane*, ChemSusChem 7 (2014) 451-456.

# CHAPTER IV

# Influence of Textural Properties

The previous chapter described the active and stable Ni/SBA-15 catalysts for dry reforming of methane at 500°C. The SBA-15 silica support stabilized small nickel metallic nanoparticles inside the pores, thus inhibiting their sintering during reaction. Coke formation was moreover very limited, possibly due to the medium temperature applied. However, the SBA-15 preparation on small scale (4g of calcined material) was not sufficient to prepare different samples and therefore, two syntheses were needed. The absence of hydrothermal treatment and irregular manual addition of TEOS produced some inconsistencies between the resulting supports. Furthermore, even if already satisfying, the surface areas and pore volumes of the impregnated samples obtained were not very high (350-600 $m^2.g^{-1}$). Consequently, in order to obtain sufficient quantities of support prepared under exactly the same conditions, it was important to pass towards a larger scale preparation. In addition, a peristaltic pump was used for a more regular TEOS addition.

In order to avoid changing more than one parameter at a time, the SBA-15 support was first prepared on a larger scale (14 times larger) and in experimental conditions close to the previous ones (1.9M HCl, without hydrothermal treatment). Hence, it was possible to compare the new support, prepared on a larger scale, to the one obtained by smaller synthesis, for validation of the preparation. This comparison will be done in the first part of this chapter. Next, the nickel impregnated samples prepared from the same synthesized SBA-15 batch will be compared to Ni-loaded samples prepared on several available commercial silica-based supports, having different textural and morphological properties. This comparison includes the evaluation of the physico-chemical properties of the samples and their activity and selectivity in dry reforming of methane. In the last part of the chapter, an amelioration of the SBA-15 synthesis by the application of a hydrothermal treatment will be considered. Perspectives will concern further possible modifications of the synthesis of Ni-based SBA-15 catalysts.

For clear comparison between samples, an intermediate nickel loading of 5 wt% was fixed for the rest of the study. Furthermore, in order to be more realistic and study the catalysts under more severe conditions (closer to industrial conditions), the dry reforming stability tests were performed at 650°C.

The same methodology as that used in the previous chapter is adopted here for samples description. Thus, in each section, the characterization results of the calcined samples are first presented, based on experimental data that are concisely grouped in one figure that includes the $N_2$ sorption isotherms of the supports (solid lines) and their corresponding impregnated samples (dashed lines) in addition to the TPR profiles and XRD patterns. The related quantitative values are reported in tables in which grey lines correspond to data of the supports. Next the results obtained during the methane dry reforming reaction are presented and discussed.

## IV.1 Comparison between small and larger SBA-15 syntheses

In the previous chapter, the SBA-$A_1$ and SBA-$A_2$ supports were prepared on small scale using a 250 ml beaker (Fig. II-1A) and simple manual techniques for the addition of TEOS (with a burette). The larger scale preparation of **SBA-$A_3$**, using a 4L double-jacketed reactor (Fig. II-1B), was achieved by multiplying the reactants proportions by 14. The addition of TEOS, in this case, was performed at a rate of 15 $ml.min^{-1}$ using a peristaltic pump and stirring was fixed at 120 rpm. The obtained batch was not subjected to hydrothermal treatment and was thus directly calcined after filtration. At this stage, it is important to make sure that the larger synthesis maintains the same textural properties as the smaller one. The comparison in this part will be limited to the SBA-$A_1$ support which was impregnated with Ni, since the SBA-$A_2$ support was also impregnated with Ce which is not in the scope of this chapter.

The textural porosity is one of the most important properties to evaluate. The $N_2$ sorption isotherms of SBA-$A_1$ (small synthesis) and SBA-$A_3$ (large synthesis) supports (Fig. IV-1a,b) present a type IV(a) isotherm with a hysteresis loop at $P/P_0$ between 0.04 and 0.06, typical of mesoporous structures. Interestingly, both supports have similar surface areas in the range of 450-500 $m^2.g^{-1}$ (Table IV-1), and comparable mesoporous surface areas (290-330 $m^2.g^{-1}$). The higher microporous area (Table IV-1) on SBA-$A_3$ indicates that the mesopores are connected with more micropores in this case. In addition, smaller pore diameters, and consequently lower pore volumes, are observed in SBA-$A_3$ in comparison to SBA-$A_1$. However, slightly different shapes of hysteresis loops are

observed between both supports. In fact, it is known that parallel adsorption and desorption branches reflect narrow range of uniform cylindrical mesopores.[1] Thus, different arrangement of mesopores are detected on the two supports. These variances can be due to: 1) TEOS rate and way of addition and 2) absence of an applied condensation hydrothermal treatment, as already discussed in the previous chapter.

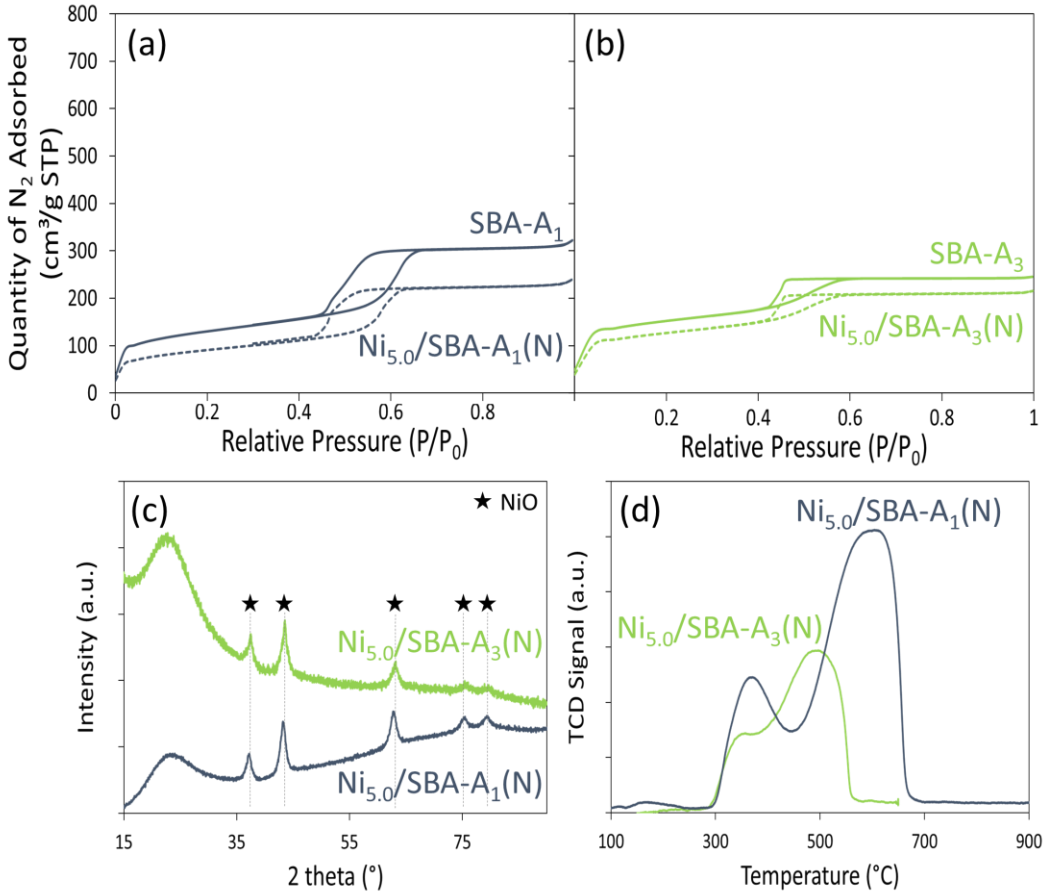


Figure IV-1: (a, b) $N_2$ sorption isotherms of SBA-$A_1$, SBA-$A_3$ and their impregnated samples, (c) X-ray diffractograms and (d) TPR profiles of calcined $Ni_{5.0}$/SBA-$A_1$(N) and $Ni_{5.0}$/SBA-$A_3$(N) samples

The impregnation of 5 wt% nickel by two solvents method on the two supports did not change the mesoporous structure of the resulting samples. Despite the fact that more important decline in surface area and pore volume is observed after addition of Ni on SBA-$A_1$ (Fig IV-1a), very similar textural properties were still observed on both $Ni_{5.0}$/SBA-$A_1$(N) and $Ni_{5.0}$/SBA-$A_3$(N) samples. Thus, the extrapolation of the support preparation scale does not significantly affect the resulting porosity.

Table IV-1: Characteristics of calcined samples prepared at different scales

| Sample Name | Total Surface area ($m^2.g^{-1}$) | Meso-porous area ($m^2.g^{-1}$) | Micro-porous area ($m^2.g^{-1}$) | Pore volume ($cm^3.g^{-1}$) | Mean des. Pore size (nm) | NiO Size[a] (nm) | TPR (% of total area) | |
|---|---|---|---|---|---|---|---|---|
| | | | | | | | 250-450 °C | 450-700 °C |
| SBA-$A_1$ | 455 | 326 | 129 | 0.51 | 4.2 | - | - | - |
| $Ni_{5.0}$/SBA-$A_1$(N) | 320 | 249 | 71 | 0.38 | 4.0 | 5 | 25 | 75 |
| SBA-$A_3$ | 522 | 290 | 232 | 0.35 | 3.5 | - | - | - |
| $Ni_{5.0}$/SBA-$A_3$(N) | 436 | 262 | 174 | 0.30 | 3.6 | 6.2 | 25 | 75 |

[a]Calculated from XRD, using Scherrer equation

With respect to the nature and size of the particles obtained on SBA-$A_3$, the XRD patterns confirm the formation of NiO nickel oxides (Fig. IV-1c). Based on the Scherrer equation, these nanoparticles are estimated to be in the range of 5-6 nm, as already observed on calcined $Ni_{5.0}$/SBA-$A_1$(N) (Fig IV-1c and Table IV-1). Therefore, the dispersion of NiO nanoparticles is not greatly affected by the different supports preparation scales and experimental conditions (in particular the way of adding TEOS, either manually or automatically).

Furthermore, the reduction of the calcined $Ni_{5.0}$/SBA-$A_3$(N) sample under 5% $H_2$/Ar is in accordance with that of the $Ni_{5.0}$/SBA-$A_1$(N) sample. Indeed, two main reduction peaks are observed on both profiles (Fig. IV-1d); the first one in the temperature range of 250-450°C and the second between 450 and 700°C. Interestingly, the relative quantification of the two peaks is identical on both samples (Table IV-1). This means that the reduction behavior of nickel oxides into metallic nickel is also not modified.

Accordingly, we can conclude that the extrapolation of the SBA-15 synthesis scale maintains comparable physico-chemical properties as the one prepared on smaller scale. Next, it would have been important to compare the catalytic activity of both samples. However, the catalytic tests performed on $Ni_{5.0}$/SBA-$A_1$(N) were conducted in a U-shaped fixed bed quartz reactor using diluted test conditions ($CH_4$:$CO_2$:Ar = 1:1:98) that were no longer applied (and no longer available) in the present chapter. Indeed, in parallel with the larger scale synthesis, the MAR catalytic reactor was mounted, as described in section II.3, to replace the previous installation and

allow handling the test in more severe catalytic conditions. Since the diluted conditions previously employed were hard to apply on the MAR catalytic reactor, it was unfortunately not possible to compare the activity of the $Ni_{5.0}$/SBA-$A_1$(N) and $Ni_{5.0}$/SBA-$A_3$(N) catalysts under the same operating conditions in methane dry reforming test. From their comparable physicochemical properties, we can nevertheless assume that their performances are similar.

Summary of section IV.1: Comparison between small and larger SBA-15 syntheses

- The extrapolation of the SBA-15 preparation quantity from small scale (SBA-$A_1$) to larger scale (SBA-$A_3$) maintains comparable textural properties, as well as nickel oxide dispersion and reducibility behavior of impregnated samples similar as the ones of samples prepared on the small scale synthesized support.
- The comparison of catalytic activity in dry reforming of methane was unfortunately impossible, due to a technical problem (replacement of the reactor at the time of the experiments).

## IV.2 Comparison between synthesized SBA-$A_3$ and commercial supports

Once the extrapolation validated, the properties of the prepared **SBA-$A_3$** support of bimodal porosity (connected mesopores and micropores) are compared to easily accessible commercial silica-based supports with different textural properties, as previously introduced in section II.1:

- **com-SBA-15** (a commercial mesoporous SBA-15 support) used as a reference
- Non-porous **$SiO_2$** used to check the effect of textural porosity
- **meso-$SiO_2$** used to study the effect of grain morphology (spherical grains)

These different supports were impregnated with 5 wt% nickel using either two solvents or incipient wetness impregnation methods (Table II-3).

### IV.2.1 Porosity of calcined samples

The $N_2$ sorption isotherms of SBA-$A_3$ and $Ni_{5.0}$/SBA-$A_3$(N) (previously shown) are reported in comparison to those of the commercial supports and their impregnated samples (Fig. IV-2a-d and

Table IV-2). Table IV-2 also reports the values of four additional samples that will be discussed in the following section.

The SBA-$A_3$, meso-$SiO_2$ and com-SBA-15 supports and their equivalent impregnated samples present a typical type IV(a) isotherm, characteristic of mesoporous materials while both the $SiO_2$ support and the $Ni_{5.0}/SiO_2$(N) sample display, as expected, typical isotherms of nonporous or macroporous solids (Fig. IV-2b). However, it appears that synthesized SBA-$A_3$ is less porous than the commercial mesoporous supports. Its surface area (522 $m^2.g^{-1}$) is situated between that of non-porous $SiO_2$ (239 $m^2.g^{-1}$) and the ones of com-SBA-15 (701 $m^2.g^{-1}$) and meso-$SiO_2$ (980 $m^2.g^{-1}$). In addition, among these porous samples, the SBA-$A_3$ support and the $Ni_{5.0}$/SBA-$A_3$(N) sample present the smallest pore volumes with pore widths in the range of 3.4-3.5 nm while the mean pore diameters are significantly larger on com-SBA-15 support and $Ni_{5.0}$/com-SBA-15 sample (around 6.5-6.7 nm).

Table IV-2: Textural properties of the calcined samples

| **Sample Name** | **Total Surface area ($m^2.g^{-1}$)** | **Meso-porous area ($m^2.g^{-1}$)** | **Micro-porous area ($m^2.g^{-1}$)** | **Pore volume ($cm^3.g^{-1}$)** | **Mean ads. Pore size (nm)** | **Mean des. Pore size (nm)** |
|---|---|---|---|---|---|---|
| SBA-$A_3$ | 522 | 290 | 232 | 0.35 | 3.4 | 3.5 |
| $Ni_{5.0}$/SBA-$A_3$(N) * | 436 | 262 | 174 | 0.30 | 3.5 | 3.6 |
| $SiO_2$ | 239 | - | - | - | - | - |
| $Ni_{5.0}/SiO_2$(N) ** | 247 | - | - | - | - | - |
| meso-$SiO_2$ | 980 | 966 | 14 | 1.19 | 3.4 | 4.0 |
| $Ni_{5.0}$/meso-$SiO_2$(N) * | 779 | 739 | 40 | 0.93 | 3.3 | 3.8 |
| com-SBA-15 | 701 | 640 | 61 | 1.04 | 6.7 | 6.6 |
| $Ni_{5.0}$/com-SBA-15(N) * | 529 | 480 | 49 | 0.75 | 6.5 | 6.3 |
| SBA-$B_1$ | 832 | 678 | 154 | 0.97 | 6.4 | 6.0 |
| $Ni_{5.0}$/SBA-$B_1$(N)* | 620 | 551 | 69 | 0.71 | 5.7 | 5.5 |
| SBA-$B_2$ | 915 | 750 | 165 | 1.04 | 6.4 | 6.2 |
| $Ni_{5.0}$/SBA-$B_2$(N)* | 706 | 556 | 150 | 0.80 | 6.3 | 6.0 |

* Prepared by two solvents impregnation
** Prepared by incipient wetness impregnation

Furthermore, the shape of the hysteresis loop is not the same for all mesoporous samples. On one hand, SBA-$A_3$, $Ni_{5.0}$/SBA-$A_3$(N) (Fig. IV-2a), meso-$SiO_2$ and $Ni_{5.0}$/meso-$SiO_2$(N) (Fig. IV-2c) show type H2(a) hysteresis loop that is usually obtained in the case of pore-blocking/percolation in a narrow range of pore necks or in the case of cavitation-induced evaporation.[1,2] The absence of parallel adsorption and desorption branches in the hysteresis loops of these samples indicates the absence of cylindrical uniform mesopores. The $Ni_{5.0}$/SBA-$A_3$(N) and $Ni_{5.0}$/meso-$SiO_2$(N) are thus characterized by a poor porosity. On the other hand, both com-SBA-15 and $Ni_{5.0}$/com-SBA-15(N) samples present a type H1 hysteresis loop (Fig. IV-2d), indicating narrow distribution of uniform mesopores or of ink-bottle pores. In spite of these differences, the trend is similar on all mesoporous samples upon addition of nickel oxide, with a decrease in surface area, pore volume and mean pore diameter (Fig. IV-2a,b,c,d and Table IV-2), indicative of either metal deposition inside the pores or partial pore plugging, as already discussed in the previous chapter.

## IV.2.2 Size, dispersion and reducibility of supported nanoparticles

The different textural properties of calcined samples appear to influence the nickel nanoparticles size and dispersion, as revealed by XRD measurements (Fig. IV-2e). As in chapter III, all diffractograms are composed of a broad signal at around 22° corresponding to X-rays diffusion by amorphous silica walls and of narrower diffractions peaks at 37, 43, 63, 75 and 79° attributed to nickel oxide nanoparticles (ICDD 78-4374) compatible with a rhombohedral crystal system (R-3m).

The width of these diffractions peaks and their overall intensities significantly vary from one sample to another, indicating that the mean size of nickel oxide nanoparticles is not identical on all supports (Fig. IV-2e and Table IV-3). From the FWHM analysis of the most intense diffraction peak at 43°, the average size of the NiO crystallographic domains increases in the following order: $Ni_{5.0}$/meso-$SiO_2$(N) (3.6 nm) < $Ni_{5.0}$/com-SBA-15(N) (3.9 nm) < $Ni_{5.0}$/SBA-$A_3$(N) (6.2 nm) < $Ni_{5.0}$/$SiO_2$(N) (9 nm). This increasing order is in accordance with the decrease in surface area of the supports. Thus, among the porous supports, the higher dispersion on meso-$SiO_2$ in comparison to com-SBA-15 is due to the higher surface area of the former and its smaller pore diameters. Despite the comparable pore diameters of SBA-$A_3$ and meso-$SiO_2$, the lower dispersion achieved on the former is in line with its lower surface area. The absence of mesoporous structure on the non-porous $SiO_2$ support results in the poorest dispersion.

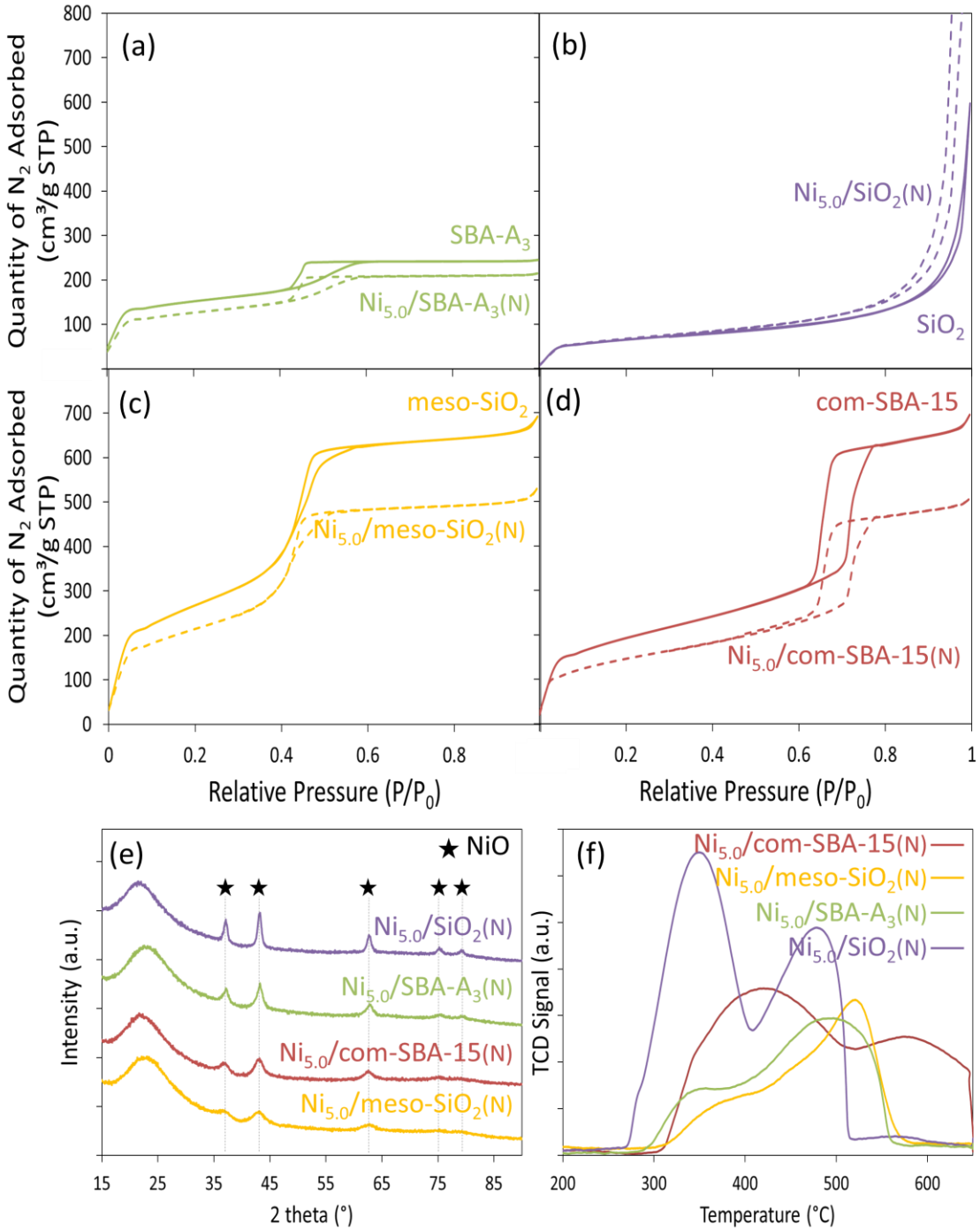


Figure IV-2: (a, b, c, d) $N_2$ sorption isotherms for the calcined supports and impregnated samples, (e) X-ray diffractograms and (f) TPR profiles of calcined impregnated samples

Table IV-3: Mean particles size for calcined, reduced and spent samples

| Sample name | NiO size (nm) | $Ni^0$ size Reduced (nm) | $Ni^0$ size Spent (nm) |
|---|---|---|---|
| $Ni_{5.0}/SBA\text{-}A_3(N)$ | 6.2 | - | - |
| $Ni_{5.0}/SiO_2(N)$ | 9.0 | - | 7.6 |
| $Ni_{5.0}/meso\text{-}SiO_2(N)$ | 3.6 | - | 7.7* |
| $Ni_{5.0}/com\text{-}SBA\text{-}15(N)$ | 3.9 | 3.8 | 4.3 |
| $Ni_{5.0}/SBA\text{-}B_1(N)$ | 6.0 | 6.4 | 6.3 |
| $Ni_{5.0}/SBA\text{-}B_2(N)$ | 6.4 | 5.7 | 5.5 |

* Estimated from TEM images

The lower NiO dispersion on SBA-$A_3$ in comparison to the remaining mesoporous supports is further depicted on the TEM images of the calcined supports (Fig. IV-3). First, the $Ni_{5.0}/SBA\text{-}A_3(N)$ sample appears to be composed of linked elongated grains of about 700-800 nm width (Fig. IV-3a). Second, external particles appear on the outer surface of the SBA-$A_3$ support (Fig. IV-3a) in addition to very small particles that can be dispersed either inside the channels or on the surface. In fact, the alignment of these small nanoparticles along the channels of the support allows us to confirm their internal presence inside the pores (Fig. IV-3a'). The evaluation obtained by TEM is thus compatible with the one obtained by XRD and validates the average particle size of 6.2 nm estimated by XRD. Indeed, the presence of micropores connecting the mesopores in SBA-$A_3$ (support synthezised without hydrothermal treatment) can cause particles diffusion to the external surface, throughout the various thermal treatments applied.

On the mesoporous com-SBA-15 and meso-$SiO_2$ supports, the high dispersion of nickel oxides is validated by the presence of very small particles homogeneously distributed inside the grains of the support (Fig. IV-3b',c'). However, these grains do not show the same morphology because the $Ni_{5.0}/com\text{-}SBA\text{-}15(N)$ support appears to be formed of elongated grains of 700-800 nm in length and 500-600 nm in width (Fig. IV-3b) while the meso-$SiO_2$ support is composed of spherical grains of 200-300 nm in diameter (Fig. IV-3c). The last TEM image (Fig. IV-3d) reveals the amorphous aspect of the $Ni_{5.0}/SiO_2(N)$ sample without any well-defined shape and validates the formation of large NiO nanoparticles (Fig. IV-3d'), as also viewed by XRD (Table IV-3).

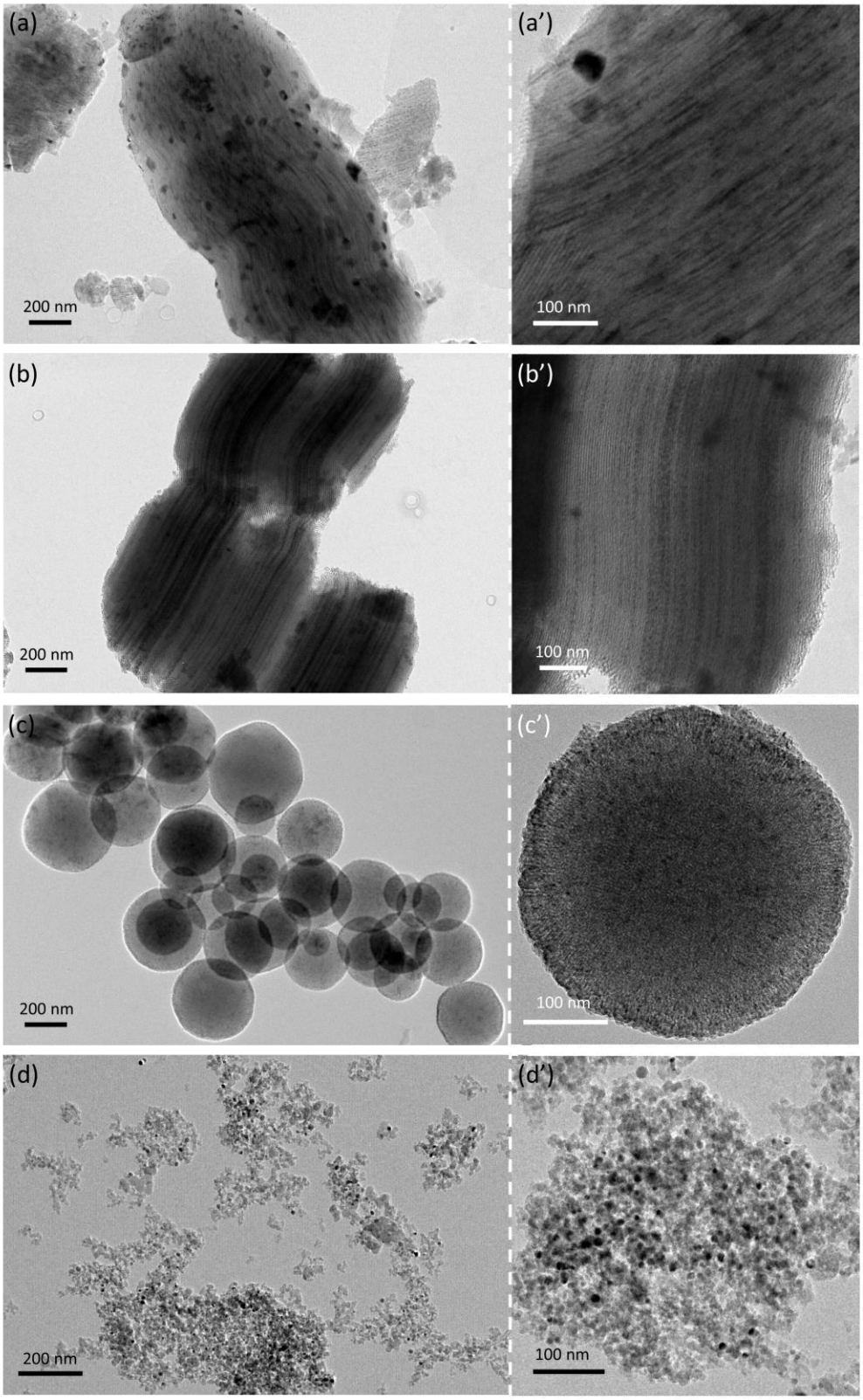


Figure IV-3: TEM images of (a,a') $Ni_{5.0}$/SBA-$A_3$(N), (b,b') $Ni_{5.0}$/com-SBA-15(N), (c,c') $Ni_{5.0}$/meso-$SiO_2$(N) and (d,d') $Ni_{5.0}$/$SiO_2$(N) calcined samples

Furthermore, these differences in NiO dispersion, observed by XRD and TEM, on the various supports result in different reducibility behaviors during $H_2$-TPR (Fig. IV-2f). Although the four samples show two main reduction peaks, these peaks are centered at different temperatures. The reducibility of nickel oxides on the non-porous $SiO_2$ support is achieved upon reaching 500°C while the signal is shifted towards higher values for nickel oxides on the mesoporous supports. This is probably due to the presence of nickel oxide nanoparticles inside the channels of the mesoporous supports. $Ni_{5.0}$/com-SBA-15(N) is the only sample that shows a reduction peak centered at around 600°C, which suggest the formation of Ni species in stronger interaction with silica like surface Ni-silicate.[3]

Summary of section IV.2.1 and IV.2.2: Physico-chemical properties of Ni-based samples supported on synthesized SBA-$A_3$ and on commercial supports

- The mesoporous SBA-$A_3$ support (with connected mesopores) synthesized without hydrothermal treatment is less porous than the remaining mesoporous commercial supports and this remains valid for the impregnated samples.
- The different textural properties of the supports significantly affect the dispersion and reducibility of the NiO nanoparticles. The main observations are as follow:
  - $Ni_{5.0}$/SBA-$A_3$(N): mesoporous sample, elongated grains, NiO = 6.2 nm
  - $Ni_{5.0}$/$SiO_2$(N): nonporous/macropous sample, NiO = 9 nm
  - $Ni_{5.0}$/com-SBA-15(N): mesoporous sample, elongated grains, NiO = 3.9 nm
  - $Ni_{5.0}$/meso-$SiO_2$(N): mesoporous sample, spherical grains, NiO = 3.6 nm

### IV.2.3 Catalytic activity and stability

To check the influence of these different textural properties (and consequent changes in Ni dispersion) on the catalytic performance of the samples, the dry reforming tests were performed as detailed in section II.3. Briefly, 100 mg of powder was positioned inside the tubular fixed bed reactor of the recently installed MAR microactivity reactor. After *in-situ* reduction of the sample at 650°C for 2 hours, as before, the temperature is cooled down to 200°C and the reactants are introduced. The dilution of the reactants feed was set to $CH_4$:$CO_2$:Ar = 5:5:90 (lower dilution than before) and the gas hourly space velocity (GHSV) was fixed at 36 $L.g^{-1}.h^{-1}$ for practical reasons.

The evolution of $CH_4$ and $CO_2$ conversions as well as the $H_2$:CO molar ratio are followed while increasing the temperature from 200 up to 800°C (Figure IV-4A,B,C). The thermodynamic curves, used for comparison, are adapted to the new dilution ratio employed, as previously discussed in section II.4.1. No major differences between samples are revealed during the catalytic activity measurements. The increment in both reactants conversions and $H_2$:CO ratios follows the same trend as the thermodynamic equilibrium curves (dashed lines on the figure) expected under the used conditions. These equilibrium curves correspond to the simulation of the main methane dry reforming reaction with the simultaneous reverse water gas shift, without considering carbon deposition. The differences between the experimental results and simulated ones might be due to the occurrence of side reactions (Boudouard reaction or methane decomposition). Also, heat and mass transfer could play a role, as already suggested in the previous chapter, since the measurements are done in dynamic mode, without waiting for temperature stabilization. In addition, the $H_2$:CO also increases with the increase of temperature (Figure IV-4C). At low temperature values, the reaction does not take place and no products are formed; consequently, the $H_2$:CO molar ratio becomes significant only after the increase of reactants conversions. At high temperatures, the increase of the $H_2$:CO molar ratio beyond the equilibrium values can be explained by a higher quantity of $H_2$ formed due to methane decomposition ($CH_4 \rightarrow 2H_2 + C$).

From these data, it is concluded again, as in the last chapter, that thermodynamic equilibrium is reached under the used reaction conditions. Despite this, the behavior during catalytic stability after decreasing the temperature and maintaining it at 650°C is no longer the same (Fig. IV-4A',B',C'). First, higher levels of conversions at stable state are achieved on both mesoporous $Ni_{5.0}$/SBA-$A_3$(N) and $Ni_{5.0}$/com-SBA-15(N) catalysts in comparison to non-porous $Ni_{5.0}/SiO_2$(N) on which conversion decrease takes place (purple curves). This agrees with the fact that large metal particles were formed on the surface when non-porous $SiO_2$ was used as support, leading to poorer active phase dispersion. This result reveals the important influence of the mesoporous structure towards catalytic activity and stability, in agreement with other published work on this subject.[4,5,6] As reported, the mesoporous structure enhances metal dispersion and mainly limits metal growth up to the pore size, thus preventing the sintering effect of the high temperature employed during the test.

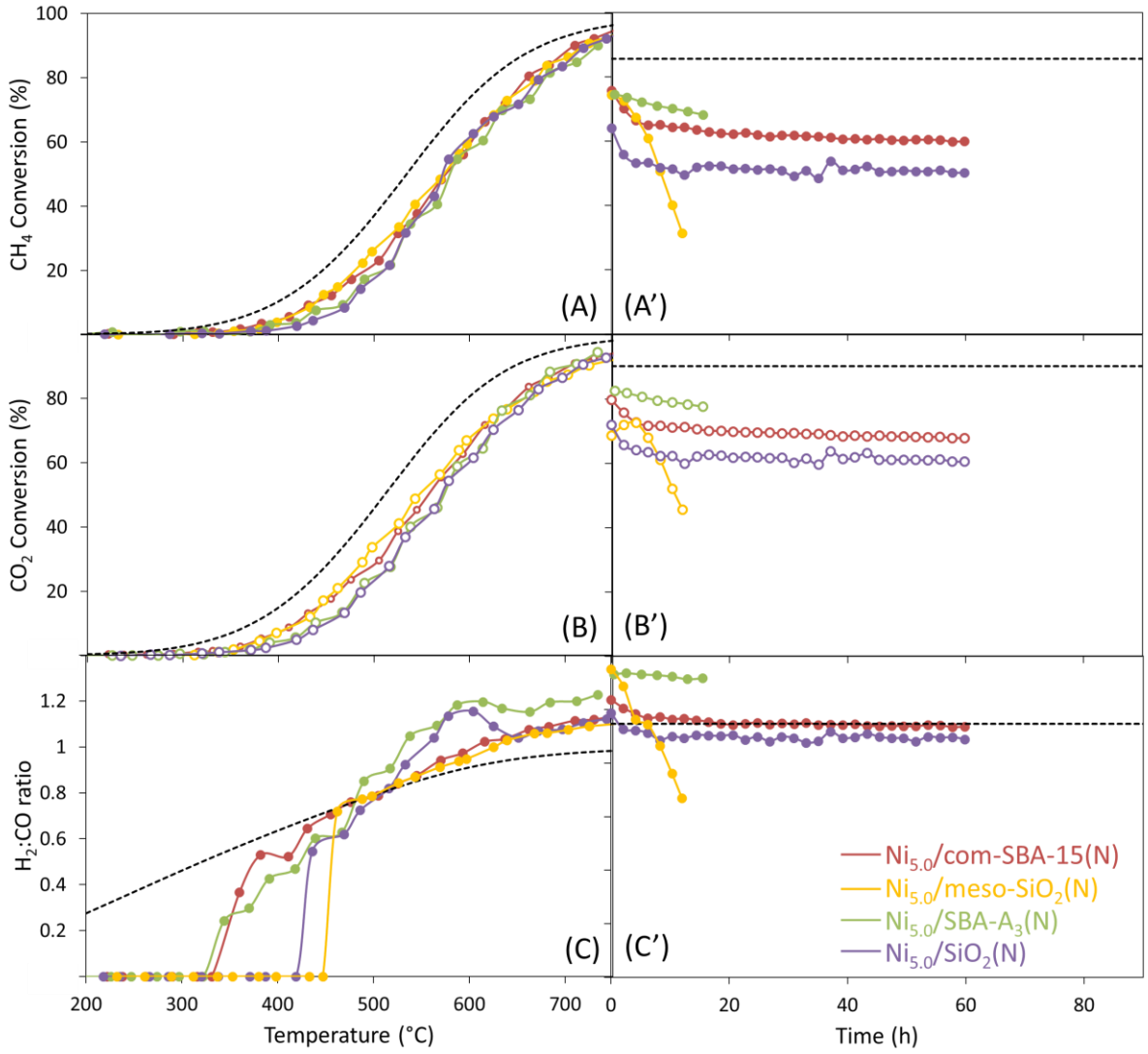


Figure IV-4: Evolution of (A,A') $CH_4$ conversion, (B,B')$CO_2$ conversion and (C,C') $H_2$:CO ratio as a function of temperature (A,B,C) and time at 650°C (A',B',C')at 1bar, 36 $L.g^{-1}.h^{-1}$ and $CH_4$:$CO_2$:Ar = 5:5:90 (dashed lines represent thermodynamic data under the used conditions)

Second, the conversions over $Ni_{5.0}$/SBA-$A_3$(N) are slightly higher than those over $Ni_{5.0}$/com-SBA-15(N) while, on the contrary, the $H_2$:CO ratio is closer to the equilibrium value on $Ni_{5.0}$/com-SBA-15(N). These data reveal the higher selectivity of $Ni_{5.0}$/com-SBA-15(N) catalyst towards the main dry reforming reaction and the occurrence of side reactions (RWGS and methane decomposition) on $Ni_{5.0}$/SBA-$A_3$(N) that increase the $H_2$:CO ratio. This is in agreement with the SEM/TEM images of the spent catalysts (Fig. IV-5) that show important carbon deposition on $Ni_{5.0}$/SBA-$A_3$(N) catalyst (Fig. IV-5a). In opposition, no carbon deposition is seen on the spent $Ni_{5.0}$/com-SBA-

15(N) catalyst (Fig. IV-5b) on which good dispersion of the active sites is maintained inside the uniform mesoporous arrangement.

Third, severe deactivation is observed on the mesoporous $Ni_{5.0}$/meso-$SiO_2$(N) catalyst (with less ordered mesoporous structure) during the test during 12 hours, with a decrease from 75 to 30% and from 70 to 45% for $CH_4$ and $CO_2$ conversions, respectively. The $CO_2$ conversion increased during the first few hours of the stability test prior to a drastic decrease. This is associated to the occurrence of reverse water gas shift reaction ($CO_2 + H_2 \rightarrow CO + H_2O$) on this sample, as also reflected by the $H_2$:CO ratio greater than one in the first 5 hours of the stability test. Furthermore, in view of the TEM images of spent $Ni_{5.0}$/meso-$SiO_2$(N) (Fig. IV-5c), an increase of the metal particles size is observed (Table IV-3). The dispersion of these particles on the meso-$SiO_2$ support is also altered since many particles are observed on the external surface of the grains. This implies a migration of the metallic nickel particles to the outer surface of the meso-$SiO_2$ support, during either the reduction or the reaction steps. The presence of short pores in the spherical grains in this case could have caused this $Ni^0$ metal expulsion. More importantly, the mesoporous structure which is not well organized on this sample further contributed in the lower stability of the nickel nanoparticles inside the pores. Once outside the silica pores, the nickel particles are easily subjected to high carbon deposition (Fig. IV-5c), hindering the accessibility of reactants to these active sites and causing deactivation. These data correlate with the quick decline in conversions and rapid deactivation observed on this catalyst. Further details on carbon deposition will be thoroughly provided in Chapter VI.

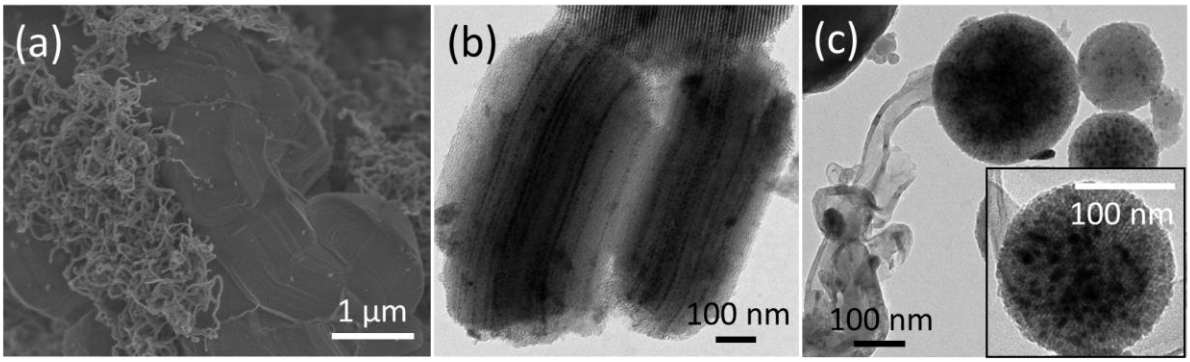


Figure IV-5: (a) SEM image of spent $Ni_{5.0}$/SBA-$A_3$(N) and TEM images of spent (b) $Ni_{5.0}$/com-SBA-15(N) and (c) $Ni_{5.0}$/meso-$SiO_2$(N)

Consequently, it appears that a well-defined mesoporous structure, having high surface area and narrow pore size distribution, is essential to obtain superior catalytic activity. This structure allows good confinement of nickel nanoparticles inside the pores, preventing their sintering and blocking carbon deposition on their surface. Nevertheless, the morphology of silica grains forming the support also plays an important role in the catalytic stability. While spherical grains tend to facilitate the expulsion of the metallic particles to the external surface of the support, elongated grains permit their better confinement and occlusion inside the channels, as in com-SBA-15 support. However, such a commercial catalyst is expensive and is not adequate for industrial use. Therefore, in the next part, an improvement of the SBA-15 batch prepared in the lab through hydrothermal treatment will be evaluated and compared to the best commercial catalyst seen.

Summary of section IV.2.3: Catalytic performance of the catalysts

- A well-defined mesoporous structure is necessary for a superior catalytic activity.
- The short pores in spherical grains and their less organized mesoporous structure reduced the stability and confinement of nickel particles inside the pores and caused rapid catalyst deactivation.
- Among the studied supports, the com-SBA-15, with the highest surface area and pore volume compared to SBA-A syntheses, appears to be most suitable for the dry reforming reaction under the experimental conditions employed.

## IV.3 Improvement of the synthesized SBA-15 support

The previous part showed the superior activity, stability and selectivity of highly dispersed nickel supported on commercial SBA-15 catalyst. Furthermore, the size of the silica grain seemed to affect the stability of the catalysts. Therefore, in this part, we will try to improve the SBA-15 synthesis, by applying a hydrothermal treatment during the preparation, to obtain an enhanced catalytic activity and selectivity. For this purpose, two SBA-15 silica supports are prepared:

- the **SBA-B$_1$**, hydrothermally treated at 95°C in order to obtain different diameters of mesopores and different pore connections than the SBA-A$_3$,
- the **SBA-B$_2$**, prepared similarly to SBA-B$_1$ but under less acidic conditions, to obtain more elongated silica grains, as already observed in previous studies within the group (PhD

thesis of N. El Hassan, UPMC, 2008). The last suggestion might either provide improved contact time between reactants and active phase, leading to higher catalytic performance or lower accessibility to the active sites, leading to lower performance.

To facilitate comparisons, the data of com-SBA-15 and $Ni_{5.0}$/com-SBA-15(N) samples (same as in the previous part) are reported again on the figures.

### IV.3.1 Physico-chemical properties of the samples

The porosity of the resulting samples was first analyzed by $N_2$ sorption (Fig. IV-6). Similar to com-SBA-15 and $Ni_{5.0}$/com-SBA-15(N) (Fig. IV-6a), the synthesized SBA-$B_1$ and SBA-$B_2$ supports and their impregnated samples (Fig. IV-6b and c) present a type IV(a) isotherm with a type H1 hysteresis loop, characteristic of well-ordered mesoporous structure. As expected, the application of a hydrothermal treatment during preparation of the SBA-B supports generated higher surface areas (700-900 $m^2.g^{-1}$) and pore volumes (0.7-1 $cm^3.g^{-1}$) compared to the samples of the previous SBA-A series (obtained without hydrothermal treatment step). These values decreased upon addition of nickel oxide (Table IV-2), the tailing at relative pressures between 0.6 and 0.4 being more pronounced on $Ni_{5.0}$/SBA-$B_2$(N) than on $Ni_{5.0}$/SBA-$B_1$(N). This can be associated to pore structures containing both open and partially blocked mesopores, as recently reported in the updated IUPAC report.[1,2] While no details are provided about the synthesis of the commercial SBA-15, it appears that this sample has the lowest microporosity in comparison to $Ni_{5.0}$/SBA-$B_1$(N) and $Ni_{5.0}$/SBA-$B_2$(N), suggesting the presence of more connections between mesopores on the latter.

The wide angle XRD patterns obtained for the calcined samples (Figure IV-6d) show again the contributions at 37, 43, 63, 75 and 79° typical of nickel oxide nanoparticles (ICDD 78-4374). Regardless of the similar textural properties, the dispersion of nickel oxides and metallic nickel particles varied depending on the support. Slightly larger NiO particles are formed on both $Ni_{5.0}$/SBA-$B_1$(N) and $Ni_{5.0}$/SBA-$B_2$(N) samples (Table IV-3) in comparison to those on $Ni_{5.0}$/com-SBA-15(N) sample. This remains also valid for the $Ni^0$ metallic nanoparticles (ICDD 65-0380), detected on the reduced samples (Figure IV-6e) with characteristic diffraction peaks at 44, 52 and 76°, attributable to a face-centered cubic lattice (Fm-3m). The lower microporous connections

between the mesopores on $Ni_{5.0}$/com-SBA-15(N) could have contributed in better occlusion of the nickel nanoparticles and in prevention of their migration or movement inside the pores.

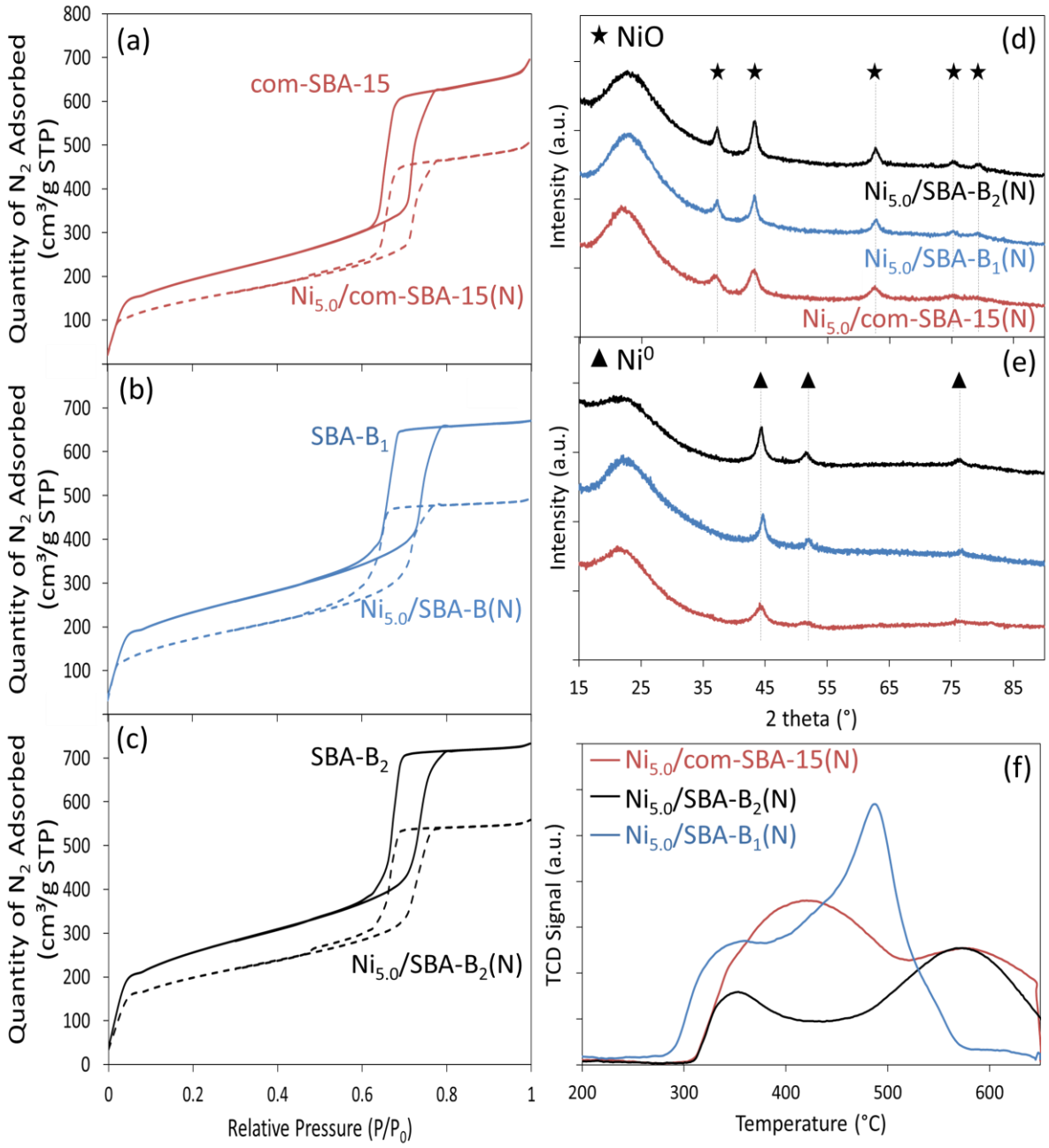


Figure IV-6: (a, b, c) $N_2$ sorption isotherms for calcined samples, X-ray diffractograms of (d) calcined and (e) reduced samples and (f) TPR profiles of calcined impregnated samples

Furthermore, the reducibility of nickel oxides on the SBA-15 supports also takes place in two main reduction peaks (Figure IV-6f). The first peak is at around 350-400°C for all samples while the second peak is centered near 500°C for $Ni_{5.0}$/SBA-$B_1$(N) and delayed to 600°C for both $Ni_{5.0}$/SBA-$B_2$(N) and $Ni_{5.0}$/com-SBA-15 samples. The higher reduction temperature can suggest higher metal-support interaction; however, all nickel oxide particles on $Ni_{5.0}$/SBA-$B_1$(N) appear to be reduced up to 650°C for 2 hours (conditions adopted for the catalytic test) while this is not the case on the remaining samples. Therefore, an easier reduction of nickel oxides can be proposed on $Ni_{5.0}$/SBA-$B_1$(N) sample compared to the remaining samples. The longer grains of $Ni_{5.0}$/SBA-$B_2$(N) sample could be the reason behind the retarded nickel oxide reduction on this sample.

### IV.3.2 Catalytic activity and stability

During catalytic testing in dry reforming of methane (Fig. IV-7), the activity of $Ni_{5.0}$/SBA-$B_1$(N) catalyst is identical to that of $Ni_{5.0}$/com-SBA-15(N) but is slightly better than that on $Ni_{5.0}$/SBA-$B_2$(N), especially at elevated temperatures. The lower performance of $Ni_{5.0}$/SBA-$B_2$(N) is more pronounced during the stability test. Indeed, lower reactants conversions and lower stability are observed on this sample after 20 hours. This can be related to the longer grains on $Ni_{5.0}$/SBA-$B_2$(N), which delayed the reduction of nickel oxides as shown above and affected the catalytic performance of this sample. More importantly, $Ni_{5.0}$/SBA-$B_1$(N) catalyst revealed higher conversions than those on $Ni_{5.0}$/com-SBA-15(N) catalyst; around 76 and 80% $CH_4$ and $CO_2$ conversions were respectively maintained for about 90 hours under stream at 650°C. These results suggest that nickel supported on synthesized SBA-B material can be as active as nickel supported on commercial SBA-15 and even more stable for long duration in dry reforming of methane. Despite that the preparation procedure for commercial SBA-15 is not known (data not provided by the supplier), the hydrothermally treated SBA-$B_1$ support appear to be very promising in such application. It is worth noting that during this PhD thesis, I contributed in a project consisting on the synthesis of three dimensional SBA-16 support containing micropores and cage like mesopores and its use to confine Ni nanoparticles for dry reforming of methane. The results further revealed the superior catalytic performance of Ni/SBA-B over Ni/SBA-16 catalysts.

Furthermore, it is interesting to recall that, on one hand, poorer performance was obtained when using meso-$SiO_2$ as support with spherical grain morphology and, on the other hand, lower conversions were attained when using SBA-$B_2$ support with longer silica grains. Consequently, it seems that there exists

a certain optimum for grain length above which the catalytic activity and stability are no longer enhanced. Experiments are still in progress in this direction. The TEM micrographs of the SBA-$B_2$ support and its impregnated sample will validate the shape of these grains and will allow better evaluation of the effect of grain length on the catalytic activity and stability.

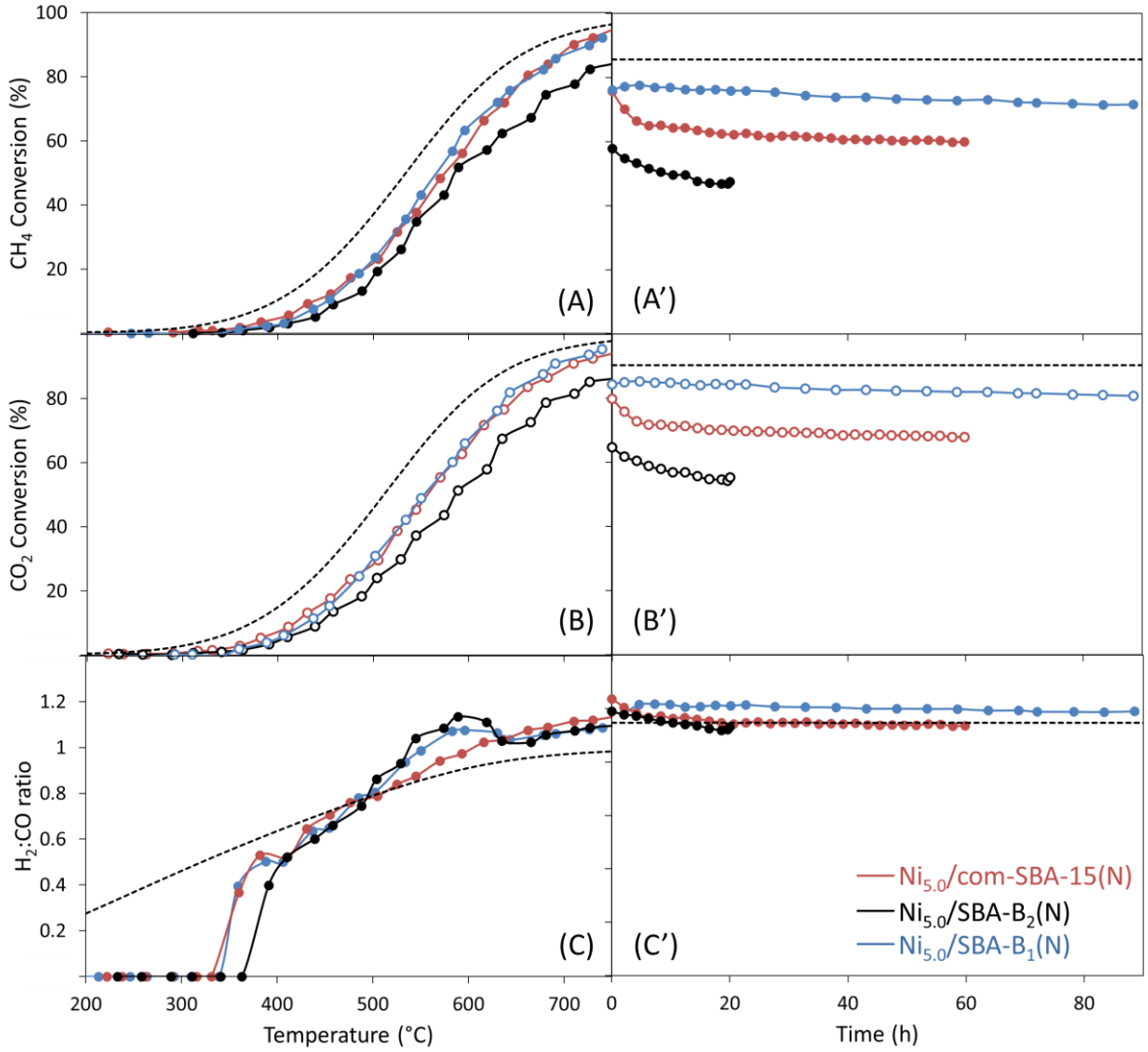


Figure IV-7: Variation of (A,A') $CH_4$ conversion, (B,B') $CO_2$ conversion and (C,C') $H_2$:CO ratio as a function of temperature (A,B,C) and time at 650°C (A',B',C') at 1bar, 36 $L.g^{-1}.h^{-1}$ and $CH_4$:$CO_2$:Ar = 5:5:90 (dashed lines represent thermodynamic data under the used conditions)

After test, the spent $Ni_{5.0}$/SBA-$B_1$(N) maintained good active phase dispersion, as seen by TEM (Fig. IV-8a). Some carbon deposition was detected only on the external particles of this sample

(Fig. IV-8b), in the form of carbon nanotubes having average diameters of about 20-30 nm. In opposition, much larger carbon nanotubes (average diameters of 40-50 nm) were observed on the surface of the spent $Ni_{5.0}$/meso-$SiO_2$(N) (Fig. IV-5c). Nickel oxide nanoparticles were much smaller on $Ni_{5.0}$/meso-$SiO_2$(N) (3.6 nm) than on $Ni_{5.0}$/SBA-$B_1$(N) sample (6.2 nm); nevertheless, carbon nanotubes appeared much thinner on $Ni_{5.0}$/SBA-$B_1$(N) than on $Ni_{5.0}$/meso-$SiO_2$ catalyst. Indeed, S. de Llobet et al. studied the effect of carbon morphology on catalyst deactivation in the decomposition of biogas using Ni, Co or Fe supported on $Al_2O_3$ catalysts.[7] They reported that the diameter of filamentous carbons depends on the diameter of nickel particles. Therefore, more particles sintering took place on $Ni_{5.0}$/meso-$SiO_2$(N) than on $Ni_{5.0}$/SBA-$B_1$(N). As mentioned earlier, carbon deposition will be discussed in more details in Chapter VI.

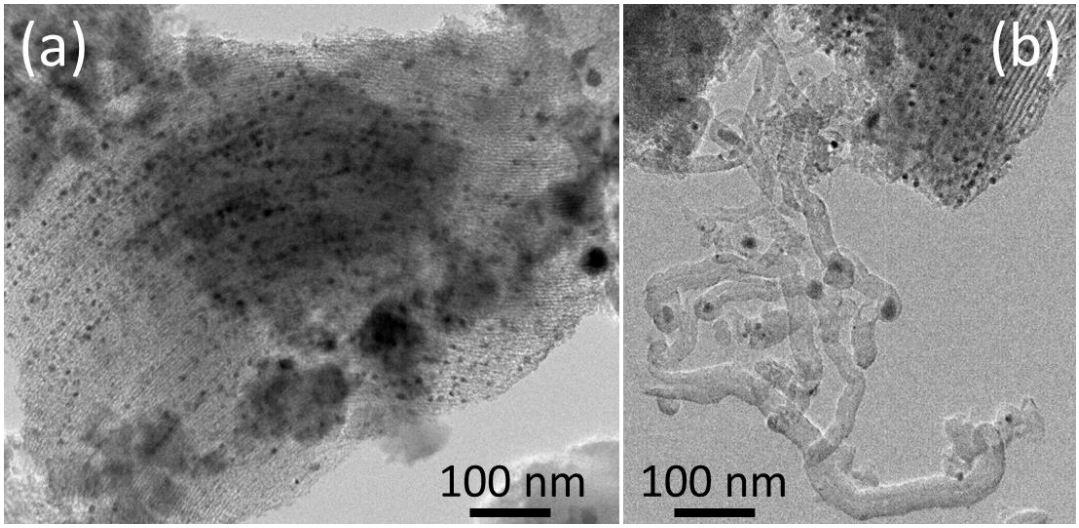


Figure IV-8: TEM images showing of spent (a,b) $Ni_{5.0}$/SBA-$B_1$(N) catalysts

### IV.3.3 Effect of hydrothermal treatment

The hydrothermal treatment applied to the SBA-15 support improved the textural properties of the support, which contributed in the enhancement of the catalytic performance. This improvement can be explained in view of the small-angle XRD results (Fig. IV-9) of the reduced $Ni_{5.0}$/SBA-$B_1$(N) and the $Ni_{5.0}$/SBA-$A_3$(N) samples. On the former, the three well-resolved diffraction peaks, indexed as (100), (110) and (200), are characteristic of the highly ordered p6mm hexagonal mesoporous structure.[8] On the $Ni_{5.0}$/SBA-$A_3$(N) reduced sample, the (110) and (200) diffraction

peaks are not detected while the (100) diffraction peak is shifted towards higher angles. This shift is reflected by a lower $d_{100}$ spacing of about 7.8 nm, in comparison to 9.3 nm in the case of $Ni_{5.0}$/SBA-$B_1$(N) sample. In addition, the (100) diffraction peak is much less intense on $Ni_{5.0}$/SBA-$A_3$(N) than on $Ni_{5.0}$/SBA-$B_1$(N), suggesting that the structure is much less developed without hydrothermal treatment. This is in agreement with previous reports showing that the hydrothermal treatment causes the formation of more condensed silica walls and larger pore diameters.[9,10,11] Consequently, the microporous area (connections between mesopores) is more important on $Ni_{5.0}$/SBA-$A_3$(N) than on $Ni_{5.0}$/SBA-$B_1$(N) (Table IV-2). Therefore, during thermal treatments (calcination, reduction…), external particles are easier to form on the surface of $Ni_{5.0}$/SBA-$A_3$(N), because of these microporous connections. These particles become thus more prone to carbon deposition due to lower metal-support interaction. Hence, the hydrothermal treatment is important because it increases the thermal stability of the support and ameliorates the confinement of nickel nanoparticles inside the pores, leading to higher catalytic activity during methane dry reforming.

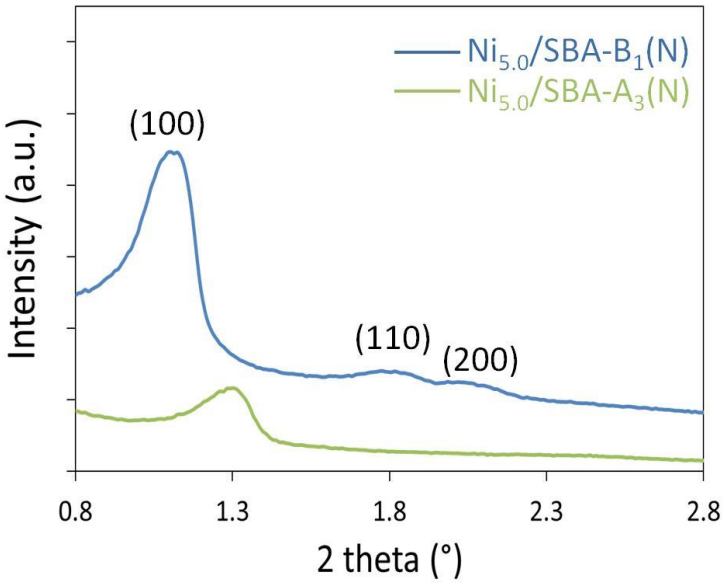


Figure IV-9: Small-angle XRD of reduced $Ni_{5.0}$/SBA-$B_1$(N) and $Ni_{5.0}$/SBA-$A_3$(N) samples

Summary of section IV.3: improvement of the SBA-15 synthesis

- The catalyst supported on synthesized SBA-$B_1$, hydrothermally treated at 95°C, can be as active as the one supported on commercial SBA-15 and even more stable for long duration in methane dry reforming.
- While elongated grains result in better stability than the spherical ones, an optimum grain length exists, above which the catalytic activity and stability are no longer enhanced. Further experiments are on-going in this direction to clarify this point.
- The hydrothermal treatment does not only improve the thermal stability of the support but also the occlusion of nickel nanoparticles inside the porosity.

## IV.4 Conclusion

The preparation of SBA-$A_3$ support at larger scale (14 times greater) maintained comparable textural properties as the SBA-$A_1$ prepared at small scale. However, the resulting SBA-$A_3$ support and impregnated sample were less porous than other mesoporous commercial supports. The differences in porosities on these supports resulted in different dispersions of the nickel active phase and consequently different catalytic behavior. Thus, not all commercial silica-based supports were efficient in order to obtain highly dispersed nickel nanoparticles.

The textural and morphological properties of the supports played an important role in the dispersion of nickel oxides, their reducibility into metallic nickel and the consequent catalytic performance in dry reforming of methane. It turned out that the porous structure is essential in order to maintain good active phase dispersion. The spherical grain morphology of meso-$SiO_2$ support and less ordered mesoporous structure reduced the stability of nickel nanoparticles inside the pores and facilitated their expulsion towards the external surface, leading to severe deactivation. Consequently, the highly organized mesoporous $Ni_{5.0}$/com-SBA-15(N) catalyst marked the highest activity and stability. However, for economic reasons, this catalyst cannot be commercialized.

The hydrothermal treatment at (95°C) applied to obtain SBA-$B_1$ improved the mesoporous structure of the support and resulted in higher surface areas. Thus comparable activity and even better stability were obtained when nickel was dispersed on SBA-$B_1$. The latter was highly stable at 650°C for more than 90 hours under reactants stream. Due to its large specific surface area and pore volume together with uniform and ordered mesopores distribution, the SBA-15 matrix

stabilizes the nickel nanoparticles inside the pores. The spatial restriction due the confinement effect blocks the nanoparticles inside the porous channels, thus inhibiting their sintering and limiting coke formation during reaction.

Nevertheless, additional ameliorations can still be experienced on the Ni/SBA-15 catalyst in an attempt to further limit carbon deposition and achieve even better durability in dry reforming of methane. These improvements can be carried out during preparation of the catalyst (like changing the nickel precursor salt, method of deposition, reduction…), as will be detailed in the following chapter.

**Outcome of this work:**

- K. Jabbour, **M.N. Kaydouh**, N. El Hassan, H. El Zakhem, S. Casale, P. Massiani, A. Davidson, IEEE conference paper
  DOI: 10.1109/MedGO.2015.7330318
- Participation in the 11th conference and exhibition of the Lebanese Industrial Research Achievements (LIRA) program, Lebanon 2014.
- An article regarding the effects of grain morphology and length of silica grains is under preparation.
- The results demonstrating the superior catalytic performance of Ni/SBA-15 over Ni/SBA-16 catalysts are under publication.

## IV.5 References

[1] M. Thommes, K. Kaneko, A.V. Neimark, J.P. Olivier, F. Rodriguez-Reinoso, J. Rouquerol, K.S.W. Sing, *Physisorption of gases, with special reference to the evaluation of surface area and pore size distribution (IUPAC Technical Report)*, Pure Applied Chemistry 87(9-10) (2015) 1051-1069.

[2] M. Ogura, R. Guillet-Nicolas, D. Brouri, S. Casale, J. Blanchard, K.A. Cychosz, M. Thommes, C. Thomas, *Insights into the accessibility of Zr in Zr/SBA-15 mesoporous silica supports with increasing Zr loadings*, Microporous and Mesoporous Materials 225 (2016) 440-449.

[3] B. Mile, D. Stirling, M.A. Zammitt, A. Lovell, M. Webb, *The Location of nickel oxide and nickel in silica-supported catalysts: Two forms of "NiO" and the assignment of temperature-programmed reduction profiles*, Journal of Catalysis 114 (1988) 217-229.

[4] L. Xu, H. Song, L. Chou, *Ordered mesoporous MgO-$Al_2O_3$ composite oxides supported Ni based catalysts for $CO_2$ reforming of $CH_4$: Effects of basic modifier and mesopore structure*, International Journal of Hydrogen Energy 38 (2013) 7307-7325.

[5] N. Sun, X. Wen, F. Wang, W. Wei, Y. Sun, *Effect of pore structure on Ni catalyst for $CO_2$ reforming of $CH_4$*, Energy Environmental Science 3 (2010) 366-369.

[6] S. Sokolov, E.V. Kondratenko, M.M. Pohl, A. Barkschat, U. Rodemerck, *Stable low-temperature dry reforming of methane over mesoporous $La_2O_3$-$ZrO_2$ supported Ni catalyst*, Applied Catalysis B: Environmental 113-114 (2012) 19-30.

[7] S. de Llobet, J.L. Pinilla, R. Moliner, I. Suelves, *Relationship between carbon morphology and catalyst deactivation in the catalytic decomposition of biogas using Ni, Co and Fe based catalysts*, Fuel 139 (2015) 71–78.

[8] D. Zhao, J. Feng, Q. Huo, N. Melosh, G.H. Fredrickson, B.F. Chmelka, G.D. Stucky, *Triblock Copolymer Syntheses of Mesoporous Silica with Periodic 50 to 300 Angstrom Pores*, Science 279 (1998) 548-552.

[9] M. Imperor-Clerc, P. Davidson, A. Davidson, *Existence of a Microporous Corona around the Mesopores of Silica-Based SBA-15 Materials Templated by Triblock Copolymers*, Journal of American Chemical Society 122 (2000) 11925-11933.

[10] A. Galarneau, H. Cambon, F. Di Renzo, F. Fajula, *True Microporosity and Surface Area of Mesoporous SBA-15 Silicas as a Function of Synthesis Temperature*, Langmuir 17 (2001) 8328-8335.

[11] A. Galarneau, H. Cambon, F. Di Renzo, R. Ryoo, M. Choi, F. Fajula, *Microporosity and connections between pores in SBA-15 mesostructured silicas as a function of the temperature of synthesis*, New Journal of Chemistry 27 (2003) 73-79.

# CHAPTER V

# Influence of Preparation Procedure

As seen in the previous chapter, the application of a hydrothermal treatment reduced the microporous connections between mesopores and resulted in higher mesoporous area of the resulting $Ni_{5.0}$/SBA-$B_1$(N) sample. The catalytic activity and stability was thus improved. Nevertheless, some carbon deposition was still observed on this catalyst, due to the presence of few external particles on the surface of the support. The preparation procedure can play an important role in the dispersion of the active phase and the consequent activity and stability of the resulting catalysts. In this chapter, the same SBA-$B_1$ support will be used to prepare nickel-based catalysts while modifying: (i) the nickel deposition method, (ii) the nature of the nickel precursor salt, (iii) the activation procedure (direct reduction without prior calcination), and (iv) the type of promoter/dopant added to nickel. The chapter finally considers the possibility of using mesoporous $CeO_2$ as a support for nickel species, instead of SBA-15.

In each part of the chapter, we will first show the catalytic test results on the prepared samples, next their physicochemical properties will be presented to explain the catalytic performances. The $Ni_{5.0}$/SBA-$B_1$(N) sample (already studied in Chapter IV) is used as reference, for comparison with the new samples.

## V.1 Effect of nickel addition method

Nickel was deposited in previous chapters using the two solvents method in order to favor internal deposition of the active phase in the porous support. However, this was not completely achieved due to some particles migration through micropores to the external surface of the support. Therefore, in this section, other deposition methods will be tested in an attempt to improve the nickel dispersion. The techniques used are simple, cheap and less time-consuming. In details, the two solvents technique (**$Ni_{5.0}$/SBA-$B_1$(N)** sample) will be compared: (i) to classical incipient wetness impregnation which consists on simple addition of metal precursor aqueous solution to the support (**$Ni_{5.0}$/SBA-$B_1$($N_{IWI}$)** sample) and (ii) to the direct synthesis procedure (also known as one-pot

synthesis) consisting on direct addition of nickel salt before TEOS decomposition-condensation during the SBA-15 support preparation (**$Ni_{5.0}$/SBA-$B_1$($N_{DS}$)** sample).

### V.1.1 Catalytic activity and stability

The calcined samples are first evaluated in methane dry reforming reaction. After *in-situ* reduction of the catalysts at 650°C under 5% $H_2$/Ar for 2 hours, the reactor was cooled down to about 200°C and catalytic measurements were carried out while increasing the temperature again to around 750°C. The variations of $CH_4$ and $CO_2$ conversions as a function of temperature are shown in Fig. V-1(left). On the three catalysts, the conversions gradually increased with increasing temperature, following again the same trend as that thermodynamically expected, but with a slight shift possibly due to the dynamic character of light-off curve measurements (increasing - meaning not yet stable - temperature), as discussed earlier. They started to increase after 400°C, until reaching around 92% $CH_4$ conversion and 94% $CO_2$ conversion. This was accompanied with a similar increase in the $H_2$:CO molar ratio, up to around 1.1.

After lowering the temperature and maintaining it at 650°C, an approximate decrease of 15-20% of the reactants conversions was observed on $Ni_{5.0}$/SBA-$B_1$($N_{DS}$) within 12 hours. The most stable catalyst was $Ni_{5.0}$/SBA-$B_1$(N) on which an average of 75 and 82% $CH_4$ and $CO_2$ conversions were respectively maintained for more than 90 hours. The $Ni_{5.0}$/SBA-$B_1$($N_{IWI}$) catalyst showed intermediate conversions, between the above two catalysts.

### V.1.2 Porosity of calcined samples

The superior stability of the $Ni_{5.0}$/SBA-$B_1$(N) catalyst prepared by two solvents method can be first explained by the textural properties of the calcined impregnated samples analyzed and compared by $N_2$ sorption (Fig. V-2A,B,C and Table V-1). The formation of the mesoporous structure is verified by the type IV(a) isotherm on all samples (Fig. V-2A), regardless of the preparation method. The surface area, pore volume and pore size on $Ni_{5.0}$/SBA-$B_1$($N_{DS}$) were larger than on $Ni_{5.0}$/SBA-$B_1$(N) and even much larger than on $Ni_{5.0}$/SBA-$B_1$($N_{IWI}$) (Table V-1). Similar results were reported on Ni/SBA-15[1] and CuNi/SBA-15[2] prepared by direct synthesis in comparison to incipient wetness impregnation.

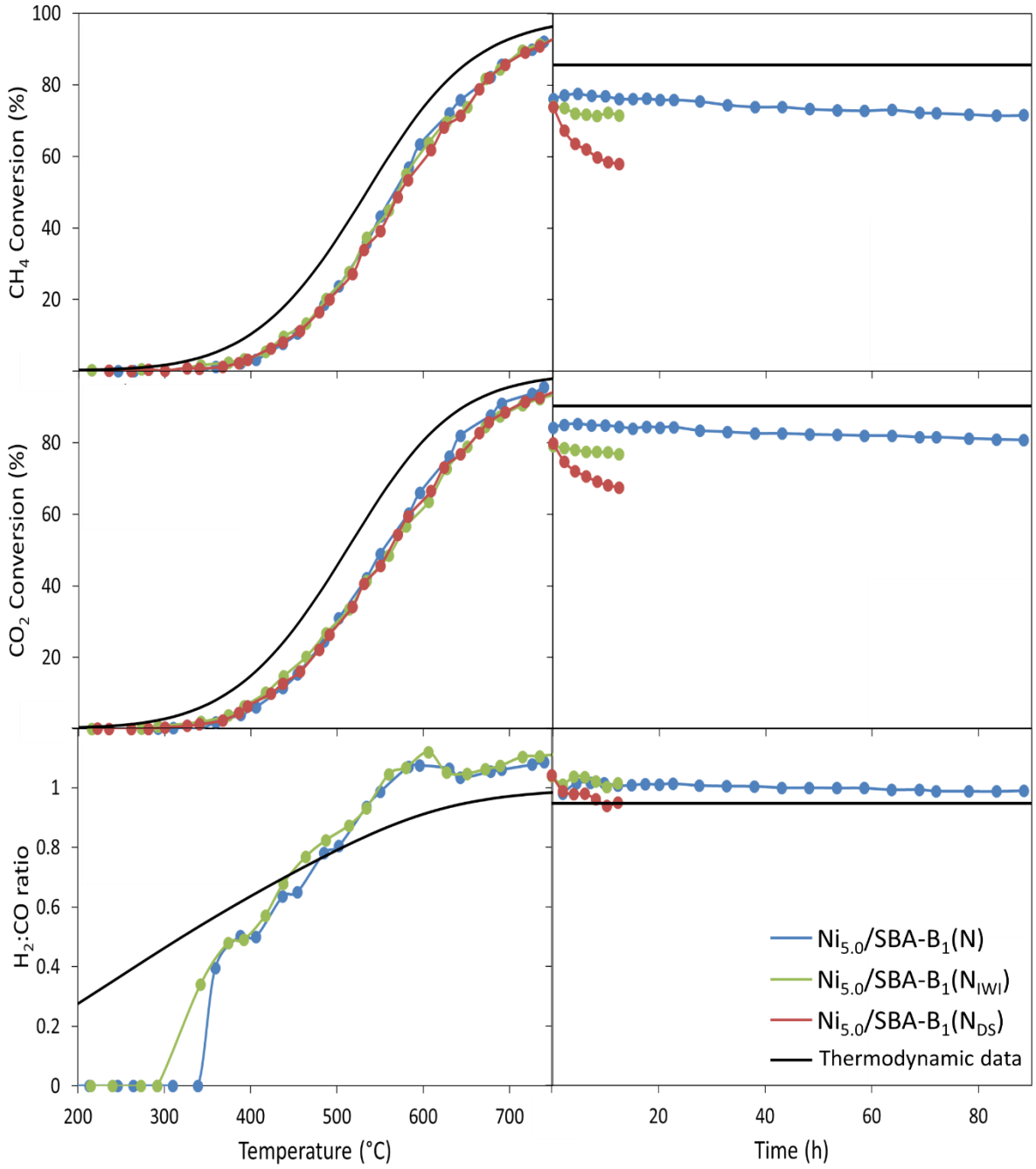


Figure V-1: Variation of $CH_4$ conversion, $CO_2$ conversion and $H_2$:CO molar ratio as a function of temperature (left) and time at 650°C (right) at 1 bar, 36 $L.g^{-1}.h^{-1}$ and $CH_4$:$CO_2$:Ar = 5:5:90

Nevertheless, parallel adsorption and desorption branches were observed on $Ni_{5.0}$/SBA-$B_1$(N) sample along with a narrow pore size distribution (Fig. V-2B,C). This reveals homogeneous filling of the pores by the particles due to the two solvents procedure. On the contrary, the use of incipient

wetness impregnation or direct synthesis resulted in the formation of more blocked mesopores, as indicated by the pronounced tailing at relative pressures between 0.6 and 0.4.[3] This observation is further supported by the pore size distribution during both adsorption and desorption (Fig. V-2B,C and Table V-1). Indeed, a broad distribution is obtained on $Ni_{5.0}$/SBA-$B_1$($N_{IWI}$) and even much broader on $Ni_{5.0}$/SBA-$B_1$($N_{DS}$) sample, indicating a heterogeneous distribution of oxides inside the pores. On $Ni_{5.0}$/SBA-$B_1$($N_{DS}$), the much larger pore size distribution can be explained by the presence of partially filled macropores, seen on the isotherm at high relative pressures between 0.8 and 1 (Fig. V-2A), in addition to some mesopores blocked by metals.

Table V-1: Textural properties of calcined samples

| Sample Name | Total surface area ($m^2.g^{-1}$) | Meso-porous area ($m^2.g^{-1}$) | Micro-porous area ($m^2.g^{-1}$) | Pore volume ($cm^3.g^{-1}$) | Mean ads. pore size (nm) | Mean des. pore size (nm) |
|---|---|---|---|---|---|---|
| SBA-$B_1$ | 832 | 678 | 154 | 0.97 | 6.4 | 6.0 |
| $Ni_{5.0}$/SBA-$B_1$(N) | 620 | 551 | 69 | 0.70 | 5.7 | 5.5 |
| $Ni_{5.0}$/SBA-$B_1$($N_{IWI}$) | 503 | 443 | 60 | 0.58 | 5.2 | 4.8 |
| $Ni_{5.0}$/SBA-$B_1$($N_{DS}$) | 677 | 501 | 176 | 0.76 | 7.0 | 6.6 |
| $Ni_{5.0}$/SBA-$B_1$(R) | 509 | 445 | 64 | 0.66 | 6.4 | 6.0 |
| $Ni_{5.0}$/SBA-$B_1$(Cl) | 545 | 491 | 54 | 0.68 | 5.7 | 5.3 |
| $Ni_{5.0}$/SBA-$B_1$(A) | 549 | 495 | 54 | 0.70 | 5.8 | 5.5 |
| $Ni_{5.0}Ce_6$/SBA-$B_1$(N) | 567 | 458 | 109 | 0.54 | 5.0 | 4.7 |
| $Ni_{5.0}Mg_6$/SBA-$B_1$(N) | 585 | 531 | 54 | 0.62 | 5.2 | 4.9 |
| $Ni_{5.0}La_6$/SBA-$B_1$(N) | 572 | 485 | 87 | 0.58 | 4.4 | 4.9 |
| $Ni_{5.0}Rh_{0.1}$/SBA-$B_1$(N) | 623 | 515 | 108 | 0.65 | 5.4 | 5.1 |
| $Ni_{5.0}Rh_{0.5}$/SBA-$B_1$(N) | 596 | 496 | 100 | 0.65 | 5.7 | 5.5 |

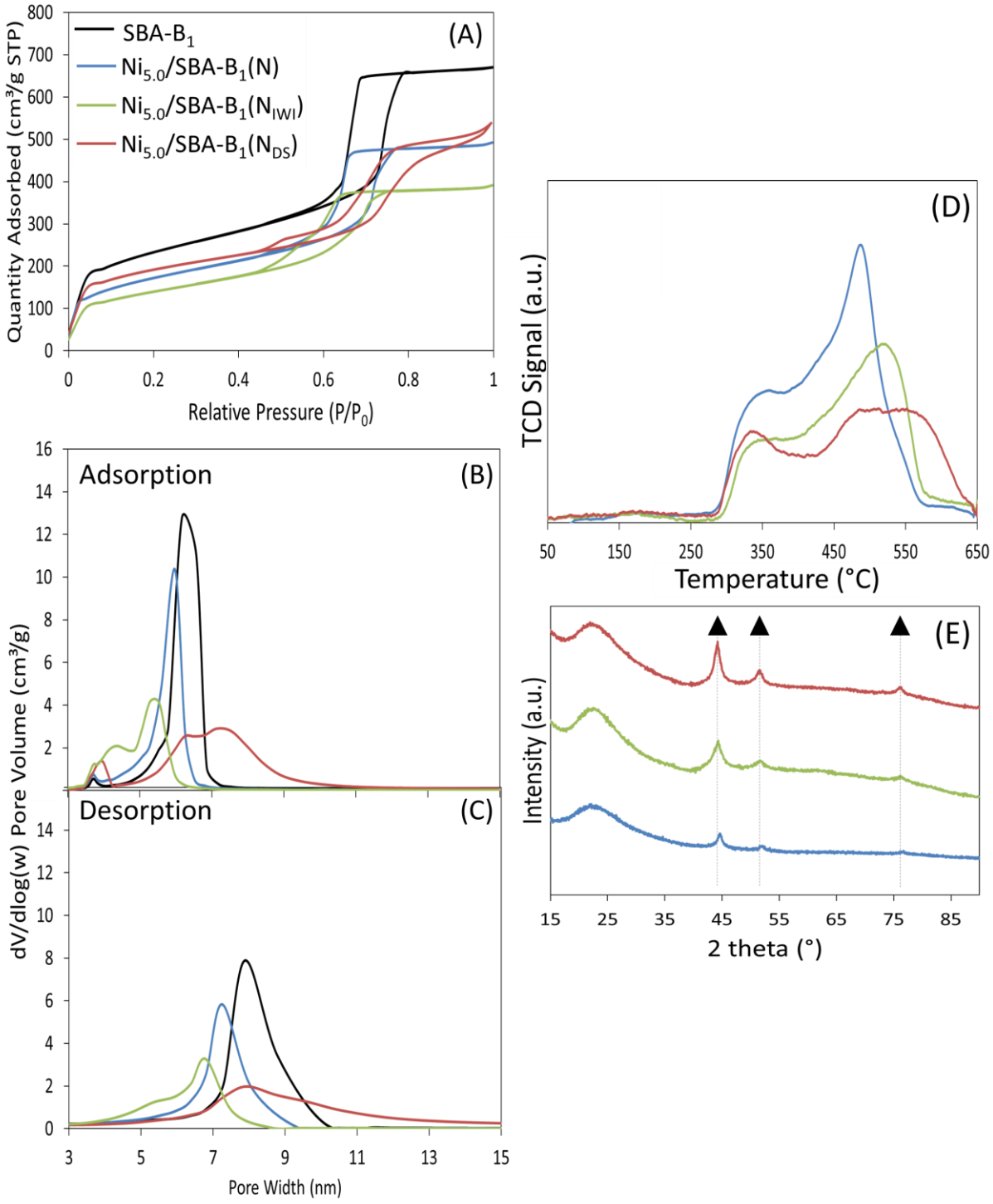


Figure V-2: (A) $N_2$-sorption isotherms, (B) adsorption and(C) desorption pore size distributions of calcined samples, (D)TPR profiles, (E) X-ray diffractograms of the reduced samples (▲: $Ni^0$) prepared using different nickel addition methods

Pore blockage by metals similar to that in $Ni_{5.0}$/SBA-$B_1$($N_{DS}$) could have been as well the reason for the lower performance of CuNi/SBA-15 catalysts prepared by direct synthesis in ethanol steam reforming.[2] However, despite the similar conditions used, these data disagree with the ones previously reported by Park et al.[1] that showed narrow pore size distributions on samples prepared by DS or IWI. These variances can be related to small details of preparation, like the stirring rate or order of addition of nickel nitrate and TEOS.

### V.1.3 Reducibility of the samples

Concerning the reducibility of nickel oxides on these samples, their TPR profiles (Fig. V-2D) always showed a first reduction peak between 300 and 400°C, attributable to the reduction of nickel oxides with weak interaction with the support. The second reduction peak was centered at around 480°C for both $Ni_{5.0}$/SBA-$B_1$(N) and $Ni_{5.0}$/SBA-$B_1$($N_{DS}$), but at 520°C for $Ni_{5.0}$/SBA-$B_1$($N_{IWI}$) demonstrating easier reducibility of NiO nanoparticles on the former samples. On $Ni_{5.0}$/SBA-$B_1$($N_{DS}$), a third peak, observed with a maximum at 560°C, can be assigned to the reduction of nickel oxides incorporated inside the porous system of the SBA-15 support during preparation or to the reduction of surface nickel silicates in strong interaction with the support.[4,5]

### V.1.4 Size and dispersion of the supported nanoparticles

After reduction, the X-ray diffractograms of the reduced samples (Fig. V-2E) show again the three main diffraction peaks of metallic $Ni^0$ nanoparticles with a face-centered cubic lattice (Fm-3m), positioned at 44, 52 and 76° (ICDD 65-0380). This indicates complete NiO reduction at 650°C.

The intensity of the diffraction peaks varied with respect to the preparation method and followed the same order as for the pore size distribution (Fig. V-2B,C). Thus, the largest $Ni^0$ particles (Table V-2) were found on $Ni_{5.0}$/SBA-$B_1$($N_{DS}$) which had the broader pore size distribution while $Ni_{5.0}$/SBA-$B_1$(N) showed the smallest $Ni^0$ nanoparticles in agreement with its narrow pore size distribution. These data are not in accordance with previous reports that reported better metal dispersion on NiCeAl catalyst prepared by direct synthesis.[6] In their study, the authors proposed that the enhanced dispersion obtained by direct synthesis resulted in better catalytic activity and stability in dry reforming of methane. Nevertheless, in another work, the use of the two solvents method for the deposition of cobalt on SBA-15, in comparison to impregnation, was shown highly

effective, giving homogeneous cobalt oxide deposition inside the pores and resulting in higher conversions during cyclohexanol oxidation.[7]

The data found in this section correlate with the findings in Chapter IV regarding the essential need of a well-defined mesoporous structure, as in $Ni_{5.0}$/SBA-$B_1$(N), in order to achieve high and stable conversions. Indeed, on our samples, it was shown above that the catalytic stability was maintained on the samples in the following decreasing order: $Ni_{5.0}$/SBA-$B_1$(N) > $Ni_{5.0}$/SBA-$B_1$($N_{IWI}$) > $Ni_{5.0}$/SBA-$B_1$($N_{DS}$). The latter showed the lowest ordered mesoporous structure. In addition, this order was in accordance with the decreasing sequence of $Ni^0$ metal particle size: $Ni_{5.0}$/SBA-$B_1$(N) < $Ni_{5.0}$/SBA-$B_1$($N_{IWI}$) < $Ni_{5.0}$/SBA-$B_1$($N_{DS}$). Thus, the better Ni dispersion of $Ni_{5.0}$/SBA-$B_1$(N) should be one important reason of the higher catalytic activity and stability of this sample.

Table V-2: Particles size after calcination, reduction and catalytic test

| **Sample Name** | **NiO Size[a] (nm)** | **$Ni^0$ size Reduced[b] (nm)** | **$Ni^0$ size Spent[b] (nm)** |
|---|---|---|---|
| $Ni_{5.0}$/SBA-$B_1$(N) | 6.0 | 6.4 | 6.3 |
| $Ni_{5.0}$/SBA-$B_1$($N_{IWI}$) | n.d. | 7.0 | n.d. |
| $Ni_{5.0}$/SBA-$B_1$($N_{DS}$) | n.d. | 7.4 | n.d. |
| $Ni_{5.0}$/SBA-$B_1$(R) | - | 4.4 | 4.7 |
| $Ni_{5.0}$/SBA-$B_1$(Cl) | 9.0 | 8.2 | 10.3 |
| $Ni_{5.0}$/SBA-$B_1$(A) | n.d. | 2.9 | 3.7 |
| $Ni_{5.0}Ce_6$/SBA-$B_1$(N) | n.d. | 3.3 | - |
| $Ni_{5.0}Mg_6$/SBA-$B_1$(N) | 5.6 | 5.5 | 5.6 |
| $Ni_{5.0}La_6$/SBA-$B_1$(N) | n.d. | 5.9 | n.d. |
| $Ni_{5.0}Rh_{0.1}$/SBA-$B_1$(N) | 6.7 | 6.7 | n.d. |
| $Ni_{5.0}Rh_{0.5}$/SBA-$B_1$(N) | 7.0 | 6.5 | 6.4 |

[a]estimated from the diffraction peak at 43°
[b]estimated from the diffraction peak at 44°

Summary of section V.1: Effect of nickel addition method

- Under the used conditions, the catalyst prepared by two solvents method was the most active and stable catalyst and this can be attributed to its narrow pore size distribution, and to the smaller metallic $Ni^0$ particles well dispersed inside the pores of the SBA-15 support.
- The incipient wetness impregnation and direct synthesis procedures resulted in more heterogeneous pore size distribution and in the formation of larger particles and consequently leading to lower catalytic performances.

## V.2 Effect of nickel precursor and pre-treatment

Based on the above results, the two solvents procedure is applied in the following for the deposition of nickel precursors inside the support. In order to promptly expose the positive confinement effect of nickel particles inside porous systems, different nickel precursors were used to reach different particle sizes and dispersions. Particularly, nickel chloride is reported to generate large external nickel particles[8,9,10,11,12] while nitrate and acetate nickel precursors favor internal dispersion of small nanoparticles.[9,13] As explained in Chapter II, the samples prepared using nickel chloride, nickel acetate and nickel nitrate are denoted **$Ni_{5.0}$/SBA-$B_1$(Cl)**, **$Ni_{5.0}$/SBA-$B_1$(A)** and **$Ni_{5.0}$/SBA-$B_1$(N)**, respectively. Furthermore, Ni/SBA-15 catalysts prepared in literature[14,15,16] are commonly calcined for some time then reduced under a reducing atmosphere (in general hydrogen) in order to obtain the active phase. Few studies[13,17] evaluate the importance of such thermal treatments and their impact on the dispersion of the active phase and its consequent activity and stability. Therefore, in this section, the $Ni_{5.0}$/SBA-$B_1$(N) catalyst classically calcined at 450°C for 5 hours at 0.5°C.min$^{-1}$ then reduced *in-situ* at 650°C for 2 hours before test is compared to another one prepared under similar conditions but directly reduced *in-situ* at 600°C for 10 min without prior calcinations (**$Ni_{5.0}$/SBA-$B_1$(R)** sample) in order to favor particularly small reduced nanoparticles.

### V.2.1 Catalytic activity and stability

During catalytic activity measurements (Fig. V-3), the $Ni_{5.0}$/SBA-$B_1$(A) catalyst showed slightly lower performance than $Ni_{5.0}$/SBA-$B_1$(N) while $Ni_{5.0}$/SBA-$B_1$(R) followed the same trend as $Ni_{5.0}$/SBA-$B_1$(N).

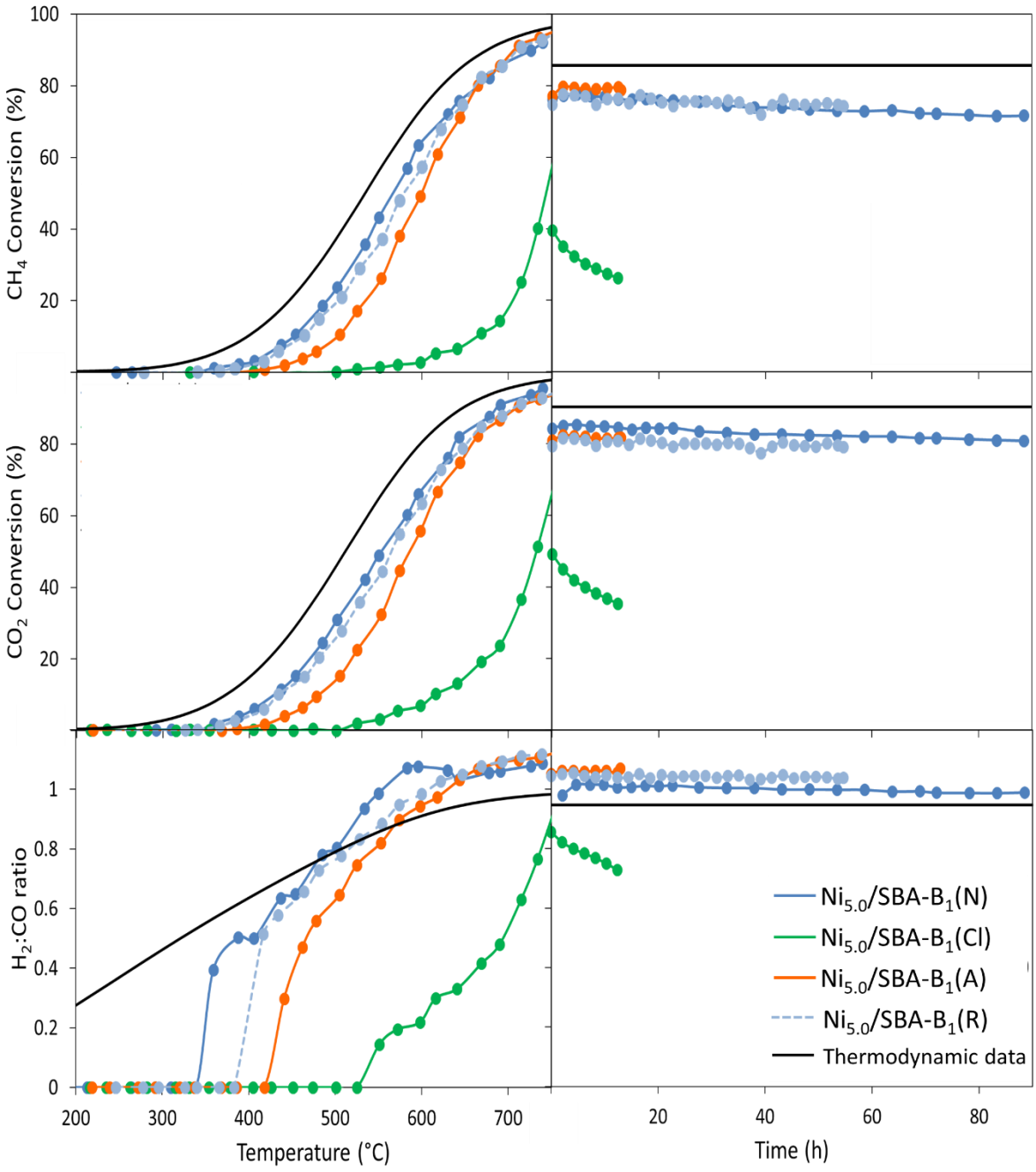


Figure V-3: Variation of $CH_4$ conversion, $CO_2$ conversion and $H_2$:CO molar ratio as a function of temperature (left) and time at 650°C (right) at 1 bar, 36 $L.g^{-1}.h^{-1}$ and $CH_4$:$CO_2$:Ar = 5:5:90

As expected, $Ni_{5.0}$/SBA-$B_1$(Cl) was clearly the least active amongst all tested catalysts. On this catalyst, a temperature of at least 500°C was needed in order for the reaction to begin and at 750°C, the $CH_4$ and $CO_2$ conversions only reached about 58 and 66%, respectively. These trends remained

also valid for the catalytic stability results. Indeed, $Ni_{5.0}$/SBA-$B_1$(N), $Ni_{5.0}$/SBA-$B_1$(A) and $Ni_{5.0}$/SBA-$B_1$(R) preserved high $CO_2$ and $CH_4$ conversions near 80-85% and 80%, respectively. The catalytic performances of $Ni_{5.0}$/SBA-$B_1$(Cl) were much lower, with initial $CO_2$ and $CH_4$ conversions close to 50% and 40%, respectively.

### V.2.2 Porosity of calcined samples

The evaluation of the textural properties of calcined samples by $N_2$ sorption (Fig. V-4A,B,C) remarkably shows that the shape of the isotherm remained the same regardless of the nickel precursor used. This interestingly demonstrates the reproducibility of the two solvents method. The surface areas and pore volumes of $Ni_{5.0}$/SBA-$B_1$(N), $Ni_{5.0}$/SBA-$B_1$(Cl) and $Ni_{5.0}$/SBA-$B_1$(A) samples were around 550-620 $m^2.g^{-1}$ and 0.68-0.70 $cm^3.g^{-1}$, respectively with pore sizes between 5.3 and 5.7 nm (Table V-1 and Fig. V-4A). Likewise, a type IV(a) isotherm was still obtained in the case of direct reduction and therefore such treatment did not affect the mesoporous structure of the resulting sample. However, the directly reduced $Ni_{5.0}$/SBA-$B_1$(R) catalyst revealed slightly lower surface area and pore volume than those of the calcined $Ni_{5.0}$/SBA-$B_1$(N) sample. The average pore widths of $Ni_{5.0}$/SBA-$B_1$(R) were similar to those of the initial SBA-B silica support (Fig. V-4B,C), indicating good filling of the channels in this case without major pore blockage.

### V.2.3 Reducibility of the samples

The NiO reduction on $Ni_{5.0}$/SBA-$B_1$(N) and $Ni_{5.0}$/SBA-$B_1$(Cl) took place in two main steps, at around 350 and 480°C (Fig. V-4D), assigned (as mentioned before) to the reduction of large NiO particles in weak interaction with the support and smaller NiO nanoparticles in strong interactions with the support,[18,19,20] respectively. However, the NiO reduction profile on $Ni_{5.0}$/SBA-$B_1$(A) was shifted towards higher temperatures, suggesting higher interaction of oxides with the support. This decreased reducibility on $Ni_{5.0}$/SBA-$B_1$(A) can be also explained by the presence of surface nickel silicates, in strong interaction with the support, which formation would be favored by the presence of carbon derivatives in the sample (prepared using nickel acetate) that generates highly exothermic reaction during calcination.[4,5]

### V.2.4 Size and dispersion of the supported nanoparticles

Similar to the previous observations on the XRD profiles of the calcined, reduced and spent samples (Fig. V-4E,F,G), the narrow peaks at 37, 43, 62, 76, and 81° (Fig. V-4E) on the

diffractograms of calcined samples correspond to NiO nanoparticles (ICDD 73-1523) with a face-centered cubic lattice (Fm-3m) while those at 44, 52 and 76° (Fig. V-4F,G) for reduced and spent samples correspond to metallic $Ni^0$ nanoparticles (ICDD 65-0380) with a face-centered cubic lattice (Fm-3m). While the same nickel loading (5 wt%) was used for all samples, the intensities of the diffraction peaks were not the same. The absence of NiO characteristic peaks on the calcined $Ni_{5.0}$/SBA-$B_1$(A) indicates the formation of very small nickel oxide nanoparticles or nickel silicates on this sample, which are also barely observable on TEM micrographs (Figure V-5a). Nevertheless, their presence did not seem to affect the catalytic performance, since comparable conversions were obtained on both $Ni_{5.0}$/SBA-$B_1$(A) and $Ni_{5.0}$/SBA-$B_1$(N) catalysts.

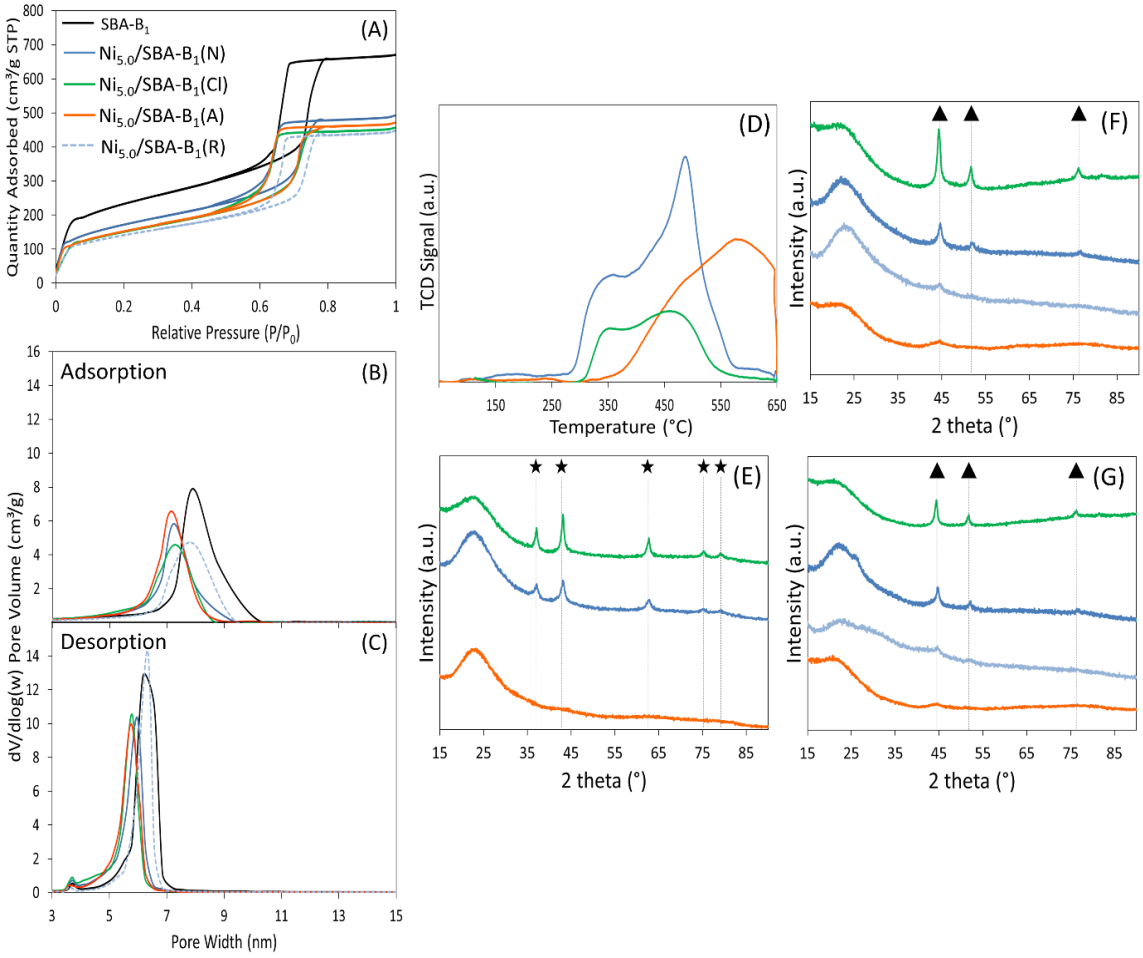


Figure V-4: (A) $N_2$-sorption isotherms, (B) adsorption and (C) desorption pore size distributions of calcined samples,(D) TPR profiles and X-ray diffractograms of (E) calcined, (F) reduced and (G) spent samples (★: NiO, ▲: $Ni^0$) prepared using different nickel precursor salts

During thermal decomposition of the nickel nitrate precursor in air (calcination treatment), the generation of oxygen radicals ($NO_2/O_2$) can lead to some NiO sintering.[12] For this reason, slightly better nickel dispersion can be obtained upon using the nickel acetate precursor,[21] unless the catalyst was directly reduced in $H_2$ atmosphere without calcination. In this case, no oxygen radicals are formed even if nickel nitrate was used as precursor. In this direction, the elimination of the calcination step before reduction, during the preparation of our $Ni_{5.0}/SBA\text{-}B_1(R)$ sample, contributed in the formation of smaller nickel particles (Table V-2). Indeed, the mean sizes of NiO and $Ni^0$ maintained the following ascending order: $Ni_{5.0}/SBA\text{-}B_1(A) < Ni_{5.0}/SBA\text{-}B_1(R) < Ni_{5.0}/SBA\text{-}B_1(N) < Ni_{5.0}/SBA\text{-}B_1(Cl)$. This order is in agreement with the TEM images taken on the reduced (Figure V-5a-d) and spent samples (Figure V-5a'-d'). Similar results were also obtained by direct reduction on $Ni/Al_2O_3$ catalysts for DRM[17] and Ni/SBA-15 catalysts for the hydrogenation of naphthalene.[13] Consequently, the direct reduction without prior calcination emerges as a promising route to save energy, time and money while forming highly stable catalysts for dry reforming of methane. Nevertheless, this procedure does not seem to be attractive from an industrial point of view due to problems of nickel reoxidation upon contact with air, especially when the catalyst is activated in a reactor and transferred to another one for reaction, as is usually the case in industries. More detailed investigations can be thus anticipated regarding this issue, to check the stability of the metallic phase under such conditions.

Furthermore, large $Ni^0$ nanoparticles of about 9 nm were found on $Ni_{5.0}/SBA\text{-}B_1(Cl)$ and they were predominantly localized on the external surface of the support (Figure V-5d), similar to what is classically reported when using nickel chloride as precursor nickel salt.[22] It is worth noting that, after nickel chloride impregnation on the $SBA\text{-}B_1$ support, the calcination of the dried powder at 450°C for 5 hours ($0.5°C.min^{-1}$) was sufficient to remove all chloride ions from the sample. This was confirmed by the absence of the characteristic Cl peak in the EDS analysis (Fig. V-6).

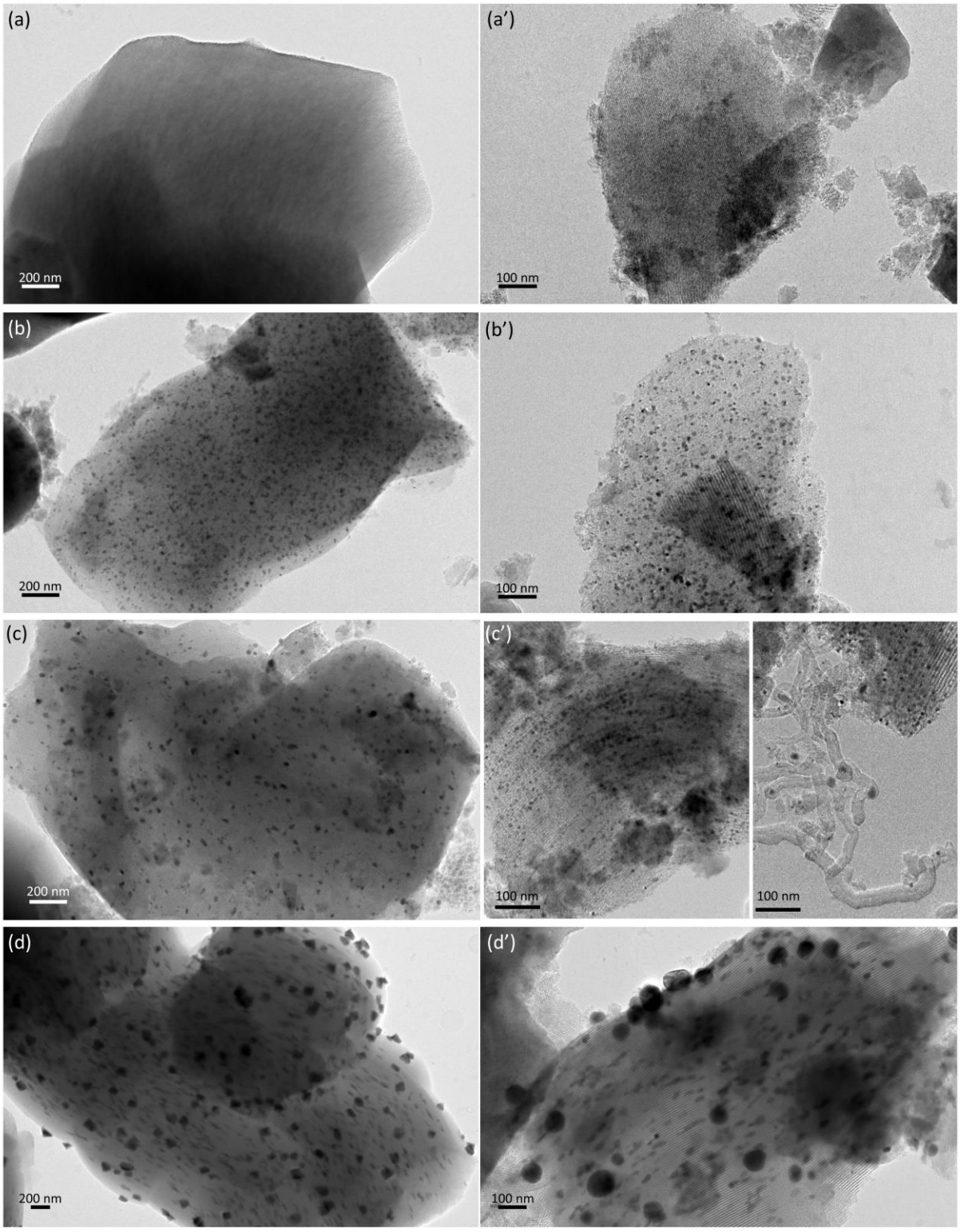


Figure V-5: TEM images of (a,a') $Ni_{5.0}$/SBA-$B_1$(A), (b,b') $Ni_{5.0}$/SBA-$B_1$(R), (c,c') $Ni_{5.0}$/SBA-$B_1$(N) and (d,d') $Ni_{5.0}$/SBA-$B_1$(Cl) before (a,b,c,d) and after (a',b',c',d') dry reforming tests

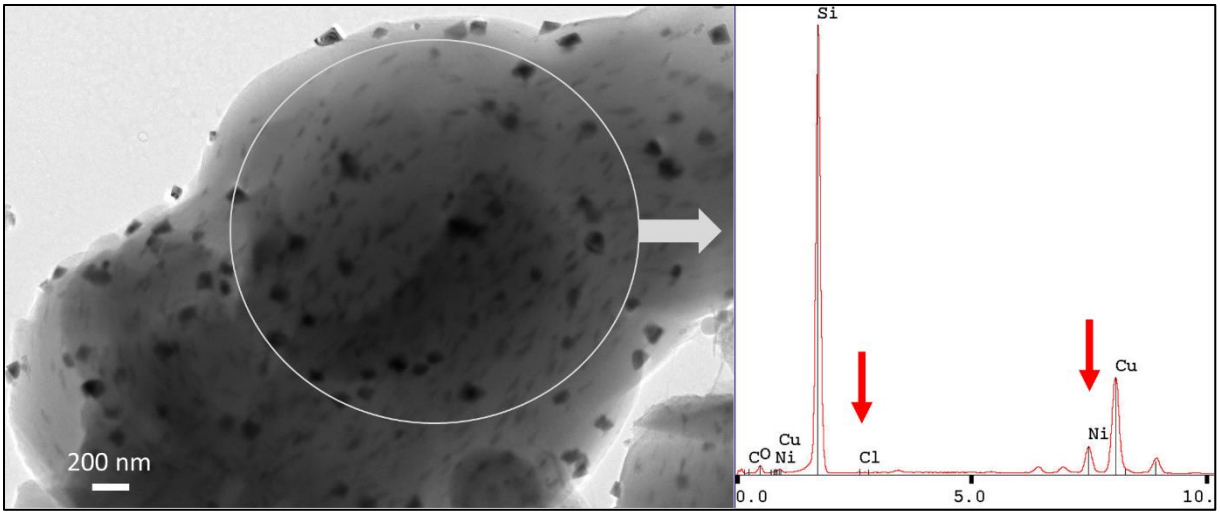


Figure V-6: TEM micrograph of calcined $Ni_{5.0}$/SBA-$B_1$(Cl) sample with corresponding EDS of the indicated area

The formation of large external particles when using chloride precursors is due to the high volatility of nickel chloride during reduction, resulting in the vaporization of nickel particles and their subsequent agglomeration to form large crystals.[10,12] Even if an average $Ni^0$ particles size of 10.3 nm was estimated by XRD after reaction, the TEM images of the spent $Ni_{5.0}$/SBA-$B_1$(Cl) show the simultaneous presence of very small nanoparticles inside the channels of some grains, on one hand, and the aggregation of large nickel clusters, of about 50 nm in diameter, on the external surface of the support, on the other hand. Consequently, the nickel particles formed were very large. As will be discussed in Chapter VI, these particles are even too large to induce the formation and growth of carbon nanotubes. Therefore, the rapid continuous deactivation in this case can be mainly attributed to (i) lower initial active surface area accessible to the reactants, (ii) absence of confinement of nickel particles inside well-defined mesoporous channels and consequently (iii) higher mobility of metallic phase leading to (iv) continuously reduced accessible surface area.

Large particles were also found in literature when using nickel chloride on $CeO_2$ and SiC,[10] $TiO_2$[9] and $Al_2O_3$ supports.[8,23] As obtained in our study, the large particles resulted in lower catalytic conversions due to lower number of active sites and high degrees of deactivation due to weaker metal-support interaction. Alternatively, the smaller metal particles formed on the samples prepared using nickel nitrate or nickel acetate favored good catalytic activity and stability in tri-reforming of methane,[10] selective CO methanation[9] and glycerol steam reforming.[23] In dry reforming of methane in particular, Wang et al.[8] reported similar reactants conversions on Ni/$Al_2O_3$ catalyst prepared using

nickel nitrate but, in their case, the tests were conducted using lower space velocity of 18 $L.g^{-1}.h^{-1}$ and higher temperature (700°C). While both nickel nitrate and nickel acetate precursor salts favor good dispersion of the active phase inside the support, nickel nitrate remains cheaper than nickel acetate and this explains its wider use in research and industrial work.

Summary of section V.2: Effect of nickel precursor and pre-treatment

- The $Ni_{5.0}$/SBA-$B_1$(Cl) prepared using nickel chloride showed severe deactivation during DRM, that could be attributable to strong nickel sintering due to important nickel location outside the mesoporous silica grains. In opposition, the $Ni_{5.0}$/SBA-$B_1$(A) prepared using nickel acetate, $Ni_{5.0}$/SBA-$B_1$(N) prepared using nickel nitrate and $Ni_{5.0}$/SBA-$B_1$(R) directly reduced without calcination maintained high Ni dispersion and high $CO_2$ and $CH_4$ conversions during DRM reaction.
- Regardless of the nickel precursor, comparable textural properties were obtained and $Ni_{5.0}$/SBA-$B_1$(A) revealed the highest metal-support interaction.
- The mean nickel particle size in ascending order was the following: $Ni_{5.0}$/SBA-$B_1$(A)<$Ni_{5.0}$/SBA-$B_1$(R)<$Ni_{5.0}$/SBA-$B_1$(N)<$Ni_{5.0}$/SBA-$B_1$(Cl).
- Although beneficial, the direct reduction is not highly recommended in industry; consequently, nickel nitrate – cheaper than nickel acetate – remains an efficient precursor for a good metal dispersion.

## V.3 Effect of promoters/dopants

In order to achieve better stabilities, researches have tried to control the metal nanoparticles size by adding a promoter, doping with noble metals and/or modifying surface basicity of the support.[24,25,26] To cover this aspect, 6 wt% Ce, Mg or La were co-impregnated with 5 wt% Ni on the SBA-$B_1$ support, to obtain **$Ni_{5.0}Ce_6$/SBA-$B_1$(N)**, **$Ni_{5.0}Mg_6$/SBA-$B_1$(N)** and **$Ni_{5.0}La_6$/SBA-$B_1$(N)**, respectively. Moreover, to test the interest of doping with noble metals, the $Ni_{5.0}$/SBA-$B_1$(N) sample was doped with 0.1 (**$Ni_{5.0}Rh_{0.1}$/SBA-$B_1$(N)** sample) and 0.5 wt% Rh (**$Ni_{5.0}Rh_{0.5}$/SBA-$B_1$(N)** sample).

### V.3.1 Catalytic activity and stability

The same operating conditions as those mentioned previously were used to perform the DRM test. During the increase of temperature from 200 up to 750°C (Fig. V-7A), both reactants conversions and $H_2$:CO molar ratios increased, following the shape of the thermodynamic curves. Under the used operating conditions, the conversions on both $Ni_{5.0}Mg_6/SBA\text{-}B_1(N)$ and $Ni_{5.0}La_6/SBA\text{-}B_1(N)$ catalysts were close to those on $Ni_{5.0}/SBA\text{-}B_1(N)$ catalyst, while a slight improvement was observed upon addition of Ce. The higher performance of the Ce-containing $Ni_{5.0}Ce_6/SBA\text{-}B_1(N)$ sample was even more distinctly observed during stability measurements at 650°C (Fig. V-7B), especially in terms of $CH_4$ conversion.

With respect to Rh, the conversions were identical when considering light-off curves, on the $Ni_{5.0}/SBA\text{-}B_1(N)$, $Ni_{5.0}Rh_{0.1}/SBA\text{-}B_1(N)$, $Ni_{5.0}Rh_{0.5}/SBA\text{-}B_1(N)$ or $Rh_{0.5}/SBA\text{-}B_1$ catalyst (Fig. V-7A'). However, during stability measurements at 650°C (Fig. V-7B'), the use of the Ni-free $Rh_{0.5}/SBA\text{-}B_1$ catalyst resulted in lower conversions and inferior stability. The addition of 0.1 wt% Rh did not seem to affect the catalytic behavior of $Ni_{5.0}/SBA\text{-}B_1(N)$. Alternatively, an enhanced stability was obtained on $Ni_{5.0}Rh_{0.5}/SBA\text{-}B_1(N)$ catalyst in comparison to the remaining samples for 60 hours.

### V.3.2 Porosity of calcined samples

In view of the $N_2$ sorption data of the calcined samples (Fig. V-8A), the co-impregnation of 6 wt% Ce, Mg or La with Ni resulted in an important decrease of both surface areas and pore volumes (Table V-1). In addition, the shape of the hysteresis loop was also altered, with more inclined adsorption and desorption branches. This can be explained by the partial pore plugging due to the presence of oxides in the pore apertures, as demonstrated by the braod pore size distirbution, in adsoprtion and desorption, over these samples (Fig. V-8B,C). Consequently, a more heterogeneous pore size ditribution was obtained over co-impregnated samples due to the distrubiton of both Ni and the second metal (Ce, Mg or La) inside the channels of $SBA\text{-}B_1$ porous support.

The addition of 0.1 and 0.5 wt% Rh to $Ni_{5.0}/SBA\text{-}B_1(N)$ did not greatly affect the shape of the $N_2$ isotherms. The surface area and pore volume (Table V-1) did not evolve neither, most probably because of the low amount of rhodium added (only 0.1 and 0.5 wt%).

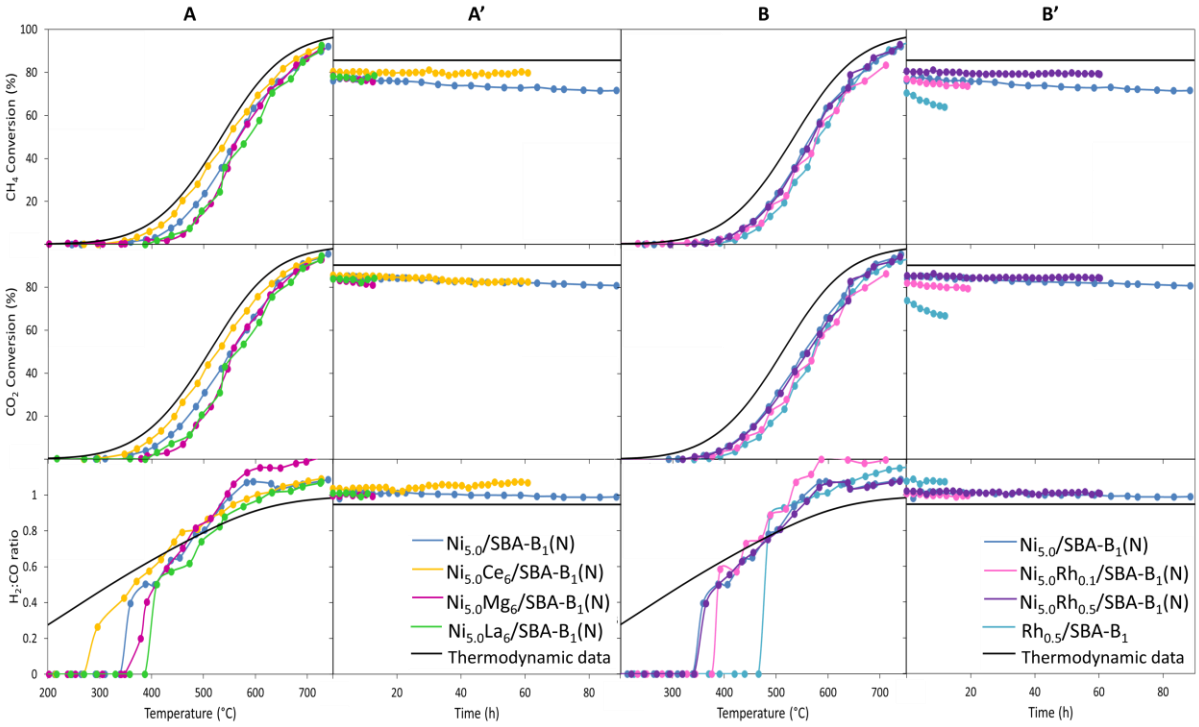


Figure V-7: Variation of $CH_4$ conversion, $CO_2$ conversion and $H_2$:CO molar ratio as a function of temperature (A,B) and time at 650°C (A',B') at 1 bar, 36 $L.g^{-1}.h^{-1}$ and $CH_4$:$CO_2$:Ar = 5:5:90

## V.3.3 Reducibility of the samples

During $H_2$-TPR (Figure V-8D, the co-impregnated $Ni_{5.0}Ce_6/SBA\text{-}B_1(N)$ and $Ni_{5.0}La_6/SBA\text{-}B_1(N)$ revealed the two $H_2$ consumption peaks like those on $Ni_{5.0}/SBA\text{-}B_1(N)$, that are in the range of 250-400°C and 400-600°C, respectively. Thus, as previously shown in Chapter III, no significant difference in the nickel reduction process was noted upon addition of Ce. The use of Mg apparently shifted the TPR profile towards higher temperatures. Nevertheless, on all these samples, the second peak was always more important than the first one. Based on the attribution of the lower temperature peak to the reduction of large NiO crystals, and the one at higher temperatures to the reduction of smaller particles,[4,27,28] it can be suggested that the majority of NiO particles on these samples are small in addition to few larger ones weakly interacting with the support.

Concerning the effect of Rh on the reducibility of Ni/SBA-15 catalysts, the two NiO reduction peaks on the $Ni_{5.0}Rh_{0.1}/SBA\text{-}B_1(N)$ and $Ni_{5.0}Rh_{0.5}/SBA\text{-}B_1(N)$ samples appear to be shifted towards lower values, i.e. 200-350°C and 400-550°C, respectively (Figure V-8D). This can be

related to the $H_2$ spillover effect of rhodium, when $H_2$ molecules dissociate on the surface of the noble metalto hydrogen species, which are diffused to adjacentones via the support surface.[29,30,31,32] Furthermore, the reduction peak at around 110°C is only observed on the $Ni_{5.0}Rh_{0.5}$/SBA-$B_1$(N) sample and can be assigned to the reduction of $Rh_2O_3$ species[33] or isolated $RhO_x$ species.[34] The absence of this peak on the $Ni_{5.0}Rh_{0.1}$/SBA-$B_1$(N) sample is due to the very low amount of rhdoium added in this case. Consequently, Rh improves the reducibility of NiO and Ni-silicate by increasing the amount of metallic Ni during reaction, leading to superior behavior compared to the remaining samples.[35]

### V.3.4 Structural ordering of reduced and spent catalysts

For all reduced (Fig. V-8E) and spent (Fig. V-8F) samples, the small-angle XRD showed the well-resolved (100) diffraction peak and the smaller (110) and (200) ones characteristic of the highly ordered p6mm hexagonal mesoporous structure.[36,37,38] The conservation of these peaks before and after caralytic reaction validates the preservation of the 2D hexagonal structure. However, the positions of these peaks are not identical on all samples.

Based on the (100) diffraction peak, the unit cell parameter was estimated to be 9.3 nm on both $Ni_{5.0}$/SBA-$B_1$(N) and $Ni_{5.0}Ce_6$/SBA-$B_1$(N), 9.6 nm on $Ni_{5.0}Mg_6$/SBA-$B_1$(N) and 9.7 nm on $Ni_{5.0}La_6$/SBA-$B_1$(N). After reaction, the Ce-containing sample maintained the same unit cell parameter while a shrinkage was observed on $Ni_{5.0}$/SBA-$B_1$(N), $Ni_{5.0}Mg_6$/SBA-$B_1$(N) and $Ni_{5.0}La_6$/SBA-$B_1$(N) to 8.9, 9.3 and 9.4 nm, respectively. This indicates some collapse of the porous structure, as also demonstrated by the lower intensity of the diffraction peaks, espacially on $Ni_{5.0}Mg_6$/SBA-$B_1$(N). Consequently, the changes in relative intensity between the first (100) diffraction peak and those at higher angles suggest changes in pore wall thickness,[39,40] that can be related to the movement of particles inisde the pores.

On $Ni_{5.0}Rh_{0.5}$/SBA-$B_1$(N), the unit cell parameter was estimated to around 8.9 nm and maintained at this valut after reaction. The maintenance of the well-ordered hexagonal structure on both $Ni_{5.0}Ce_6$/SBA-$B_1$(N) and $Ni_{5.0}Rh_{0.5}$/SBA-$B_1$(N) samples is one of the possible explanations of their superior stability in DRM.

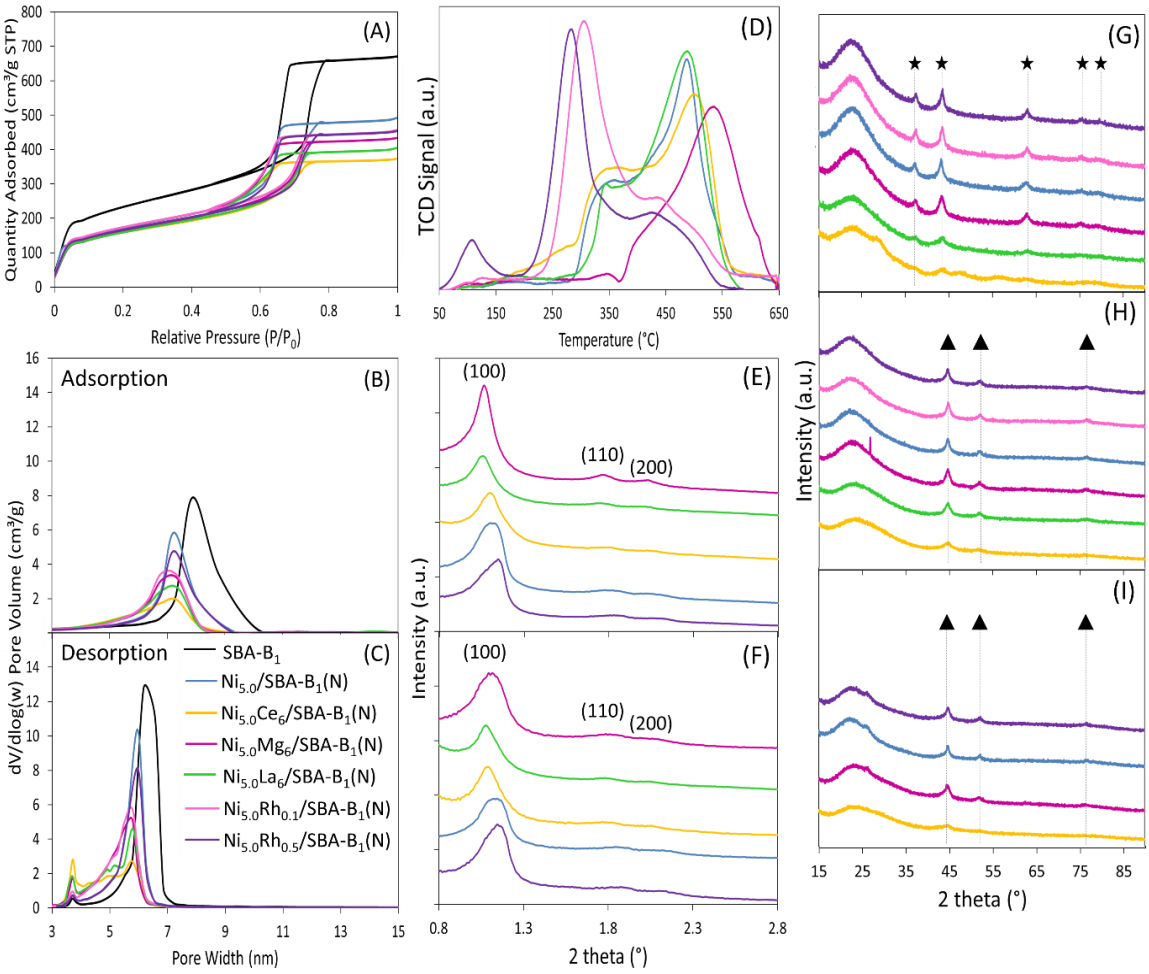


Figure V-8: (A) $N_2$ sorption isotherms, (B) adsorption and (C) desorption pore size distributions of calcined samples, (D) TPR profiles, small-angle XRD of (E) reduced and (F) spent catalysts and wide-angle XRD of (G) calcined, (H) reduced and (I) spent samples (★: NiO, ▲: $Ni^0$)

## V.3.5 Size and dispersion of supported nanoparticles

The crystalline phases formed and the mean particle diameter sizes were obtained from the wide-angle XRD patterns (Fig. V-8G,H,I), which are similar to previously obtained diffractograms with narrow peaks typical of NiO nanoparticles (ICDD 73-1523) with a face-centered cubic lattice (Fm-3m) for calcined samples (Fig. V-8G) and peaks of metallic $Ni^0$ nanoparticles (ICDD 65-0380) with a face-centered cubic lattice (Fm-3m) on both reduced (Fig. V-8H) and spent (Fig. V-8I) samples. Although not clearly distinguished, the peaks at 29, 34, 48, 57, and 70° on calcined $Ni_{5.0}Ce_6/SBA\text{-}B_1(N)$ are assignable to cerium oxide (ICDD 81-0792) with a face-centered cubic

lattice (Fm-3m). The characteristic peaks of Mg, La or Rh oxides on the corresponding impregnated samples are not visible, suggesting good dispersion of these oxides in the support.

More importantly, the widths of the observed diffraction peaks varied from one sample to another, indicating that the mean size of metallic nickel and nickel oxides is not identical on all supports (Fig. V-8G,H,I and Table V-2). In general, the order in NiO nanoparticles size (that will be precised below) was almost maintained for metallic $Ni^0$ nanoparticles on reduced samples, without major sintering of the active phase during reduction. Furthermore, the width of the diffraction peaks did not vary between reduced and spent catalysts, indicating once again the beneficial confinement effect of the SBA-15 mesoporous support in the prevention of particles growth.

From the FWHM analysis of the peak at 43°, the average size of NiO crystallographic domains decreased in the following order: $Ni_{5.0}$/SBA-$B_1$(N) > $Ni_{5.0}Mg_6$/SBA-$B_1$(N) > $Ni_{5.0}Ce_6$/SBA-$B_1$(N) > $Ni_{5.0}La_6$/SBA-$B_1$(N). The co-impregnation of promoters with Ni contributes in the reduction of the nickel particles size. This is in line with the previous observation of majorly small NiO particles based on the TPR profiles.

Contrary to what was found earlier in Chapter III, the promotion with Ce in this chapter contributed in the formation of smaller NiO particles, similar to what is usually reported in literature.[41,42,43] Although being close to the thermodynamic equilibirum during the catalytic teste, the enhanced stability observed on $Ni_{5.0}Ce_6$/SBA-$B_1$(N) can be mainly related to the use of co-impregnation in this chapter in comparison to sequential impregnation ($Ni_{5.0}Ce_6$/SBA-$A_2$ sample) in Chapter III (sample prepared by addition of cerium oxide precursor to SBA-15 support, calcination then addition of nickel nitrate to the resulting $Ce_6$/SBA-$A_2$). The latter procedure resulted in heterogeneous ditribution of Ni and Ce on the support, since some grains contained only Ce-species while others were only filled with NiO. However, on the co-impregnated $Ni_{5.0}Ce_6$/SBA-$B_1$(N) sample, both Ni and $CeO_2$ nanoparticles are found homogeneously dispersed on the grains of the support, as validated by EDS measurements (Fig. V-9). This intercation between the two species was important for the reduction of the NiO nanoparticles size and the enhancement of the catalytic perfomance. Similar interactions due to homogeneous Ni-Ce distribution were also observed on CeNi/SBA-15 catalysts for ethanol steam reforming.[44] In both cases, the strong interaction between nickel particles and ceria, together with the confinement of SBA-15 support,

retained the small nickel particles size, revealing excellent sintering-resistance and high catalytic activity.

In a similar manner, the average size of NiO crystallographic domains decreased in the following order: $Ni_{5.0}Rh_{0.5}$/SBA-$B_1$(N) > $Ni_{5.0}Rh_{0.1}$/SBA-$B_1$(N) > $Ni_{5.0}$/SBA-$B_1$(N). The addition of Rh slightly increased the NiO particles size, probably because rhodium was added in the second place after nickel deposition on SBA-B and calcination.

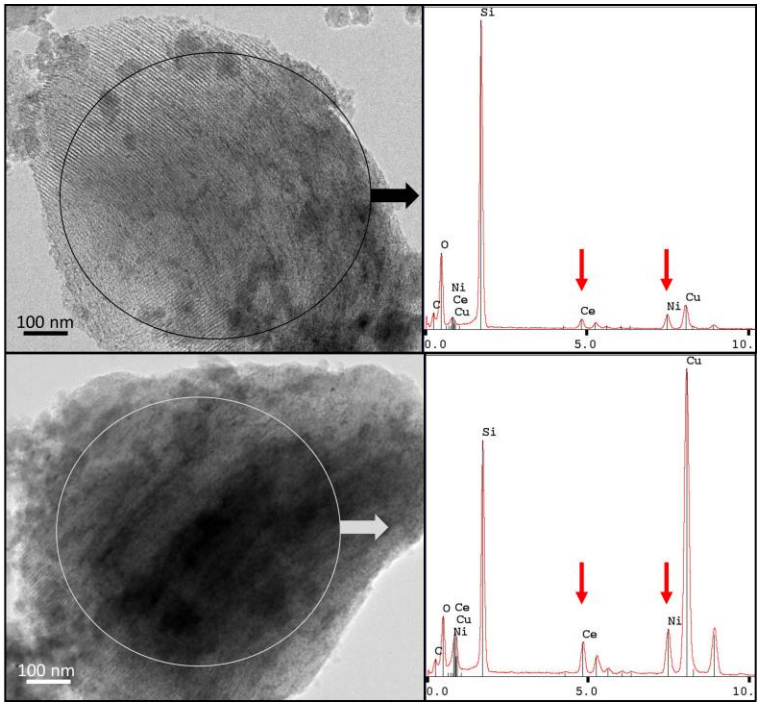


Figure V-9: TEM micrographs of calcined $Ni_{5.0}Ce_6$/SBA-$B_1$(N) sample with corresponding EDS of the indicated areas

On the TEM images of the spent $Ni_{5.0}Ce_6$/SBA-$B_1$(N) catalyst (Fig. V-10a), almost no carbon deposition is observed, in agreement with the highest stablility of this catalyst. In opposition, some carbon deposition is seen on spent $Ni_{5.0}Rh_{0.5}$/SBA-$B_1$(N). Nevertheless, similar to previous observations on $Ni_{5.0}$/SBA-$B_1$(N), good dispersion of metallic nickel particles is maintained for the particles located inside the grains (Fig. V-10b). Carbon deposition is only detected on the external particles (Fig. V-10b'). This suggests that the confinement of Ni nanoparticles inside the pores of the SBA-15 support favors their carbon-resistance as will be indeed discussed in details in Chapter VI.

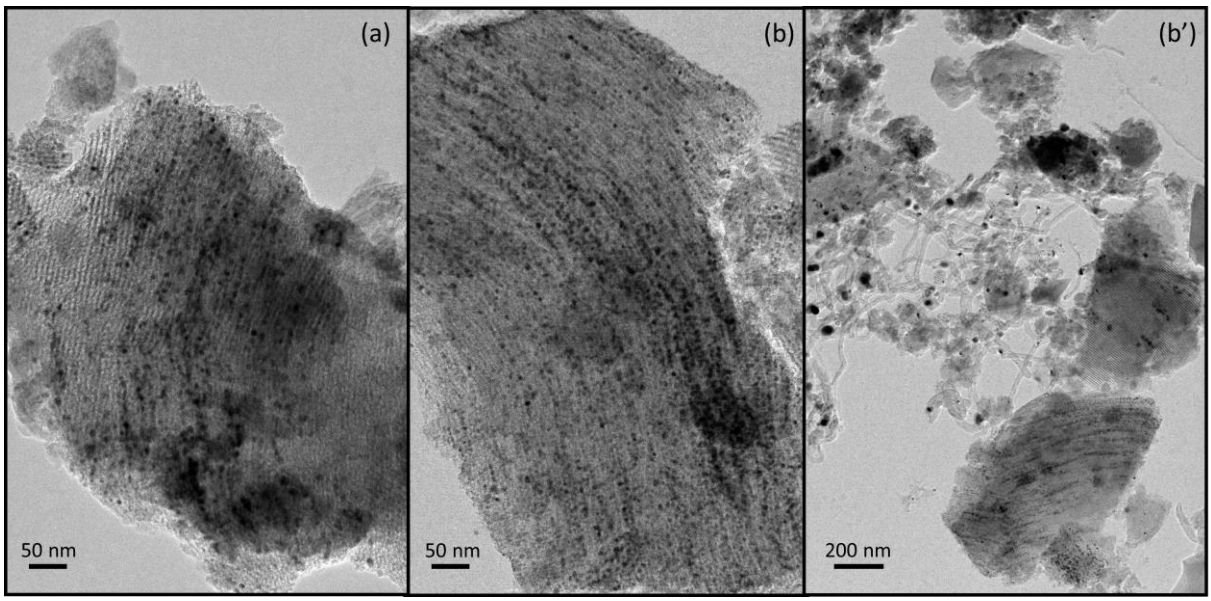


Figure V-10: TEM images of spent (a) $Ni_{5.0}Ce_6/SBA\text{-}B_1(N)$ and (b,b') $Ni_{5.0}Rh_{0.5}/SBA\text{-}B_1(N)$ catalysts

Summary of section V.3: Effect of promoters/dopants

- The addition of Ce or Rh to Ni/SBA-15 resulted in an amelioration of the catalytic stability in dry reforming of methane at 650°C for more than 60 hours.
- While the addition of Ce did not affect the reduction behavior of NiO, the $H_2$ spillover effect of Rh was reflected by a shift of the reduction profile towards lower temperatures.
- The preservation of the 2D hexagonal mesoporous structure was validated by small-angle XRD.
- The superior perfomance of $Ni_{5.0}Ce_6/SBA\text{-}B_1(N)$ and $Ni_{5.0}Rh_{0.5}/SBA\text{-}B_1(N)$ was attributed to the formation of small metallic nickel particles well-dispersed inside the pores of SBA-15 support and associated to low carbon deposition observed by TEM.

## V.4 Influence of the nature of support – preliminary results

Mesoporous SBA-15 revealed important advantages related to the good confinement of metallic nickel particles, limiting both sintering and carbon deposition and contributing in the superior catalytic performance in dry reforming of methane. Moreover, the addition of either Ce or Rh resulted in an improvement of the catalytic stability for reasons clarified above. Nevertheless, cerium is much cheaper than noble metals, therefore, it is much more preferred from an economic

point of view. Consequently, the idea of the following part is to combine the benefits of both mesoporous SBA-15 support and $CeO_2$ oxides in the formulation of a mesoporous $CeO_2$ support than can stabilize nickel particles and maintain high catalytic activity throughout the test.

In order to achieve this goal, three catalysts were prepared according to the hard-template procedure described in Chapter II:

- $Ni_{6.2}/CeO_2$-C(N), prepared from **SBA-C** template (hydrothermally treated at 130°C for 24 hours) with **6.2 wt% Ni** loading,
- $Ni_{6.2}/CeO_2$-A(N), prepared from **SBA-A** template (not subjected to hydrothermal treatment) with **6.2 wt% Ni** loading,
- $Ni_{16}/CeO_2$-C(N), prepared from **SBA-C** template (hydrothermally treated at 130°C for 24 hours) with **16 wt% Ni** loading.

### V.4.1 Catalytic activity and stability

As before, after reduction at 650°C for 2 hours, the catalytic activity was measured between 250 and 750°C (Fig. V-11A,B). The reactants conversions and $H_2$:CO ratios start to increase with temperature after 500°C. This temperature is higher than the one usually encountered on the previous Ni/SBA-15 samples studied. While $Ni_{6.2}/CeO_2$-C(N) and $Ni_{6.2}/CeO_2$-A(N) show similar performances, the increment of nickel loading on $Ni_{16}/CeO_2$-C(N) catalyst enhances the catalytic activity and favors higher conversions and higher $H_2$:CO ratio. Nevertheless, these values remain lower than the expected ones, calculated under the used operating conditions.

At steady-state operations (Fig. V-11A',B'), i.e. at constant temperature of 650°C, all the catalysts are relatively stable for 12 hours under reactants stream. Although all catalysts showed limited levels of conversions and $H_2$:CO ratio, quite far from equilibrium, their values depended greatly on the nature of the template employed and on the nickel loading. The conversions and $H_2$:CO ratios decreased in the following order: $Ni_{16}/CeO_2$-C(N) > $Ni_{6.2}/CeO_2$-C(N) > $Ni_{6.2}/CeO_2$-A(N). This order suggests that the samples prepared from the SBA-C template ($Ni_{6.2}/CeO_2$-C(N) and $Ni_{16}/CeO_2$-C(N) samples) were more active than the one issuing from the SBA-A template ($Ni_{6.2}/CeO_2$-A(N) sample). The increase in nickel loading favors higher conversions of $CH_4$ and $CO_2$, in agreement with more numerous active metal sites.

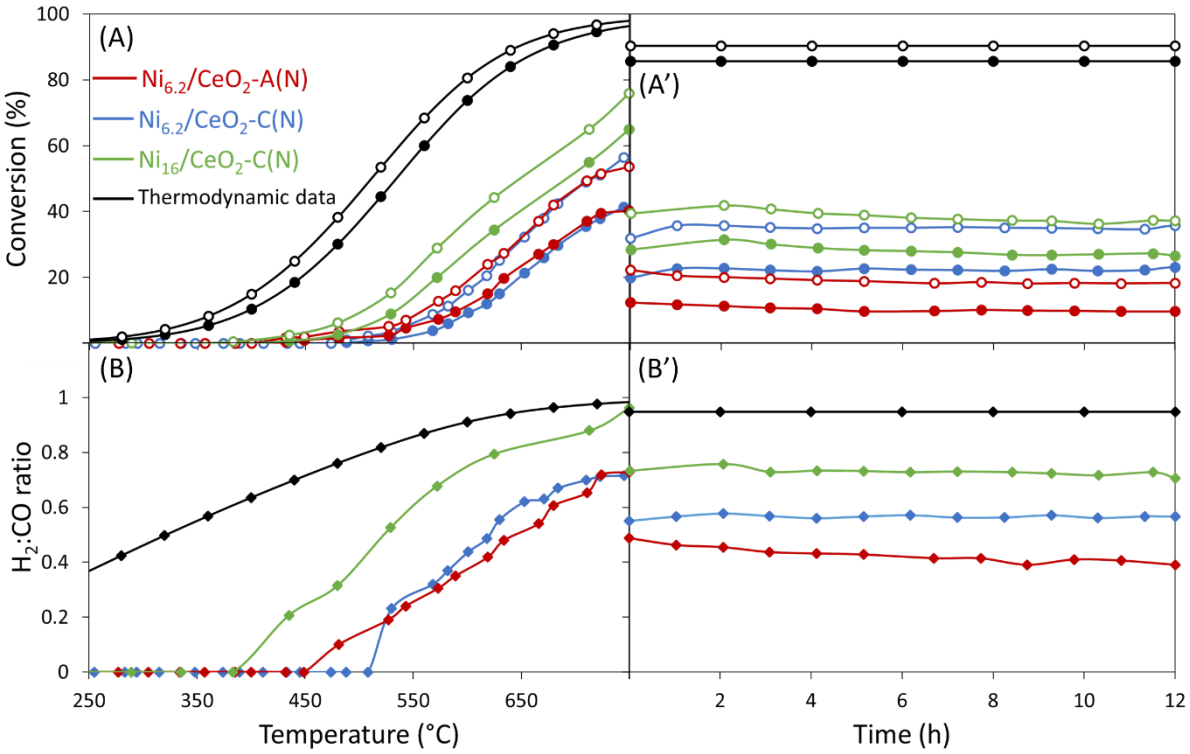


Figure V-11: Variation of $CH_4$ (filled circles) and $CO_2$ (empty circles) conversions and $H_2$:CO ratio as a function of temperature (A,B) and time at 650°C (A',B') at 1 bar, 7200 $mL.g^{-1}.h^{-1}$ and $CH_4$:$CO_2$:Ar = 5:5:90

## V.4.2 Porosity of calcined samples

The evaluation of the textural properties by $N_2$ sorption show type IV(a) isotherm for all samples, revealing the mesoporous aspect of the samples (Fig. V-12A). However, the shape of the hysteresis loop varies depending on the sample. In details, both $Ni_{6.2}/CeO_2$-C(N) and $Ni_{16}/CeO_2$-C(N) samples present an H1 type hysteresis loop, but the adsorption and desorption branches of the $Ni_{16}/CeO_2$-C(N) sample are more parallel while the loop is more inclined for $Ni_{6.2}/CeO_2$-C(N) sample. This indicates a more uniform mesoporous arrangement on the $Ni_{16}/CeO_2$-C(N) sample.[45] On the other hand, the $Ni_{6.2}/CeO_2$-A(N) sample presents a type H3 hysteresis loop, attributed to the formation of partially filled macropores.

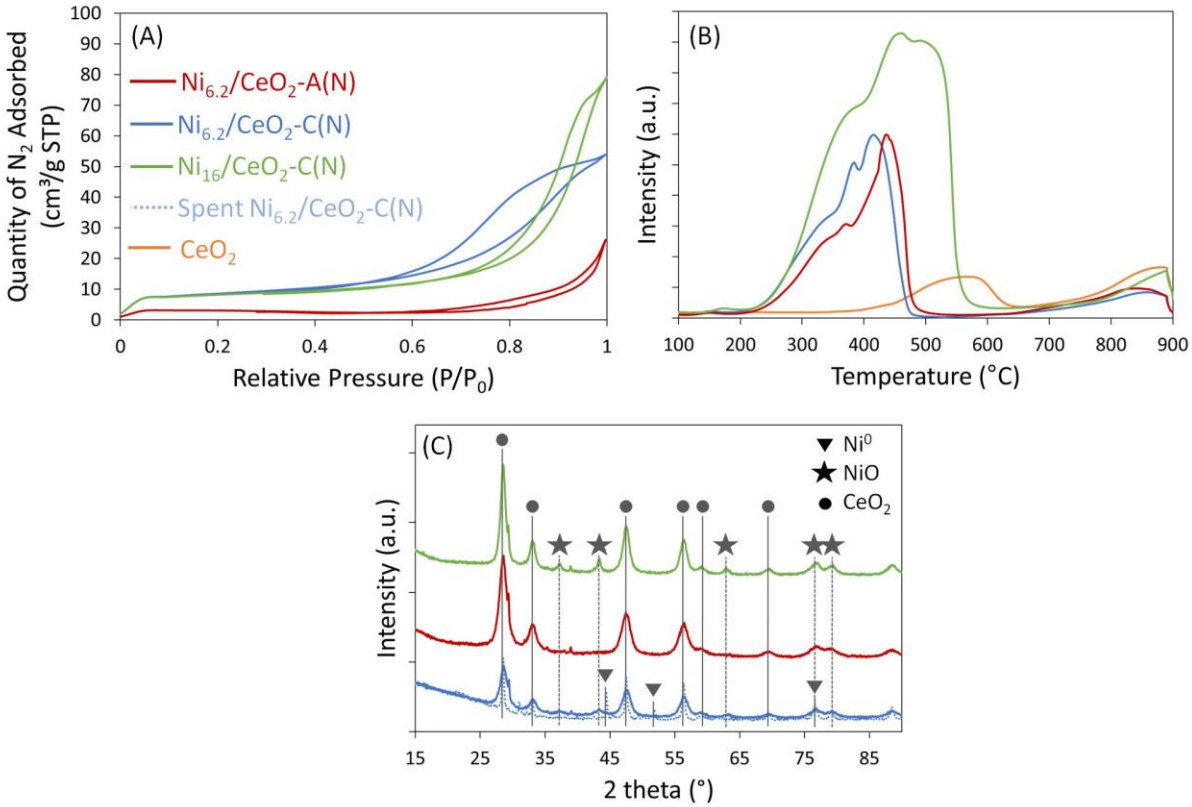


Figure V-12: (A) $N_2$ sorption isotherms, (B) TPR profiles and (C) XRD patterns of Ni/$CeO_2$ samples

The use of SBA-A as hard-template for the $Ni_{6.2}/CeO_2$-A(N) preparation resulted in a material with very low surface area (Table V-3), while the samples issuing from SBA-C template ($Ni_{6.2}/CeO_2$-C(N) and $Ni_{16}/CeO_2$-C(N)) had similar surface areas, regardless of the nickel content (~30 $m^2.g^{-1}$). Consequently, the use of SBA-C template appears to be more convenient for such preparations since the hydrothermal treatment decreases the microporosity and results in larger pore sizes and more condensed silica walls,[46,47] as explained earlier. The larger pores provide more space to accommodate the nickel particles and maintain the mesoporous structure.

The lower performance of these catalysts in comparison to the previous SBA-15 supported materials can be thus explained by their poor mesoporous structure not well-defined. In addition, the surface areas of the resulting samples were unfortunately lower than those usually reported in literature. In fact, NiO/$CeO_2$ samples prepared from KIT-6 hard-template had surface areas of 80-110 $m^2.g^{-1}$,[48] Ag/$CeO_2$-HP sample prepared from SBA-15[49] had a surface area also within this range while even

higher value was obtained on Au/$CeO_2$-48 sample resulting from MCM-48.[50] These differences can be mainly related to different preparation conditions. The lower values obtained in this study can be explained first by the two filling cycles of $CeO_2$ that were done before silica removal and second by the consecutive calcination steps applied after each cycle and after silica removal.

Table V-3: Characteristics of Ni/$CeO_2$ samples

| Catalyst | BET Surface Area ($m^2/g$) | Mesoporous Volume ($cm^3/g$) | $CeO_2$ Size[a] (nm) | NiO Size[b] (nm) | Total Hydrogen Consumption (µmol/g) |
|---|---|---|---|---|---|
| $Ni_{6.2}/CeO_2$-A(N) | 9 | 0.03 | 4.3 | Not detected | 5607 |
| $Ni_{6.2}/CeO_2$-C(N) | 29 | 0.08 | 4.6 | 5.6 | 6600 |
| $Ni_{16}/CeO_2$-C(N) | 28 | 0.11 | 5.7 | 10.0 | 16445 |

[a]Calculated using Scherrer equation, based on the diffraction peak at 47°
[b]Calculated using Scherrer equation, based on the diffraction peak at 43°

### V.4.3 Reducibility of the samples

Insights on the reducibility of NiO particles, revealed by $H_2$-TPR (Fig. V-12B), are as follows. First, the $CeO_2$ support presents a small reduction peak at 550°C, attributable to surface reduction of $Ce^{4+}$ to $Ce^{3+}$,[51] whereas the main reduction peak does not appear before 800°C.[52,53] Second, the reduction profiles of $Ni_{6.2}/CeO_2$-C(N) and $Ni_{6.2}/CeO_2$-A(N) samples are quite identical, due to the similar nickel loading, also reflected by comparable hydrogen consumption (Table V-3). The increase in nickel loading in $Ni_{16}/CeO_2$-C(N) from 6.2 to 16 wt% caused an increase of hydrogen consumption, due to the increment of NiO content on the support. Furthermore, complete reduction of NiO is observed on all samples up to 650°C, the temperature that will be used to activate the catalysts.

### V.4.4 Identification and size of the supported nanoparticles

The nature of the crystalline phases obtained on the calcined samples was identified by XRD (Fig. V-12C), as before. For the three samples, the diffraction peaks detected at 28, 33, 47, 56, 59 and 69°, are attributed to $CeO_2$ particles (ICDD 75-8371) with a cubic lattice (Fm-3m). The remaining

diffraction peaks detected are attributed to NiO particles (ICDD 75-0197) having a cubic structure (Fm-3m). On $Ni_{6.2}/CeO_2$-A(N) sample, the NiO characteristic peaks were not detectable, whereas their size increased on the remaining samples with increasing nickel loading (Table V-3). The crystallite size domains of the $CeO_2$ particles were almost the same on all samples, due to the similar preparation method employed.

The evaluation of the spent $Ni_{6.2}/CeO_2$-C(N) catalyst by XRD (Fig. V-12C) reveals diffraction peaks at 44, 52 and 76° attributable to $Ni^0$ particles (ICDD 01-1258) having cubic structure (Fm-3m). The widths of these peaks is very small, indicative of massive active phase sintering from 4.3 nm of NiO on the calcined sample to 56.2 nm of $Ni^0$ on the spent catalyst. This phenomenon suggests a possible collapse of the mesoporous structure, which will be validated by further experiments like low-angle XRD, $N_2$ sorption and TEM.

Summary of section V.4: Influence of the nature of support – preliminary results

- The hard-template method using SBA-15 was employed to prepare the mesoporous $CeO_2$.
- $Ni/CeO_2$ samples with low surface areas were obtained, but the mesoporous structure was better defined when the SBA-15 template was hydrothermally treated at 130°C.
- Although low levels of conversion were obtained on these catalysts, they were rather stable at 650°C for at least 12 hours.
- The amelioration of the synthesis of such materials might allow them to become potential candidates for this type of applications.

## V.5 Conclusion

Different activities and stabilities were observed on the various catalysts studied, depending on the preparation procedure.

First, by varying the nickel deposition method on SBA-B, the most stable catalyst was the one prepared by two solvents method. Its superior performance was attributed to its well-defined mesoporous structure, narrow pore size distribution, easier reducibility of NiO and formation of the smallest $Ni^0$ nanoparticles.

Second, the use of nickel chloride salt generated large nickel particles on the external surface of the support. Their lack of confinement facilitated their mobility and resulted in large nickel clusters during reaction, leading to rapid catalyst deactivation. The use of nickel nitrate, nickel acetate or direct reduction without calcination allowed high conversions to be reached and maintained. The formation of surface nickel silicates in strong interaction with the support on the sample prepared using the acetate precursor salt did not improve the catalytic activity. The direct reduction can be a promising route that still faces industrial concerns, mainly related to nickel reoxidation upon contact with air.

Third, the addition of Mg or La did not ameliorate the performance of $Ni_{5.0}$/SBA-$B_1$(N). However, the stability of the latter was enhanced through Ce-promotion or Rh-doping. On one hand, rhodium improved the reducibility of NiO due to its $H_2$ spilover effect whereas on the other hand, the co-presence of Ni and Ce on the same silica grains was important for the enhancement of stability.

Forth, the use of SBA-15 as a hard template for the preparation of mesoporous $CeO_2$ support is a promising strategy. However, the experimental procedure still needs to be improved in order to achieve better structured mesoporous materials with higher surface areas for increased dispersion of the active phase.

These studied parameters help in the elaboration of a stable catalyst that can maintain high $CH_4$ and $CO_2$ conversions for long time. The $Ni_{5.0}$/SBA-$B_1$(N) sample prepared by two solvents impregnation using nickel nitrate remains among the most promising catalysts. However, it is important to check if the stable catalysts can still maintain high activity under more severe conditions (lower space velocity, higher pressure…).These tests will constitute one of the main objectives of the following chapter. Furthermore, throughout the study we have shown that carbon deposition (on external particles) varied depending on the structure of the support and the methods of preparation of the catalyst. This challenging problem in dry reforming of methane will be addressed in more details in Chapter VI, based on the characterizations of the various spent catalysts obtained.

**Outcome of this work:**

- **M.N. Kaydouh**, N. El Hassan, H. El Zakhem, A. Davidson, S. Casale, P. Massiani, IEEE conference paper
  DOI: 10.1109/MedGO.2015.7330335
- **Oral presentation** at the MedGO conference, "Rh-Ni/SBA-15 prepared by two solvents method as stable catalysts for the dry reforming of methane at high pressure", Lebanon 2015.
- **Oral presentation** at the IZC-18 conference, "Influence of nickel confinement in SBA-15 on catalytic performances in methane dry reforming", Brazil 2016.

## V.6 References


[1] Y. Park, T. Kang, J. Lee, P. Kim, H. Kim, J. Yi, *Single-step preparation of Ni catalysts supported on mesoporous silicas (SBA-15 and SBA-16) and the effect of pore structure on the selective hydrodechlorination of 1,1,2-trichloroethane to VCM*, Catalysis Today 97 (2004) 195-203.

[2] A. Carrero, J.A. Calles, A.J. Vizcaino, *Hydrogen production by ethanol steam reforming over Cu-Ni/SBA-15 supported catalysts prepared by direct synthesis and impregnation*, Applied Catalysis A: General 327 (2007) 82-94.

[3] M. Ogura, R. Guillet-Nicolas, D. Brouri, S. Casale, J. Blanchard, K.A. Cychosz, M. Thommes, C. Thomas, *Insights into the accessibility of Zr in Zr/SBA-15 mesoporous silica supports with increasing Zr loadings*, Microporous and Mesoporous Materials 225 (2016) 440-449.

[4] B. Mile, D. Stirling, M.A. Zammitt, A. Lovell, M. Webb, *The Location of nickel oxide and nickel in silica-supported catalysts: Two forms of "NiO" and the assignment of temperature-programmed reduction profiles*, Journal of Catalysis 114 (1988) 217-229.

[5] H.M. Swaan, V.C.H. Kroll, G.A. Martin, C. Mirodatos, *Deactivation of supported nickel catalysts during reforming of methane by carbon dioxide*, Catalysis Today 21 (1994) 571-578.

[6] N. Wang, Z. Xu, J. Deng, K. Shen, X. Yu, W. Qian, W. Chu, F. Wei, *One-pot synthesis of ordered mesoporous NiCeAl oxide catalysts and a study of their performance in methane dry reforming*, ChemCatChem 6 (2014) 1470-1480.

[7] J. Taghavimoghaddam, G.P. Knowles, A.L. Chaffee, *Preparation and characterization of mesoporous silica supported cobalt oxide as a catalyst for the oxidation of cyclohexanol*, Journal of Molecular Catalysis A: Chemical 358 (2012) 79-88.

[8] S. Wang, G.Q. Lu, *Reforming of methane with carbon dioxide over $Ni/Al_2O_3$ catalysts: Effect of nickel precursor*, Applied Catalysis A: General 169 (1998) 271-280.

[9]K. Urasaki, Y. Tanpo, Y. Nagashima, R. Kikuchi, S. Satokawa, *Effects of preparation conditions of Ni/$TiO_2$ catalysts for selective CO methanation in the reformate gas*, Applied Catalysis A: General 452 (2013) 174-178.

[10] J. Manuel García-Vargas, J. Luís Valverde, A. de Lucas-Consuegra, B. Gómez-Monedero, P. Sánchez, F. Dorado, *Precursor influence and catalytic behaviour of Ni/$CeO_2$ and Ni/SiC catalysts for the tri-reforming process*, Applied Catalysis A: General 431-432 (2012) 49-56.

[11] C. Cornu, J.L. Bonardet, S. Casale, A. Davidson, S. Abramson, G. Andre, F. Porcher, I. Grcic, V. Tomasic, D. Vujevic, N. Koprivanac, *Identification and location of iron species in Fe/SBA-15 Catalysts: Interest for catalytic Fenton reactions*, Journal of Physical Chemistry C 116 (2012) 3437-3448.

[12] C. Hoang-Van, Y. Kachaya, S.J. Teichner, *Characterization of nickel catalysts by chemisorption techniques, X-ray diffraction and magnetic measurements: Effects of support, precursor and hydrogen pretreatment*, Applied Catalysis 46 (1989) 281-296.

[13] R. Shi-Biao, S. Zhou, Z. Ping, W. Zhi-Cai, L. Zhi-Ping, P. Chun-Xiu, K. Shi-Gang, S. Heng-Fu, *Highly dispersed Ni/SBA-15 catalysts prepared with different nickel salts as nickel precursors: Effects of activation atmospheres*, Journal of Fuel Chemistry and Technology 42(5) (2014) 591-596.

[14] W.J. Cai, L.P. Qian, B. Yue, H. He, *Rh doping effect on coking resistance of Ni/SBA-15 catalysts in dry reforming of methane*, Chinese Chemical Letters 25 (2014) 1411-1415.

[15] L. Qian, Z. Ma, Y. Ren, H. Shi, B. Yue, S. Feng, J. Shen, S. Xie, *Investigation of La promotion mechanism on Ni/SBA-15 catalysts in $CH_4$ reforming with $CO_2$*, Fuel 122 (2014) 47-53.

[16] M.E. Gálvez, A. Albarazi, P. Da Costa, *Enhanced catalytic stability through non-conventional synthesis of Ni/SBA-15 for methane dry reforming at low temperatures*, Applied Catalysis A: General 504 (2015) 143-150.

[17] J. Juan-Juan, M.C. Roman-Martinez, M.J. Illan-Gomez, *Nickel catalyst activation in the carbon dioxide reforming of methane-Effect of pretreatments*, Applied Catalysis A: General 355 (2009) 27-32.

[18] M. Tao, X. Meng, Y. Lv, Z. Bian, Z. Xin, *Effect of impregnation solvent on Ni dispersion and catalytic properties of Ni/SBA-15 for CO methanation reaction*, Fuel 165 (2016) 289-297.

[19] A. Ungureanu, B. Dragoi, A. Chirieac, S. Royer, D. Duprezb, E. Dumitriu, *Synthesis of highly thermostable copper-nickel nanoparticles confined in the channels of ordered mesoporous SBA-15 silica*, Journal of Materials Chemistry 21 (2011) 12529-12541.

[20] D. Liu, X.Y. Quek, H. Hui, A. Wah, G. Zeng, Y. Li, Y. Yang, *Carbon dioxide reforming of methane over nickel-grafted SBA-15 and MCM-41 catalysts*, Catalysis Today 148 (2009) 243-250.

[21] F. Li, X. Yi, W. Fang, *Effect of organic nickel precursor on the reduction performance and hydrogenation activity of Ni/$Al_2O_3$ catalysts*, Catalysis Letters 130 (2009) 335-340.

[22] N. Tabaja, S. Casale, D. Brouri, A. Davidson, H. Obeid, J. Toufaily, T. Hamieh, *Quantum-dots containing Fe/SBA-15 silica as ''green'' catalysts for the selective photocatalytic oxidation of alcohol (methanol, under visible light)*, Comptes Rendus Chimie 18 (2015) 358-367.

[23] G. Wu, C. Zhang, S. Li, Z. Han, T. Wang, X. Ma, J. Gong, *Hydrogen production via glycerol steam reforming over Ni/$Al_2O_3$: Influence of nickel precursors*, ACS Sustainable Chemistry & Engineering 1 (2013) 1052-1062.

[24] S. Li, J. Gong, *Strategies for improving the performance and stability of Ni-based catalysts for reforming reactions*, Chemical Society Reviews 43(2014) 7245-7256.

[25] V. Dal Santo, A. Gallo, A. Naldoni, M. Guidotti, R. Psaro, *Bimetallic heterogeneous catalysts for hydrogen production*, Catalysis Today 197 (2012) 190- 205.

[26] Y.T. Shah, T.H. Gardner, *Dry reforming of hydrocarbon feedstocks*, Catalysis Reviews: Science and Engineering, 56:4 (2014) 476-536.

[27] H.P. Ren, Y.H. Song, Q.Q. Hao, Z.W. Liu, W. Wang, J.G. Chen, J. Jiang, Z.T. Liu, Z. Hao, J. Lu, *Highly active and stable Ni-$SiO_2$ prepared by a complex-decomposition method for pressurized carbon dioxide reforming of methane*, Industrial & Engineering Chemistry Resources 53 (2014) 19077-19086.

[28] X. Yan, Y. Liu, B. Zhao, Z. Wang, Y. Wang, C. Liu, *Methanation over Ni/$SiO_2$: Effect of the catalyst preparation methodologies*, International Journal of Hydrogen Energy 38 (2013) 2283-2291.

[29] W. Curtis Conner, J.L. Falconer, *Spillover in Heterogeneous Catalysis*, Chemical Reviews 95 (1995) 759-708.

[30] R. Ueda, T. Kusakari, K. Tomishige, K. Fujimoto, *Nature of spilt-over hydrogen on acid sites in zeolites: Observation of the behavior of adsorbed pyridine on zeolite catalysts by means of FTIR*, Journal of Catalysis 194 (2000) 14-22.

[31] P. Djinovic, J. Batista, A. Pintar, *Efficient catalytic abatement of greenhouse gases: Methane reforming with $CO_2$ using a novel and thermally stable Rh-$CeO_2$ catalyst*, International Journal of Hydrogen Energy 37 (2012) 2699-2707.

[32] A.F. Lucrédio, J.M. Assaf, E.M. Assaf, *Methane conversion reactions on Ni catalysts promoted with Rh: Influence of support*, Applied Catalysis A: General 400 (2011) 156-165.

[33] W. Cai, F. Wang, A.C. Van Veen, H. Provendier, C. Mirodatos, W. Shenn, *Autothermal reforming of ethanol for hydrogen production over an Rh/$CeO_2$ catalyst*, Catalysis Today 138 (2008) 152-156.

[34] M. Ocsachoque, F. Pompeo, G. Gonzalez, *Rh-Ni/$CeO_2$-$Al_2O_3$ catalysts for methane dry reforming*, Catalysis Today 172 (2011) 226-231.

[35] N. El Hassan, M.N. Kaydouh, H. Geagea, H. El Zein, K. Jabbour, S. Casale, H. El Zakhem, P. Massiani, *Low temperature dry reforming of methane on rhodium and cobalt based catalysts: Active phase stabilization by confinement in mesoporous SBA-15*, Applied Catalysis A: General 520 (2016) 114-121.

[36] D. Zhao, J. Feng, Q. Huo, N. Melosh, G.H. Fredrickson, B.F. Chmelka, G.D. Stucky, *Triblock Copolymer Syntheses of Mesoporous Silica with Periodic 50 to 300 Angstrom Pores*, Science 279 (1998) 548-552.

[37] S.P. Naik, S.P. Elangovan, T. Okubo, I. Sokolov, *Morphology Control of Mesoporous Silica Particles*, Journal of Physical Chemistry C 111 (2007) 11168-11173.

[38] M. Kruk, M. Jaroniec, *Characterization of the Porous Structure of SBA-15*, Chemistry of Materials 12 (2000) 1961-1968.

[39] M. Choi, W. Heo, F. Kleitz, R. Ryoo, *Facile synthesis of high quality mesoporous SBA-15 with enhanced control of the porous network connectivity and wall thickness*, Chemical Communications (2003) 1340-1341.

[40] J. Sauer, F. Marlow, F. Schuth, *Simulation of powder diffraction patterns of modified ordered mesoporous materials*, Physical Chemistry Chemical Physics 3 (2001) 5579-5584.

[41] J. Zhu, X. Peng, L. Yao, J. Shen, D. Tong, C. Hu, *The promoting effect of La, Mg, Co and Zn on the activity and stability of Ni/$SiO_2$ catalyst for $CO_2$ reforming of methane*, International Journal of Hydrogen Energy 36 (2011) 7094-7104.

[42] N. Wang, X. Yu, K. Shen, W. Chu, W. Qian, *Synthesis, characterization and catalytic performance of MgO-coated Ni/SBA-15 catalysts for methane dry reforming to syngas and hydrogen*, International Journal of Hydrogen Energy 38 (2013) 9718-9731.

[43] Y. Fu, Y. Wu, W. Cai, B. Yue, H. He, *Promotional effect of cerium on nickel-containing mesoporous silica for carbon dioxide reforming of methane*, Science China Chemistry 58 (2015) 148-155.

[44] D. Li, L. Zeng, X. Li, X. Wang, H. Ma, S. Assabumrungrat, J. Gong, *Ceria-promoted Ni/SBA-15 catalysts for ethanol steam reforming with enhanced activity and resistance to deactivation*, Applied Catalysis B: Environmental 176-177 (2015) 532-541.

[45] M. Thommes, K. Kaneko, A.V. Neimark, J.P. Olivier, F. Rodriguez-Reinoso, J. Rouquerol, K.S.W. Sing, *Physisorption of gases, with special reference to the evaluation of surface area and pore size distribution (IUPAC Technical Report)*, Pure Applied Chemistry 87(9-10) (2015) 1051-1069.

[46] M. Imperor-Clerc, P. Davidson, A. Davidson, *Existence of a Microporous Corona around the Mesopores of Silica-Based SBA-15 Materials Templated by Triblock Copolymers*, Journal of American Chemical Society 122 (2000) 11925-11933.

[47] A. Galarneau, H. Cambon, F. Di Renzo, F. Fajula, *True Microporosity and Surface Area of Mesoporous SBA-15 Silicas as a Function of Synthesis Temperature*, Langmuir 17 (2001) 8328-8335.

[48] C. Tang, J. Li, X. Yao, J. Sun, Y. Cao, L. Zhang, F. Gao, Y. Deng, L. Dong, *Mesoporous NiO-$CeO_2$ catalysts for CO oxidation: Nickel content effect and mechanism aspect*, Applied Catalysis A: General 494 (2015) 77-86.

[49] Z. Qu, F. Yu, X. Zhang, Y. Wang, J. Gao, *Support effects on the structure and catalytic activity of mesoporous Ag/$CeO_2$ catalysts for CO oxidation*, Chemical Engineering Journal 229 (2013) 522-532.

[50] F. Ying, S. Wang, C.T. Au, S.Y. Lai, *Highly active and stable mesoporous Au/$CeO_2$ catalysts prepared from MCM-48 hard-template*, Microporous and Mesoporous Materials 142 (2011) 308-315.

[51] I. Luisetto, S. Tuti, E. Di Bartolomeo, *Co and Ni supported on $CeO_2$ as selective bimetallic catalyst for dry reforming of methane*, International Journal of Hydrogen Energy 37 (2012) 15992-15999.

[52] M. Yu, Y. Zhu, Y. Lu, G. Tong, K. Zhu, X. Zhou, *The promoting role of Ag in Ni-$CeO_2$ catalyzed $CH_4$-$CO_2$ dry reforming reaction*, Applied Catalysis B: Environmental 165 (2015) 43-56.

[53] Z. Wang, X. Shao, A. Larcher, K. Xie, D. Dong, C.Z. Li, *A study on carbon formation over fibrous NiO/$CeO_2$ nanocatalysts during dry reforming of methane*, Catalysis Today 216 (2013) 44-49.

# CHAPTER VI

# Carbon Analysis and More Severe Reaction conditions

We have seen in the previous chapter that the use of two solvents method, nickel nitrate precursor salt and direct reduction are all factors that contribute in the good dispersion of small Ni nanoparticles inside the SBA-15 support, for a suitable catalyst in dry reforming of methane. The $Ni_{5.0}$/SBA-$B_1$(N) marked superior catalytic performances in comparison to the remaining catalysts, regardless of the carbon deposition on the external support surface. In this last chapter of the thesis, we will carefully examine carbon deposition on all studied catalysts and we will analyze in more details the carbon deposition behavior with time on the $Ni_{5.0}$/SBA-$B_1$(N) sample. In addition, the latter will be tested under more severe reaction conditions like higher space velocities. Furthermore, since the $Ni_{5.0}Rh_{0.5}$/SBA-$B_1$(N) catalyst showed a better stability than $Ni_{5.0}$/SBA-$B_1$(N), it will be evaluated at higher pressure and after regeneration.

## VI.1 Carbon analysis on spent catalysts

Many researchers have been interested in the study of the growth of carbon filaments and the formation of carbon systems with defined shapes (sheets, nanotubes…).[1,2] Helveg et al. focused on the growth of carbon nanofibers, in particular, and observed an elongation of the Ni particle due to the formation of graphene layers at the interface.[3] After some time, the nickel particle contracts to its initial spherical shape. The growth of the nanofiber continues with this periodic elongation/contraction manner and it only stops when the particle becomes completely encapsulated.

Considering the metallic nickel nanoparticles well-confined inside the SBA-15 porosity described in previous chapters, such carbon growth process cannot be considered because of the limited space inside the pores that prevents any carbon nanotube formation around the metal particle. In opposition, external nickel particles induce the diffusion of carbon on their surface.[4] The kind of carbon species formed on these particles is influenced by the metal-support interaction.[5,6] In details, when the Ni metallic particle is away from the support, it can be easily encapsulated with carbon to form shell-like deposits (Fig. VI-1). This type completely covers the nickel particle, blocking the reaction and causing deactivation.[7] In the case of weak metal-support interaction, the

metallic Ni particle can be lifted with the carbon nucleation to form carbon nanotubes (Fig. VI-1). The Ni particle on top of such nanotubes remains accessible, allowing the reaction to proceed.[8,9] This type is not toxic but can cause plugging of the pores or even of the reactor, and sometimes catalyst cracking.

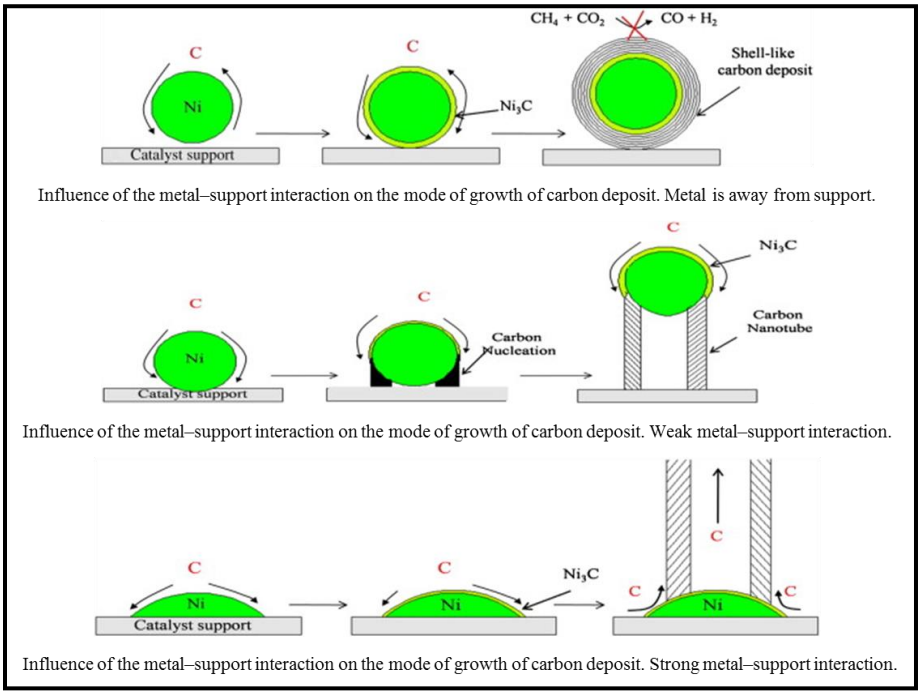


Figure VI-1: Influence of metal-support interaction on the mode of growth of carbon deposit[5]

In dry reforming of methane, the reaction equilibrium for the main DRM reaction (R1) is influenced by the simultaneous reverse water-gas shift reaction (RWGS, R2). At 650°C, carbon deposition on the surface of the catalyst can be generated by $CH_4$ decomposition (R3) and/or Boudouard reaction (R4).[10] This carbon deposition can be either gasified by the water formed during RWGS (R5) or accumulated on the catalyst leading to activity loss.[11]

$$CH_{4\,(g)} + CO_{2\,(g)} \rightarrow 2H_{2\,(g)} + 2CO_{\,(g)} \qquad (R1)$$

$$CO_{2\,(g)} + H_{2\,(g)} \rightarrow H_2O_{\,(g)} + CO_{\,(g)} \qquad (R2)$$

$$CH_{4\,(g)} \rightarrow C_{\,(s)} + 2H_{2(g)} \qquad (R3)$$

$$2CO_{\,(g)} \rightarrow C_{\,(s)} + CO_{2\,(g)} \qquad (R4)$$

$$C_{\,(s)} + H_2O_{\,(g)} \rightarrow CO/CO_{2\,(g)} + H_{2\,(g)} \qquad (R5)$$

Consequently, the catalyst deactivation rate depends greatly on the difference in rates of formation and gasification of carbon.[12] If the rate of carbon gasification (R5) is equal to or greater than that of its formation (R3, R4), carbon will not accumulate and stable activity will be maintained.[13]

During the present study, we have demonstrated that the occlusion of nickel nanoparticles inside well-defined porosity is an essential element for excellent stability of the catalysts. The confinement of nanoparticles inside the porous channels of the SBA-15 mesoporous supports does not only prevent active phase sintering but also inhibits carbon formation on the internal particles. In opposition, carbon deposition is highly promoted on external nanoparticles present outside the porous system (Fig. VI-2), as particularly observed on the poorly structured $Ni_{5.0}$/SBA-$A_3$(N) and $Ni_{5.0}$/meso-$SiO_2$(N), due to the weak metal-support interaction on the external surface.

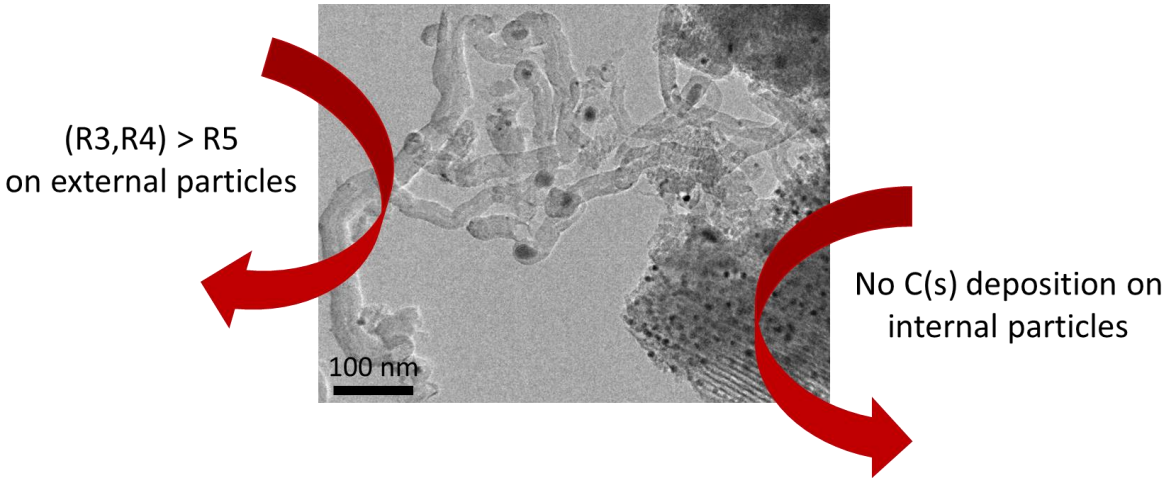


Figure VI-2: Illustration of carbon deposition and gasification rates

By analogy, the external particles can be compared to nanoparticles on non-porous supports. On such systems, many authors attributed the reduction of carbon deposition to the decrease of metal particle size, as explained and illustrated by Zhang et al.[14] over Ni-Co bimetallic catalyst (Fig. VI-3). When the particle size exceeds 20 nm, only Ni-C formed near the periphery can react with $CO_2$ adsorbed on the support while the remaining carbon on the surface accumulate with time, causing deactivation. If the particle size is lower than 10 nm, all Ni-Cs can easily react with adsorbed $CO_2$, leading to continuous carbon formation and gasification.

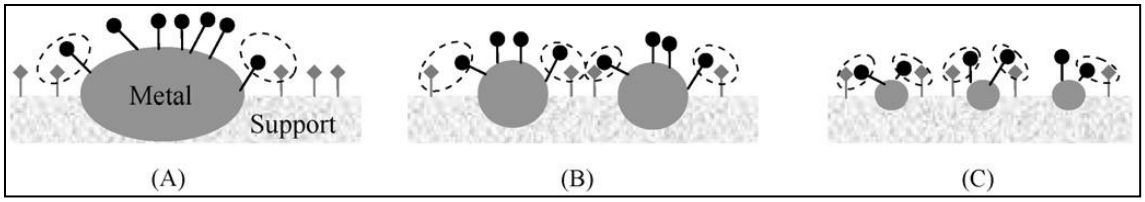


Figure VI-3: Conceptual model of carbon removal and carbon formation over the Ni-Co bimetallic catalyst for $CO_2$ reforming of $CH_4$[14]

### VI.1.1 Effect of stability test duration

As observed in Chapter IV, the $Ni_{5.0}$/SBA-$B_1$(N) catalyst was stable at 650°C and carbon deposition was only detected on the surface and associated to the presence of external nickel nanoparticles. In this part, the process of carbon deposition with time under reactants stream is evaluated on this sample.

For this purpose, each catalytic test was done at the same operating conditions as before using each time 100 mg of fresh catalyst (equivalent to 36 $L.g^{-1}.h^{-1}$), but varying the duration time of the stability test. Thus, after reduction of the sample, the activity is evaluated from 200 up to 750°C, followed by stability measurements at 650°C, and the experiment is stopped after 0, 5, 20, 60, and 90 hours at this steady temperature. The resulting spent catalysts are named **$Ni_{5.0}$/SBA-$B_1$(N)-x**, where x corresponds to the duration of the stability test. For example, $Ni_{5.0}$/SBA-$B_1$(N)-0 refers to the catalyst evaluated after 0 hours under reactants stream (after only activity evaluation up to 750°C) and $Ni_{5.0}$/SBA-$B_1$(N)-5 to the one evaluated after 5 hours under reactants stream. These spent catalysts were characterized by TGA-MS, Raman, XRD and the results are coded as follows:

- Red data correspond to **$Ni_{5.0}$/SBA-$B_1$(N)-0**
- Blue data correspond to **$Ni_{5.0}$/SBA-$B_1$(N)-5**
- Green data correspond to **$Ni_{5.0}$/SBA-$B_1$(N)-20**
- Purple data correspond to **$Ni_{5.0}$/SBA-$B_1$(N)-60**
- Orange data correspond to **$Ni_{5.0}$/SBA-$B_1$(N)-90**

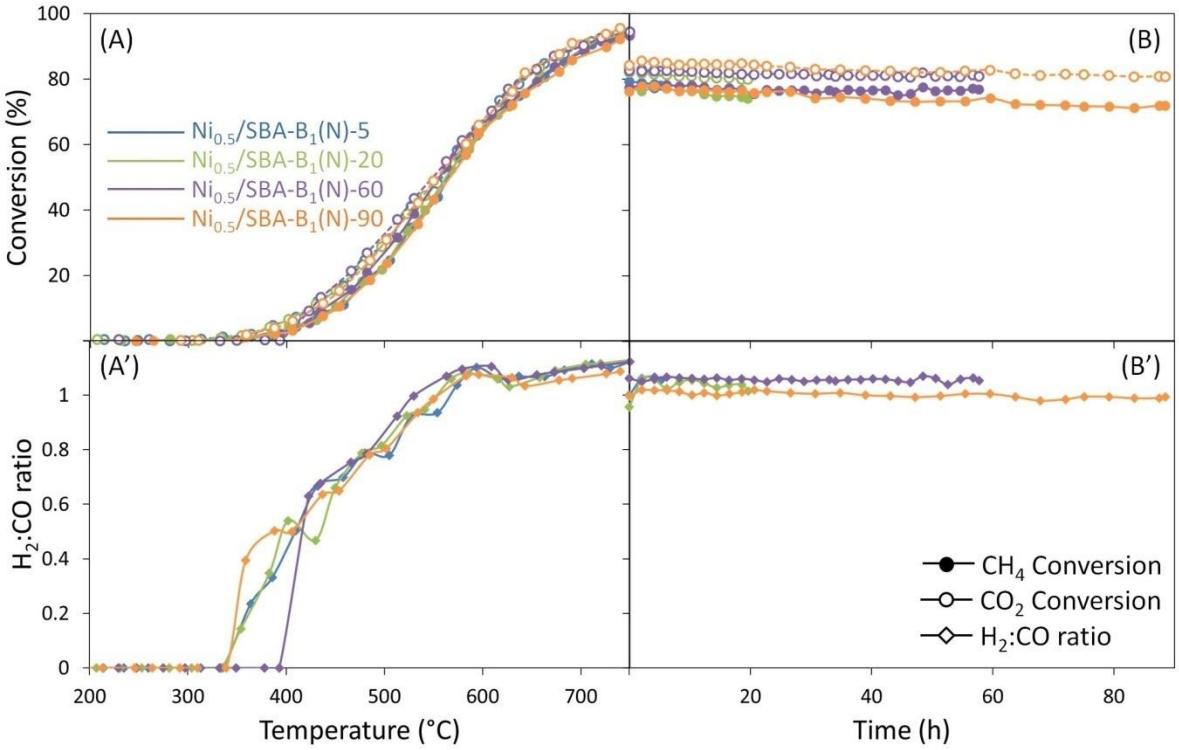


Figure VI-4: Evolution of (A,B) $CH_4$ (filled circles) and $CO_2$ conversions (empty circles) and (A',C') $H_2$:CO ratio as a function of temperature (A,A') and time at 650°C (B,B') at 1 bar, 36 $L.g^{-1}.h^{-1}$ and $CH_4$:$CO_2$:Ar = 5:5:90

The catalytic test results (activity, stability and selectivity) are reported in Figure VI-4 to recall the reproducibility of the tests performed in the MAR microactivity reactor. The repeated tests confirm the very close values of reactants conversions and $H_2$:CO molar ratios. At 750°C (Fig VI-4A,A'), the samples reached around 90% $CH_4$ and $CO_2$ conversions and an $H_2$:CO molar ratio of about 1.1. At 650°C (Fig VI-4B,B'), the reactants conversions are maintained at almost 80 and 85%, respectively with an $H_2$:CO molar ratio close to unity.

The carbon formation on the spent catalysts after reaction was first quantified by TGA-MS (Fig. VI-5). The difference in the weights of initial and final spent catalysts after heating from room temperature to 900°C at a rate of 10°C.$min^{-1}$ under air are reported in terms of percentage of weight loss as a function of test duration time at the steady temperature of 650°C (Fig. VI-5A). Around 5% weight loss is observed on $Ni_{5.0}$/SBA-$B_1$(N)-5, then this percentage remains almost constant as the stability time increases. This indicates that carbon accumulation mainly takes place during the first few hours of the test then it seems to stabilize with time. A similar trend was found on a Ni/MgO-

AN catalyst during DRM reaction at 750°C under 15 bars, but with much more significant carbon deposition within 10 hours.[15] The peak corresponding to the MS signal of mass 44 (Fig. VI-5B) validates the gasification of coke into $CO_2$. The same form of the signal is observed between 500 and 730 °C for all the samples, corresponding to the elimination of carbon nanotubes by oxidation as reported by Braga et al.[16] This is in agreement with the formation of carbon nanotubes, observed by TEM on $Ni_{5.0}$/SBA-$B_1$(N)-90 in Chapter IV.

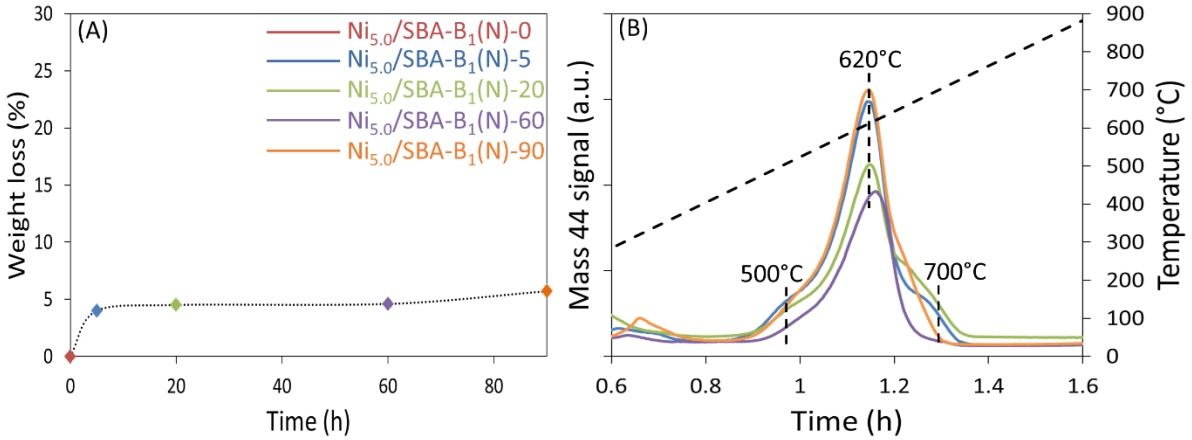


Figure VI-5: (A) Percentage weight loss during TGA and (B) MS signal for mass 44

Furthermore, the nature of the supported particles and their size is evaluated by XRD (Fig. VI-6). As before, the narrow peaks observed at 44, 53 and 76° are characteristic of the crystalline $Ni^0$ phase. Regardless of the stability test duration, the widths of these peaks remains almost constant. Using Scherrer equation, the average sizes of metallic nickel particles are estimated to be in the range of 6-6.5 nm, similar to the nickel nanoparticles size on the reduced sample. This points out that no sintering took place and the size of the metallic nanoparticles was maintained as the quantity of carbon stabilized with time.

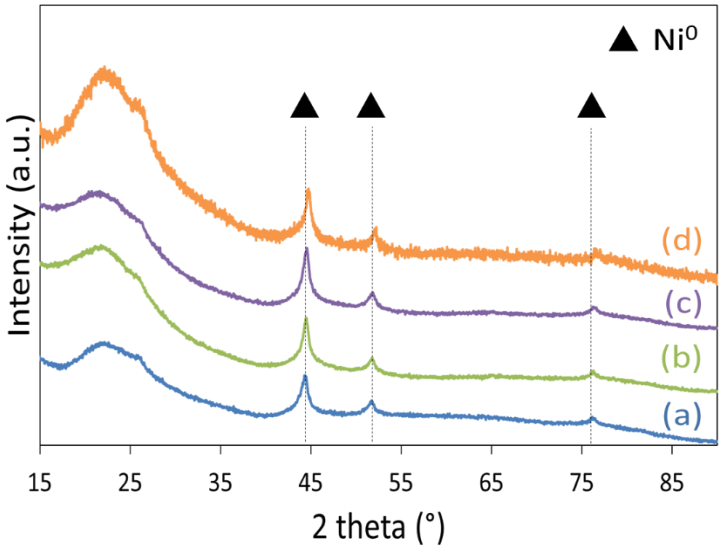


Figure VI-6: X-ray diffractograms of spent (a) $Ni_{5.0}$/SBA-$B_1$(N)-5, (b) $Ni_{5.0}$/SBA-$B_1$(N)-20, (c) $Ni_{5.0}$/SBA-$B_1$(N)-60 and (d) $Ni_{5.0}$/SBA-$B_1$(N)-90 catalysts

Summary of section VI.1.1: Effect of stability test duration

- During the first few hours of the catalytic methane dry reforming reaction, carbon accumulation takes place exclusively on external particles.
- Later, the quantity of deposited carbon remains stable, once all external nickel nanoparticles are trapped at the tip of the formed nanotubes.
- The nickel nanoparticles occluded and stabilized inside the pores of the SBA-15 support are well protected against sintering and carbon deposition. Hence, their catalytic performance is maintained.

### VI.1.2 Carbon quantification on spent catalysts

The above carbon quantification was helpful in the comprehension of carbon deposition behavior. Therefore, the quantity of carbon deposited after reaction on several of our spent catalysts was assessed by TGA-MS. The recorded weight loss is plotted as a function of temperature (Fig. VI-7A) while setting the final weight (carbon free catalyst) as 100%. The data show a first weight loss up to 150°C (250°C for $Ni_{5.0}Mg_6$/SBA-$B_1$(N)) attributed to the removal of adsorbed water, as confirmed by the MS signal for mass 18 (not shown). A more important weight loss takes place between 550 and 650°C and corresponds to the oxidation of carbon species into $CO_2$, as validated

by the MS signal for mass 44 (Fig. VI-7B) and the exothermic peak in the DTA profiles in this temperature range (not shown). The results reveal analogous carbon deposition (of about 6%) on the spent $Ni_{5.0}Mg_6/SBA\text{-}B_1(N)$, $Ni_{5.0}/SBA\text{-}B_1(N)$ and $Ni_{5.0}Rh_{0.5}/SBA\text{-}B_1(N)$ which were tested for 12, 90 and 60 hours under reactants stream, respectively. This agrees with the previous observation of constant carbon accumulation after few hours of the test. Furthermore, this is also in accordance with previous findings stating that the stability of the catalyst is affected by the type of carbon deposition rather than its quantity.[17,18]

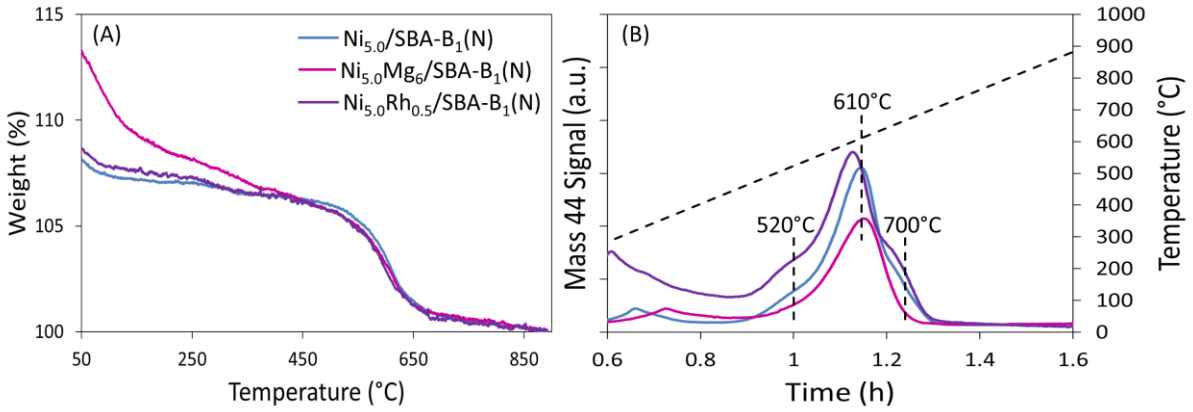


Figure VI-7: (A) Percentage weight loss and (B) MS signal for mass 44 MS signal during TGA of spent catalysts

### VI.1.3 Carbon structure on spent catalysts

Based on the previous findings, we will focus more on the type of carbon deposits on the spent catalysts rather than their quantity. During this PhD thesis, the type of deposited carbon was characterized by TPH, Raman and XPS.

During the hydrogenation of the spent catalysts by TPH (Figure VI-8), carbon is gasified into $CH_4$. The temperature of formation of methane reflects the reactivity of surface carbon, meaning that higher hydrogenation temperature corresponds to harder to remove carbon species.[19] In general, Cα (superficial graphene-like carbon) are hydrogenated at low temperatures (<400°C), Cβ (carbon nanotubes) at intermediate temperatures (400-600°C) and Cγ at elevated temperatures (>650°C).[20,21] The latter is the most inert type (most difficult to react with $H_2$) that can cause severe deactivation.

Based on this classification, Cγ was only observed during the hydrogenation of the $Ni_{5.0}$/SBA-$A_3$(N) catalyst with low organized mesoporous structure (Figure VI-8). The absence of Cγ on the remaining samples explains their relatively high performance in general. On $Ni_{5.0}$/SBA-$B_1$(N), the deposited carbon was majorly in the form of Cα, with some Cβ. This is in agreement with the maintained good dispersion of nickel nanoparticles inside the pores without carbon deposits and the few carbon nanotubes observed on the external nanoparticles. The $Ni_{5.0}$/SBA-$A_3$(N) and $Ni_{5.0}$/SBA-$B_1$(N) catalysts only differed by the hydrothermal treatment applied at 95°C on the SBA-$B_1$ support. Thus, the less-developed mesoporous structure (without hydrothermal treatment) was subjected to higher carbon deposition, mainly in the form of Cγ, that results in lower catalytic performance.[7,22,23] This result further supports the necessity of hydrothermal treatment during the SBA-15 support synthesis for enhancement of the mesoporous structure and better stability, as discussed in Chapter IV.

Similar to $Ni_{5.0}$/SBA-$B_1$(N), the presence of Cβ (carbon nanotubes) on $Ni_{5.0}Mg_6$/SBA-$B_1$(N) and $Ni_{5.0}Rh_{0.5}$/SBA-$B_1$(N) catalysts is in agreement with the TGA data reported in the previous section. Interestingly, almost no carbon deposition is detected on $Ni_{5.0}$/SBA-$B_1$(R) catalyst. The latter was remarkably stable at 650°C with almost full internal deposition of nickel particles inside the pores, as seen by TEM (Fig. V-5b'). This result further consolidates the idea that the occlusion of the nickel active phase inside the pores allows the dry reforming reaction to be carried out without carbon deposition.

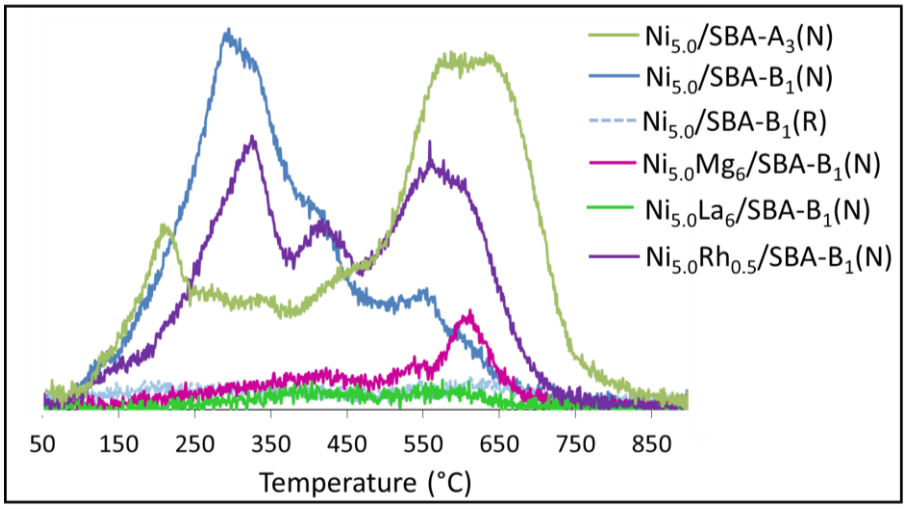


Figure VI-8: MS signal for mass 16 during TPH of spent catalysts

Further insights on the kind of deposited carbon on the surface of the catalysts can be obtained by XPS.

- The XPS spectra of C1s core electrons (Fig. VI-9A) confirm: (i) the low carbon deposition on the spent $Ni_{5.0}$/SBA-$B_1$(R) and $Ni_{5.0}Ce_6$/SBA-$B_1$(N) and (ii) the accumulation of different types of carbon on the surface of $Ni_{5.0}$/SBA-$B_1$(N) and $Ni_{5.0}Rh_{0.5}$/SBA-$B_1$(N) catalysts during the methane dry reforming reaction. Indeed, the central peak observed at around 284.6 eV corresponds to graphitic carbon species (–C–C–).[24] The small peak at 286.5 eV can be attributed to graphitic-like carbon (C=O and C-O), originating from the activation of $CO_2$ on the metallic and/or support surface.[25] The shoulder at around 283 eV correspond to silicon carbide (SiC) species, according to the NIST X-ray photoelectron spectroscopy database. However, some authors attributed this peak to amorphous carbon in the form of nickel carbide ($Ni_xC$) species,[24] serving as reaction intermediate. Pawelec et al.[26] reported that the chemical nature of these carbon species is graphitic ($sp^2$ carbon), and specified that these species grow above the surface without physical contact with the catalyst surface. This is in agreement with the carbon nanotubes observations on the TEM micrographs of $Ni_{5.0}$/SBA-$B_1$(N) and $Ni_{5.0}Rh_{0.5}$/SBA-$B_1$(N) catalysts after reaction.
- The absence of Ni signals on $Ni_{5.0}$/SBA-$B_1$(N) and $Ni_{5.0}Rh_{0.5}$/SBA-$B_1$(N) (Fig. VI-9B) is in accordance with the coverage of the surface nickel nanoparticles by carbon deposits, as confirmed from the C1s spectra and the preceding results. On the Ni2p spectra of $Ni_{5.0}$/SBA-$B_1$(R) and $Ni_{5.0}Ce_6$/SBA-$B_1$(N) spent catalysts, two spin-orbit peaks at about 856 and 874 eV are noticed, corresponding to $Ni2p_{3/2}$ and $Ni2p_{1/2}$, respectively.[27] Their accompanying satellites are not clearly observed. The major peak at 856 eV is attributed to $Ni^{2+}$ whereas the small shoulder at 853 eV is identified as metallic Ni. Keeping in mind that XPS is a surface analysis technique (<10 nm),[28] the NiO present on the surface of these catalysts can be due to oxidation of the outermost nickel nanoparticles upon contact with air[29] while most of the metallic $Ni^0$ nanoparticles remained inside the pores of the silica support, as confirmed by XRD in Chapter V. The additional peaks at 882 and 886 eV on $Ni_{5.0}Ce_6$/SBA-$B_1$(N) spent catalyst are related to $Ce^{4+}$ and $Ce^{3+}$ ions, respectively.[29] The presence of these two species is related to the redox properties of $CeO_2$.

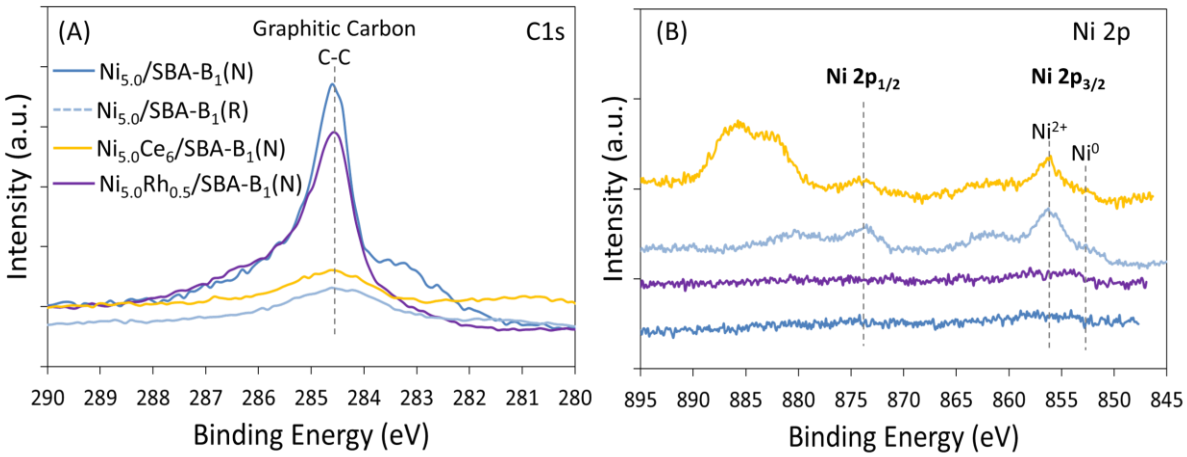


Figure VI-9: XPS spectra of (A) C1s and (B) Ni 2p core electrons of spent catalysts

Further clarification on the type of carbon deposition is also given by Raman spectroscopy. A representative Raman profile (Fig. VI-10A) of the spent catalysts show two main peaks: the G-band near 1600 $cm^{-1}$ is assigned to the in-plane displacement of carbon atoms (C $sp^2$) in the hexagonal sheets and the D-band at around 1310 $cm^{-1}$ indicative of the presence of disordered graphite.[17] The latter can refer to defects such as pentagons and heptagons in graphite, carbonaceous impurities with $sp^3$ bonding, broken $sp^2$ bonds in the sidewalls or amorphous carbonaceous products. The G'-band at 2620 $cm^{-1}$ is characteristic of long-range order in a sample. The absence of Radial Breathing Mode (RBM) at low Raman shift and the presence of an intense D-band indicate the presence of multi-walled rather than single-walled carbon nanotubes. The higher intensity of the D-band illustrates the presence of carbonaceous disordered species as by-products of the reaction. Furthermore, its intensity relative to that of the G-band is often used as a measure of the quality of nanotubes. A low value of $I_D/I_G$ points out on higher crystallinity, while a higher ratio suggests on the higher disorder within the crystalline structure.

The evaluation of the crystallinity of deposited carbon on $Ni_{5.0}/SBA\text{-}B_1(N)$ as a function of stability test duration reveals the presence of the D-band and G-band on the Raman profiles (Fig. VI-10B). This indicates the presence of carbon nanotubes, in accordance with the results obtained by TGA-MS (section VI.1.1). After 5, 60 or even 90 hours, the samples maintain the ratio of intensities of the two bands ($I_D/I_G$) in the range of 1.6-1.7. This means that limited defects are formed in the carbonaceous structure. In addition to the equilibrium in the quantity of carbon

deposition and the size of metallic nickel particles (section VI.1.1), the crystallinity of the formed carbon is also conserved as the quantity of carbon equilibrates.

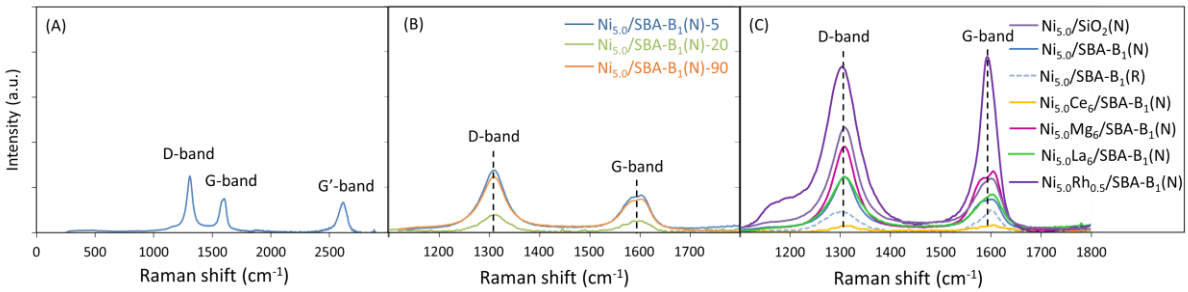


Figure VI-10: (A) Representative Raman spectrum, (B) Raman spectra of the spent $Ni_{5.0}/SBA\text{-}B_1(N)$ after different stability test durations and (C) Raman spectra of the remaining spent catalysts

On the remaining samples (Fig. VI-10C), the ratio of intensities of the D and G-bands ($I_D/I_G$) vary depending on the sample. The highest $I_D/I_G$ ratios (Table VI-1) are obtained on the spent $Ni_{5.0}/SiO_2(N)$, $Ni_{5.0}/SBA\text{-}B_1(N_{DS})$ and $Ni_{5.0}/SBA\text{-}B_1(N_{IWI})$ catalysts, indicative of high degree of defects in the carbonaceous structure. On the non-porous structure or the poorly defined mesoporous structures, more defects due to graphitic sheets with more distorted angles than the straight tubes are present in the carbonaceous structure.[7] These distortions can limit the accessibility to the active surface area, leading to lower catalytic activity.

The addition of promoters (like Ce, Mg or La) or dopants (like Rh) and the direct reduction treatment without calcination favor the reduction of the $I_D/I_G$ ratio. More specifically, the $Ni_{5.0}/SBA\text{-}B_1(R)$, $Ni_{5.0}Ce_6/SBA\text{-}B_1(N)$ and $Ni_{5.0}Rh_{0.5}/SBA\text{-}B_1(N)$ catalysts are characterized with the lowest $I_D/I_G$ ratios (Table VI-1). This points out the formation of highly ordered carbon nanotubes on these samples (if any) which are rather straight nanotubes with concentric parallel carbon sheets.[7] This observation further justifies their superior catalyic perfomance at 650°C.

Table VI-1: $I_D/I_G$ in Raman spectra of the spent catalysts

| Sample Name | $I_D/I_G$ |
|---|---|
| $Ni_{5.0}/SiO_2(N)$ | 2.0 |
| $Ni_{5.0}/SBA\text{-}B_1(N_{DS})$ | 1.9 |
| $Ni_{5.0}/SBA\text{-}B_1(N_{IWI})$ | 1.8 |

| Sample Name | $I_D/I_G$ |
|---|---|
| $Ni_{5.0}/SBA\text{-}B_1(N)$ | 1.6 |
| $Ni_{5.0}La_6/SBA\text{-}B_1(N)$ | 1.5 |
| $Ni_{5.0}Mg_6/SBA\text{-}B_1(N)$ | 1.4 |
| $Ni_{5.0}Ce_6/SBA\text{-}B_1(N)$ | 1.0 |
| $Ni_{5.0}Rh_{0.5}/SBA\text{-}B_1(N)$ | 1.0 |
| $Ni_{5.0}/SBA\text{-}B_1(R)$ | 0.95 |

Summary of section VI.1.2 and VI.1.3: Quantity and nature of carbon deposition on the spent catalysts

- Regardless of the test duration time, the quantity of carbon deposited on the spent $Ni_{5.0}Mg_6/SBA\text{-}B_1(N)$, $Ni_{5.0}/SBA\text{-}B_1(N)$ and $Ni_{5.0}Rh_{0.5}/SBA\text{-}B_1(N)$ was almost the same. This is in agreement with the constant carbon accumulation as the stability time increases and validates that the catalytic stability is affected by the type of carbon deposition rather than its quantity.
- The type of carbon deposition was affected by the porosity of the support. The non-porous or poorly defined mesoporous structures result in the formation of either Cγ inert carbon or Cβ carbon nanotubes with high degree of defects, which cause deactivation.
- The addition of Ce or Rh and the direct reduction treatment without calcination favor the formation of highly ordered carbon nanotubes (if any) which do not affect the catalytic activity.

## VI.2 Study of more severe reaction conditions

### VI.2.1 Effect of gas hourly space velocity (GHSV)

Despite this very limited carbon deposition, the use of 100 mg of the $Ni_{5.0}/SBA\text{-}B_1(N)$ catalyst in the reaction of methane dry reforming resulted in high reactants conversions and remarkable stability at 650°C (Fig. VI-4). Under similar conditions, many catalysts were able to reach

conversions close to the expected thermodynamic values, due to the presence of sufficient number of stable active sites for the reaction. Subsequently, it is important to check if this comparable behavior remains also valid under more severe conditions. For this reason, the following part will evaluate the most stable catalysts at different gas hourly space velocities.

In the following part, the selected catalysts are tested at different space velocities as indicated in their nomenclature. For example, **$Ni_{5.0}$/SBA-$B_1$(N)-36** indicates that the catalyst is tested at 36 $L.g^{-1}.h^{-1}$ (100 mg, 60 $ml.min^{-1}$ reactants flow), **$Ni_{5.0}$/SBA-$B_1$(N)-72** is tested at 72 $L.g^{-1}.h^{-1}$ (50 mg, 60 $ml.min^{-1}$ reactants flow), and **$Ni_{5.0}$/SBA-$B_1$(N)-180** is tested at 180 $L.g^{-1}.h^{-1}$ (20 mg, 60 $ml.min^{-1}$ reactants flow). More generally, the results are represented as follow:

- Blue data for **GHSV = 36 $L.g^{-1}.h^{-1}$**
- Red data for **GHSV = 72 $L.g^{-1}.h^{-1}$**
- Green data for **GHSV = 180 $L.g^{-1}.h^{-1}$**

In addition, the curves shown in **purple** for the $Ni_{5.0}$/SBA-$B_1$(N) catalyst are equivalent to a GHSV of **72 $L.g^{-1}.h^{-1}$** obtained using 100 mg of catalyst and 120 $ml.min^{-1}$ reactants flow.

For reproducibility, the tests were repeated at least two times using the same quantity of catalysts under the same conditions and the resulting data are drawn on the same graph using gradients of the same color (Fig. VI-11). With respect to this issue, the data show that blue curves (using 100 mg of catalyst) coincide with each other while slight differences are observed between the green curves (using 20 mg of catalyst) during activity measurement and more pronounced variations are noted on these curves during stability assessment. This reveals that the use of 100 mg of catalysts is good for well reproducible tests whereas using 20 mg of powder is too low and the results in this case can be quite misleading. This can be explained by some heterogeneous filling of the grains or also by the low volume of powder formed inside the reactor, the loss of this powder in the quartz wool bed, and the changes in temperature gradient among the powder. Consequently, it appears more logical to compare the use of 100 and 50 mg of catalysts, rather than 20 mg.

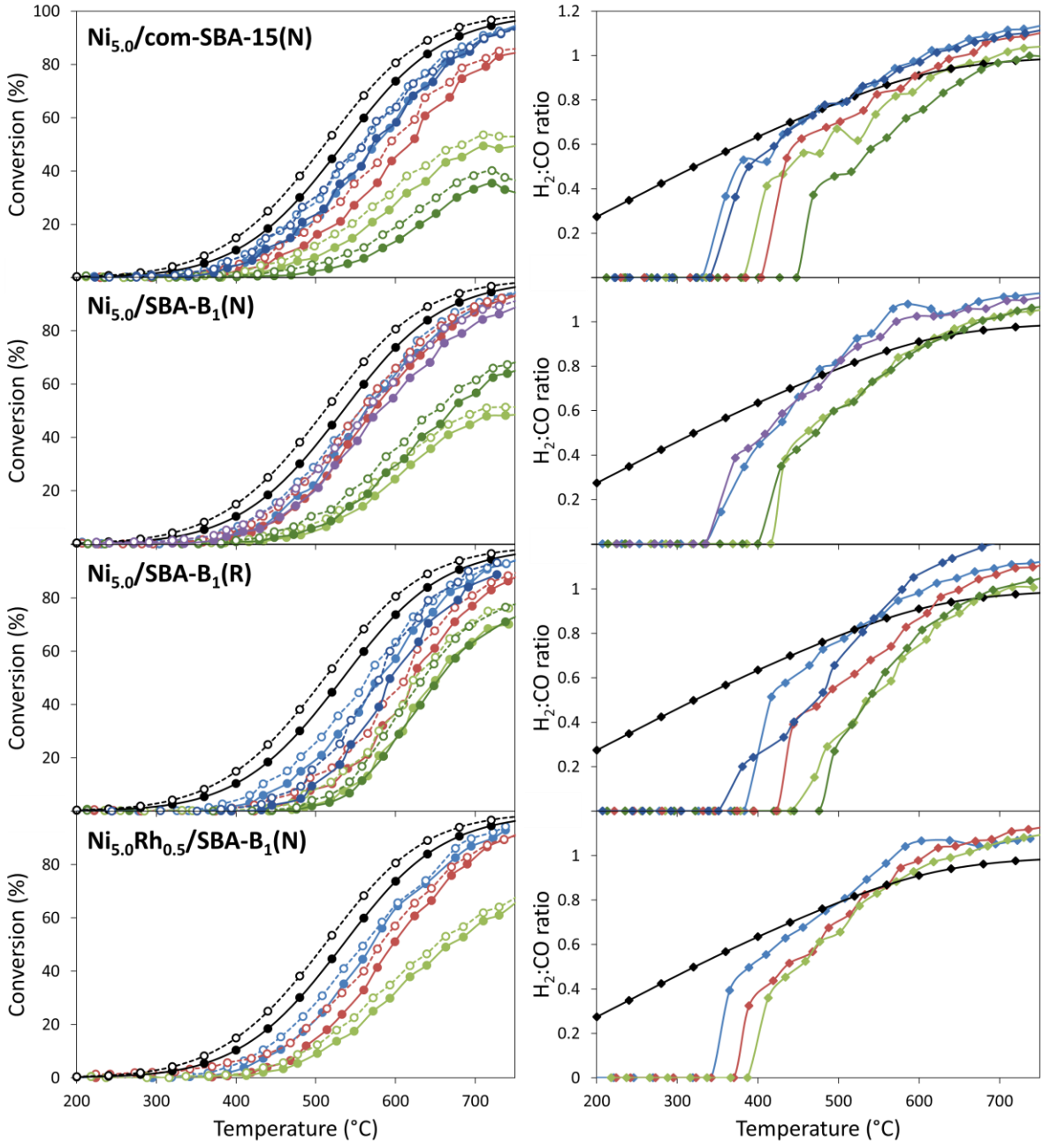


Figure VI-11: Evolution of (left) $CH_4$ (filled circles) and $CO_2$ conversions (empty circle) and (right) $H_2$:CO ratio as a function of temperature at 1 bar and $CH_4$:$CO_2$:Ar = 5:5:90 (black data represent thermodynamic data under the used conditions)

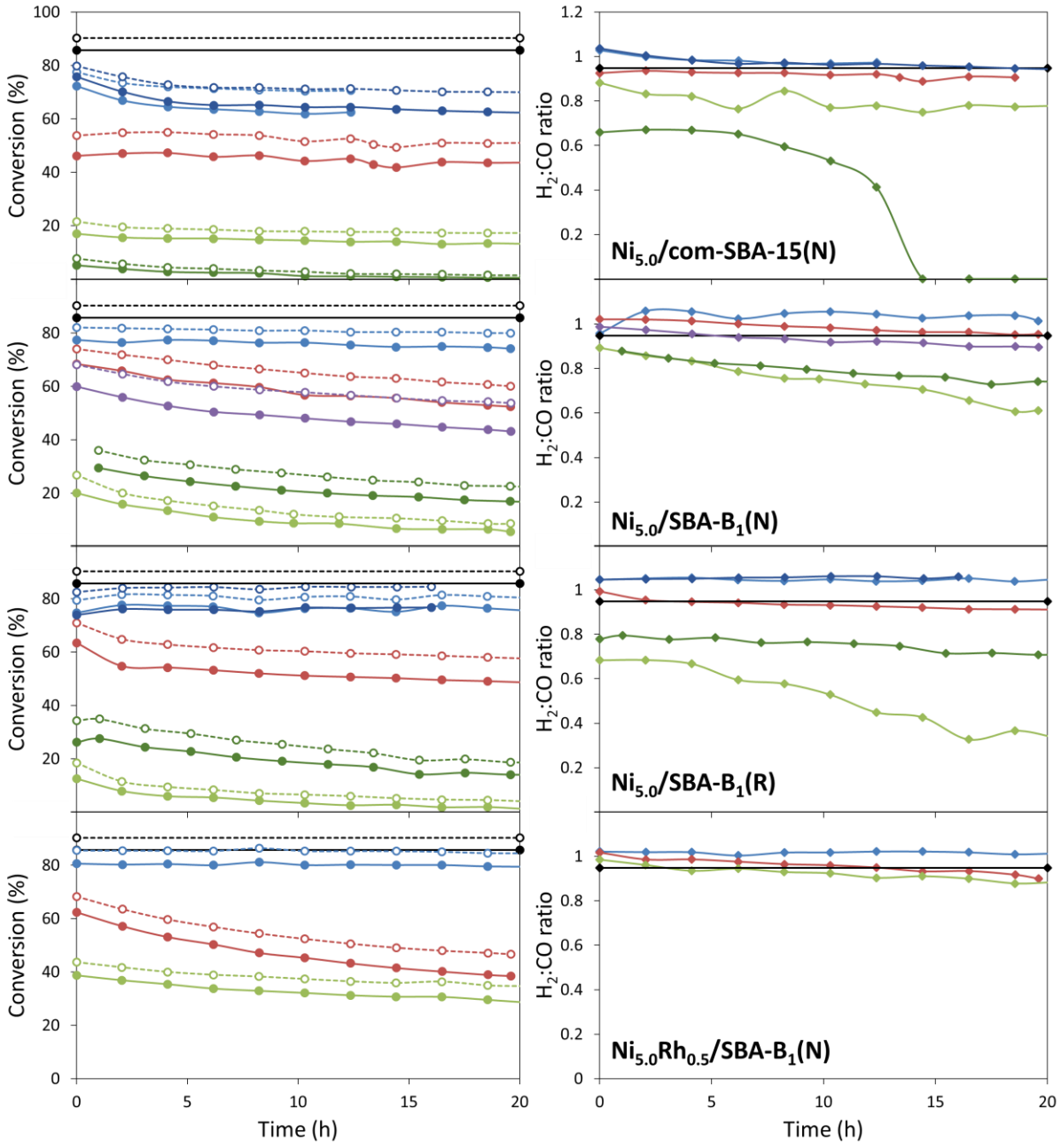


Figure VI-12: Evolution of (left) $CH_4$ (filled circles) and $CO_2$ conversions (empty circles) and (right) $H_2$:CO ratio as a function of time at 650°C, 1 bar and $CH_4$:$CO_2$:Ar = 5:5:90 (black data represent thermodynamic data under the used conditions)

As expected for all samples, the reactants conversions and $H_2$:CO molar ratios decrease with increasing GHSV by the reduction of the catalyst weight used, due to the consequent reduction of the total number of active sites in the catalytic bed (Fig. VI-11). These observations are valid during

both activity and stability evaluations (Fig. VI-12). At 36 $L.g^{-1}.h^{-1}$ (blue curves-100 mg of powder), the thermodynamic equilibrium is attained. When the tests are conducted at 72 $L.g^{-1}.h^{-1}$ (red curves-50 mg of powder), the catalysts depart from equilibrium and more variances can be detected between the samples. At 650°C, a reduction of about 25-30% in reactants conversions is observed upon increasing the GHSV by 2 folds (i.e. when passing from 100 to 50 mg). Thus very limited diffusional limitations occur; all active sites are accessible and exploited during DRM reaction.

Moreover, at 650°C, the $Ni_{5.0}$/com-SBA-15(N)-72 catalyst is the most stable and only loses about 4% of its activity within 20 hours. The remaining samples are less stable and the reactants conversions decrease by about 20% over $Ni_{5.0}$/SBA-$B_1$(N)-72 and $Ni_{5.0}$/SBA-$B_1$(R)-72 samples within 20 hours. Nevertheless, the final conversions after 20 hours of time-on-stream on $Ni_{5.0}$/SBA-$B_1$(N)-72 and $Ni_{5.0}$/SBA-$B_1$(R)-72 catalysts remain higher than those on $Ni_{5.0}$/com-SBA-15(N)-72 catalyst. This further validates the superior performance of the catalysts prepared using SBA-$B_1$ as support.

Summary of section VI.2: Effect of gas hourly space velocity

- The catalytic tests performed on 20 mg of powder are not reproducible. This quantity is very low and can be easily dispersed in the quartz wool bed and subjected to different temperature gradients.
- At 650°C, using 50 mg of catalyst, the final conversions on the $Ni_{5.0}$/SBA-$B_1$(N) and $Ni_{5.0}$/SBA-$B_1$(R) catalysts are higher than those on the $Ni_{5.0}$/com-SBA-15(N) catalyst after 20 hours. This validates the superior performance of the samples prepared using the synthesized SBA-15 support rather than the commercial one.

### VI.2.2 Effect of pressure

In general, methane is stored and transported under high pressures, while methanol and Fischer-Tropsch synthesis are also performed under high pressures of $H_2$ and CO reactants. Therefore, from an economical point of view, it is highly desirable to run dry reforming of methane at high pressures,[30,31] even if the reaction is thermodynamically limited in this case. In order to prevent the cost and time of depressurizing the system, the industrial applications encourage the research under pressure. In this section, among the best catalysts, the $Ni_{5.0}Rh_{0.5}$/SBA-$B_1$(N) sample is selected for

assessment of its behavior under high pressure. This choice is done because this catalyst presented a better stability than $Ni_{5.0}$/SBA-$B_1$(N) at 650°C, under atmospheric pressure.

At 9 bars, the results are very promising (Figure VI-13): the $H_2$:CO molar ratio is maintained around one while both $CH_4$ and $CO_2$ conversions are preserved at values near 50% and 60%, respectively compared to 80% $CH_4$ conversion and 85% $CO_2$ conversion at atmospheric pressure. This decrease in conversions is expected in such systems at high pressures according to Le Chatelier's Principle discussed earlier at the end of Chapter II. Nevertheless, this decrease in conversions is not as drastic as the one observed over Ni/MgO-AN catalyst on which the $CH_4$ and $CO_2$ conversions dropped from 83% and 85% at atmospheric pressure to 25% and 28% at 15 bars, respectively.[15] Furthermore, it should be noted that these conversions are very close to the equilibrium conversions expected under similar experimental conditions, unlike the behavior observed by others on 0.5 wt% Co/$TiO_2$ catalyst that did attain equilibrium at 20 bars.[32] In addition, higher temperature and higher space velocity were also required in order to achieve comparable results with a 7mol% Co-MgO catalyst.[33] Therefore, these results reveal the superior performance of the $Ni_{5.0}Rh_{0.5}$/SBA-$B_1$(N) catalyst, that appears very promising for up-scaling.

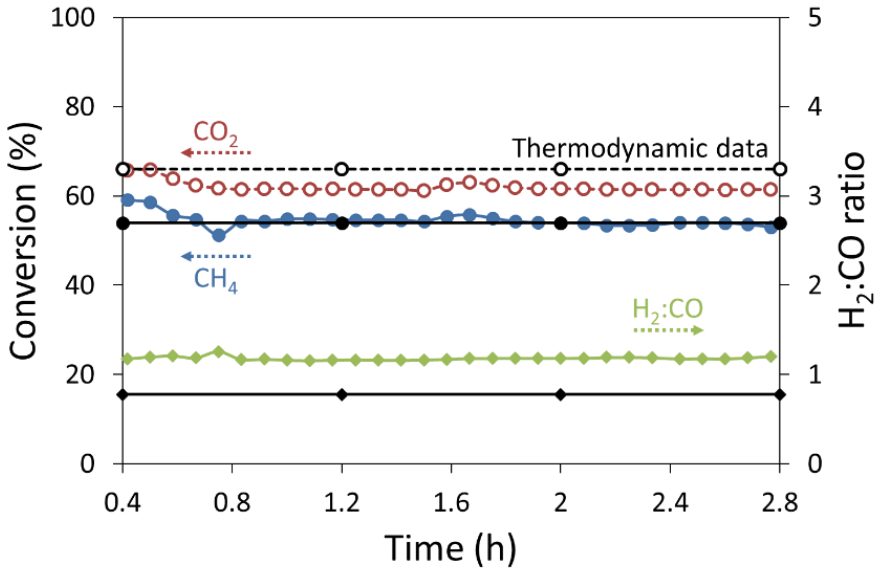


Figure VI-13: Evolution of $CH_4$ conversion (blue), $CO_2$ conversion (red) and $H_2$:CO molar ratio (green) as a function of time on $Ni_{5.0}Rh_{0.5}$/SBA-$B_1$(N) catalyst at 650°C, 9 bar and $CH_4$:$CO_2$:Ar = 5:5:90 (black data represent thermodynamic data under the used conditions)

Summary of section VI.3: Effect of pressure

- The $Ni_{5.0}R_{h0.5}$/SBA-$B_1$(N) catalyst, which was more stable than the $Ni_{5.0}$/SBA-$B_1$(N), was tested at 9 bars, using 100 mg of powder.
- The results show not only that high $CH_4$ and $CO_2$ conversions are maintained during the test, but also that they are close to the equilibrium conversions.
- This catalyst is thus promising for up-scaling and further experiments under industrial conditions.

### VI.2.3 Effect of regeneration

After decline of the catalytic activity to a critical level, regeneration of the catalyst is usually the preferred solution. In reforming, deactivation is mainly caused by carbon and coke deposition that can be removed through gasification with hydrogen or oxygen. In order to test this point, the $Ni_{5.0}Rh_{0.5}$/SBA-$B_1$(N) catalyst that showed a deactivation at GHSV = 72 $L.g^{-1}.h^{-1}$ (50 mg of powder) was selected to study the effect of regeneration as follows:

1. Usual catalytic test (60 $ml.min^{-1}$, 72 $L.g^{-1}.h^{-1}$, 1 bar, $CH_4$:$CO_2$:Ar = 5:5:90) performed at 650°C for 20 hours
2. Reactor cooling to 200°C without flow
3. Hydrogenation: temperature increase up to 650°C (rate of 5°$C.min^{-1}$) for 2 hours under 5 vol% $H_2$/Ar (30 $ml.min^{-1}$)
4. Repetition of the catalytic under the same conditions (60 $ml.min^{-1}$, 72 $L.g^{-1}.h^{-1}$, 1 bar, $CH_4$:$CO_2$:Ar = 5:5:90)

Based on the previous TPH results shown in section VI.1.3 for the spent $Ni_{5.0}Rh_{0.5}$/SBA-$B_1$(N) catalyst, the selection of the temperature of 650°C for 2 hours was reasonable in order to gasify the deposited carbon. The results in Figure VI-14 show that the conversions and $H_2$:CO molar ratio after regeneration match the values of the fresh catalyst. Indeed, at 650°C, comparable $CH_4$ and $CO_2$ conversions are obtained before and after regeneration. Furthermore, the regenerated catalyst was less prone to deactivation and enhanced stability was observed on this sample during the 20 hours on stream. This potential result can be extended to the remaining promising catalysts, if an industrial commercialization is to be considered afterwards.

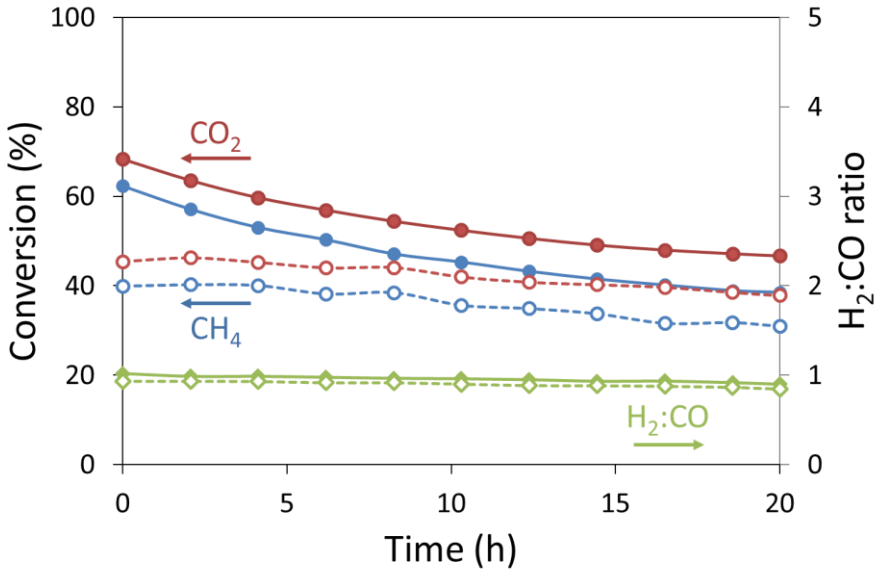


Figure VI-14: Evolution of $CH_4$ conversion (blue), $CO_2$ conversion (red) and $H_2$:CO molar ratio (green) as a function of time at 650°C, 1 bar and $CH_4$:$CO_2$:Ar = 5:5:90, before (solid lines) and after (dashed lines) regeneration of $Ni_{5.0}Rh_{0.5}$/SBA-$B_1$(N) catalyst

Summary of section VI.4: Effect of regeneration

- The potential $Ni_{5.0}R_{h0.5}$/SBA-$B_1$(N) catalyst, test using 50 mg of powder, was regenerated at 650°C under $H_2$/Ar.
- The results demonstrate that, after regeneration, comparable $CH_4$ and $CO_2$ conversions are obtained.

## VI.3 Conclusion

Carbon deposition is a major challenge in dry reforming applications that results in loss of catalytic activity. In this work, we have shown that the occlusion of nickel nanoparticles inside well-ordered pores enhances the stability of the catalysts. The deposition of carbon is restricted to the external nanoparticles, due to their weak metal-support interaction.

With the increase of stability test duration on $Ni_{5.0}$/SBA-$B_1$(N), at steady temperature of 650°C, carbon accumulation takes place during the first few hours of the test and then remains constant afterwards, once all external nickel nanoparticles are trapped at the tip of the formed nanotubes.

The type of carbon deposition on the catalysts was found to depend on the structure of the support and the catalyst preparation method. On non-porous or poorly defined mesoporous structures, the higher carbon deposition resulted in lower catalytic performance. In this case, carbon was not easy to remove, it was characterized with defects in the form of graphitic sheets with distorted angles that limit the accessibility to the active surface area, leading to lower catalytic activity. Alternatively, the use of promoters or dopants and the direct reduction of uncalcined samples limit carbon deposition and favor the formation of highly ordered carbon nanotubes on these samples (if any).

Under more severe reaction conditions, the $Ni_{5.0}$/SBA-$B_1$(N) and $Ni_{5.0}$/SBA-$B_1$(R) catalysts showed higher conversions than those on the $Ni_{5.0}$/com-SBA-15(N) catalyst after 20 hours at 650°C, using 50 mg of powder. This confirms the superior performance of the samples prepared using the synthesized SBA-15 support rather than the commercial one. Furthermore, the most stable $Ni_{5.0}Rh_{0.5}$/SBA-$B_1$(N) sample maintained high $CH_4$ and $CO_2$ conversions at high pressures. The regeneration of this catalyst (using 50 mg of powder) was able to preserve the same conversion values after 20 hours.

The dispersion of small nickel nanoparticles fully inside the pores of well-defined mesoporous structure inhibits active phase sintering, carbon deposition and provides high reactants conversions. The promising results obtained in this work, even under more severe conditions, can be further exploited for future scale-up activity as will be detailed in the following conclusion.

## VI.4 References

[1] M. Nurunnabi, Y. Mukainakano, S. Kado, T. Miyao, S. Naito, K. Okumura, K. Kunimori, K. Tomishige, *Catalytic performance and characterization of Pd/$Ni_{0.2}Mg_{0.8}Al_2O_4$ in oxidative steam reforming of methane under atmospheric and pressurized conditions*, Applied Catalysis A: General 325 (2007) 154-162.

[2] J.M. Bermúdez, B. Fidalgo, A. Arenillas, J.A. Menéndez, *Dry reforming of coke oven gases over activated carbon to produce syngas for methanol synthesis*, Fuel 89 (2010) 2897-2902.

[3] S. Helveg, C. Lopez-Cartes, J. Sehested, P.L. Hansen, B.S. Clausen, J.R. Rostrup-Nielsen, F. Abild-Pedersen, J.K. Norskov, *Atomic-scale imaging of carbon nanofibre growth*, Nature 427 (2004) 426-429.

[4] M. Yu, Y. Zhu, Y. Lu, G. Tong, K. Zhu, X. Zhou, *The promoting role of Ag in Ni-$CeO_2$ catalyzed $CH_4$-$CO_2$ dry reforming reaction*, Applied Catalysis B: Environmental 165 (2015) 43-56.

[5] T. Huang, W. Huang, J. Huang, P. Ji, *Methane reforming reaction with carbon dioxide over SBA-15 supported Ni-Mo bimetallic catalysts*, Fuel Processing Technology 92 (2011) 1868-1875.

[6] N. Wang, Z. Xu, J. Deng, K. Shen, X. Yu, W. Qian, W. Chu, F. Wei, *One-pot synthesis of ordered mesoporous NiCeAl oxide catalysts and a study of their performance in methane dry reforming*, ChemCatChem 6 (2014) 1470-1480.

[7] A. Serrano-Lotina, L. Daza, *Long-term stability test of Ni-based catalyst in carbon dioxide reforming of methane*, Applied Catalysis A: General 474 (2014) 107-113.

[8] C. Wang, N. Sun, N. Zhao, W. Wei, Y. Sun, C. Sun, H. Liu, C.E. Snape, *Coking and deactivation of a mesoporous Ni-CaO-$ZrO_2$ catalyst in dry reforming of methane: A study under different feeding compositions*, Fuel 143 (2015) 527-535.

[9] S. de Llobet, J.L. Pinilla, R. Moliner, I. Suelves, *Relationship between carbon morphology and catalyst deactivation in the catalytic decomposition of biogas using Ni, Co and Fe based catalysts*, Fuel 139 (2015) 71–78.

[10] M.S. Fan, A. Zuhairi Abdullah, S. Bhatia, *Catalytic technology for carbon dioxide reforming of methane to synthesis gas*, ChemCatChem 1 (2009) 192-208.

[11] Y. Kyu Han, C. Ahn, J. Bae, R. Kim, G. Young Han, *Effects of carbon formation on catalytic performance for $CO_2$ reforming with methane on Ni/$Al_2O_3$ catalyst: Comparison of fixed-bed with fluidized-bed reactors*, Industrial and Engineering Chemistry Research 52 (2013) 13288-13296.

[12] M.D. Argyle, C.H. Bartholomew, *Heterogeneous catalyst deactivation and regeneration: A review*, Catalysts 5 (2015) 145-269.

[13] S. de Llobet, J.L. Pinilla, R. Moliner, I. Suelves, *Relationship between carbon morphology and catalyst deactivation in the catalytic decomposition of biogas using Ni, Co and Fe based catalysts*, Fuel 139 (2015) 71-78.

[14] J. Zhang, H. Wang, A.K. Dalai, *Effects of metal content on activity and stability of Ni-Co bimetallic catalysts for $CO_2$ reforming of $CH_4$*, Applied Catalysis A: General 339 (2008) 121-129.

[15] Y.H. Wang, H. Wang, Y. Li, Q.M. Zhu, B.Q. Xu, *Performance of Ni/MgO-AN catalyst in high pressure $CO_2$ reforming of methane*, Topics in Catalysis 32 (2005) 109-116.

[16] T.P. Braga, R.C.R. Santos, B.M. C. Sales, B.R. da Silva, A.N. Pinheiro, E.R. Leite, A. Valentini, *$CO_2$ mitigation by carbon nanotube formation during dry reforming of methane analyzed by factorial design combined with response surface methodology*, Chinese Journal of Catalysis 35 (2014) 514-523.

[17] C.H. Bartholomew, *Carbon deposition in steam reforming and methanation*, Catalysis Reviews Science and Engineering 24 (1982) 67-112.

[18] P.G. Menon, *Coke on catalysts-harmful, harmless, invisible and beneficial types*, Journal of Molecular Catalysis, 59 (1990) 207-220.

[19] N. Wang, X. Yu, Y. Wang, W. Chu, M. Liu, *A comparison study on methane dry reforming with carbon dioxide over $LaNiO_3$ perovskite catalysts supported on mesoporous SBA-15, MCM-41 and silica carrier*, Catalysis Today 212 (2013) 98-107.

[20] Z.L. Zhang, X.E. Verykios, *Carbon dioxide reforming of methane to synthesis gas over supported Ni catalysts*, Catalysis Today 21 (1994) 589-95.

[21] Y.G. Chen, K. Tomishige, K. Fujimoto, *Formation and characteristic properties of carbonaceous species on nickel-magnesia solid solution catalysts during $CH_4$-$CO_2$ reforming reaction*, Applied Catalysis A: General 161 (1997) 11-17.

[22] K. Jabbour, N. El Hassan, A. Davidson, P. Massiani, S. Casale, *Characterizations and performances of Ni/diatomite catalysts for dry reforming of methane*, Chemical Engineering Journal 264 (2015) 351-358.

[23] H. Silvester A. de Sousa, A.N. da Silva, A.J.R. Castro, A. Campos, J.M. Filho, A.C. Oliveira, *Mesoporous catalysts for dry reforming of methane: Correlation between structure and deactivation behavior of Ni-containing catalysts*, International Journal of Hydrogen Energy 37 (2012) 12281-12291.

[24] C. Wang, N. Sun, N. Zhao, W. Wei, Y. Sun, C. Sun, H. Liu, C.E. Snape, *Coking and deactivation of a mesoporous Ni-CaO-$ZrO_2$ catalyst in dry reforming of methane: A study under different feeding compositions*, Fuel 143 (2015) 527-535.

[25] S.R. de Miguel, I.M.J. Vilella, S.P. Maina, D. San José-Alonso, M.C. Román-Martínez, M.J. Illán-Gómez, *Influence of Pt addition to Ni catalysts on the catalytic performance for long term dry reforming of methane*, Applied Catalysis A: General 435-436 (2012) 10-18.

[26] B. Pawelec, S. Damyanova, K. Arishtirova, J.L.G. Fierro, L. Petrov, *Structural and surface features of PtNi catalysts for reforming of methane with $CO_2$*, Applied Catalysis A: General 323 (2007) 188-201.

[27] T. Xie, X. Zhao, J. Zhang, L. Shi, D. Zhang, *Ni nanoparticles immobilized Ce-modified mesoporous silica via a novel sublimation-deposition strategy for catalytic reforming of methane with carbon dioxide*, International Journal of Hydrogen Energy 40 (2015) 9685-9695.

[28] D. Liu, Y. Wang, D. Shi, X. Jia, X. Wang, A. Borgna, R. Lau, Y. Yang, *Methane reforming with carbon dioxide over a Ni/$ZiO_2$-$SiO_2$ catalyst: Influence of pretreatment gas atmospheres*, International Journal of Hydrogen Energy 37 (2012) 10135-10144.

[29] M. Yu, Y. Zhu, Y. Lu, G. Tong, K. Zhu, X. Zhou, *The promoting role of Ag in Ni-$CeO_2$ catalyzed $CH_4$-$CO_2$ dry reforming reaction*, Applied Catalysis B: Environmental 165 (2015) 43-56.

[30] Y. Wang, B. Xu, *Comparative study of atmospheric and high pressure $CO_2$ reforming of methane over Ni/MgO-AN catalyst*, Catalysis Letters 99 (2005) 89-96.

[31] K. Tomishige, Y. Matsuo, Y. Yoshinaga, Y. Sekine, M. Asadullah, K. Fujimoto, *Comparative study between fluidized bed and fixed bed reactors in methane reforming combined with methane combustion for the internal heat supply under pressurized condition*, Applied Catalysis A: General 223 (2002) 225-238.

[32] K. Nagaoka, K. Takanabe, K. Aika, *Influence of the reduction temperature on catalytic activity of Co/$TiO_2$ (anatase-type) for high pressure dry reforming of methane*, Applied Catalysis A: General 255 (2003) 13-21.

[33] K. Omata, N. Nukui, T. Hottai, M. Yamada, *Cobalt-magnesia catalyst by oxalate co-precipitation method for dry reforming of methane under pressure*, Catalysis Communications 5 (2004) 771-775.

# Conclusion and Perspectives

Even though more than 300 papers were published on dry reforming of methane till mid-2016, this challenging reaction still faces many obstacles related to (i) sintering of the active phase with consequent reduction of the metal active surface area and (ii) carbon deposition on the catalyst surface leading to active sites poisoning. Both aspects result in continuous catalyst deactivation and loss of activity.

During this PhD thesis, we have **successfully installed and validated the catalytic methane dry reforming test** which was not yet established at the University of Balamand in Lebanon. With few adjustments, it constitutes now a useful tool for the assessment of the activity and stability of catalysts even in other reforming reactions as well.

More importantly, during this work, we have shown that a key parameter for the prevention of active phase sintering is the **use of a mesoporous support**, characterized with high surface area and pore volume. Indeed, mesoporous channels impose a spatial restriction on metal particles and prevent their sintering. In addition, the **occlusion of nickel nanoparticles inside the porous channels** of the mesoporous support favors high activity and stability, since it hinders the deposition of carbon in such a constrained space.

However, we have seen that not any mesoporous support can be suitable for good confinement of the active phase. In fact, an accentuated catalytic deactivation was observed when using poorly defined mesoporous structures, like the commercial meso-$SiO_2$ silica support and the SBA-A support synthesized in the absence of hydrothermal treatment step. In this case, the less ordered pore distribution does not stabilize nickel particles inside the pores, which results in their migration to the external surface and subsequent carbon deposition together with nickel sintering. Consequently, the use of a **well-organized mesoporous silica support** with a rather elongated grain morphology was more adequate for a better confinement effect.

The application of a hydrothermal treatment during the synthesis of SBA-15 support also appears of strong importance since it enhances the support crystalline order while limiting interconnections between mesopores, therefore reducing the possibility of nickel oxides migration to the outer surface during thermal treatments. The **hydrothermal treatment** (at 95°C) carried out in the present PhD thesis work thus reduced these pore connections and resulted in improved internal deposition of nickel oxides. However, a complete internal

deposition was not yet fully achieved and the few external $Ni^0$ particles formed were **exclusively** prone to carbon deposition in the form of carbon nanotubes during the first few hours of the test. Their quantity remained constant afterwards, once all external nickel nanoparticles are sintered and trapped at the tip of formed nanotubes. Nevertheless, the catalytic performances are maintained due to the conservation of good nickel dispersion, the **majority of nickel nanoparticles being occluded and stabilized inside the pores**. For future studies, the application of *hydrothermal treatments at higher temperatures* (e.g. 130°C) could probably lead to even better supports with no interconnections between mesopores for improved stability of the active phase.

In addition to the well-structured mesoporous support, an improved stability is achieved by **controlling the deposition method of nanoparticles inside the well-defined mesoporous structure**. The use of nickel chloride as precursor salt is not appropriate since it causes external deposition of large nickel particles, and subsequent activity loss. Alternatively, both nickel nitrate and nickel acetate precursor salts favor good dispersion of the active phase inside the support. The former is more convenient (cheaper) for wider use in research and industry.

Moreover, better dispersion of small nanoparticles inside the pores can be also achieved through the **direct reduction treatment** to uncalcined samples. In fact, the reduction of the number of steps required for the formation of a catalyst is always advantageous to save time, energy and money. It would thus be important to continue on this route by (i) trying to *improve the direct synthesis method* employed in this study in order to obtain enhanced mesoporous materials, without macroporosity and (ii) further evaluating the effect of direct reduction on the active phase dispersion while *varying the reducing atmosphere* (pure $H_2$, $H_2$/He, NO) and/or the *heating rate*.

Furthermore, other procedures also beneficial for the suppression of carbon formation include the **addition of noble metals like Rh in small quantities** or the **addition of promoters like Ce**. It is important to note that the addition of Ce was only beneficial when both Ni and Ce were co-impregnated and both dispersed inside one grain of the support. The enhancement of redox properties of the support through the *preparation of mesoporous $CeO_2$ using SBA-15 as hard template* could be also advantageous. However, this preparation is not yet well controlled and further ameliorations should be realized to obtain better structured materials with high surface area. For this purpose, we can try to avoid the progressive calcination steps after each impregnation and lower nickel loading for better assessment of the activity.

The previous results are summarized in the schematic illustration below that shows the beneficial confinement effect of nickel nanoparticles inside the pores of the SBA-15 mesoporous support. Complete deactivation due to encapsulation by inert carbon was not observed on our samples. On the external particles, carbon was mainly deposited in the form of carbon nanotubes.

**Schematic illustration of the effect of nickel particles location on DRM reaction**

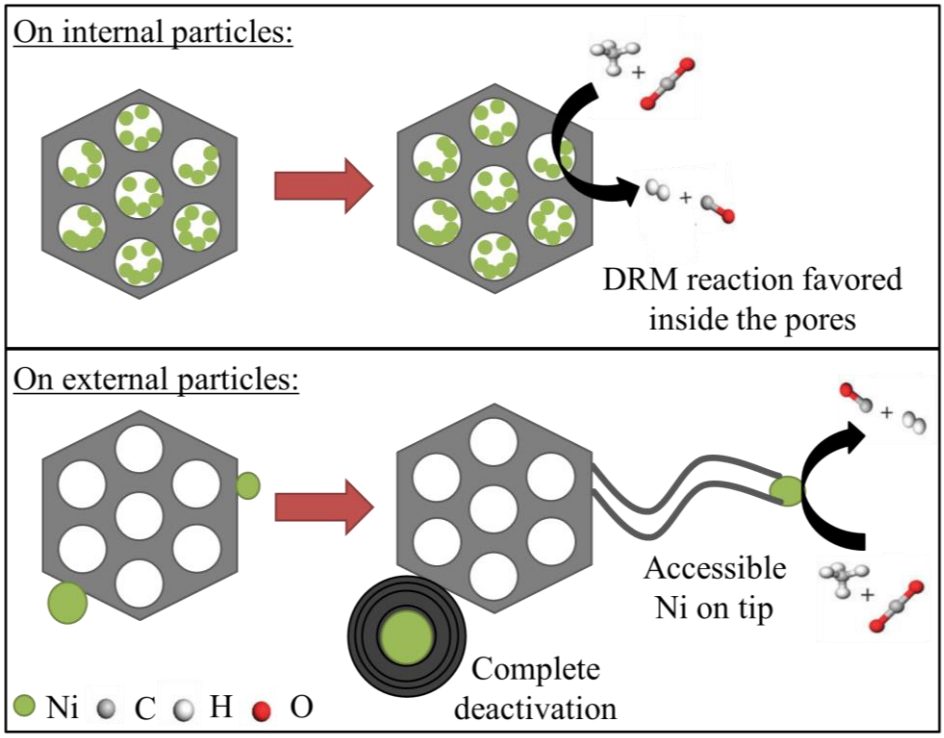


Furthermore, the stable catalysts obtained in this study also maintained **good stability under more severe reaction conditions**, especially at high pressure. For an industrial application, it would be interesting to perform additional tests at *high pressures* and for *longer durations*, followed by detailed characterization of the spent catalysts afterwards. It would be also beneficial to find suitable *regeneration methods* (adequate flow, temperature, time…) to recover the catalytic activity. **Shaping** of the powders, which was initiated at the end of this PhD thesis, is also an interesting industrial topic that is not frequently reported in literature. An extrapolation of the study towards larger scales imply the focus on *catalyst shaping* and its effects on catalytic activity. In order to pass from an idea up to plant testing (as shown in the

scheme below),[1] the research consumes time and money. The required optimization of the result after testing can even bring back the research to its initial stages. Catalytic scale up is important for the successful implementation of new catalytic technologies. However, the pathway from research catalyst to technical catalysts for pilot and plant testing is never easy.

**Typical sequence of interactive tasks followed in a catalyst development program**

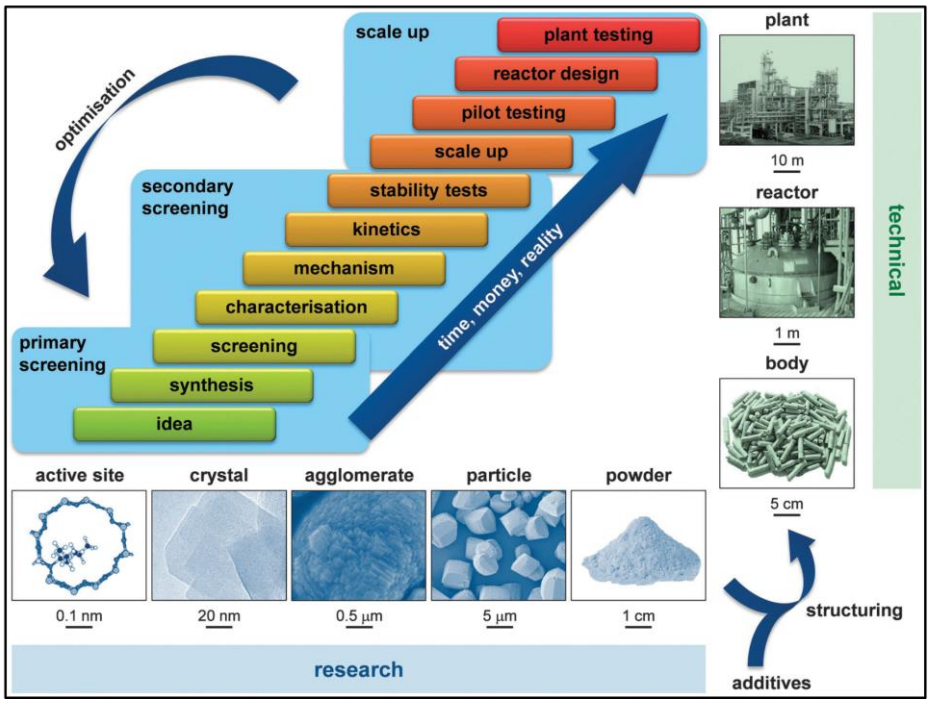


In the industry, it is widely acknowledged that there is a growing need for more environmentally friendly processes. In this direction, methane dry reforming reaction presents a great potential due to the consumption of greenhouse gases into higher value products. In addition, for future studies, the *template removal* by calcination during the SBA-15 preparation could be replaced by more *"eco-friendly" methods* like solvent extraction, during which the copolymer surfactant is removed without decomposition and can be recovered and reused[2,3]. Furthermore, *biomass* as a renewable source is expected to replace natural gas for the production of syngas. Therefore, it

[1] S. Mitchell, N.L. Michels, J. Perez-Ramirez, *From powder to technical body: the undervalued science of catalyst scale up*, Chemical Society Reviews 42 (2013) 6094-6112.

[2] R. van Grieken, G. Calleja, G.D. Stucky, J.A. Melero, R.A. Garcia, J. Iglesias, *Supercritical fluid extraction of a nonionic surfactant template from SBA-15 Materials and Consequences on the porous structure*, Langmuir 19 (2003) 3966-3973.

[3] K. Moller, T. Bein, R.X. Fischer, *Synthesis of ordered mesoporous methacrylate hybrid systems: Hosts for molecular polymer composites*, Chemistry of Materials 11 (1999) 665-673.

is interesting to continue the study of dry reforming of methane while adapting the feed composition, so that it resembles the product composition from biomass gasification or pyrolysis. Indeed, the conversion of biomass mainly generates $CH_4$, $CO_2$, $H_2$ and CO, in addition to $C_2H_4$ and $C_2H_6$, in various proportions[4,5,6,7,8].

[4] P. Lv, Z. Yuan, C. Wu, L. Ma, Y. Chen, N. Tsubaki, *Bio-syngas production from biomass catalytic gasification*, Energy Conversion and Management 48 (2007) 1132-1139.

[5] T. Wang, J. Chang, X. Cui, Q. Zhang, Y. Fu, *Reforming of raw fuel gas from biomass gasification to syngas over highly stable nickel-magnesium solid solution catalysts*, Fuel Processing Technology 87 (2006) 421-428.

[6] M.J.A. Tijmensen, A.P.C. Faaij, C.N. Hamelinck, M.R.M. van Hardeveld, *Exploration of the possibilities for production of Fischer Tropsch liquids and power via biomass gasifcation*, Biomass and Bioenergy 23 (2002) 129-152.

[7] X. Xu, E. Jiang, M. Wang, Y. Xu, *Dry and steam reforming of biomass pyrolysis gas for rich hydrogen gas*, Biomass and Bioenergy 78 (2015) 6-16.

[8] M. Cho, Y. Choi, J. Kim, *Air gasification of PVC (polyvinyl chloride)-containing plastic waste in a two-stage gasifier using Ca-based additives and Ni-loaded activated carbon for the production of clean and hydrogen-rich producer gas*, Energy 87 (2015) 586-593.

# APPENDIX 1

# Bibliographic Data

Table A-1: Literature data of some non-nickel-based catalysts and their performances in dry reforming of methane

| Ref | Catalyst Name | type | Metal | (wt%) | Ni (nm) | Ni spent (nm) | **Test conditions** Reactor, catalyst weight, pressure Reduction Reaction ($CH_4$:$CO_2$=1) | $X(CH_4)_i$ (%) | $X(CO_2)_i$ (%) | $(H_2:CO)_i$ | Time (h) | $X(CH_4)_f$ (%) | $X(CO_2)_f$ (%) | $(H_2:CO)_f$ |
|---|---|---|---|---|---|---|---|---|---|---|---|---|---|---|
| 1 | 0.3Pt/$Al_2O_3$ | Non-porous | Pt | 0.3 | | | Fixed-bed quartz reactor, n.d., atm 500°C, $H_2$, 50 ml/min, 2h ($CH_4$:$CO_2$), 15.6 L/g.h, 650°C | 0 | | | 4 | 0 | | |
| 2 | Pt(0.5%)/$Al_2O_3$ | | Pt | 0.5 | | | Flow equipment, 170 mg, n.d. 750°C, $H_2$,3h ($CH_4$:$CO_2$), 20 mL/min, 700°C | 78 | 92 | 0.75 | 108 | 18 | 30 | 0.4 |
| | Pt(0.2%)/$Al_2O_3$ | | | 0.2 | | | | 42 | 50 | | 6 | 8 | 10 | |
| 3 | 0.4Pt/$Al_2O_3$IM | | Pt | 4 | | | Fixed-bed SS reactor, 100 mg, atm 700°C, 3%$H_2$/He, 30 ml/min, 2h 40%($CH_4$:$CO_2$)/He, 30 L/g.h, 700°C | | 73 | | 14 | | 67 | |
| | 0.4Pt/$Al_2O_3$ME | | | | | | | | 66 | | | | 66 | |
| 4 | Co/$Al_2O_3$ | | Co | 10 | | | Quartz reactor, 50 mg, atm 800°C, $H_2$, 1h 100%($CH_4$:$CO_2$), 60 L/g.h, 800°C | 56 | 66 | | 4 | 36.9 | 50.3 | |
| | Ru/$Al_2O_3$ | | Ru | 5 | | | | 39.2 | 51.9 | | | 36.9 | 63.8 | |
| | Rh/$Al_2O_3$ | | Rh | | | | | 57.2 | 64.4 | | | 56.9 | 63.8 | |
| | Pt/$Al_2O_3$ | | Pt | | | | | 26.5 | 31.1 | | | 11 | 17 | |
| | Pd/$Al_2O_3$ | | Pd | | | | | 38.8 | 41.2 | | | 12.7 | 15.8 | |
| | Ir/$Al_2O_3$ | | Ir | | | | | 25.6 | 38.1 | | | 26.6 | 39.3 | |
| | Rh/Yas3-8 | Mesoporous | Rh | | | | | 84.4 | 85.2 | | | 84.8 | 85.5 | |
| 5 | 4Co-MCM-41 | | Co | 4 | 4.2 ± 1.6 | 16.1 ± 5.7 | Fixed-bed reactor, n.d., atm 750°C, $H_2$, 2h 50%($CH_4$:$CO_2$)/He, 50 L/g.h, 750°C | 68 | | | 10 | 28 | | |
| | 0.8Pt/MCM-41 | | Pt | 0.8 | 7 ± 5.1 | 16 ± 15.2 | | 82 | | | 72 | 76 | | |
| 6 | 0.5% Pt/MgO | | Pt | 0.5 | | | Fixed-bed reactor, n.d., atm 750°C, $H_2$, 2h 50%($CH_4$:$CO_2$)/He, 50 L/g.h, 750°C | 20 | 28 | | 50 | 20 | 28 | |
| 7 | 2% Rh-$CeO_2$ | | Rh | 2 | | | Hastelloy-C reactor, 150 mg, 1.2 bar 400°C, 20%$H_2$/He, 1h 100%($CH_4$:$CO_2$), 16 L/g.h | | | 0.66 | 21 | 42 | 50 | 0.62 |
| | 2% Rh-$CeO_2$ | | | | | | | 48.6 | 57 | 0.73 | 70 | 44.1 | 50.1 | 0.7 |
| 8 | 0.5Rh/MCF | | Rh | 0.5 | | | Fixed-bed SS reactor, 40 mg, atm 450°C, $H_2$,1h 40%($CH_4$:$CO_2$)/$N_2$, 13.5 L/g.h, 750°C | 72 | 72 | 0.93 | 100 | 72 | 70 | 0.93 |
| | 1Rh/MCF | | | 1 | | | | 78 | 78 | 0.94 | | 76 | 76 | 0.92 |
| | 2Rh/MCF | | | 2 | | | | 82 | 87 | 0.93 | | 82 | 87 | 0.94 |
| | 3Rh/MCF | | | 3 | | | | 90 | 93 | 0.95 | | 92 | 93 | 0.92 |

Table A-2: Literature data of some nickel-based catalysts and their performances in dry reforming of methane

| Ref | Catalyst Name | type | Ni (wt%) | Ni (nm) | Ni spent (nm) | **Test conditions** Reactor, catalyst weight, pressure Reduction Reaction ($CH_4$:$CO_2$=1) | $X(CH_4)_i$ (%) | $X(CO_2)_i$ (%) | $(H_2:CO)_i$ | Time (h) | $X(CH_4)_f$ (%) | $X(CO_2)_f$ (%) | $(H_2:CO)_f$ |
|---|---|---|---|---|---|---|---|---|---|---|---|---|---|
| 9 | $LaNiO_3$ | Non-porous | | 15 | 17 | n.d., 20 mg, n.d. 700°C, $H_2$, 1h 20%($CH_4$:$CO_2$)/He, 300 L/g.h, 700°C | | | | 15 | 65 | 81 | 0.82 |
| | $La_2NiO_4$ | | | 7 | 10 | | | | | | 80 | 90 | 0.84 |
| | 1%Ni/$La_2O_3$ | | 1 | 12 | | | | | | | 32 | 48 | 0.47 |
| | 5%Ni/$La_2O_3$ | | 5 | | | | | | | | 59 | 73 | 0.66 |
| | 17%Ni/$La_2O_3$ | | 17 | 19 | | | | | | | 62 | 75 | 0.84 |
| | $LaNiO_3$ | | | | 18 | | | | | | 60 | 75 | 0.68 |
| | $La_2NiO_4$ | | | | 20 | | | | | | 80 | 90 | 1.03 |
| 2 | Ni(10%)/$Al_2O_3$ | | 10 | | | Flow equipment, 170 mg, n.d. 750°C, $H_2$, 3h ($CH_4$:$CO_2$), 20 mL/min, 700°C | 70 | 77 | | 6 | 70 | 77 | |
| | Ni(10%)/$Al_2O_3$ | | | | | | 68 | 92 | 0.6 | 108 | 68 | 90 | 0.6 |
| 10 | NM5Z2 | | 10 | | | Fixed-bed quartz reactor, 20 mg, atm 750°C, 5%$H_2$/Ar, 2h 20%($CH_4$:$CO_2$)/Ar, 150 L/g.h, 750°C | 90 | | | 14 | 80 | | |
| 11 | 0PrT500 | | 10 | 17 | 16 | Fixed-bed quartz reactor, 50 mg, n.d. 10%$H_2$/Ar, 30 ml/min 100%($CH_4$:$CO_2$), 96 L/g.h, 700°C | 0 | 0 | | 5 | 37 | 48 | 0.67 |
| | 0PrT800 | | | 17 | 17 | | 0 | 0 | | | 30 | 36 | 0.55 |
| 4 | $Ni/Al_2O_3$ | | 10 | | | Quartz reactor, 50 mg, atm 800°C, $H_2$, 1h 100%($CH_4$:$CO_2$), 60 L/g.h, 800°C | 71.5 | 77.1 | | 4 | 67.4 | 73.7 | |
| 12 | 5%Ni/NP-5Mg95Al | | 5 | | | Fixed-bed quartz reactor, 100 mg, atm 800°C, 33%$H_2$/$N_2$, 30 ml/min, 2h ($CH_4$:$CO_2$), 15 L/g.h, 700°C | 81 | 77 | 0.85 | 100 | 50 | 47 | 0.7 |
| 13 | Ni/γ-$Al_2O_3$ | | 10 | | | Fixed-bed quartz reactor, 50 mg, atm 750°C, $H_2$, 1h 100%($CH_4$:$CO_2$), 50 L/g.h, 750°C | 60.8 | 62.9 | | 10 | 31.8 | 29.2 | 0.88 |
| | Ni/MgO/$Al_2O_3$ | | 10 | | | | 81 | 94.4 | | | 76.7 | 88.37 | 0.9 |
| | Ni/$MgAl_2O_4$ | | 1 | | | | 72.2 | 85.2 | | | 66.1 | 77 | 0.78 |
| | Ni/$MgAl_2O_4$ | | 3 | | | | 78.2 | 83.5 | | | 78 | 83.9 | 0.9 |
| | Ni/$MgAl_2O_4$ | | 5 | | | | 82.6 | 87.7 | | | 82.9 | 88.7 | 0.99 |
| | Ni/$MgAl_2O_4$ | | 5 | | | | 83 | 87 | | 55 | 82.5 | 88 | |
| | Ni/$MgAl_2O_4$ | | 10 | | | | 83.8 | 91.8 | | 10 | 84.7 | 92.6 | 0.98 |
| | Ni/MgAl2O4 | | 15 | | | | 83.7 | 93.5 | | | 85.3 | 96.2 | 0.91 |

Table A-2: *Continued*

| Ref | Catalyst Name | type | Ni (wt%) | Ni (nm) | Ni spent (nm) | **Test conditions**<br>Reactor, catalyst weight, pressure<br>Reduction<br>Reaction ($CH_4$:$CO_2$=1) | $X(CH_4)_i$ (%) | $X(CO_2)_i$ (%) | $(H_2:CO)_i$ | Time (h) | $X(CH_4)_f$ (%) | $X(CO_2)_f$ (%) | $(H_2:CO)_f$ |
|---|---|---|---|---|---|---|---|---|---|---|---|---|---|
| 14 | Ni/MgO-AN | | 8.8 | | | Fixed-bed quartz reactor, 100 mg,1.5MPa<br>850°C, $H_2$, 20 ml/min, 1h<br>($CH_4$:$CO_2$), 16 L/g.h, 750°C | 38 | 33 | | 50 | 23 | 25 | |
| 15 | Ni-Ce-$ZrO_2$ | | 30 | | | Fixed-bed microreactor, n.d., n.d.<br>700°C, 5%$H_2$/$N_2$, 2h<br>67%( $CH_4$:$CO_2$)/$N_2$, 108 L/g.h, 800°C[a] | 96 | 96 | | 20 | 82 | 82 | |
| | Ni-Ce-$ZrO_2$ | | 15 | | | | 95 | 95 | | 35 | 88 | 90 | |
| | Ni-Ce-$ZrO_2$ | Non-porous | 10 | | | | 85 | 86 | | 20 | 77 | 80 | |
| | Ni-Ce-$ZrO_2$ | | 5 | | | | 81 | 83 | | 20 | 73 | 75 | |
| 16 | Ni/MgO-AN | | 8.8 | | | Fixed-bed quartz reactor, 100 mg, atm<br>850°C, $H_2$, 20 ml/min, 1h<br>($CH_4$:$CO_2$), 16 L/g.h, 750°C[b] | 87 | 88 | | 50 | 87 | 88 | |
| | Ni/MgO-AN | | | | | | 37 | 33 | | | 23 | 25 | |
| 3 | 4Ni/$Al_2O_3$ IM | | 10 | | 23 | Fixed-bed SS reactor, 100 mg, atm<br>700°C, 3%$H_2$/He, 30 ml/min, 2h<br>40%($CH_4$:$CO_2$)/He, 30 L/g.h, 700°C | | 67 | | 14 | | 50 | |
| | 4Ni/$Al_2O_3$ ME | | | | 14 | | | 65 | | | | 58 | |
| 17 | Ni/$Ce_2Zr_2$ (imp) | | 5 | | | Fixed-bed quartz reactor, 100 mg, n.d.<br>750°C,100%$H_2$, 4h<br>100%($CH_4$:$CO_2$), 12 L/g.h, 650°C[c] | 18 | 42 | | 24 | 16 | 40 | |
| | $NiCe_{0.6}Zr_{2.97}$ (sg) | | | | | | 19 | 45 | | | 16 | 40 | |
| | $NiCe_2Zr_{1.51}$ (sg) | | | | | | 18 | 43 | | | 15 | 36 | |
| 18 | Ni/$SiO_2$ | | 10 | | 17 | Fixed-bed quartz reactor, 250 mg, atm<br>800°C, $H_2$/Ar, 60 ml/min, 1h<br>100%($CH_4$:$CO_2$), 14.4 L/g.h, 800°C | | | | 10 | 17.9 | 23.3 | |
| 19 | Ni-Al | | 33 | | 26 | Fixed-bed quartz reactor, 50 mg, atm<br>650°C, 50%$H_2$/$N_2$<br>33%($CH_4$:$CO_2$)/$N_2$, 360 L/g.h, 700°C | 34 | 43 | | 4 | 48 | 64 | |
| 20 | SAA10 | | | 2.1 | 6.3 | Fixed-bed quartz reactor, 50 mg, atm<br>700°C, $H_2$, 2h<br>50%($CH_4$:$CO_2$)/$N_2$, 48 L/g.h, 700°C | 61 | 66 | | 30 | 47 | 54 | |
| | SAA15 | | | 3.3 | 7.1 | | 64 | 69 | | | 55 | 62 | |
| | SAA20 | | | 3.9 | 7.4 | | 69 | 73 | | | 66 | 67 | |
| | SAA25 | | | 7.9 | 8.3 | | 70 | 75 | | | 66 | 71 | |
| | ICN | | 10 | 10..15 | | | 66 | 68 | | 5 | | | |
| 21 | Ni-ZrLa | | 5 | | | Fixed-bed quartz reactor, 10 mg, atm<br>500°C, 25%$H_2$/He, 100 ml/min, 2h<br>20%($CH_4$:$CO_2$)/He, 600 L/g.h, 450°C | | | | 0.5 | 9.8 ± 0.5 | 12.9 ± 0.6 | 0.58 |
| | Ni-ZrLa | | | | | | 21 | | | 14 | 0 | | |

Table A-2: *Continued*

| Ref | Catalyst Name | type | Ni (wt%) | Ni (nm) | Ni spent (nm) | **Test conditions** Reactor, catalyst weight, pressure Reduction Reaction ($CH_4$:$CO_2$=1) | $X(CH_4)_i$ (%) | $X(CO_2)_i$ (%) | $(H_2:CO)_i$ | Time (h) | $X(CH_4)_f$ (%) | $X(CO_2)_f$ (%) | $(H_2:CO)_f$ |
|---|---|---|---|---|---|---|---|---|---|---|---|---|---|
| 22 | Ni/Al | Non-porous | 5 | 23 | | Fixed-bed quartz reactor, 30 mg, atm 750°C, $H_2$, 1h ($CH_4$:$CO_2$)/He, 200 L/g.h, 750°C[d] | | | | 20 | | | |
| | Ni/Ce(3)Al | | | 22 | 24 | | 78 | | | | 70 | | |
| | Ni/Ce(5)Al | | | 19 | 23 | | 62 | | | | 53 | | |
| 23 | Ni/CeZr | | 5 | | | Fixed-bed quartz reactor, 100 mg, n.d. 750°C, 5%$H_2$/Ar, 2.5 ml/min, 4h 20%($CH_4$:$CO_2$)/Ar, 3 L/g.h, 750°C | 75 | | | 90 | 40 | | |
| | Ni/CeZrRh | | | | | | 79 | | | | 70 | | |
| | Ni/CeZrRu | | | | | | 87 | | | | 75 | | |
| 24 | Ni/$CeO_2$ | | 10 | | | Fixed-bed quartz reactor, 300 mg, atm 800°C, 100%$H_2$, 60 ml/min, 2h 73%($CH_4$:$CO_2$)/$N_2$, 13.6 L/g.h, 760°C | 81.85 | 90 | 0.9 | 100 | 65.18 | 80 | 0.82 |
| 25 | NiAl | | 4 | 11 | | Fixed-bed reactor, 50mg, n.d. 750°C, 5%$H_2$/Ar, 1h 30%($CH_4$:$CO_2$)/He, 60 L/g.h, 750°C | 82 | 89 | | 24 | 78 | 85 | |
| | NiAlMg | | | | | | 82 | 90 | | | 81 | 89 | |
| | NiAlCe | | | | | | 85 | 92 | | | 83 | 90 | |
| 26 | N-NiCaZr | | | | | Fixed-bed SS reactor, 200 mg, atm 600°C, 10%$H_2$/$N_2$, 60 ml/min, 1h 100%($CH_4$:$CO_2$), 36 L/g.h, 700°C | 57 | | | 32 | 13.3 | | |
| 27 | Ni/α-$Al_2O_3$ | | 5 | | | Fixed-bed quartz reactor, 20 mg, atm 650°C, $H_2$/Ar, 100 ml/min, 1h ($CH_4$:$CO_2$), 450000$h^{-1}$, 650°C[d] | 25.3 | 37 | | | | | |
| | Ni-Al/α-$Al_2O_3$ | | | | | | 40 | 50 | | | | | |
| | (Ni/γ-$Al_2O_3$)k | | | | | | 25 | 57 | | | | | |
| 28 | Ni/Ce-$ZrO_2$/θ-$Al_2O_3$ | | 3 | | | Fixed-bed microreactor, n.d., n.d. 700°C, 5%$H_2$/$N_2$, 2h 40%($CH_4$:$CO_2$)/$N_2$, 60 L/g.h, 800°C | 98 | | | 20 | 78 | | |
| | Ni/θ-$Al_2O_3$ | | | | | | 98 | | | 20 | 62 | | |
| | Ni/γ-$Al_2O_3$ | | | | | | 92 | | | 12 | 80 | | |
| | Ni/Ce-$ZrO_2$/θ-$Al_2O_3$ | | 6 | | | | 97 | 98 | | 20 | 97 | 98 | 0.96 |
| | Ni/Ce-$ZrO_2$/θ-$Al_2O_3$ | | 9 | | | | 98 | 99 | | 20 | 98 | 99 | 0.97 |
| | Ni/Ce-$ZrO_2$/θ-$Al_2O_3$ | | 12 | | | | 97 | 98 | | 20 | 97 | 98 | 0.96 |
| | Ni/Ce-$ZrO_2$/θ-$Al_2O_3$ | | 15 | | | | 97 | 98 | | 20 | 97 | 98 | 0.96 |
| 29 | NiAl | | 33 | | | SS reactor 50 mg, atm 800°C, $H_2$, 50 ml/min, 1h ($CH_4$:$CO_2$), 630°C | 35 | | 0.93 | 11 | 18 | | |
| | NiAlPP | | | | | | 38 | | | | 54 | | |

Table A-2: *Continued*

| Ref | Catalyst Name | type | Ni (wt%) | Ni (nm) | Ni spent (nm) | **Test conditions** Reactor, catalyst weight, pressure Reduction Reaction ($CH_4$:$CO_2$=1) | $X(CH_4)_i$ (%) | $X(CO_2)_i$ (%) | $(H_2:CO)_i$ | Time (h) | $X(CH_4)_f$ (%) | $X(CO_2)_f$ (%) | $(H_2:CO)_f$ |
|---|---|---|---|---|---|---|---|---|---|---|---|---|---|
| 30 | NiAl-1A | Non-porous | 10 | | 9.4 | Quartz reactor, 180 mg, n.d. 500°C, 100%$H_2$, 60 ml/min, 2h 20%($CH_4$:$CO_2$)/He, 20 L/g.h, 700°C | 90 | | | 6 | 87 | 91 | |
| | NiAl-1B | | | | | | | | | | 87 | 91 | |
| | NiAl-2A | | | | 7.6 | | 89 | | | | 86 | 92 | |
| | NiAl-2B | | | | | | | | | | 85 | 92 | |
| | NiAl-3* | | | | 10.1 | | 87 | | | | 84 | 91 | |
| 31 | $LaNiO_3$ | | | | | Fixed-bed quartz reactor, 200 mg, atm 600°C, $H_2$, 20 ml/min, 4h 20%($CH_4$:$CO_2$)/Ar, 24 L/g.h, 700°C | 85 | | | 24 | 85 | | |
| | $La_{0.8}Ca_{0.2}NiO_3$ | | | | | | 55 | | | | 56 | | |
| | $La_{0.8}Ca_{0.2}Ni_{0.6}Co_{0.4}O_3$ | | | | | | 60 | | | | 67 | | |
| 32 | OM0 | | | | | Quartz reactor, 50 mg, atm 700°C, 100%$H_2$, 30 ml/min, 1h 40%($CH_4$:$CO_2$)/He, 48 L/g.h, 700°C | 34.9 | 77 | 0.6 | 6 | 55.9 | 69.4 | 0.4 |
| 33 | 5% Ni/γ-$Al_2O_3$ | | 5 | | | Fixed-bed quartz reactor, 200 mg, atm 500°C, 100%$H_2$, 40 ml/min, 1h 91.2%($CH_4$:$CO_2$)/AR, 12 L/g.h, 700°C[e] | 59.2 | 82.28 | 0.89 | 8 | | | |
| | 7% Ni/γ-$Al_2O_3$ | | 7 | | | | 59.82 | 81.95 | 0.89 | | | | |
| | 10% Ni/γ-$Al_2O_3$ | | 10 | | | | 61.26 | 81.63 | 0.82 | | | | |
| | 15% Ni/γ-$Al_2O_3$ | | 15 | | | | 64.72 | 81.87 | 0.92 | | | | |
| 34 | $Ni/MgAl_2O_4$ | | 8.8 | | | Plug flow reactor, 60 mg, atm 700°C, 8%$H_2$/He, 2h 100%($CH_4$:$CO_2$), 20 L/g.h, 675°C[f] | 10 | 20 | | 20 | 5 | 10 | |
| 1 | $10Ni/Al_2O_3$ | | 10 | | | Fixed-bed quartz reactor, n.d., atm 500°C, $H_2$, 50 ml/min, 2h ($CH_4$:$CO_2$), 15.6 L/g.h, 650°C | 40 | | | 4 | 0 | | |
| 35 | $5Ni/SiO_2$ | porous | 5 | | | Quartz microreactor, 100 mg, atm 600°C, $H_2$, 1h ($CH_4$:$CO_2$), 30 L/g.h, 700°C | 72 | 77 | | 24 | | | |

Table A-2: *Continued*

| Ref | Catalyst Name | type | Ni (wt%) | Ni (nm) | Ni spent (nm) | **Test conditions**<br>Reactor, catalyst weight, pressure<br>Reduction<br>Reaction ($CH_4$:$CO_2$=1) | $X(CH_4)_i$ (%) | $X(CO_2)_i$ (%) | $(H_2:CO)_i$ | Time (h) | $X(CH_4)_f$ (%) | $X(CO_2)_f$ (%) | $(H_2:CO)_f$ |
|---|---|---|---|---|---|---|---|---|---|---|---|---|---|
| 36 | 3%Ni/zeolite A | Microporous | 3 | | | Fixed-bed reactor, 200 mg, atm<br>600°C, $H_2$, 1h<br>100%($CH_4$:$CO_2$), 30 L/g.h, 700°C | 7 | 10 | | 5 | 0 | 0 | |
| | 5%Ni/zeolite A | | 5 | | | | 35 | 50 | | | 0 | 0 | |
| | 7%Ni/zeolite A | | 7 | | | | 70 | 80 | | | 13 | 20 | 0.31 |
| | 3%Ni/zeolite X | | 3 | | | | 75 | 80 | | | 20 | 25 | |
| | 5%Ni/zeolite X | | 5 | | | | 77 | 80 | | | 60 | 70 | |
| | 7%Ni/zeolite X | | 7 | 54.39 | | | 85 | 85 | | | 72 | 80 | 1.27 |
| | 3%Ni/zeolite Y | | 3 | | | | 88 | 88 | | | 62 | 70 | |
| | 5%Ni/zeolite Y | | 5 | | | | 92 | 92 | | | 92 | 92 | |
| | 7%Ni/zeolite Y | | 7 | 54.39 | | | 92 | 92 | | | 92 | 92 | 1.79 |
| | 3%Ni/ZSM-5 | | 3 | | | | 90 | 92 | | | 58 | 70 | |
| | 5%Ni/ZSM-5 | | 5 | | | | 72 | 80 | | | 63 | 73 | |
| | 7%Ni/ZSM-5 | | 7 | 27.28 | | | 90 | 92 | | | 58 | 70 | 1.03 |
| 37 | Ni-S1 | | 5 | | | Quartz reactor, 200 mg, atm<br>400°C, $H_2$, 20 ml/min, 1h<br>($CH_4$:$CO_2$), 30 L/g.h, 700°C | 73 | 85 | 1.2 | 25 | 56 | 83 | 1.22 |
| | Ni-S111 | | | | | | 70 | 80 | 1.2 | | 61 | 84 | 1.25 |
| | Ni-S111S | | | | | | 75 | 82 | 1.05 | | 72 | 80 | 1.05 |
| 38 | Ni/MCM-41 | Mesoporous | | | | Quartz flow reactor, 100 mg, n.d.<br>n.d.<br>($CH_4$:$CO_2$)/Ar, 36 L/g.h, 600°C | 32 | 47 | | 4 | 28 | 40 | |
| | Ni/MCM-41 | | | | | | 29 | 42 | | 14 | 20 | 33 | |
| | Ni/MCM-41 | | | 24 | | | 32 | 47 | | 4 | 33 | 40 | |
| 39 | Ni/yttria-doped SBA-15 | | | 35.3 | | Fixed-bed quartz reactor, n.d., atm<br>700°C, 100%$H_2$, 60 ml/min, 0.5h<br>100%($CH_4$:$CO_2$), 15000 $h^{-1}$, 750°C | 36 | 42 | 0.5 | 6 | 21 | 15 | 0.3 |
| | Ni/yttria-doped SBA-15 | | | 20.4 | | | 50 | 52 | 0.61 | | 31 | 32 | 0.58 |
| | Ni/yttria-doped SBA-15 | | | 18.4 | | | 57 | 60 | 0.63 | | 50 | 51 | 0.58 |
| | Ni/yttria-doped SBA-15 | | | 18.6 | | | 53 | 51 | 0.63 | | 41 | 33 | 0.6 |
| | Ni/yttria-doped SBA-15 | | | 25.3 | | | 50 | 49 | 0.61 | | 41 | 39 | 0.62 |
| 40 | Ni/SBA-15 | | 10 | 17.2 | 17 | Fixed-bed quartz reactor, 100 mg, atm<br>700°C, $H_2$, 1h<br>($CH_4$:$CO_2$), 36 L/g.h, 700°C | 63 | 62 | 1 | 40 | 42 | 37 | 0.82 |
| | Ni/8MgO-SBA-15 | | | 10.8 | 12 | | 71 | 66 | 1.13 | 40 | 66 | 62 | 0.84 |
| | Ni/8MgO/SBA-15-IMP | | | 11.6 | 13.3 | | 70 | 65 | 1.1 | 40 | 63 | 50 | 0.82 |

Table A-2: *Continued*

| Ref | Catalyst Name | type | Ni (wt%) | Ni (nm) | Ni spent (nm) | **Test conditions**<br>Reactor, catalyst weight, pressure<br>Reduction<br>Reaction ($CH_4$:$CO_2$=1) | $X(CH_4)_i$ (%) | $X(CO_2)_i$ (%) | $(H_2:CO)_i$ | Time (h) | $X(CH_4)_f$ (%) | $X(CO_2)_f$ (%) | $(H_2:CO)_f$ |
|---|---|---|---|---|---|---|---|---|---|---|---|---|---|
| 41 | Ni/SBA-15 | Mesoporous | 12 | 20.6 | 22.3 | Fixed-bed quartz reactor, 400 mg, atm<br>800°C, 20%$H_2$/$N_2$, 3h<br>($CH_4$:$CO_2$), 4 L/g.h, 800°C | 97.2 | | | 60 | | | |
| 42 | 13% Ni/$ZrO_2$ (comm) | | 13 | | | Fixed-bed reactor, n.d., atm<br>700°C, 5%$H_2$/$N_2$<br>($CH_4$:$CO_2$), 37.6 L/g.h, 700°C | 50 | | | 3 | 30 | | |
| | 13% Ni/$ZrO_2$ (Reflux) | | | | | | 75 | | | 5 | 62 | | |
| | 13% Ni/$ZrO_2$ (HY) | | | | | | 67 | | | 5 | 33 | | |
| | 13% Ni/$ZrO_2$ (CP) | | | | | | 70 | | | 3 | 53 | | |
| | 13% Ni/$ZrO_2$ (AL) | | | | | | 75 | | | 5 | 55 | | |
| | 5% Ni/$ZrO_2$ (AL) | | 5 | | | | 75 | 71 | | | 58 | 58 | |
| | 5Ni/$CeO_2$ (CTAB) | | | | | | 78 | 80 | | | 67 | 67 | |
| | 5Ni/$Ce_{0.4}Zr_{0.6}O_2$ (CTAB) | | | | | | 62.5 | | | | 61.8 | | |
| | 5Ni/$Ce_{0.5}Zr_{0.5}O_2$ (CTAB) | | | | | | 63 | | | | 61.5 | | |
| | 5Ni/$Ce_{0.6}Zr_{0.4}O_2$ (CTAB) | | | | | | 64 | | | | 62.8 | | |
| | 5Ni/$Ce_{0.68}Zr_{0.32}O_2$ (CTAB) | | | | | | 64 | | | | 60.5 | | |
| | 5Ni/$Ce_{0.78}Zr_{0.22}O_2$ (CTAB) | | | | | | 63.5 | | | | 61.5 | | |
| | 5Ni/$Ce_{0.85}Zr_{0.15}O_2$ (CTAB) | | | | | | 65 | | | | 62.2 | | |
| | 5Ni/$Ce_{0.92}Zr_{0.02}O_2$ (CTAB) | | | | | | 63.5 | | | | 61.5 | | |
| 43 | 5Ni/CZ100 | | 5 | | | Fixed-bed plug flow reactor, 100 mg, atm<br>800°C, 10%$H_2$/$N_2$, 40 ml/min, 1h<br>100%($CH_4$:$CO_2$), 30 L/g.h, 700°C | 25 | | | 24 | 21 | 35 | |
| | 5Ni/CZ75 | | | | | | 49 | | | | 34 | 48 | |
| | 5Ni/CZ44 | | | | | | 46 | | | | 31 | 45 | |
| | 5Ni/CZ28 | | | | | | 51 | | | | 38 | 52 | |
| 4 | Ni/Yas3-8 | | | | | Quartz reactor, 50 mg, atm<br>800°C, $H_2$, 1h<br>100%($CH_4$:$CO_2$), 60 L/g.h, 800°C | | | | 4 | 62 | 68 | |
| 44 | Ni-MCM-41 | | 2 | 19.5 | 27 | Quartz reactor, 120 mg, atm<br>750°C, He, 2h<br>50%($CH_4$:$CO_2$)/He, 50 L/g.h, 750°C | 94 | | 0.98 | 72 | 50 | | 0.88 |
| 45 | Ni/SBA-15 | | 4.8 | 10.7 | | Fixed-bed quartz reactor, 200 mg, atm<br>600°C, 20%$H_2$/Ar, 2h<br>100%($CH_4$:$CO_2$), 12.9 L/g.h, 700°C | 72 | 85 | 1 | 50 | 66 | 81 | 0.95 |

Table A-2: *Continued*

| Ref | Catalyst Name | type | Ni (wt%) | Ni (nm) | Ni spent (nm) | **Test conditions**<br>Reactor, catalyst weight, pressure<br>Reduction<br>Reaction ($CH_4$:$CO_2$=1) | $X(CH_4)_i$ (%) | $X(CO_2)_i$ (%) | $(H_2:CO)_i$ | Time (h) | $X(CH_4)_f$ (%) | $X(CO_2)_f$ (%) | $(H_2:CO)_f$ |
|---|---|---|---|---|---|---|---|---|---|---|---|---|---|
| [46] | 10%Ni/SBA-15 | Mesoporous | 10 | | | Fixed-bed quartz reactor, 300 mg, atm<br>800°C, 3%$H_2$/Ar, 50 ml/min, 3h<br>20%($CH_4$:$CO_2$)/Ar, 20 L/g.h, 600°C | 52 | 87 | 0.8 | 30 | 39 | 70 | 0.75 |
| [12] | 5%Ni/OMA | | 5 | | | Fixed-bed quartz reactor, 100 mg, atm<br>800°C, 33%$H_2$/$N_2$, 30 ml/min, 2h<br>($CH_4$:$CO_2$), 15 L/g.h, 700°C | 77 | 77 | 0.8 | 100 | 75 | 75 | 0.8 |
| [26] | C-NiCaZr | | 9.3 | | | Fixed-bed SS reactor, 50 mg, atm<br>600°C, 10%$H_2$/$N_2$, 60 ml/min, 1h<br>100%($CH_4$:$CO_2$), 96 L/g.h, 700°C | 72 | 84 | 0.9 | 40 | 73 | 84 | 0.91 |
| | CN-NiCaZr | | 10.4 | | | | 30 | 52 | 0.5 | | 34 | 56 | 0.52 |
| | I-NiCaZr | | 13.12 | | | | 60 | 73 | 0.8 | | 48 | 65 | 0.67 |
| [47] | Ni-MCM-41 | | | 9.7 | | Fixed-bed quartz reactor, 100 mg, atm<br>550°C, $H_2$, 3h<br>66%($CH_4$:$CO_2$)/Ar, 36 L/g.h, 600°C | | | | 4 | 28 | 39 | 0.63 |
| [48] | Ni-$ZrO_2$-CR-10 | | 10 | 7.3 | | Fixed-bed quartz reactor, 500 mg, atm<br>700°C, 10%$H_2$/Ar, 100 ml/min, 1h<br>($CH_4$:$CO_2$), 24 L/g.h, 750°C | 60 | 66 | | 10 | 52 | 60 | |
| | Ni-$ZrO_2$-CR-15 | | 15 | 7.2 | 7.3 | | 93 | 96 | | | 93 | 96 | |
| | Ni-$ZrO_2$-CR-20 | | 20 | 12.4 | | | 93 | 95 | | | 91 | 95 | |
| | Ni-$ZrO_2$-CR-25 | | 25 | 13.2 | | | 93 | 94 | | | 85 | 90 | |
| | Ni-$ZrO_2$-C | | 15 | 15.3 | | | 76 | 96 | | | 52 | 61 | |
| | Ni-$ZrO_2$-IMP | | 15 | 15.5 | | | 90 | 98 | | | 69 | 77 | |
| | Ni-$ZrO_2$-CR-15 | | 15 | 7.2 | 7.3 | | 86 | 87 | 0.95 | 80 | 86 | 87 | 0.94 |
| [49] | Ni/Yas1-2 | | 10 | < 10 | 12.1 | Fixed-bed quartz reactor, 50 mg, atm<br>800°C, $H_2$, 1h<br>100%($CH_4$:$CO_2$), 60 L/g.h, 800°C | 85.6 | 86.8 | | 4 | 84.4 | 85.7 | |
| | Ni/Yas3-8 | | | < 10 | 10.5 | | 85.8 | 86.6 | | | 85 | 86 | |
| | Ni/γ-$Al_2O_3$ | | | 10.6 | 18.3 | | 78.2 | 81.6 | | | 76.5 | 80.6 | |
| | Ni/α-$Al_2O_3$ | | | 54.3 | 72.5 | | 71.5 | 77.1 | | | 67.4 | 73.7 | |
| | Ni/$SiO_2$ | | | 48.8 | 59.1 | | 69.4 | 72.7 | | | 61.5 | 68.6 | |
| | Ni/MgO | | | < 10 | < 10 | | 67.8 | 75.1 | | | 65.2 | 72.7 | |
| | Ni/$La_2O_3$ | | | 79.1 | > 100 | | 66.1 | 66.2 | | 1 | 56.7 | 63.4 | |
| | Ni/$CeO_2$ | | | 87.5 | 94.5 | | 62.5 | 69.8 | | 4 | 51.6 | 63 | |
| | Ni/$ZrO_2$ | | | | | | 9.7 | 15.2 | | | 9.8 | 15.2 | |

Table A-2: *Continued*

| Ref | Catalyst Name | type | Ni (wt%) | Ni (nm) | Ni spent (nm) | **Test conditions** Reactor, catalyst weight, pressure Reduction Reaction ($CH_4$:$CO_2$=1) | $X(CH_4)_i$ (%) | $X(CO_2)_i$ (%) | $(H_2:CO)_i$ | Time (h) | $X(CH_4)_f$ (%) | $X(CO_2)_f$ (%) | $(H_2:CO)_f$ |
|---|---|---|---|---|---|---|---|---|---|---|---|---|---|
| 50 | $Ni/Al_2O_3$ | Mesoporous | 10 | 22.8 | 33 | Fixed-bed quartz reactor, 50 mg, atm 800°C, $H_2$, 4h 100%($CH_4$:$CO_2$), 60 L/g.h, 800°C | 74.7 | 78.9 | | 4 | 72.9 | 77.7 | |
| | $Ni/Mg_{0.2}Al_{0.8}O_x$ | | | 16.8 | 19.3 | | 78.5 | 82.6 | | | 80.8 | 84.3 | |
| | $Ni/Mg_{0.3}Al_{0.7}O_x$ | | | 15.3 | 18.4 | | 85 | 86.3 | | | 86.3 | 87.2 | |
| | $Ni/Mg_{0.4}Al_{0.6}O_x$ | | | 11.6 | 14.7 | | 84.7 | 86.1 | | | 85.1 | 86.8 | |
| | $Ni/Mg_{0.6}Al_{0.5}O_x$ | | | 11.9 | 12.4 | | 83.6 | 85.4 | | | 84.4 | 86.2 | |
| | $Ni/Mg_{0.8}Al_{0.2}O_x$ | | | 9.4 | 10.7 | | 82.7 | 85 | | | 83.7 | 85.9 | |
| | Ni/MgO | | | | | | 54.1 | 64.1 | | | 54.7 | 64 | |
| | $Ni/\alpha\text{-}Al_2O_3$ | | | 54.3 | 72.5 | | 71.5 | 77.1 | | | 67.4 | 73.7 | |
| | Ni/MgO | | | | | | 67.8 | 75.1 | | | 65.2 | 72.7 | |
| 51 | Ni/Yas3-8 | | 10 | < 10 | 27.8 | Quartz reactor, 50 mg, n.d. 800°C, $H_2$, 1h 100%($CH_4$:$CO_2$), 60 L/g.h, 800°C | 86.4 | 87.3 | | 4 | 84.9 | 86.2 | |
| | Ni/Yas3-8 | | | < 10 | 27.2 | | 86.4 | 87.3 | | | 85.1 | 86 | |
| | Ni/Yas3-8 | | | < 10 | 19.6 | | 86.5 | 87.5 | | | 85.5 | 86.5 | |
| | Ni/Yas3-8 | | | < 10 | 16.2 | | 85.8 | 86.5 | | | 85 | 86 | |
| | Ni/Yas3-8 | | | < 10 | 10.5 | | 85.8 | 86.6 | | | 85 | 86 | |
| 26 | M-NiCaZr | | | | | Fixed-bed SS reactor, 200 mg, atm 600°C, 10%$H_2$/$N_2$, 60 ml/min, 1h 100%( $CH_4$:$CO_2$), 36 L/g.h, 700°C | 60.9 | | | 32 | 55.7 | | |
| | M-NiCaZr | | | | | | 76 | 86 | | 100 | 78 | 87 | |
| 52 | $5Ni/SiO_2$ | | 5 | 7.6 | | Inconel reactor, 100 mg, n.d. 700°C, $H_2$, 1h ($CH_4$:$CO_2$), 4.8 L/g.h, 650°C | 64 | 75 | 0.6 | 24 | 50 | 62 | 0.6 |
| | $10Ni/SiO_2$ | | 10 | 9.2 | | | 60 | 74 | 0.6 | 24 | 46 | 60 | 1.1 |
| | $5Ni\text{-}CNTs/SiO_2$ | | 5 | 6.9 | | | 40 | 48 | 0.6 | 24 | 38 | 47 | 0.6 |
| | $10Ni\text{-}CNTs/SiO_2$ | | 10 | 9.9 | | | 44 | 52 | 0.6 | 24 | 50 | 59 | 0.6 |
| 53 | $6.7\%Ni/meso\text{-}SiO_2$ | | 6.7 | 21.4 | | Fixed-bed SS reactor, 30 mg, atm 650°C, $H_2$, 2h 40%($CH_4$:$CO_2$)/$N_2$, 24 L/g.h, 650°C | | | | 6 and 30 | | | 0.9-1 |
| | $3.1\%Ni\text{-}SiO_2$ | | 3.1 | 4.1 | | | | | | 6 | | | 0.9-1 |
| | $6.2\%Ni\text{-}SiO_2$ | | 6.2 | 6.2 | | | | | | 6 | | | 0.9-1 |
| | $6.7\%Ni\text{-}SiO_2$ | | 6.7 | 7.7 | | | | | | 6 and 30 | | | 0.9-1 |
| | $8.8\%Ni\text{-}SiO_2$ | | 8.8 | 10.5 | | | | | | 6 and 30 | | | 0.9-1 |
| | $13.2\%Ni\text{-}SiO_2$ | | 13.2 | 14 | | | | | | 6 | | | 0.9-1 |

Table A-2: *Continued*

| Ref | Catalyst Name | type | Ni (wt%) | Ni (nm) | Ni spent (nm) | **Test conditions** Reactor, catalyst weight, pressure Reduction Reaction ($CH_4$:$CO_2$=1) | $X(CH_4)_i$ (%) | $X(CO_2)_i$ (%) | $(H_2:CO)_i$ | Time (h) | $X(CH_4)_f$ (%) | $X(CO_2)_f$ (%) | $(H_2:CO)_f$ |
|---|---|---|---|---|---|---|---|---|---|---|---|---|---|
| [54] | 4.8Ni/SBA-15 | Mesoporous | 4.8 | | | Fixed-bed quartz reactor, 200 mg, atm 600°C, 20%$H_2$/Ar, 2h 100%($CH_4$:$CO_2$), 34.5 L/g.h, 800°C | 67 | 81 | | 50 | 50 | 75 | |
| [55] | NiAl | | 7 | 9 | 7.4 | Fixed-bed quartz reactor, 100 mg, atm 700°C, $H_2$, 1h ($CH_4$:$CO_2$), 36 L/g.h, 700°C | 55 | | 0.9 | 80 | 45 | | 0.8 |
| [56] | Ni/m$SiO_2$-S | | 10.1 | | | Fixed-bed quartz reactor, 150 mg, n.d. 800°C, 10%$H_2$/$N_2$, 30 ml/min, 1h ($CH_4$:$CO_2$), 6 L/g.h, 750°C | 90 | 96 | 1.03 | 20 | 88 | 93 | 1 |
| | Ni/m$SiO_2$-I | | 12.2 | | | | 88 | 96 | 1 | | 82 | 90 | 0.94 |
| [57] | NCZ-0.5 | | 9.3 | | | Fixed-bed quartz reactor, 100 mg, atm 650°C, 25%$H_2$/$N_2$, 80 ml/min, 1h 100%($CH_4$:$CO_2$), 48 L/g.h, 750°C[d] | 65 | | | 50 | 50 | | |
| | NCZ-1 | | 9.3 | | | | 83 | | | | 77 | | |
| | NCZ-1.2 | | 9.3 | | | | 87 | | | | 82 | | |
| | NCZ-2 | | 9.3 | | | | 95 | | | | 93 | | |
| [58] | $Ni/SiO_2$ | | 5 | 15 | | Fixed-bed reactor, 100 mg, atm 650°C, $H_2$, 20 ml/min, 2h ($CH_4$:$CO_2$), 21.1 L/g.h, 650°C | 61 | 70 | 0.9 | 12 | 59 | 69 | 0.9 |
| [59] | 0.3Ni/MCM-41 | | | | | Fixed-bed quartz reactor, 50 mg, atm 500°C, 10%$H_2$/$N_2$, 50 ml/min, 1h 40%($CH_4$:$CO_2$)/$N_2$, 120 L/g.h, 550°C | 28 | 40 | | 12 | 9 | 18 | 0.69 |
| [60] | 1Ni-SBA-15 | | 1 | | | Fixed-bed quartz reactor, n.d., atm 750°C, $H_2$, 2h 50%($CH_4$:$CO_2$)/He, 50000 $h^{-1}$, 750°C | | | | 72 | | | |
| | 5Ni-SBA-15 | | 5 | | 8.4 | | 79 | | 0.92 | | 78 | | 0.88 |
| | 5Ni/SBA-15 | | | | 19.4 | | 79 | | 0.92 | | 65 | | 0.62 |
| | 5Ni-MCM-41 | | | | 7.3 | | 75 | | | | 55 | | 0.44 |
| | 5Ni/MCM-41 | | | | 14 | | 75 | | | | 71 | | 0.78 |
| [5] | 4Ni-MCM-41 | | 4 | 4.1 ± 1 | 8.3 ± 2 | Fixed-bed reactor, n.d., atm 750°C, $H_2$, 2h 50%($CH_4$:$CO_2$)/He, 50 L/g.h, 750°C | 68 | | | 10 | 25 | | |
| [6] | 5% Ni/MgO | | 5 | 11.04 | | Fixed-bed reactor, 200 mg, atm 650°C, $H_2$, 30 ml/min, 4h 100%($CH_4$:$CO_2$), 15 L/g.h, 700°C | 68 | 75 | | 50 | 68 | 75 | |

Table A-2: *Continued*

| Ref | Catalyst Name | type | Ni (wt%) | Ni (nm) | Ni spent (nm) | Test conditions<br>Reactor, catalyst weight, pressure<br>Reduction<br>Reaction ($CH_4$:$CO_2$=1) | $X(CH_4)_i$ (%) | $X(CO_2)_i$ (%) | $(H_2:CO)_i$ | Time (h) | $X(CH_4)_f$ (%) | $X(CO_2)_f$ (%) | $(H_2:CO)_f$ |
|---|---|---|---|---|---|---|---|---|---|---|---|---|---|
| 61 | NCZ | Mesoporous | 5 | | | Packed-bed reactor, 160 mg, n.d.<br>700°C, 5%$H_2$/$N_2$, 100 ml/min, 3h<br>80%($CH_4$:$CO_2$)/$N_2$, 0.773 L/g.h, 800°C | 85 | | | 8 | 75 | | |
| | NCZ(1.25) | | | | | | 85 | | | | 86 | | |
| | NCZ(0.8) | | | | | | 85 | | | | 85 | | |
| | NCZ(0.5) | | | | | | 85 | | | | 82 | | |
| 58 | Ni/AW2 | | 5 | 24 | | Fixed-bed reactor, 100 mg, atm<br>650°C, $H_2$, 20 ml/min, 2h<br>($CH_4$:$CO_2$), 21.1 L/g.h, 650°C | 34 | 43 | 0.78 | 12 | 31 | 41 | 0.76 |
| | Ni/MN3 | | | 11 | | | 39 | 49 | 0.88 | | 28 | 39 | 0.79 |
| 12 | 5%Ni/OM-5Mg95Al | | 5 | | | Fixed-bed quartz reactor, 200 mg, atm<br>600°C, 20%$H_2$/Ar, 2h<br>100%($CH_4$:$CO_2$), 12.9 L/g.h, 700°C | 80 | 81 | 0.8 | 100 | 75 | 76 | 0.8 |
| 62 | I-Ni/CNTs | | 10 | 7.1 ± 1.7 | | Fixed-bed quartz reactor, n.d., atm<br>500°C, 5%$H_2$,40 ml/min, 2h<br>90%($CH_4$:$CO_2$)/Ar, 1 g.h/mol, 750°C | 70.2 | 83.4 | 0.91 | 8 | 65.4 | 78.8 | 0.84 |
| | O-Ni/CNTs | | | 7.5 ± 1.1 | | | 58.9 | 75.6 | 0.84 | | 50.1 | 66.1 | 0.78 |

[a] $CH_4$:$CO_2$=0.96
[b] test at 1.5MPa
[c] $CH_4$:$CO_2$=7:3
[d] $CH_4$:$CO_2$=0.5
[e] $CH_4$:$CO_2$=0.93
[f] $CH_4$:$CO_2$=2.38
* test performed without reduction

Table A-3: Literature data of some nickel-based catalysts promoted with noble metals and their performances in dry reforming of methane

| Ref | Catalyst Name | type | Ni (wt%) | Co-metal | Ni (nm) | Ni spent (nm) | **Test conditions** Reactor, catalyst weight, pressure Reduction Reaction ($CH_4$:$CO_2$=1) | $X(CH_4)_i$ (%) | $X(CO_2)_i$ (%) | $(H_2:CO)_i$ | Time (h) | $X(CH_4)_f$ (%) | $X(CO_2)_f$ (%) | $(H_2:CO)_f$ |
|---|---|---|---|---|---|---|---|---|---|---|---|---|---|---|
| 22 | Rh-Ni/Ce(3)Al | Non-porous | 5 | Rh | 20 | 23 | Fixed-bed quartz reactor, 30 mg, atm 750°C, $H_2$, 1h ($CH_4$:$CO_2$)/He, 200 L/g.h, 750°C[a] | 90 | | | 20 | 85 | | |
| | Rh-Ni/Ce(5)Al | | | | 20 | 24 | | 85 | | | 20 | 80 | | |
| 25 | NiAuAl | | 4 | Au | 6.6 | | Fixed-bed reactor, 50mg, n.d. 750°C, 5%$H_2$/Ar, 1h 30%($CH_4$:$CO_2$)/He, 60 L/g.h, 750°C | 82 | 89 | | 24 | 78 | 86 | |
| | NiPtAl | | | Pt | 6.2 | | | 86 | 92 | | 24 | 85 | 90 | |
| | NiAuPtAl | | | AuPt | 6.1 | | | 87 | 92 | | 24 | 83 | 91 | |
| 1 | 0.3Pt-10Ni/$Al_2O_3$ | | 10 | Pt | 12.6 | 12.8 | Fixed-bed quartz reactor, n.d., atm 500°C, $H_2$ ,50 ml/min, 2h ($CH_4$:$CO_2$), 15.6 L/g.h, 650°C | 78 | 72 | 0.85 | 4 | 75 | 75 | 0.85 |
| | 0.3Pt-15Ni/$Al_2O_3$ | | 15 | | | | | 53 | 50 | 1.15 | 4 | 55 | 42 | 0.9 |
| | 0.2Pt-10Ni/$Al_2O_3$ | | 10 | | | | | 43 | 50 | 0.8 | 4 | 45 | 45 | 0.85 |
| | 0.2Pt-15Ni/$Al_2O_3$ | | 15 | | 19.8 | 20.1 | | 32 | 40 | 1.1 | 4 | 0 | 0 | 0 |
| 2 | Pt(0.5%)Ni(10%)/$Al_2O_3$ | | 10 | Pt | | | Flow equipment, 170 mg, n.d. 750°C, $H_2$, 3h ($CH_4$:$CO_2$), 20 mL/min, 700°C | 78 | 95 | 0.63 | 108 | 78 | 98 | 0.63 |
| 3 | 0.04Pt4Ni/$Al_2O_3$ IM | | 10 | Pt | | 13 | Fixed-bed SS reactor, 100 mg, atm 700°C, 3%$H_2$/He,30 ml/min,2h 40%($CH_4$:$CO_2$)/He, 30 L/g.h, 700°C | | 74 | | 14 | | 68 | |
| | 0.04Pt4Ni/$Al_2O_3$ ME | | | | | 8 | | | 72 | | 14 | | 70 | |
| 35 | 3.75Ni-1.25Rh/$SiO_2$ | porous | 3.75 | Rh | | | Quartz microreactor, 100 mg, atm 600°C, $H_2$, 1h ($CH_4$:$CO_2$), 30 L/g.h, 700°C | 81 | 82 | | 24 | | | |
| | 2.5Ni-2.5Rh/$SiO_2$ | | 2.5 | | | | | 82 | 83 | | 24 | | | |
| | 1.25Ni-3.75Rh/$SiO_2$ | | 1.25 | | | | | 83 | 84 | | 24 | | | |
| | 5Rh/$SiO_2$ | | 0 | | | | | 84 | 84 | | 24 | | | |
| | 2.5Ni-2.5Rh/SiO2 (n) | | 2.5 | | | | | 84 | 85 | | 24 | | | |

Table A-3: *Continued*

| Ref | Catalyst Name | type | Ni (wt%) | Co-metal | Ni (nm) | Ni spent (nm) | **Test conditions**<br>Reactor, catalyst weight, pressure<br>Reduction<br>Reaction ($CH_4$:$CO_2$=1) | $X(CH_4)_i$ (%) | $X(CO_2)_i$ (%) | $(H_2:CO)_i$ | Time (h) | $X(CH_4)_f$ (%) | $X(CO_2)_f$ (%) | $(H_2:CO)_f$ |
|---|---|---|---|---|---|---|---|---|---|---|---|---|---|---|
| 38 | Rh@Ni/MCM-41 | Mesoporous | | Rh | | | Quartz flow reactor, 100 mg<br>n.d.<br>($CH_4$:$CO_2$)/Ar, 36 L/g.h, 600°C | 34 | 46 | | 14 | 15 | 43 | |
| | Rh-Ni/MCM-41 | | | | | | | 34 | 42 | | 14 | 25 | 37 | |
| 4 | 0.01Rh-Ni/Yas3-8 | | | Rh | | | Quartz reactor, 50 mg, atm<br>800°C, $H_2$, 1h<br>100%($CH_4$:$CO_2$), 120 L/g.h, 800°C | | | | 4 | 64 | 71 | |
| | 0.1Rh-Ni/Yas3-8 | | | | | | | | | | 4 | 70 | 76 | |
| 47 | 0.5Ru@Ni-MCM-41 | | | Ru | 13.4 | | Fixed-bed quartz reactor, 100 mg, atm<br>550°C, $H_2$, 3h<br>66%($CH_4$:$CO_2$)/Ar, 36 L/g.h, 600°C | 34 | 44 | | 4 | 35 | 38 | |
| | 1Ru@Ni-MCM-41 | | | | 19 | | | 28 | 44 | | 4 | 35 | 38 | |
| | 3Ru@Ni-MCM-41 | | | | 17.2 | | | 28 | 46 | | 4 | 35 | 43 | |
| 5 | 0.8Pt/4Ni-MCM-41 | | 4 | Pt | 4.7 ± 1.1 | 12.6 ± 6.9 | Fixed-bed reactor, n.d., atm<br>750°C, $H_2$, 2h<br>50%($CH_4$:$CO_2$)/He, 50 L/g.h, 750°C | 88 | | | 72 | 90 | | |
| 6 | 5% Ni-0.1% Pt/MgO | | 5 | Pt | 8.44 | | Fixed-bed reactor, 200 mg, atm<br>650°C, $H_2$, 30 ml/min, 4h<br>100%($CH_4$:$CO_2$), 15 L/g.h, 700°C | 80 | 82 | | 50 | 80 | 82 | |
| | 5% Ni-0.3% Pt/MgO | | | | 9.34 | | | 75 | 82 | | 50 | 75 | 82 | |
| 59 | 0.2PdNi/MCM-41 | | | Pd | | | Fixed-bed quartz reactor, 50 mg, atm<br>500°C, 10%$H_2$/$N_2$, 50 ml/min, 1h<br>40%($CH_4$:$CO_2$)/$N_2$, 120 L/g.h, 550°C | 25 | 32 | | 12 | 22 | 30 | 0.83 |
| | 0.3PdNi/MCM-41 | | | | | | | 36 | 54 | | 12 | 35 | 50 | 0.81 |
| | 0.4PdNi/MCM-41 | | | | | | | 30 | 42 | | 12 | 28 | 40 | 0.81 |

[a] $CH_4$:$CO_2$=0.5

Table A-4: Literature data of some nickel-based promoted catalysts and their performances in dry reforming of methane

| Ref | Catalyst Name | type | Ni (wt%) | Co-metal | Ni (nm) | Ni spent (nm) | Test conditions<br>Reactor, catalyst weight, pressure<br>Reduction<br>Reaction ($CH_4$:$CO_2$=1) | $X(CH_4)_i$ (%) | $X(CO_2)_i$ (%) | $(H_2:CO)_i$ | Time (h) | $X(CH_4)_f$ (%) | $X(CO_2)_f$ (%) | $(H_2:CO)_f$ |
|---|---|---|---|---|---|---|---|---|---|---|---|---|---|---|
| 63 | $LaNiO_3$ | Non-porous | 10 | La | | | Fixed-bed quartz reactor, 100 mg, n.d.<br>700°C, $H_2$, 1h<br>($CH_4$:$CO_2$), 36 L/g.h, 700°C | 45 | 56 | 1.05 | 60 | 25 | 37 | 0.78 |
| 10 | 0.5K-Ni/MgO-$ZrO_2$ | | 10 | K | | | Fixed-bed quartz reactor, 20 mg, atm<br>750°C, 5%$H_2$/Ar, 2h<br>20%($CH_4$:$CO_2$)/Ar, 150 L/g.h, 750°C | 87 | | | 14 | 87 | | |
| | 0.9K-Ni/MgO-$ZrO_2$ | | | | | | | 85 | | | | 81 | | |
| | 1.4K-Ni/MgO-$ZrO_2$ | | | | | | | 72 | | | | 69 | | |
| | 1.9K-Ni/MgO-$ZrO_2$ | | | | | | | 65 | | | | 65 | | |
| 11 | 1PrT500 | | 10 | Pr | 16 | 15 | Fixed-bed quartz reactor, 50 mg, n.d.<br>10%$H_2$/Ar, 30 ml/min<br>100%($CH_4$:$CO_2$), 96 L/g.h, 700°C | 0 | 0 | | 5 | 42 | 51 | 0.64 |
| | 3PrT500 | | | | 13 | 14 | | 0 | 0 | | | 45 | 56 | 0.62 |
| | 5PrT500 | | | | 15 | 15 | | 0 | 0 | | | 45 | 47 | 0.67 |
| | 1PrT800 | | | | 18 | 17 | | 0 | 0 | | | 35 | 38 | 0.53 |
| | 3PrT800 | | | | 16 | 15 | | 0 | 0 | | | 38 | 43 | 0.57 |
| | 5PrT800 | | | | 15 | 15 | | 0 | 0 | | | 35 | 40 | 0.58 |
| 18 | Ni-La/$SiO_2$ | | 10 | La | | 8 | Fixed-bed quartz reactor, 250 mg, atm<br>800°C, $H_2$/Ar, 60 ml/min, 1h<br>100%($CH_4$:$CO_2$), 14.4 L/g.h, 800°C | | | | 10 | 83.5 | 86.5 | |
| | Ni-Mg/$SiO_2$ | | | Mg | | 18 | | | | | | 74.6 | 78.6 | |
| | Ni-Co/$SiO_2$ | | | Co | | 25 | | | | | | 37.5 | 50.3 | |
| | Ni-Zn/$SiO_2$ | | | Zn | | 14 | | | | | | 32.8 | 43.9 | |
| | Ni-La(0.25)/$SiO_2$ | | | La | | | | 63.5 | 74 | | | 54.1 | 66.4 | 0.57 |
| | Ni-La(1)/$SiO_2$ | | | | | | | 49.1 | 60.9 | | | 40.9 | 52.6 | 0.42 |
| | Ni-La(5)/$SiO_2$ | | | | | | | 91.7 | 93.1 | | | 90.8 | 92.8 | 0.7 |
| | Ni-La(10)/$SiO_2$ | | | | | | | 89.1 | 91.3 | | | 88.4 | 90.5 | 0.65 |
| | Ni-La(15)/$SiO_2$ | | | | | | | 90 | 91.4 | | | 88.2 | 91.2 | 0.67 |
| 19 | Ni-Al-La | | 33 | $La_2O_3$ | | 11.3 | Fixed-bed quartz reactor, 50 mg, atm<br>650°C, 50%$H_2$/$N_2$<br>33%($CH_4$:$CO_2$)/$N_2$, 360 L/g.h, 700°C | 43 | 49 | | 4 | 58 | 66 | |
| | Ni-Al-La | | | | | 12.1 | | 51 | 55 | | | 64 | 71 | |
| | Ni-Al-La | | | | | 24.3 | | 54 | 61 | | | 55 | 61 | |
| | Ni-Al-La | | | | | 31.2 | | | | | 74 | 40 | | |

Table A-4: *Continued*

| Ref | Catalyst Name | type | Ni (wt%) | Co-metal | Ni (nm) | Ni spent (nm) | Test conditions<br>Reactor, catalyst weight, pressure<br>Reduction<br>Reaction ($CH_4$:$CO_2$=1) | $X(CH_4)_i$ (%) | $X(CO_2)_i$ (%) | $(H_2:CO)_i$ | Time (h) | $X(CH_4)_f$ (%) | $X(CO_2)_f$ (%) | $(H_2:CO)_f$ |
|---|---|---|---|---|---|---|---|---|---|---|---|---|---|---|
| 64 | $NiSn_{0.008}/SiO_2$ | Non-porous | 0.87 | Sn | | | n.d., 50 mg, n.d.<br>500°C, 50%$H_2$/$N_2$, 8h<br>40%($CH_4$:$CO_2$)/$N_2$, 3.7 L/g.h, 500°C[a] | | | 0.38 | 25 | | | 0.2 |
| | $NiSn_{0.03}/SiO_2$ | | 0.83 | | 2.3 | | | | | 0.3 | | | | 0.15 |
| | $NiSn_{0.13}/SiO_2$ | | 0.82 | | 2.3 | | | | | 0.15 | | | | 0.08 |
| | $NiSn_{0.32}/SiO_2$ | | 0.85 | | 2.8 | | | | | 0.05 | | | | 0.02 |
| 32 | OM1 | | | Ce | | | Quartz reactor, 50 mg, atm<br>700°C, 100%$H_2$, 30 ml/min, 1h<br>40%($CH_4$:$CO_2$)/He, 48 L/g.h, 700°C | 88.3 | 84 | 1 | 6 | 86.1 | 81.6 | 1 |
| | OM3 | | | | | | | 90.3 | 85.5 | 1 | | 87.6 | 83.3 | 1 |
| | OM5 | | | | | | | 71 | 86.9 | 1 | | 68 | 86.1 | 1 |
| | OM10 | | | | | | | 92.3 | 89.4 | 1 | | 88.6 | 87.2 | 1 |
| | OM3 | | | | | | | 100 | 95 | 0.67 | 100 | 97 | 95 | 0.9 |
| | OM3 | | | | | | | 90 | 88 | 1.35 | 20 | 90 | 85 | 1.4 |
| | OM3 | | | | | | | 85 | 88 | 0.95 | | 92 | 60 | 0.7 |
| 21 | Ni-Ca-ZrLa | | 5 | CaO | | | Fixed-bed quartz reactor, 10 mg, atm<br>500°C, 25%$H_2$/He, 100 ml/min, 2h<br>20%($CH_4$:$CO_2$)/He, 600 L/g.h, 450°C | | | | 0.5 | 9.1 ± 0.5 | 12.0 ± 0.6 | 0.67 |
| | Ni-Ca-ZrLa | | | | | | | 17 | | | 14 | 4 | | |
| 24 | $Ni/CeO_2$-3Ag | | 10 | Ag | | | Fixed-bed quartz reactor, 300 mg, atm<br>800°C, 100%$H_2$, 60 ml/min, 2h<br>73%($CH_4$:$CO_2$)/$N_2$, 13.6 L/g.h, 760°C | 24.92 | 45 | 0.47 | 100 | 20.96 | 40 | 0.42 |
| | $Ni/CeO_2$-6Ag | | | | | | | 14.15 | 20 | 0.37 | | 12.76 | 16 | 0.35 |
| | $Ni/CeO_2$-24Ag | | | | | | | 12.87 | 19 | 0.35 | | 11.76 | 17 | 0.31 |
| | $Ni/CeO_2$-3Ag | | | | | | | 29.47 | 25 | 0.46 | | 23.09 | 22 | 0.42 |
| | $Ni/CeO_2$-6Ag | | | | | | | 28.28 | 20 | 0.37 | | 23.04 | 19 | 0.36 |
| | $Ni/CeO_2$-24Ag | | | | | | | 22.96 | 19 | 0.34 | | 18.37 | 18 | 0.32 |
| 33 | 10% $Ni/La_2O_3$-γ-$Al_2O_3$ | | 10 | La | | | Fixed-bed quartz reactor, 200 mg, atm<br>500°C, 100%$H_2$, 40 ml/min, 1h<br>91.2%($CH_4$:$CO_2$)/Ar, 12 L/g.h, 700°C[b] | 57.5 | 80 | | 8 | | | |
| | 1%Ce-3%$La_2O_3$-10% Ni/γ-$Al_2O_3$ | | | La-Ce | | | | 76.79 | 97.15 | 1.01 | | | | |
| | 3%Ce-3%$La_2O_3$-10% Ni/γ-$Al_2O_3$ | | | | | | | 77.27 | 97.05 | 1.09 | | | | |
| | 5%Ce-3%$La_2O_3$-10% Ni/γ-$Al_2O_3$ | | | | | | | 77.17 | 96.8 | 1.15 | | | | |
| | 7%Ce-3%$La_2O_3$-10% Ni/γ-$Al_2O_3$ | | | | | | | 77.09 | 94.04 | 1.19 | | | | |

Table A-4: *Continued*

| Ref | Catalyst Name | type | Ni (wt%) | Co-metal | Ni (nm) | Ni spent (nm) | Test conditions<br>Reactor, catalyst weight, pressure<br>Reduction<br>Reaction ($CH_4$:$CO_2$=1) | $X(CH_4)_i$ (%) | $X(CO_2)_i$ (%) | $(H_2:CO)_i$ | Time (h) | $X(CH_4)_f$ (%) | $X(CO_2)_f$ (%) | $(H_2:CO)_f$ |
|---|---|---|---|---|---|---|---|---|---|---|---|---|---|---|
| 63 | $LaNiO_3$/SBA-15 | Mesoporous | 10 | La | | 7.7 | Fixed-bed quartz reactor, 100 mg, n.d.<br>700°C, $H_2$, 1h<br>($CH_4$:$CO_2$), 36 L/g.h, 700°C | 75 | 70 | 1.08 | 60 | 70 | 62 | 0.97 |
| | $LaNiO_3$/MCM-41 | | | | | 12.5 | | 80 | 70 | 1.08 | | 75 | 60 | 0.94 |
| | $LaNiO_3$/$SiO_2$ | | | | | 14.4 | | 68 | 64 | 1.03 | | 47 | 45 | 0.87 |
| 41 | 0.7Mo1Ni/SBA-15 | | 12 | Mo | 15.7 | 20.9 | Fixed-bed quartz reactor, 400 mg, atm<br>800°C, 20%$H_2$/$N_2$, 3h<br>($CH_4$:$CO_2$), 4 L/g.h, 800°C | 94.1 | | | 250 | | | |
| | 0.5Mo1Ni/SBA-15 | | | | 10.7 | 20.5 | | 94.3 | | 0.96 | 600 | 94.3 | | 0.96 |
| | 0.3Mo1Ni/SBA-15 | | | | 19.5 | 21.7 | | 95.5 | | | 130 | | | |
| 44 | 2Ni-1Zr/MCM-41 | | 1.93 | Zr | 15.4 | 21 | Quartz reactor, 120 mg, atm<br>750°C, He,2h<br>50%(CH4:CO2)/He, 50 L/g.h, 750°C | 92 | | 0.98 | 72 | 92 | | 1 |
| | 2Ni-1Ti/MCM-41 | | 1.95 | Ti | 49.8 | 21 | | 11 | | 0.08 | | 0 | | 0 |
| | 2Ni-1Mn/MCM-41 | | 1.92 | Mn | 33 | 16 | | 5 | | 0.08 | | 0 | | 0 |
| 45 | Ni/SBA-15-CD(1/1) | | 4.8 | CD | 24.2 | | Fixed-bed quartz reactor, 200 mg, atm<br>600°C, 20%$H_2$/Ar, 2h<br>100%($CH_4$:$CO_2$), 12.9 L/g.h, 700°C | 82 | 90 | 0.85 | 50 | 70 | 83 | 0.82 |
| | Ni/SBA-15-CD(1/8) | | | | 8.6 | | | 82 | 90 | 0.82 | | 77 | 87 | 0.87 |
| | Ni/SBA-15-CD(1/33) | | | | | | | 85 | 95 | 0.85 | | 84 | 95 | 0.83 |
| | Ni/SBA-15-CD(1/50) | | | | | | | 83 | 95 | 0.85 | | 82 | 95 | 0.89 |
| | Ni/SBA-15-CD(1/60) | | | | | | | 79 | 93 | 0.83 | | 77 | 93 | 0.82 |
| 46 | 5%Ni/CZ/SBA-15 | | 5 | CZ | | | Fixed-bed quartz reactor, 300 mg, atm<br>800°C, 3%$H_2$/Ar, 50 ml/min, 3h<br>20%($CH_4$:$CO_2$)/Ar, 20 L/g.h, 600°C | 42 | 48 | 0.7 | 30 | 40 | 45 | 0.7 |
| | 10%Ni/CZ/SBA-15 | | 10 | | | | | 50 | 65 | 0.78 | | 40 | 58 | 0.75 |
| | 15%Ni/CZ/SBA-15 | | 15 | | | | | 51 | 58 | 0.75 | | 40 | 48 | 0.75 |
| | 10%Ni/CZ/SBA-15 m.l. | | 10 | | | | | 48 | 51 | 0.75 | | 39 | 42 | 0.7 |
| 47 | 1Mg@1Ru@Ni-MCM-41 | | | Mg | 19 | | Fixed-bed quartz reactor, 100 mg, atm<br>550°C, $H_2$, 3h<br>66%($CH_4$:$CO_2$)/Ar, 36 L/g.h, 600°C | 32 | 45 | | 1 | 38 | 40 | 0.95 |
| 65 | IM2S | | 10 | $CeO_2$-$ZrO_2$ | | | Fixed-bed quartz reactor, 300 mg, atm<br>800°C, 3%$H_2$/Ar, 50 ml/min, 3h<br>20%($CH_4$:$CO_2$)/Ar, 20 L/g.h, 600°C | 49 | 56 | 0.77 | 24 | 42 | 48 | 0.73 |
| | IM1S | | | | | | | 45 | 51 | 0.8 | | 40 | 42 | 0.76 |
| | PM | | | | | | | 63 | 71 | 0.85 | | 61 | 68 | 0.84 |

Table A-4: *Continued*

| Ref | Catalyst Name | type | Ni (wt%) | Co-metal | Ni (nm) | Ni spent (nm) | Test conditions<br>Reactor, catalyst weight, pressure<br>Reduction<br>Reaction ($CH_4$:$CO_2$=1) | $X(CH_4)_i$ (%) | $X(CO_2)_i$ (%) | $(H_2:CO)_i$ | Time (h) | $X(CH_4)_f$ (%) | $X(CO_2)_f$ (%) | $(H_2:CO)_f$ |
|---|---|---|---|---|---|---|---|---|---|---|---|---|---|---|
| 54 | 4.8Ni/5Nd/SBA-15 | Mesoporous | 4.8 | Nd | | | Fixed-bed quartz reactor, 200 mg, atm<br>600°C, 20%$H_2$/Ar, 2h<br>100%($CH_4$:$CO_2$), 34.5 L/g.h, 800°C | 90 | 95 | | 50 | 88 | 92 | |
| | 4.8Ni/10Nd/SBA-15 | | | | | | | 88 | 95 | | | 88 | 95 | |
| | 4.8Ni/20Nd/SBA-15 | | | | | | | 84 | 91 | | | 80 | 90 | |
| | 4.8Ni/10La/SBA-15 | | | La | | | | 85 | 92 | | | 85 | 92 | |
| | 4.8Ni/10Ce/SBA-15 | | | Ce | | | | 89 | 92 | | | 86 | 92 | |
| 55 | NiCeAl (R=1) | | 7 | Ce | 7.8 | 5.8 | Fixed-bed quartz reactor, 100 mg, atm<br>700°C, $H_2$, 1h<br>($CH_4$:$CO_2$), 36 L/g.h, 700°C | 80 | | 0.95 | 80 | 80 | | 0.95 |
| | NiCeAl (R=2) | | | | 7.6 | 7.6 | | 80 | | 0.92 | 80 | 75 | | 0.87 |
| | NiCeAl-IMP (R=1) | | | | 9.6 | 8.2 | | 45 | | 0.92 | 80 | 38 | | 0.87 |
| 56 | NiCe/m$SiO_2$-S | | 9.2 | Ce | | | Fixed-bed quartz reactor, 150 mg, n.d.<br>800°C, 10%$H_2$/$N_2$, 30 ml/min, 1h<br>($CH_4$:$CO_2$), 6 L/g.h, 750°C | 90 | 98 | 1 | 20 | 90 | 97 | 1 |
| 31 | $LaNiO_3$/SBA-15 | | 10 | La | | | Fixed-bed quartz reactor, 200 mg, atm<br>600°C, $H_2$, 20 ml/min, 4h<br>20%($CH_4$:$CO_2$)/Ar, 24 L/g.h, 700°C | 90 | | | 24 | 88 | | |
| | $La_{0.8}Ca_{0.2}NiO_3$/SBA-15 | | | La-Ca | | | | 77 | | | | 82 | | |
| | $La_{0.8}Ca_{0.2}Ni_{0.6}Co_{0.4}O_3$/SBA-15 | | | La-Ca-Co | | | | 82 | | | | 86 | | |

[a] $CH_4$:$CO_2$=1.3
[b] $CH_4$:$CO_2$=0.93

## References

[1] S. Ozkara-Aydınoglu, A. Erhan Aksoylu International Journal of Hydrogen Energy 36 (2011) 2950-2959.
[2] S.R. de Miguel, I.M.J. Vilella, S.P. Maina, D. San José-Alonso, M.C. Román-Martínez, M.J. Illán-Gómez, Applied Catalysis A: General 435-436 (2012) 10-18.
[3] M. Garcıa-Dieguez, I.S. Pieta, M.C. Herrera, M.A. Larrubia, L.J. Alemany, Applied Catalysis A: General 377 (2010) 191-199.
[4] Z. Hou, P. Chen, H. Fang, X. Zheng, T. Yashima, International Journal of Hydrogen Energy 31 (2006) 555-561.
[5] D. Liu, W. Ni, E. Cheo, Y. Wen, Y. Lim, A. Borgna, R. Lau, Y. Yang, Catalysis Today 154 (2010) 229-236.
[6] F. Meshkani, M. Rezaei, International Journal of Hydrogen Energy 35 (2010) 10295-10301.
[7] P. Djinovi, J. Batista, A. Pintar, International Journal of Hydrogen Energy 37 (2012) 2699-2707.
[8] L. Qian, W. Cai, L. Zhang, L. Ye, J. Li, M. Tang, B. Yue, H. He, Applied Catalysis B: Environmental 164 (2015) 168-175.
[9] G. Sierra Gallego, F. Mondragon, J. Barrault, J.M. Tatibouet, C. Batiot-Dupeyrat, Applied Catalysis A: General 311 (2006) 164-171.
[10] B. Mallanna Nagaraja, D. A. Bulushev, S. Beloshapkin, J.R.H. Ross, Catalysis Today 178 (2011) 132-136.
[11] O. Gamba, S. Moreno, R. Molina, International Journal of Hydrogen Energy 36 (2011) 1540-1550.
[12] L. Xu, H. Song, L. Chou, International Journal of Hydrogen Energy 38 (2013) 7307-7325.
[13] J. Guo, H. Lou, H. Zhao, D. Chai, X. Zheng, Applied Catalysis A: General 273 (2004) 75-82.
[14] Y. Wang, H. Wang, Y. Li, Q. Zhu, B. Xu, Topics in Catalysis 32 (2005) 109-116.
[15] H.S. Potdar, H. Roh, K. Jun, M. Ji, Z. Liu, Catalysis Letters 84 (2002) 95-100.
[16] Y. Wang, B. Xu, Catalysis Letters 99 (2005) 89-96.
[17] A. Horváth, G. Stefler, O. Geszti, A. Kienneman, A. Pietraszek, L. Guczi, Catalysis Today 169 (2011) 102-111.
[18] J. Zhu, X. Peng, L. Yao, J. Shen, D. Tong, C. Hu, International Journal of Hydrogen Energy 36 (2011) 7094-7104.
[19] R. Martınez, E. Romero, C. Guimon, R. Bilbao, Applied Catalysis A: General 274 (2004) 139-149.
[20] J. Kim, D. Jin Suh, T. Park, K. Kim, Applied Catalysis A: General 197 (2000) 191-200.
[21] B. Bachiller-Baeza, C. Mateos-Pedrero, M.A. Soria, A. Guerrero-Ruiz, U. Rodemerck, I. Rodríguez-Ramos, Applied Catalysis B: Environmental 129 (2013) 450-459.
[22] M. Ocsachoque, F. Pompeo, G. Gonzalez, Catalysis Today 172 (2011) 226-231.
[23] A. Pietraszek, B. Koubaissy, A.C. Roger, A. Kiennemann, Catalysis Today 176 (2011) 267-271.
[24] M. Yu, Y. Zhu, Y. Lu, G. Tong, K. Zhu, X. Zhou, Applied Catalysis B: Environmental 165 (2015) 43-56
[25] H. Wu, G. Pantaleo, V. La Parola, A.M. Venezia, X. Collard, C. Aprile, L.F. Liotta, Applied Catalysis B: Environmental 156-157 (2014) 350-361.
[26] N. Sun, X. Wen, F. Wang, W. Wei, Y. Sun, Energy and Environmental Science 3 (2010) 366–369.
[27] C.E. Quincoces, E.I. Basaldella, S.P. De Vargas, M.G. Gonzalez, Materials Letters 58 (2004) 272-275.
[28] H. Roh, K. Jun, S. Baek, S. Park, Catalysis Letters 81 (2002) 147-151.
[29] A.L. Pinheiro, A.N. Pinheiro, A. Valentini, J. Mendes Filho, F.F. de Sousa, J.R. de Sousa, M. da Graça, C. Rocha, P. Bargiela, A. C. Oliveira, Catalysis Communications 11 (2009) 11-14.
[30] J. Juan-Juan, M.C. Roman-Martınez, M.J. Illan-Gomez, Applied Catalysis A: General 355 (2009) 27-32.
[31] I. Rivas, J. Alvarez, E. Pietri, M. Josefina Perez-Zurita, M.R. Goldwasser, Catalysis Today 149 (2010) 388-393.

[32] C. Enrique Daza, J. Gallego, F. Mondragón, Sonia Moreno, Rafael Molina, Fuel 89 (2010) 592-603.
[33] R. Yang, C. Xing, C. Lv, L. Shi, N. Tsubaki, Applied Catalysis A: General 385 (2010) 92-100.
[34] L. Guczi, G. Stefler, O. Geszti, I. Sajo, Z. Paszti, A. Tompos, Z. Schay, Applied Catalysis A: General 375 (2010) 236-246.
[35] W.K. Jozwiak, M. Nowosielska, J. Rynkowski, Applied Catalysis A: General 280 (2005) 233-244.
[36] A. Luengnaruemitchai, A. Kaengsilalai, Chemical Engineering Journal 144 (2008) 96-102.
[37] P. Frontera, A. Aloise, A. Macario, F. Crea, P. L. Antonucci, G. Giordano, J. B. Nagy, Research on Chemical Intermediates 37 (2011) 267-279.
[38] H. Arbag, S. Yasyerli, N. Yasyerli, G. Dogu, International Journal of Hydrogen Energy 35 (2010) 2296-2304.
[39] B. Li, X. Xu, S. Zhang, International Journal of Hydrogen Energy 38 (2013) 890-900.
[40] N. Wang, X. Yu, K. Shen, W. Chu, W. Qian, International Journal of Hydrogen Energy 38 (2013) 9718-9731.
[41] T. Huang, W. Huang, J. Huang, P. Ji, Fuel Processing Technology 92 (2011) 1868-1875.
[42] P. Kumar, Y. Sun, R.O. Idem, Energy & Fuels 21 (2007) 3113-3123.
[43] A. Kambolis, H. Matralis, A. Trovarelli, Ch. Papadopoulou, Applied Catalysis A: General 377 (2010) 16-26.
[44] Da. Liu, X. Yang Quek, W. Ni Evelyn Cheo, R. Lau, A. Borgna, Y. Yang, Journal of Catalysis 266 (2009) 380-390.
[45] H. Liu, Y. Li, H. Wu, T. Miyake, D. He, International Journal of Hydrogen Energy 38 (2013) 15200-15209.
[46] A. Albarazi, P. Beaunier, P. Da Costa, International Journal of Hydrogen Energy 38 (2013) 127-139.
[47] S. Yasyerli, S. Filizgok, H. Arbag, N. Yasyerli, G. Dogu, International Journal of Hydrogen Energy 36 (2011) 4863-4874.
[48] X. Zhang, Q. Zhang, N. Tsubaki, Y. Tan, Y. Han, Fuel 147 (2015) 243-252.
[49] Z. Hou, O. Yokota, T. Tanaka, T. Yashima, Catalysis Letters 89 (2003) 121-127.
[50] Z. Hou, T. Yashima, Applied Catalysis A: General 261 (2004) 205–209.
[51] P. Chen, Z. Hou, X. Zheng, T. Yashima, Reaction Kinetics and Catalysis Letters 86 (2005) 51-58.
[52] W. Donphai, K. Faungnawakij, M. Chareonpanich, J. Limtrakul, Applied Catalysis A: General 475 (2014) 16-26.
[53] W. Cai, L. Ye, L. Zhang, Y. Ren, B. Yue, X. Chen, H. He, Materials 7 (2014) 2340-2355.
[54] H. Liu, Y. Li, H. Wu, W. Yang, D. He, Chinese Journal of Catalysis 35 (2014) 1520-1528.
[55] N. Wang, Z. Xu, J. Deng, K. Shen, X. Yu, W. Qian, W. Chu, F. Wei, ChemCatChem 6 (2014) 1470-1480.
[56] C. Wang, N. Sun, N. Zhao, W. Wei, Y. Sun, C. Sun, H. Liu, C.E. Snape, Fuel 143 (2015) 527-535.
[57] I. Luisetto, S. Tuti, C. Battocchio, S. Lo Mastro, A. Sodo, Applied Catalysis A: General 500 (2015) 12-22.
[58] K. Jabbour, N. El Hassan, A. Davidson, P. Massiani, S. Casale, Chemical Engineering Journal 264 (2015) 351-358.
[59] S. Damyanova, B. Pawelec, K. Arishtirova, J.L.G. Fierro, C. Sener, T. Dogu, Applied Catalysis B: Environmental 92 (2009) 250-261.
[60] D. Liu, X. Quek, H. Hui, A. Wah, G. Zeng, Y. Li, Y. Yang, Catalysis Today 148 (2009) 243-250.
[61] T. Sukonket, A. Khan, B. Saha, H. Ibrahim, S. Tantayanon, P. Kumar, R. Idem, Energy Fuels 25 (2011) 864-877.
[62] Q. Ma, D. Wang, M. Wu, T. Zhao, Y. Yoneyama, N. Tsubaki, Fuel 108 (2013) 430-438.
[63] N. Wang, X. Yu, Y. Wang, W. Chu, M. Liu, Catalysis Today 212 (2013) 98-107.
[64] D. Baudouin, J.P. Candy, U. Rodemerck, F. Krumeich, L. Veyre, P.B. Webb, C. Thieuleux, C. Copéret, Catalysis Today 235 (2014) 237-244.
[65] A. Albarazi, M.E. Gálvez, P. Da Costa, Catalysis Communications 59 (2015) 108-112.

# APPENDIX 2

# Attribution of NiO Reduction Peaks

It is known that NiO is directly reduced to metallic $Ni^0$ without passing by intermediate oxides.[1] Accordingly, the reduction peaks at different temperatures on the TPR profiles are attributed to the reduction of different Ni species. In order to clarify the attribution of each reduction peak, a series of TPR-XRD experiments were done (Fig. A-1). In details, the TPR experiments were done several times under the same operating conditions (5 vol % $H_2$/Ar at 20 $mL.min^{-1}$, heating rate of $10°C.min^{-1}$) while stopping the experiments at the temperatures marked by dashed lines on the TPR profiles (Fig. A-1). The resulting reduced (green dashed lines on Fig. A-1) or partially reduced (blue or red dashed lines on Fig. A-1) samples were directly analyzed by XRD, in order to determine the oxidation state of nickel species.

Before any hydrogen consumption (T<250°C), the only diffraction peaks observed on the XRD of all samples at 37, 43 and 63° correspond to nickel oxide (Fig. A-1A,D,G,J). After complete reduction (T>700°C), narrow diffraction peaks are observed at 44, 52 and 76°, typical of metallic $Ni^0$ phase (Fig. A-1C,F,I,L). The absence of NiO characteristic peaks reveals the complete reduction of NiO, regardless of the sample.

Moreover, the XRD profiles of the partially reduced samples reveal the co-existence of both nickel oxide species and metallic $Ni^0$ species (Fig. A-1B,E,H,K). The decrease of intensities of the NiO characteristic diffraction peaks, especially the one at $2\theta = 37°$, indicates that the first peak observed in the range of 250-420°C on the TPR profiles is well ascribed to the reduction of NiO species. This behavior is detected over the four samples, however the decrease is more pronounced on $Ni_{5.0}$/SBA-$B_1$(N) and $Ni_{5.0}Rh_{0.5}$/SBA-$B_1$(N) samples. On the other hand, the diffraction peak at 37° remains significant after partial reduction of $Ni_{5.0}$/SBA-$B_1$(Cl) and $Ni_{5.0}/SiO_2$(N) samples. Manukyan et al. studied the kinetics and structural transformations of bulk NiO crystals during their reduction by hydrogen.[2] At our operating temperatures, they report the formation of a complex polycrystalline Ni/NiO porous structure. Their findings can be used to explain the differences obtained between the samples. Indeed, $Ni_{5.0}$/SBA-$B_1$(Cl) and $Ni_{5.0}/SiO_2$(N) samples contain large NiO particles with an average particle size of 9 nm and their full reduction to $Ni^0$ requires some time. Consequently, at intermediate temperature (near

400°C), a partial fraction of the biggest NiO crystals is reduced while the remaining part (small crystallites) is responsible for the NiO diffraction peak that remains detectable by XRD at 37°. Thus both $Ni^0$ and NiO characteristic peaks are detectable by XRD.

Accordingly, it appears logical to attribute the TPR peak observed at low temperatures to the reduction of large NiO crystals, and the one at higher temperatures to the reduction of smaller particles highly dispersed on the support.[3,4,5] The larger particles are evidently in weak interaction with the support while the smaller ones are strongly attached to the support. Therefore, many use the degree of metal-support interaction to correlate the peaks in TPR.[6,7,8,9]

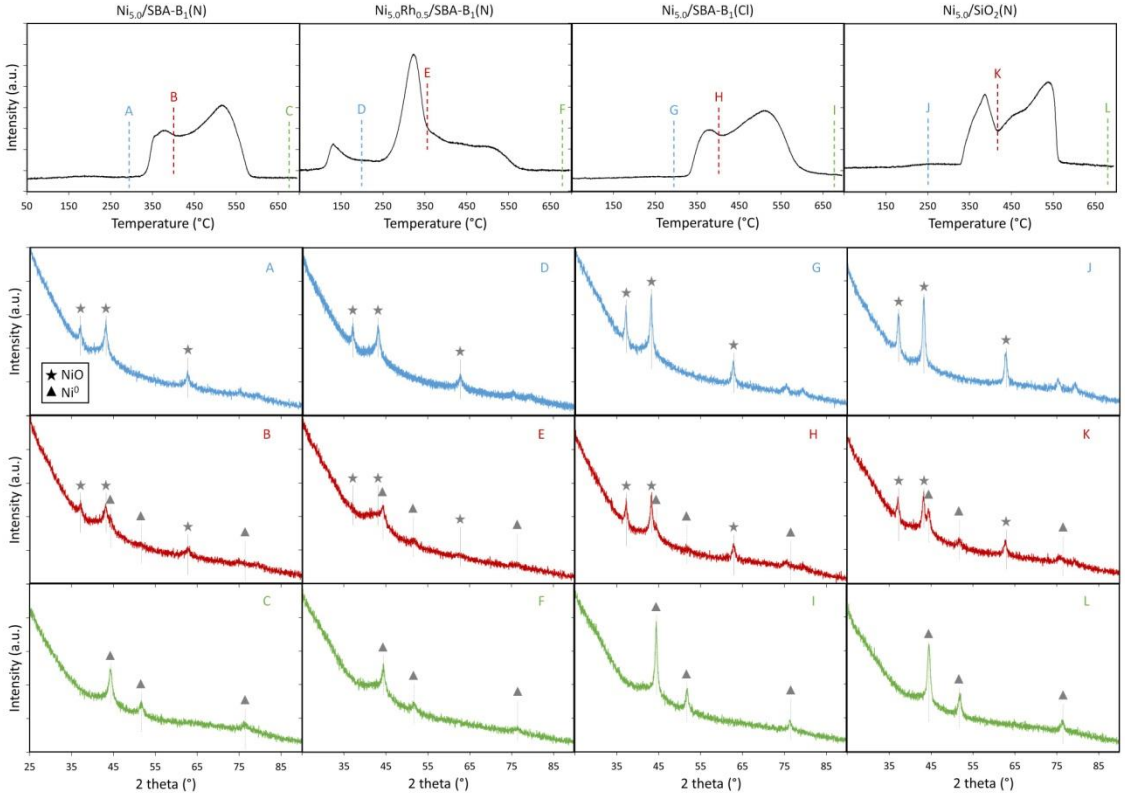


Figure A-1: TPR profiles and XRD patterns of (A,B,C) $Ni_{5.0}/SBA\text{-}B_1(N)$, (D,E,F) $Ni_{5.0}Rh_{0.5}/SBA\text{-}B_1(N)$, (G,H,I) $Ni_{5.0}/SBA\text{-}B_1(Cl)$ and (K,L,M) $Ni_{5.0}/SiO_2(N)$ samples

## References

[1] H. Wan, X. Li, S. Ji, B. Huang, K. Wang, C. Li, *Effect of Ni loading and $Ce_xZr_{1-x}O_2$ promoter on Ni-Based SBA-15 catalysts for steam reforming of methane*, Journal of Natural Gas Chemistry 16 (2007) 139-147.

[2] K.V. Manukyan, A.G. Avetisyan, C.E. Shuck, H.A. Chatilyan, S. Rouvimov, S.L. Kharatyan, A.S. Mukasyan, *Nickel oxide reduction by hydrogen: Kinetics and structural transformations*, Journal of Physical Chemistry C 119 (2015) 16131-16138.

[3] H. Ren, Y. Song, Q. Hao, Z. Liu, W. Wang, J. Chen, J. Jiang, Z. Liu, Z. Hao, J. Lu, *Highly active and stable Ni-$SiO_2$ prepared by a complex-decomposition method for pressurized carbon dioxide reforming of methane*, Industrial & Engineering Chemistry Resources 53 (2014) 19077-19086.

[4] B. Mile, D. Stirling, M.A. Zammitt, A. Lovell, M. Webb, *The location of nickel oxide and nickel in silica-supported catalysts: Two forms of "NiO" and the assignment of temperature-programmed reduction profiles*, Journal of Catalysis 114 (1988) 217-229.

[5] X. Yan, Y. Liu, B. Zhao, Z. Wang, Y. Wang, C. Liu, *Methanation over Ni/$SiO_2$: Effect of the catalyst preparation methodologies*, International Journal of Hydrogen Energy 38 (2013) 2283-2291.

[6] M. Tao, X. Meng, Y. Lv, Z. Bian, Z. Xin, *Effect of impregnation solvent on Ni dispersion and catalytic properties of Ni/SBA-15 for CO methanation reaction*, Fuel 165 (2016) 289-297.

[7] X. Zhang, Q. Zhang, N. Tsubaki, Y. Tan, Y. Han, *Carbon dioxide reforming of methane over Ni nanoparticles incorporated into mesoporous amorphous $ZrO_2$ matrix*, Fuel 147 (2015) 243-252.

[8] A. Ungureanu, B. Dragoi, A. Chirieac, S. Royer, D. Duprezb, E. Dumitriu, *Synthesis of highly thermostable copper-nickel nanoparticles confined in the channels of ordered mesoporous SBA-15 silica*, Journal of Materials Chemistry 21 (2011) 12529-12541.

[9] D. Liu, X. Quek, H. Hui, A. Wah, G. Zeng, Y. Li, Y. Yang, *Carbon dioxide reforming of methane over nickel-grafted SBA-15 and MCM-41 catalysts*, Catalysis Today 148 (2009) 243-250.

# APPENDIX 3

# Catalyst Shaping

Structuring and shaping of powders into solid bodies is essential from an industrial point of view, but it is not an easy task. Shaping methods include pelletizing, extrusion, spheronization or granulation. In general, powders can be compacted dry (mainly for pelletizing) or in the presence of a liquid, normally water, to form a paste (for extrusion, spheronization and wet granulation). Beside maintaining the high catalytic performance of the laboratory study, the shaped catalysts should also have the required mechanical strength and chemical stability to ensure smooth operation and long lifetime in industrial reactors. Additives should thus be employed to facilitate shaping and/or to enhance the properties of resulting catalysts. For example, binders (like natural clays: bentonite and sepiolite) are used to increase the mechanical strength upon hardening and plasticizers (like methyl cellulose, polyethylene glycol or water) are added to decrease the viscosity of mixtures in order to facilitate processing. These additives can alter the composition, structure, porosity, and performance of the catalysts.[1]

During this thesis, preliminary attempts for shaping Ni/SBA-15 catalysts were done using bentonite as binder and methyl cellulose as plasticizer, as found in literature.[2,3,4] The resulting mixtures were sometimes too dry to form a paste (Fig. A-2a), or too wet to form separate extrudates (Fig. A-2b,b') or even too thick to pass through the die (Fig. A-2c). A relatively good mixture (Fig. A-2d,d') apparently resisted the thermal treatment during calcination at 450°C for 2 hours (0.5°C.min$^{-1}$) and the extrudates did not break (Fig. A-2e,e'). However, these resulting extrudates were not tried in dry reforming of methane. A more developed and better focused study should be conducted in this direction.

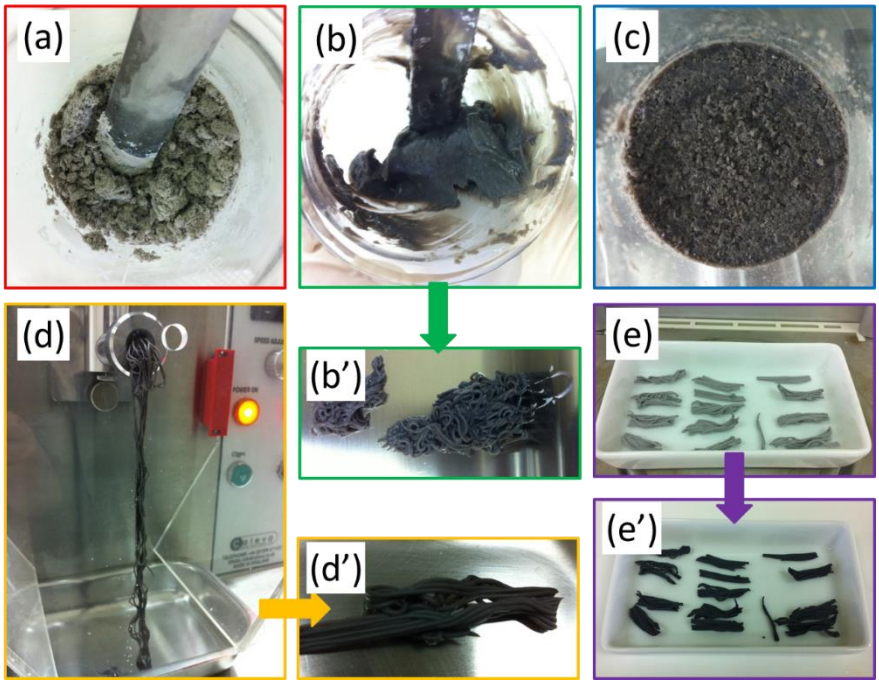


Figure A-2: Multiple trials for the extrusion of Ni/SBA-15 catalysts

## References

[1] S. Mitchell, N.L. Michels, J. Perez-Ramirez, *From powder to technical body: the undervalued science of catalyst scale up*, Chemical Society Reviews 42 (2013) 6094-6112.

[2] G. Chandrasekar, Martin Hartmann, M. Palanichamy, V. Murugesan, *Extrusion of AlSBA-15 molecular sieves: An industrial point of view*, Catalysis Communications 8 (2007) 457-461.

[3] G. Chandrasekar, M. Hartmann, V. Murugesan, *Preparation of SBA-15 extrudates: Evaluation of textural and mechanical properties*, Journal of Porous Materials 16 (2009) 175-183.

[4] J.A. Melero, J. Iglesias, J. Sainz-Pardo, P. de Frutos, S. Blazquez, *Agglomeration of Ti-SBA-15 with clays for liquid phase olefin epoxidation in a continuous fixed bed reactor*, Chemical Engineering Journal 139 (2008) 631-641.

# List of Figures

# List of Tables

## Abstract

Although economically and environmentally advantageous, the methane dry reforming process using supported nickel based catalysts still faces problems of active phase (a transition metal) sintering and of carbon deposition, which result in catalytic activity loss. This thesis is focused on the study of the confinement effect of nickel in mesoporous silica-based catalysts for syngas production by reforming of methane with $CO_2$. In this study, the samples were characterized by $N_2$ sorption, XRD, TEM/SEM, TPR, in addition to Raman, XPS, TPH/MS, TGA/MS for the spent catalysts. The results indicate that a well-structured mesoporous support with high surface area and large pore volume is important for better dispersion and stabilization of the active phase inside the porosity. The mesoporous SBA-15 silica support (prepared in large quantity), composed of elongated grains, appear to be suitable for the purpose. Moreover, it is demonstrated that the formation of small nickel particles well-confined inside the pores favors carbon resistance. This can be achieved by applying hydrothermal treatment to the support, using two solvents method for Ni deposition, using direct reduction of uncalcined samples, adding Rh in small quantities or promoting with Ce, provided that Ni and Ce are in interaction.

**Keywords**: confinement, nickel nanoparticles, mesoporous SBA-15, methane dry reforming

## Résumé

**« Effet de confinement du nickel dans des catalyseurs à base de silice mésoporeuse pour la production de gas de synthèse par reformage du méthane avec le $CO_2$ »**

Malgré ses avantages économiques et environnementaux, le procédé de reformage à sec du méthane sur des catalyseurs au nickel supporté se heurte encore à des problèmes de frittage de la phase active (un métal de transition) et de dépôt de carbone, ce qui entraîne une diminution de l'activité catalytique. Cette thèse porte sur l'étude de l'effet de confinement du nickel dans des catalyseurs à base de silice mésoporeuse pour la production de gaz de synthèse par reformage du méthane par le $CO_2$. Dans cette étude, les échantillons ont été caractérisés par physisorption de $N_2$, DRX, MET/MEB, RTP, et, en plus, par Raman, SPX, HTP/SM, ATG/SM pour les catalyseurs après test catalytique. Les résultats montrent qu'un support mésoporeux bien structuré ayant une grande surface spécifique et un grand volume poreux est important pour une meilleure dispersion et stabilisation de la phase active à l'intérieur de la porosité. La silice mésoporeuse de SBA-15 (préparée en grande quantité), composée de grains allongés, semble être appropriée pour atteindre cet objectif. Il est de plus démontré que la formation de petites particules bien confinées à l'intérieur des pores favorise la résistance au dépôt de carbone. Ceci peut être obtenu en imposant un traitement hydrothermal au support, en utilisant la méthode deux solvants pour le dépôt de Ni, en passant à une réduction directe des échantillons non calcinés, en ajoutant du Rh en faibles quantités ou en utilisant du Ce comme promoteur, à condition que le Ni et Ce soient en interaction.

**Mots clés :** confinement, nanoparticules de nickel, SBA-15 mésoporeuse, reformage à sec du méthane